Dissimilar Al6061 to Al7075 friction stir welds : processing, static and fatigue properties

Nicolas Dimov

To cite this version:

Nicolas Dimov. Dissimilar Al6061 to Al7075 friction stir welds : processing, static and fatigue properties. Materials and structures in mechanics [physics.class-ph]. Institut Polytechnique de Paris; Université catholique de Louvain (1970-..), 2022. English. NNT : 2022IPPAX128 . tel-04370244

HAL Id: tel-04370244
https://theses.hal.science/tel-04370244v1

Submitted on 3 Jan 2024

NNT : 2022IPPAX128

Thèse de doctorat

Dissimilar Al6061 to Al7075 friction stir welds: processing, static and fatigue properties

Thèse de doctorat de l'Institut Polytechnique de Paris
préparée à l'École polytechnique et à l'Université Catholique de Louvain

École doctorale n°626 École doctorale de l'Institut Polytechnique de Paris (EDIPP)
Spécialité de doctorat : Génie des procédés et énergétique

Thèse présentée et soutenue à Palaiseau, le 20 décembre 2022, par

Nicolas Dimov

Composition du Jury :

Hervé Jeanmart Professeur, Université Catholique de Louvain (iMMC)	Président
Marie-Noêlle Avettand-Fenoël Maîtresse de conférences, Université de Lille (UMET)	Rapportrice
Jean-Yves Buffière Professeur, INSA Lyon (MATEIS)	Rapporteur
Florent Hannard Docteur, Université Catholique de Louvain (iMMC)	Examinateur
Habibou Maitournam Professeur, ENSTA Paris (IMSIA)	Examinateur
Eric Charkaluk Directeur de recherche, Ecole Polytechnique (LMS)	Directeur de thèse
Aude Simar Professeure, Université Catholique de Louvain (iMMC)	Co-directrice de thèse
Julien Benoist Docteur, Thales Global Services	Invité
Thaneshan Sapanathan Docteur, Curtin University (Curtin Corrosion Center)	Invité
Daniel Weisz-Patrault Docteur, Ecole Polytechnique (LMS)	Invité

Contents

Remerciements

Je souhaite tout d'abord remercier chaleureusement mes trois encadrants Aude Simar, Eric Charkaluk et Julien Benoist. Merci du fond coeur de m'avoir accordé votre confiance ces trois (presque quatre !) dernières années. Je pense pouvoir dire sans aucun doute que vos grandes qualités scientifiques et humaines ont permis à cette thèse de voir le jour, surtout avec les évènements de ces dernières années qui n'ont clairement pas facilité votre tâche, et particulièrement combiné avec ma phobie exceptionnelle de l'administratif. Merci à Eric de m'avoir fait découvrir en premier l'univers des laboratoires au travers du LMS et pour tes connaissances scientifiques qui ont toujours fait avancer mes expériences plus loin que je ne l'aurais jamais espéré. Mon passage au LMS m'a fait devenir le scientifique que j'ai toujours rêvé d'être et je te serai éternellement reconnaissant pour cela. Merci à Julien qui m'a fait découvrir l'univers de l'entreprise chez Thales. Malgré tout le mal que j'ai pu en dire dans les moments où des contraintes industrielles se sont appliquées à mon travail, je pense que c'est malgré tout une expérience dont je garde un très bon souvenir. Enfin, un tout grand merci à Aude pour son encadrement exceptionnel, particulièrement sur les derniers mois de la thèse. La rédaction n'a pas été facile pour moi (comme pour beaucoup de doctorants), mais elle ne l'a pas été pour toi non plus et j'aurai à jamais une dette envers toi pour l'abnégation dont tu as fais preuve lors de ces longues soirées de correction.

Je souhaite également remercier Daniel Weisz-Patrault et Thaneshan Sapanathan pour avoir fait partie de mon comité d'encadrement et pour m'avoir aidé tout au travers de ma thèse. Thaneshan, thank you for everything you taught me over the past few years regarding FSW and especially the manufacturing of welded joints. I'll definitely miss breaking FMB tools with you. It's a shame we didn't have the chance to see each other as much as initially planned thanks to a certain pandemic, but I'll forever cherish those long afternoons spent on the welding machine trying to figure out the best parameters for my samples. Merci Daniel pour l'aide précieuse que tu m'as apporté tout au long de ma thèse. Je pense que je n'aurais jamais pu écrire ce satané papier ni le début de ma thèse sans tes inputs réguliers sur mon travail. Merci pour toutes ces discussions dans les moments où j'étais un peu perdu.

Je tiens aussi à remercier tous les permanents du LMS et de l'IMAP pour avoir été "mon deuxième comité d'encadrement" lors de ces dernières années. Merci à Simon et Alexandre pour toutes les connaissances que vous m'avez apportées sur la préparation d'échantillon et l'utilisation du MEB (de loin mon jouet favori au laboratoire) ainsi que pour l'aide plus que régulière lors de l'utilisation de nouveaux équipements ou de techniques d'observations. Merci à Vincent et Hakim de m'avoir appris à utiliser les machines de traction tout seul comme un grand. Merci à JC, qui j'espère passe la retraite qu'il mérite, pour tous ces moments où tu m'as aidé et pour la superbe collection de composants électroniques que tu m'as léguée lors de ton départ. Merci à Erik pour tes connaissances en

CAO, sans qui la découpe jet d'eau de mes éprouvettes de fatigue n'aurait jamais pu avoir lieu. Merci à Matthieu et Pascal pour m'avoir aidé dans ma fabrication d'échantillons sur les machines du LMS. Merci à Abdelfattah pour tes connaissances en informatique et pour les longues discussions lors du dépannage de machines dans ton bureau. Merci à John, Bruno, Alban, Marc, Ronny, Laurence et probablement bien d'autres pour m'avoir aidé lors de mes voyages belges sur toutes les techniques de fabrication et d'observation dont j'ai eu besoin.

Un immense merci à tous les doctorants et post-doctorants que j'ai rencontré lors de ces dernières années, aussi bien au LMS qu'en IMAP. Merci à Camille et Sofia de m'avoir accueilli dans leur bureau au début de ma thèse. Merci à Alexandre et Martin pour toutes ces sorties "extra-scolaires". Merci à Florian, Quentin, Nikhil, Kubra, Nina, Emilien, Geoffrey, Jérémie, Arnaud, Zahra, Théo, Filippo, Lauranne, Nicole, Yanis, Nikolai, Svetlana, Solenne, Thomas, Antoine, Chloé, Clément, etc (j'en oublie certainement) pour tous ces moments au LMS, ces soirées raclettes, soirées crêpes, soirées au bar, débats animés le midi au Magnan et lors du café. Un immense merci pour tout. Merci également du fond de mon coeur de français à tous les membres de l'UCLouvain pour leur incroyable accueil à chaque voyage que j'ai pu effectuer. Merci pour ces moments échangés lors des repas du midi et le soir dans les bars. Merci pour les 24h vélo, une expérience hors du commun que je n'oublierai jamais. Merci à Sarah pour ton sauvetage lors de la grève de la SNCB ! Merci Julie pour l'inspiration que m'a donné ton manuscrit lors de mon écriture. Merci Matthieu pour tous les innombrables conseils que tu as pu me donner tout au cours de ma thèse. Un tout grand merci Sarah, Sanjay, Nelson, Mariia, Nicolas, Antoine, Charline, Nathan, Sophie, MS, Marie-Charlotte, Catherine, etc (encore une fois, j'en oublie probablement) pour m'avoir considéré pleinement comme l'un des vôtres lors de mes escapades belges.

Un immense merci à mes collègues chez Thales. Merci Aurélien, Elodie, Ngoc, Chloé, Mélina, Julien, etc pour votre expertise, amitié et professionnalisme lors de mes passages chez Thales Global Services.

Un merci tout particulier à mes stagiaires. Merci Clément pour ton assiduité, ton abnégation face au polissage d'éprouvette, ta grande curiosité et ta bonne humeur. Mon chapitre sur la fatigue des soudures FSW n'existerait probablement pas sans ton travail. J'espère que j'ai su te repayer en margharitas ! Et qui sait, peut être que j'ai fais naître en toi une certaine passion pour la recherche ... Merci Laure pour ton travail **colossal** sur la dureté et la traction. Mon chapitre 4 n'existerait pas sans toi. Merci pour toutes ces discussions ferroviaires, ta qualité de cantatrice en salle des presses et ta bonne humeur. J'espère que ton amour pour le transport ferré ne s'altère jamais ! Enfin, merci Roméo pour les passionnantes discussions autour du FSW. Tu es malheureusement arrivé un peu tard dans ma thèse et je n'ai pas eu l'occasion de te faire souffrir au laboratoire comme les deux autres. Dommage !

Un immense merci à ma famille, qui m'a inculqué l'envie d'aller toujours plus loin, de m'avoir élevé et d'avoir fait de moi la personne que je suis, de m'avoir aidé à déménager, d'être toujours là pour moi et particulièrement en cette fin de thèse et pour après.

Un merci tout particulier à mes amis de l'ENSMA. Merci à toi Clément de m'avoir supporté en tant que colocataire malgré mon tempérament parfois électrique, surtout lors du confinement. Merci à vous Cléa et Guillaume, pour ces soirées jeux, sur Discord, ces sorties, ces randonnées. Merci Manon pour les barbecues chez tes parents dès que l'occasion se présentait ! Merci Lucas, MS, Ariane, pour les vacances, les Nouvel An, etc.

Honorable mention parmi mes amis à ma Méthée, Agathe Bernier. Merci pour tous ces moments à la Fansmare (RIP tes oreilles), à l'harmonie de Buxerolles (et le beau crâne chauve de Pascal), à la chorale (I hear the drums echoing tonight...), et ces milliers de messages sur Teams, à longueur de journée. Pour tes encouragements (quelle blague) et la régularité à laquelle tu es venue nous voir sur Paris (merci la SNCF). Plus sérieusement, merci Mithi. Sincèrement, ton Mithi.

Enfin, last but not least, merci à ma chérie, Chloé. Merci pour ces dernières années à me supporter. Pour toutes ces nuits ponctuées de ronflements, de coups de pieds, d'écrans allumés, etc. Pour toutes ces vacances, ces sorties. J'espère pouvoir t'embêter encore longtemps, et te faire des bons petits plats. Je t'aime chérie. A bientôt sur le vélo pour la nouvelle aventure !

Context

This PhD has been financed by Thales Global Services and focuses on the joining of dissimilar aluminium by Friction Stir Welding and its ensuing mechanical properties. The goal of this work is to study the link between process parameters, microstructural features of these welds and the ensuing influence on mechanical properties, tensile behavior and fatigue life. Currently, Thales is in the process of standardizing its practices across the entire Group and friction stir welding is not yet included in the tried and tested processes inside Thales. This study aims at answering key questions about friction stir welded joints in materials heavily used in this industry, with the objective of integrating the process at the design stage in further product developments.

Friction Stir Welding (FSW) is an assembly technique patented in 1991, at The Welding Institute (TWI) of Cambridge, UK [1]. FSW is considered a solid-state joining process in which a non-consumable rotating tool is plunged at the interface of two parts. The heat-induced friction of the tool on the material softens the alloy(s) of the parts and the rotary action of the tool mixes the material of both parts together. This welding technique requires a relatively low heat input compared to others fusion-based welding process. In addition, it offers great opportunity in the assembly of light alloys such as aluminium, magnesium, zinc or even copper. Additionally, the automation associated with FSW could be part of the answer regarding the shortage of skilled welders faced by some industrial sectors. In recent years, FSW has been tried and tested on higher strength metallic material such as steel, titanium and even superalloys.

Since its discovery and exploitation, aluminium has been used for its relatively excellent strength-to-weight ratio. Today, it is one of the most used metal in the world. As presented in Table 1, the density of aluminium is approximately 2700 kg/m^3. This density, combined with the good mechanical properties of high strength aluminium, allows for lighter structures in high stress environment compared with steel or even titanium.

In addition to having mechanical properties suitable for high stress applications, aluminium is also widely used for its electrical and thermal properties. As shown in Table 1, thermal and electrical conductivity of aluminium relative to its price and weight is on par with other popular metals considered for these applications such as gold, copper or silver. From the naval industry to the aerospace sector, aluminium and its numerous alloys fulfill a wide variety of tasks [2]. The aerospace industry in particular sees a wide usage of aluminium in its products. For example, it accounts for 20% of raw material usage in a Boeing 787 [3].

Aluminium alloys in general are widely used in Thales products. From cold plates (heat exchangers, see Figure 1) to multiple other potential applications, aluminium fits the requirements of a variety of Thales products. Currently, multiple assembly processes are in use to assemble said aluminium alloys and most of them are fusion-based welding techniques. Among these different welding techniques, there are:

	Al	Fe	Au	Ag	Cu
Density (metric ton/m^3)	2.7	7.8	19.3	10.5	9
Thermal conductivity (W.m^{-1}.K^{-1})	237	80	317	418	390
Electrical conductivity (MS.m^{-1})	38	10	45	62	59
Coefficient of linear expansion (10^{-6}.K^{-1})	23.1	12	14.2	18.9	16.5
Melting temperature (°C)	660	1538	1064	962	1085
Price (September 2019, k€/tonne)	1.6	0.5	45	0.5	5.5

Table 1: Comparative table of electrical and thermal properties at room temperature of different metals, as well as the price

- Arc fusion welding: used by the GBU (Group Business Unit) TOSA (Thales Optronics) and TSA (Thales Airborne Systems) for example, on alloys such as alumiunium alloys 5000 series, AA6061 or AS7G0.6 foundry aluminium alloys.

- Resistance welding (spot/roll welding): the process using the Joule effect to melt two metals is used by the TOSA and TSA GBUs on 5000 aluminium alloys and AA6061 .

- Linear friction welding: used by TMI (Thales Microelectronics) for Au/Al/Cu alloys welding on printed circuit boards.

- Electron beam welding: used by many GBUs within the group on all types of materials. From stainless steel to 5000 or 6000 series aluminium alloys. Electron beam welding is widely used for some cold plate applications. AA6061 has high thermal conductivity and good corrosion resistance, making it a prime candidate for such applications. However, limitations surrounding electron beam welding render AA6061/AA6061 welds difficult to perform. The use of FSW for AA6061 similar welds would alleviate this issue.

- Laser fusion welding: also very popular within Thales for its varied use, such as on titanium alloys like T40, TA6V, 5000 and 6000 series aluminium alloys.

- Soldering / Brazing: widely used in the world of electronics for soldering electronic components on printed circuit boards (tin, lead, silver alloys). This assembly process is also used on components requiring a guaranteed seal, such as on cold plates with 4000 and 6000 series aluminium alloys.

All these assembly processes have advantages and drawbacks. Mainly, the mechanical properties of fusion based welds can prove challenging to overcome for some applications, especially in the aerospace industry, where regulations impose high requirements for parts and products.

There are currently projects within Thales for adaptation of FSW to various parts and products. For example, FSW is being considered to potentially replace brazing or electron beam welding on parts such as heat exchangers known as "cold plates". Currently,

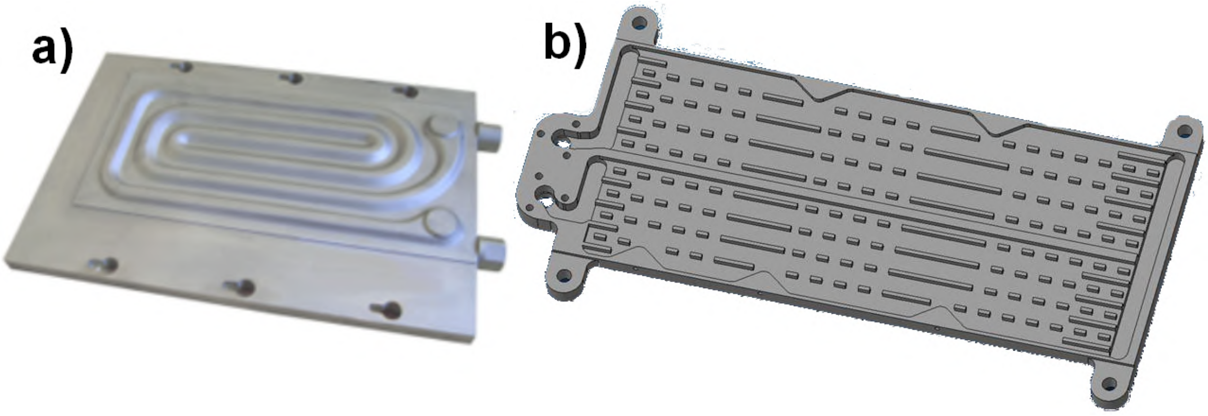

Figure 1: Examples of two cold plates: a) with a straight canal usually assembled via laser or electron beam welding and b) with multiples internal fins usually assembled via brazing.

brazed plates are made of AA6060-T6 or AA3003 aluminium and brazed with 4000 series aluminium. This assembly process requires that a heat treatment be performed on the part after the process to partially restore the aluminium alloy's mechanical strength. Brazing provides a good seal compared to other joining methods. In addition, brazing can be of interest when large series of parts are to be produced (possibility of brazing and heat treatment of multiple simultaneously). However, the complications surrounding its use and overall reliability make FSW a prime candidate to substitute this assembly process.

Figure 1 shows two different types of heat exchangers with a cover plate assembled on top of it. In an FSW assembly configuration, welding could be carried out around the perimeter of these covers to ensure the required tightness of the system. The weld would also need to be designed to withstand the operating pressure of the system.

FSW is also being considered to manufacture blanks for mechanical parts. A pre-assembly in FSW of basic parts (tubes, bars, circular sections, etc.) allows the reduction of raw material use, and this maximizes the "buy to fly" ratio of aerospace parts for example. Today, basic FSW welding of so-called "soft" alloys (such as aluminium, copper, zinc or magnesium) is relatively well mastered. For aluminium, for example, there are many applications in various fields, and these have been available since the end of the 1990s. Research into the weldability of these alloys has been facilitated by their availability, their price, and the characteristics (price, mechanical strength) of the tooling used. For example, the tools used to weld aluminium in FSW are generally made of standard H11 or H13 tool steel. More details of the different FSW tooling and its applications will be discussed in a later section.

For alloys with higher mechanical properties (steel, superalloys or titanium), research is still at a more embryonic stage. These metallic materials require more expensive tools (tungsten, intermetallic or ceramic tools) and the wear of these tools is still too high to make this method of assembly interesting in an economic standpoint.

On the other hand, it is possible to use FSW for so-called "dissimilar" assemblies such as aluminium with steel, aluminium with titanium or multiple aluminium alloys. To achieve this goal, a suitable process window of a large range of process parameters needs to be established. A flowchart presenting the investigation process of the PhD is

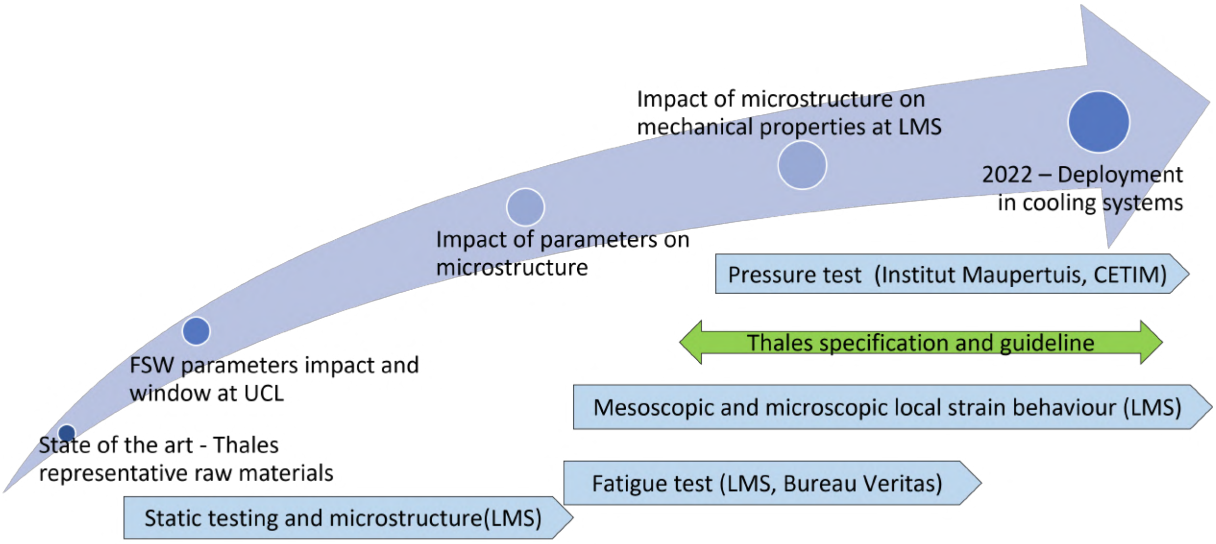

Figure 2: Flowchart of the PhD's investigation on aluminium dissimilar joints in order to deploy FSW in cold plate applications.

presented on Figure 2. At first, a state of the art on FSW in general is produced as well as identifying precisely Thales's needs. Then, hardness mapping and tensile testing following international standards will form the basis of the welded joints characterization. Currently, scientific literature on more advanced mechanical characterization is not as rich as it could be. In particular, this PhD will discuss the local micromechanical behavior and damage mechanism in layered structure in the stir zone of a dissimilar aluminium weld. Additionally, a deeper understanding of fatigue life of aluminium FSW joints is crucial for Thales. During their operational lifetime, parts previously shown as example are subjected to extreme requirements regarding fatigue life as their criticality inside their intended products are high. Thus, fatigue behavior of aluminium dissimilar and similar welds will be discussed. These dissimilar assemblies are a real opportunities for FSW as they open new industrial possibilities.

Chapter I

State of the art

I.1 Aluminium alloys

In this PhD, aluminium alloys were used as base materials in the manufacturing of the welds. Two alloys were used: Aluminium Alloy (AA) 6061 and AA7075. The AA6061 has been used in the T651 state. As for the AA7075, it has been used in the T651 state as well. General material science knowledge concerning aluminium alloys are given in this Chapter. Additional information specifically regarding the alloys used in this study will be provided in Sections II.1. These alloys have been chosen for their wide range of usage across multiple industrial branches, especially in the aerospace industry: a key sector for Thales.

The Aluminum Association [4] classifies aluminum alloys into two categories: wrought and cast alloys. The fundamental difference between cast and wrought aluminum is the following: cast aluminium is melted in a furnace and poured into a mold, where wrought aluminium is worked in its solid form with the help of specific tools such as rolling presses, matrices and/or sometimes via machining to a desired shape. These two manufacturing processes will yield two materials with very different properties.

Wrought aluminium alloys are identified by a 4-digit number. Description, applications and limitations of these alloys are as follows [2, 5]:

- 1*xxx*: Unalloyed aluminium, sometimes referred to as CP (Commercially Pure) aluminium. These alloys have excellent corrosion resistance, electrical properties and high formability. They are widely used for electrical or chemical application. They can also be found in packaging for food and beverages.

- 2*xxx*: Aluminium alloys where copper is the main alloying element. Other alloying elements, such as magnesium, are also found depending on the alloy 4 digit identifier. The 2000 series alloys are used extensively in the aerospace industry (see examples in the appropriate Section I.2.D on industrial applications of FSW) for their remarkable yield strength and ultimate tensile yield strength, in the range of 400-500 MPa.

- 3*xxx*: Aluminium alloys in which manganese is the main alloying element. These alloys have a wide range of applications. Alloy AA3003 is known to be used in cooking utensils and chemical equipment for its good corrosion resistance combined with moderate mechanical properties. Alloy AA3105 is commonly used to manufacture roofing sheets. Alloys AA3004/AA3104 are among the most used Al alloys in the world, being used to manufacture cans for beverages. Alloys AA3002/AA3003 are used in heat exchangers in the automotive and energy sectors.

- 4*xxx*: Aluminium alloys in which silicon is the main alloying element. Used in welding rods and in brazing plates due to its low susceptibility to hot tearing.
- 5*xxx*: Aluminium alloys in which magnesium is the main alloying element. It has excellent corrosion resistance, especially in salt environment. Combined with moderate strength, it is a primary candidate for multiple maritime applications. These alloys can also be found in multiple industries: AA5182 in the beverage industry, AA5754 for light structural parts (car doors stiffeners, train wagon panels, etc), AA5083 in the manufacturing of liquefied natural gas boat reservoir.
- 6*xxx*: Aluminium alloys in which magnesium and silicon are the main alloying elements. These alloys combine moderate corrosion resistance with moderately high mechanical properties. They, however, offer great extrudability due to their excellent ductility. AA6061 or AA6061 are found in many structural applications as well as decorative parts (extruded window frame for example).
- 7*xxx*: Aluminium alloys in which zinc is the main alloying element. Other elements such as copper, magnesium, chromium and zirconium are also present in some 7000 series alloys. These alloys have the highest yield strength and ultimate tensile strength (>500MPa) of all and are frequently used for aerospace applications. AA7075 is used as stiffeners for airplane skin panel for example. Their main drawbacks are their high cost, medium corrosion resistance and widely known low fusion weldability.
- 8*xxx*: Aluminium alloys with a wide range of compositions. The 8000 series includes alloys containing significant proportions of tin, lithium and iron. Iron and nickel provide strength with little loss in electrical conductivity. AA8017 is used in electrical conductors for example.

Among these different alloys, there are 2 sub-categories depending on the way the alloy obtains its mechanical properties: heat-treated alloys and work-hardened alloys (Table I.1). Table I.1 compiles data regarding aluminium alloys hardening method, chemical composition and yield strength range.

Among wrought alloys, there are different metallurgical states depending on the transformations they have undergone. We then find [6]:

- **F**: raw state of manufacture
- **O**: annealed state
- **H**: mechanically hardened state
- **W**: quenched hardened state
- **T**: heat-treated hardened state

Aluminium series	**Type of Composition**	**Hardening method**	**Yield strength (MPa)**
1*xxx*	Al	Strain hardening	70-175
2*xxx*	Al-Cu(1-2.5% Cu)-Mg	Heat Treatment	170-310
2*xxx*	Al-Cu(3-6% Cu)-Mg	Heat Treatment	380-520
3*xxx*	Al-Mn-Mg	Strain Hardening	140-280
4*xxx*	Al-Si	Strain Hardening	105-350
5*xxx*	Al-Mg(1-2.5% Mg)	Strain hardening	140-280
5*xxx*	Al-Mg(3-6% Mg)	Strain hardening	280-380
6*xxx*	Al-Mg-Si	Heat Treatment	150-380
7*xxx*	Al-Zn-Mg	Heat Treatment	380-520
7*xxx*	Al-Zn-Mg-Cu	Heat Treatment	520-620
8*xxx*	Al-Li-Cu-Mg	Heat Treatment	280-560

Table I.1: Mechanical characteristics of different wrought aluminium alloys [2]

Among these metallurgical states, the **O**, **H** and **T** states present subdivisions. The **O** state presents three subdivisions noted **O1** (annealed at high temperature and cooled slowly), **O2** (subjected to a thermomechanical treatment) and **O3** (homogenised).

The state **H** is followed by 2 or 3 digits and the state **T** is always followed by 1 to 5 digits. The meaning of these digits gives information on the state of hardening, annealing, tempering, etc for a given aluminium alloy. A detailed explanation can be found in Stucky [6] or in the standard NF EN 515 [7].

The **T6** state corresponds to a non-strained hardened artificially aged state. The metal first undergoes a high temperature heat treatment called the "solution treatment" followed by an artificial ageing at a lower temperature in order to precipitate a hardening phase in the alloy. This will be further explained in a later Section (II.1) detailing AA6061-T6 specifically.

I.2 Friction Stir Welding (FSW)

Industrially, friction welding exists in several forms. Rotary friction welding for tubular or rod shaped parts, linear friction welding for flat surfaces, friction stir welding (FSW) since the 1990's and more recently Friction Melt Bonding (FMB) since 2015. FSW and FMB stand out from the other friction based welding processes as the friction and subsequent heat is generated by a tool rather than by the parts surfaces themselves. Additionally in FSW, the material is heavily deformed in a mixing process due to the tooling used.

I.2.A Process principle

FSW is based on a particular tool consisting of a pin and a shoulder. A typical FSW tool can be seen on Figure I.1. The tool is put in rotation and approached towards the material(s) to be welded. The pin is brought in contact and enters the material until the shoulder touches the upper surface of the plates or parts to be welded. As the shoulder touches the material's surface, the ensuing friction generates a high amount of heat which softens the material(s). It is important that the melting temperature of the material is never reached, as FSW is a solid state joining process.

Figure I.1: A typical FSW tool made of tooling steel. The pin stirs the material as the shoulder generates the majority of the heat input during welding.

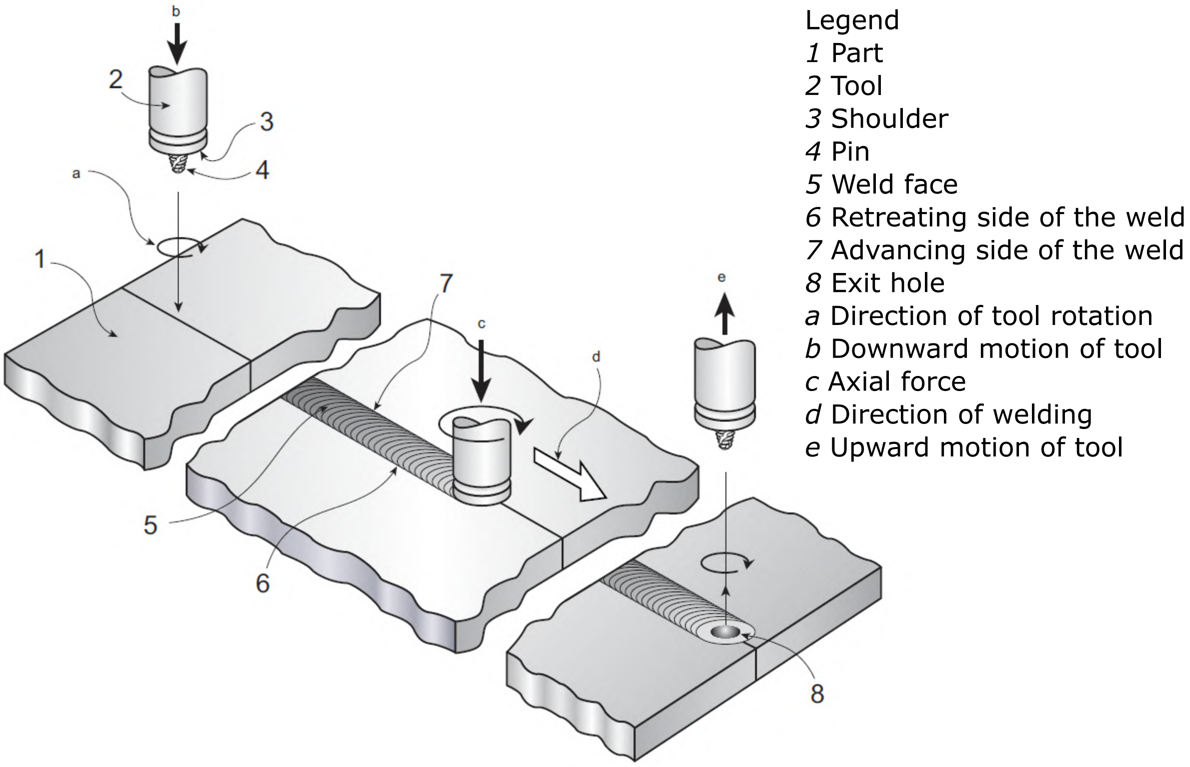

Figure I.2: Representation of a FSW weld with the appropriate terminology based on ISO 25239 [8]

To create a welded joint, the tool is then set in motion as the pin is still inside the material, as shown in Figure I.2 with the (d) arrow.

Multiple metallic materials and plastics have been joined by FSW [9]. Most commonly, aluminium is cited when mentioning friction stir welding [10]. Aluminium was originally used to establish the process principle in the 1990's [1]. Since then, multiple metallic materials have seen FSW applied to weld them. From magnesium alloys[11, 12], copper alloys [13–15], zinc alloys [16], all the way up to steel [17, 18], nickel based superalloys [19] and titanium [20–22]. Industrially speaking, FSW has mostly been applied to aluminium alloys, with some notable exception for steel and copper. Examples of friction stir welds will be provided in subsection I.2.D.

FSW can be divided in two broad categories: similar and dissimilar welding. Similar FSW occurs when all the base parts are made of the same alloy. Dissimilar FSW can take on multiple meaning. Dissimilar welding occurs when multiple alloys of the same material are welded together, i.e. AA6061 with AA7075 for example [23], or when multiple materials are welded together, i.e. aluminium and titanium welding for example [24, 25]. In this study, similar and dissimilar welding will be investigated for AA6061 and AA7075.

I.2.B Assembly possibilities

FSW joints can take on multiple forms. On Figure I.3, multiple unwelded configurations are shown, and their welded results are presented on Figure I.4 [26]. The most common welding configurations encountered in the literature and industrially are the butt-joint configuration, as seen on Figure I.3(a) and Figure I.4(a), and the overlap configuration on Figure I.3(c) and Figure I.4(c). T-shaped joint (Figure I.3(e) and Figure I.4(e)) are commonly found in skin/stringer assemblies for the aerospace industry. Fillet joint (Figure I.3(f) and Figure I.4(f)) have been used to assemble electric vehicle battery tray. Circumferential butt joint (Figure I.3(g) and Figure I.4(g)) are used to manufacture cryogenic tanks for the space sector. Pipeline assembly or small hydrogen tanks can also benefit from this type of FSW. Finally, butt-joint FSW with varying thicknesses (Figure I.3(h) and Figure I.4(h)) have seen some use in the manufacturing of tailored blanks for the automotive industry. These configurations and their real world applications are detailed in subsection I.2.D.

Generally speaking, FSW has a wide range of possible assembly configurations. These configurations are often limited by the type of welding machine and tooling used. Nonetheless, the pressure of the welding pin and shoulder shall be compensated by adequate support and fixing tools to maintain the parts to be welded. This makes FSW easier to apply on flat surfaces.

I.2.C Industrial advantages and drawbacks of FSW

Today, there is a multitude of technologies and processes available for the joining and general assembling of metallic materials. Most of these processes are currently in use in the Thales Group, hence the importance to establish how FSW compares with these processes. They are:

- Fusion based assembly processes. Tungsten Inert Gas (TIG), Metal Inert Gas (MIG), laser welding or torch welding have been used to more than half a century in industrial applications. TIG and MIG represent the vast majority of arc-welded joints

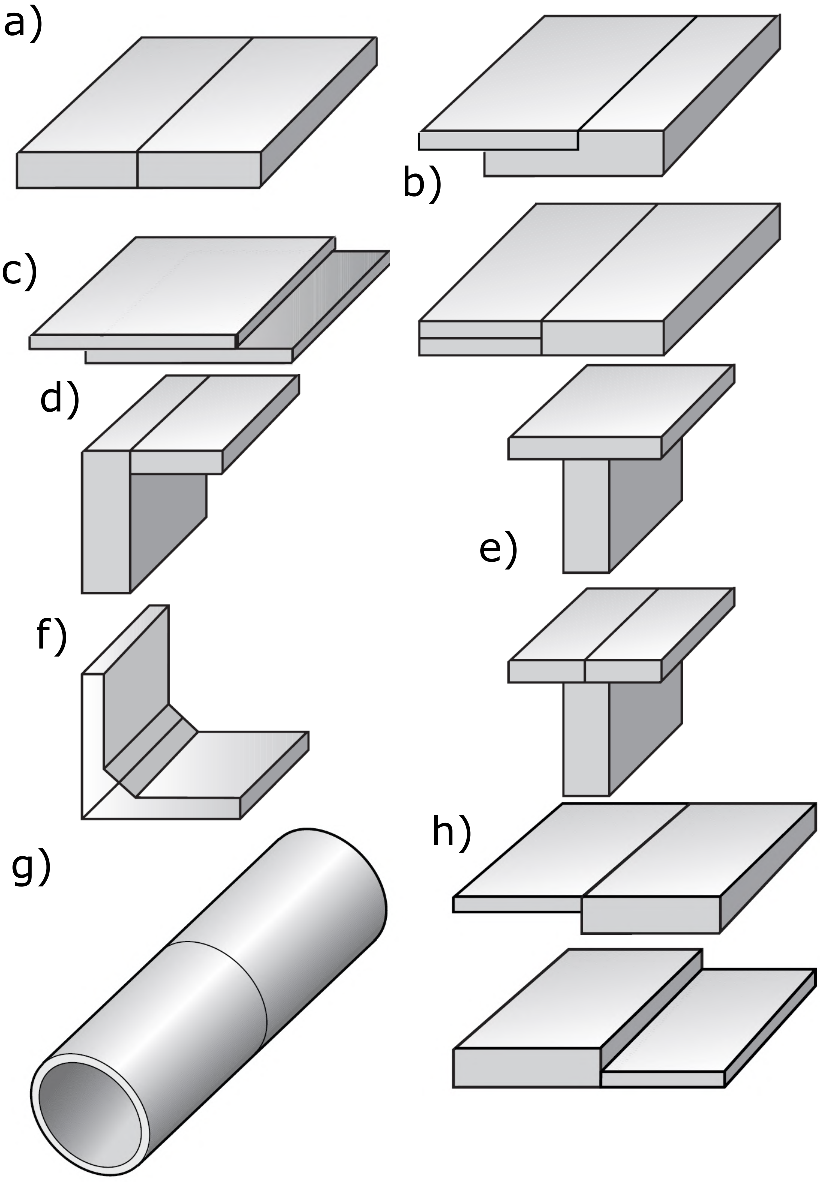

Figure I.3: Unwelded FSW configurations: (a) Butt joint (b) Half overlap joint (c) Lap joint (d) Corner joint (e) T-joint (f) Fillet joint (g) Circumferential butt joint (h) Different thicknesses butt joint [26].

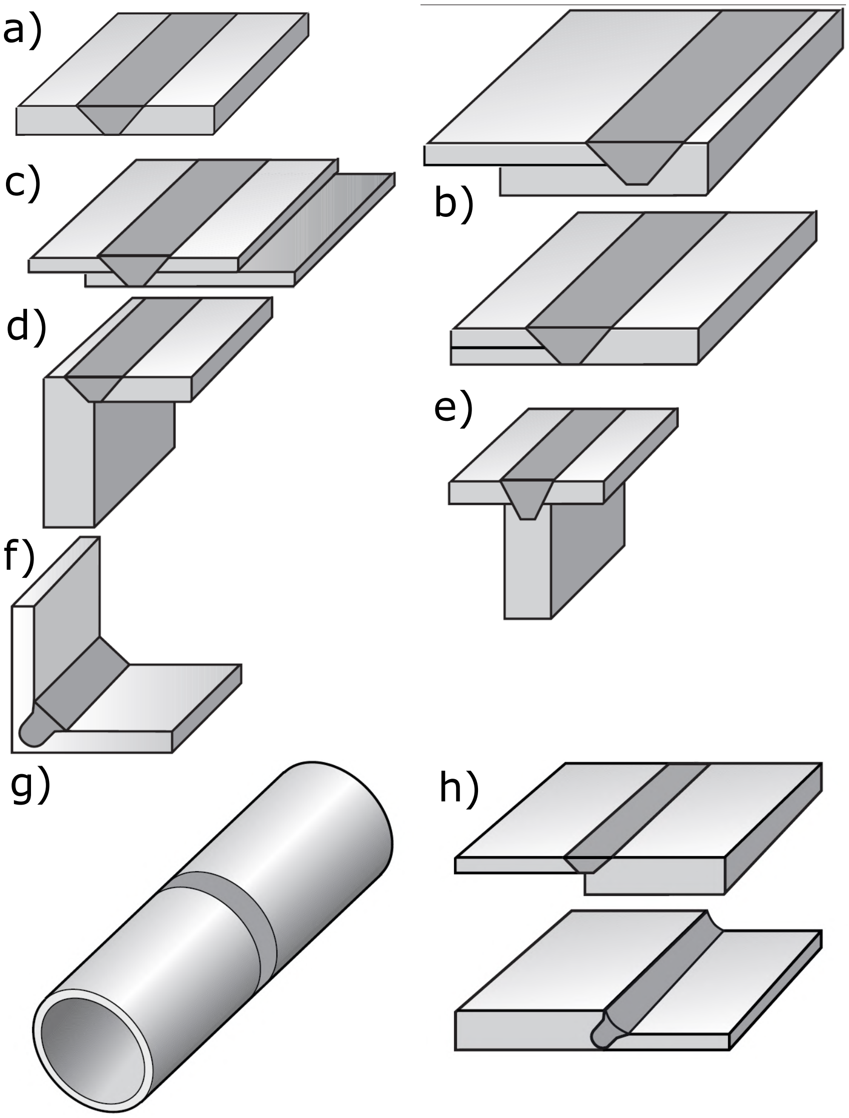

Figure I.4: Welded FSW configurations: (a) Butt joint (b) Half overlap joint (c) Lap joint (d) Corner joint (e) T-joint (f) Fillet joint (g) Circumferential butt joint (h) Different thicknesses butt joint [26].

in Thales. **The main advantage** of these assembly processes are their flexibility regarding the parts to be assembled. For example, a MIG welding machine can be transported to a manufacturing site and generally requires little physical space to be installed. A skilled welder can operate and weld multiples types of surfaces (flat, concave, etc). In the case of laser welding, automation and scale are a plus. **The main drawbacks** of MIG welding is the high skill worker required to perform MIG welding. In addition to being physically demanding, faults and defects are inevitable even for the most skilled of welders. This reliability issue can, for some applications, be an issue. MIG welding also uses high amounts of electricity and consumable fillers. The mechanical properties of a weld can also vary widely depending on the operator's skill and are generally quite low compared to the base material. In the case of laser welding, it is usually limited in terms of depth for welding and requires a certain environment, which can be a constrain. Finally, fusion based welding techniques in general are unsuitable for dissimilar welding.

- Electron beam welding. **The main advantages** of electron beam welding are the high quality and repeatability achievable by the automation of this process, the lack of filler material, the possibility of high depth penetration, as far as welding is concerned and generally the high welding speeds. **The main drawbacks** of electron beam welding are the high cost of the setup (electron beam welding required a vacuum chamber to be performed), the requirement for high skill labor to operate the welding machine, the size limitation for welded parts and the radiological risks involved with such a technology, with exceptionally high safety standards.

- Resistance welding. **The main advantages** of resistance welding processes are their cost, speed, automation capability and lack of consumables. Indeed, resistance welding in general is relatively inexpensive to establish in a production line. The welds can be fully automated (as seen in the automotive industry) or partially automated. These welds only take fractions of a second in most cases and uses only the Joule's effect induced heat to melt and weld parts together, thus avoiding the use of consumables. **Their main drawbacks** are the limitation the technology imposes on the thicknesses of the assembled parts, the strong decrease of mechanical properties in the welded spot, and the absence of sealing capabilities for rolling resistance welding.

- High heat brazing. **The main advantages** of this assembly process are the lack of melting in the parts to be manufactured, the automation capability of the process and the high scalability. The use of furnaces to melt a filler material at the interface of the parts to be assembled allows these advantages. **The main drawbacks** of this process is the high distribution of results and ensuing mechanical properties, furnaces being challenging to control, as having uniform temperature settings and evolution in a large furnace requires skill and thorough understanding of the heating process. The parts also need to undergo a full post-brazing heat treatment to fully restore the mechanical properties of the assembled alloys.

- Gluing and bonding. **The main advantages** of these compounds are the retaining of the base material's mechanical properties, the dissimilar assembly capabilities, the sealing capability, the usually good corrosion resistance and the high versatility. **The main drawbacks** are the sometimes long polymerisation time that can impact lead time on manufacturing, the surface preparation requirements, the regulations regarding the use of certain chemical compounds and the low resistance to shearing and peeling.

- Screws and bolts. **The main advantages** of using screws, rivets or bolts is the removable aspect of such a bond, the multi-material assembly capabilities, the usually good tensile mechanical properties and the inexpensiveness of such joining methods. **The main drawbacks** are the added weight to the overall assembled structure, the risk of unscrewing by vibrations which require careful monitoring and sometimes the application of thread sealant and the low shear strength these assemblies usually exhibit.

Compared to these processes, FSW offers a variety of advantages:

- **Low energy consumption.** Compared to others processes such as fusion based welding or brazing, FSW only uses a fraction of the cost in electrical power to manufacture a weld.
- **The absence of consumable material.** Tool wear set aside, FSW of aluminium alloys does not require the use of any shielding gas to perform a weld and thus, requires no consumable at all. FSW does not require the use of any filler material for aluminium alloy welding.
- **Automation.** Intrinsically, FSW is automated as it can only be performed by machines. This perk of FSW is highly sought after in multiples industrial sectors nowadays, as qualified welder are becoming rarer.
- **Cost.** FSW costs relatively little to operate compared to other assembly processes. The lack of consumables and the lower amount of electricity required to perform a weld explain this.
- **Wide range of material thicknesses.** Compared to fusion based assembly processes, FSW offers a wider range of material thicknesses to be welded, the only limitation being the welding machine itself and its tooling.
- **Dissimilar welding capabilities.** For specific examples in aluminium welding, FSW can easily perform welds that fusion based welding techniques are unable to perform. The welding of AA2024 and AA7075, two aluminium alloys widely used in the aerospace industry, can be mentioned as an example.

With all these advantages, multiple companies have added FSW to their list of qualified processes. Thales aims to do the same by understanding how welding can be implemented in an industrial environment through this work. However, FSW has also some drawbacks:

- **Tool wear.** As mentioned, FSW does not require any consumable to weld. However, friction stir tool wear can vary widely depending on the hardness and mechanical properties of the welded materials. In some instances, tools can become unusable after a couple dozen meters of weld, especially in titanium welding for example. This disadvantage of FSW is generally mild when considered for aluminium welding, as tool in this case can perform from a few hundred meters up to multiple thousands of meters.

- **Clamping.** Contrary to MIG welding or adhesive bonding, which can both be performed virtually anywhere where a worker has a physical access, FSW requires a machine (CNC, robotic arm, etc) to perform a weld. The loads generated by FSW in the welded parts mandate the use of a clamping mechanism to hold the parts during the weld.

- **Cost.** The Non Recurring Cost (NRC) of FSW is quite high compared to other fusion based assembly processes. At the lowest, CNC machines can be retrofitted to allow FSW for 70 k€. At the highest, gantry specialized CNC machine can cost up to a million euros. FSW need to be considered in its entirety before industrially implementing it, as the "cost of entry" can be quite high, especially compared to other joining process.

- **Geometrical constraints.** The range of possible FSW joints are described on Figure I.4. These joints are however limited when compared with the possibilities TIG or MIG welding offer for example. Generally speaking, the requirement of a CNC machine along with a "backing structure" make FSW less versatile in its use compared to other assembly processes.

- **Exit hole.** Inherently, in its original form, FSW leaves an exit hole at the end of a joint. The presence of this hole can be mitigated in a lot of ways: moving the hole in an area that will later be machined or cut, use of a retractable pin [27], using TIG to fill the hole at the end of a weld, etc. However, in some instances, FSW has to be ruled out because of this hole.

I.2.D Industrial applications of FSW

Nowadays, FSW is used in several transportation sectors (naval, automotive, aerospace, railway). Since its introduction in the early 90's, the technology has been used in numerous products. Some examples will be detailed in this section.

I.2.D.i Aircraft manufacturing

In aircraft manufacturing, the Eclipse 500 jet from Eclipse Aerospace, formerly Eclipse Aviation (USA), is a widely mediated application of the FSW process. Figure I.5(a) is a picture of the Eclipse 500 in flight. The repeatability of the FSW process and its ability to replace riveting in FSW spot welding has made it the technology of choice for the assembly of the Eclipse 500 panels. In aircraft manufacturing, the fuselage is usually comprised of two parts: the stringer, which gives rigidity, and the skin, comprising the outer panels of the fuselage. It is common to use 7000 series aluminium alloys to manufacture the stringers and 2000 series aluminium alloys to manufacture the skin panels. However, these Al alloys are not recommended for fusion welding, mainly due to solidification cracking within the fusion zone and poor corrosion performance [28]. Thus traditionally, riveting has been used to assemble aircraft fuselage parts. FSW allows these materials to be joined together in ways other than rivets, thanks to the relatively low heat input of FSW in the welded joints compared to fusion-based welding processes. An example of a friction stir welded stringer and skin is visible on Figure I.6, and a partially assembled fuselage part of the Eclipse 500 on Figure I.5(b).

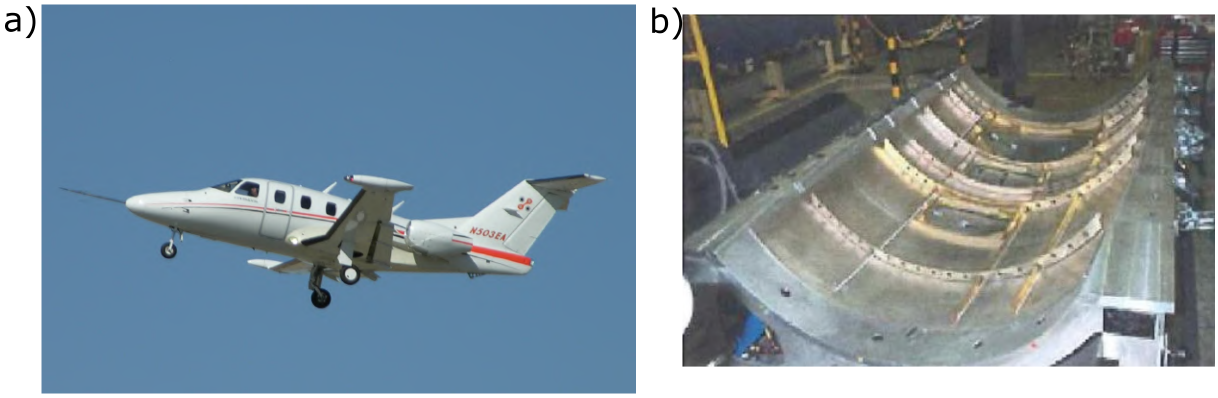

Figure I.5: (a) Eclipse 500 in flight [29]. The entire fuselage (b) of the aircraft has been assembled via FSW.

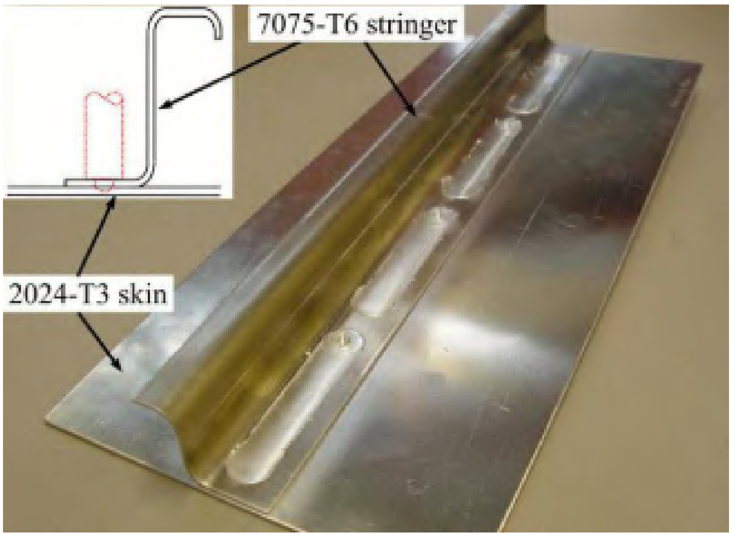

Figure I.6: Stringer and skin panel, respectively in 7000 and 2000 series aluminium alloys, assembled via FSW. FSW is here a substitute for riveting.

Figure I.7: Four aluminum domes, each created using FSW, are seen in this overhead view of the Marshall Space Flight Center Advanced Welding and Manufacturing Facility [33].

According to Gibson [30], the Eclipse 500 has 263 FSW welds for a total of 136 m, allowing the replacement of 7,378 rivets. Around 70% of all rivets of the structure were replaced with FSW [31]. The cabin, wings and fuselage were all assembled with FSW. The FSW process was found to be six times faster than automated riveting and 60 times faster than hand riveting [30]. Eclipse's internal testing would show 2.4 times the mechanical shear strength compared to a rivet line, and similar or better fatigue life properties [30].

In the aircraft manufacturing sector, there exists other examples of FSW usage. The floor panel of the A400M military transport aircraft are assembled via FSW [31]. As for aircraft fuselage, Airbus, Embraer, Dassault Aviation (Falcon 5X) and Boeing (Cargo version of the 747 and C-17 Globemaster II) have all included FSW in their manufacturing process [31].

I.2.D.ii Rocket manufacturing

In the space industry, FSW is currently mainly used for the assembly of aluminium fuel tanks. This technology replaces the traditionally used manual TIG welding. For example, according to Tongne [32], Boeing Space has been using this technology since 1999 for the assembly of fuel tanks on their Delta rockets. The choice of this technology over TIG welding allows a saving in human resources of 80% and a reduced manufacturing cycle of 71%, thanks to automation. NASA is also using this assembly technology on the fuel tank of the SLS rocket [33]. On Figure I.7, the assembly line of fuel tanks in the Advanced Welding and Manufacturing Facility, a NASA affiliated team, can be seen.

Many of today's space rockets such as Space X's Falcon 9 (see Figure I.8), Jeff Bezos Blue Origin [35], and the upcoming Ariane 6 [36] rocket use the FSW technology to assemble their fuel tanks. Similarly to NASA's use case of FSW, it allows the automation of the assembly process. In the case of Ariane 6, the caps and vertical walls of the fuel

Figure I.8: A Space X Falcon 9 booster tank assembled in FSW [34].

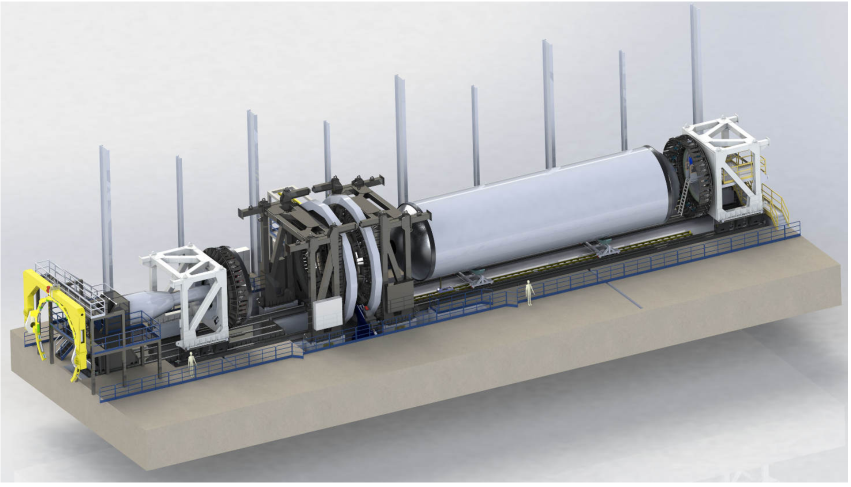

Figure I.9: FSW machine used to manufacture Ariane 6 cryogenic fuel tanks [36].

tanks are made of different wrought aluminium. A dissimilar AA2219/AA2195 FSW joint is realized to assemble these parts and create a complete fuel tank.

The main advantages of FSW in these specific applications in the space industry are the mechanical strength, which is comparable or even superior to TIG welded joints, the reliability of the weld seal and the possibility of joining different aluminium materials while guaranteeing strong mechanical properties.

I.2.D.iii Maritime ship building

In the naval industry, FSW is mainly used for the assembly of extruded aluminium panels. Extruded aluminium structures combine strength and lightness. However, the width limit of an extruded part is about 50 to 60 cm. Traditionally, these extruded panels were assembled by TIG/MIG welding, usually manually. Sometimes, the process was automated. However, the thermal distortion of the panels induced by the fusion-based

Figure I.10: Prefabricated FSW panel for a catamaran sidewall. Straight panel for ship transportation at Marine Aluminium in Haugesund, Norway [37].

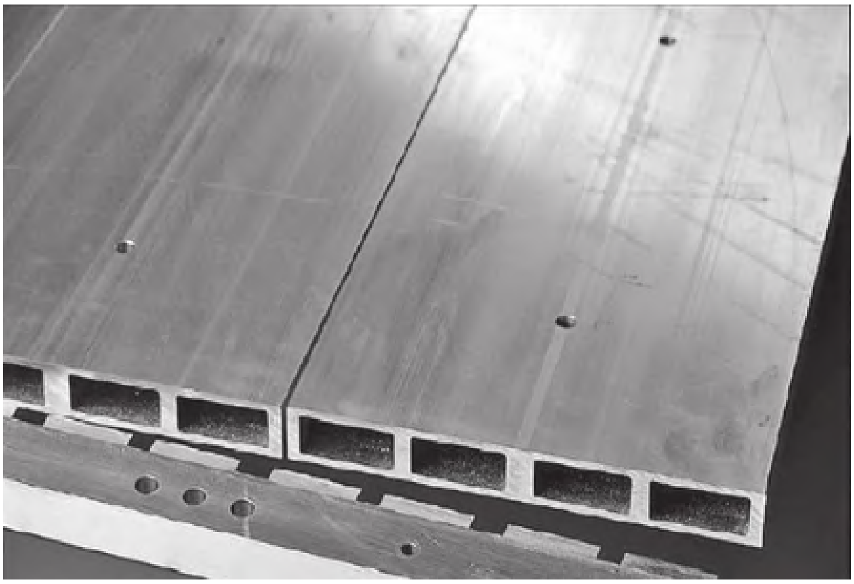

Figure I.11: Joint design of Sapa's freezer panels (weld penetration 4.5mm, total weld length 16m) for quick fish freezing on fishing boats [37].

welding process required the parts to be run through a straightening machine to correct this defect. As the thermal distortion caused by FSW is much lower (local temperature of about 400-500°C in the aluminium compared to over 1000°C with TIG/MIG), the technology was adopted before the year 2000 by companies such as Marine Aluminium in Norway, Hydro SAPA, or Sumitomo Light Metal in Japan. On Figure I.10, a prefabricated FSW panel for a catamaran sidewall is visible [37].

Another application suitable for FSW is the manufacturing of quick fish freezing panels. On Figure I.11, such a panel is visible. These panels are manufactured using extruded aluminium parts. The minimal heat distortion and the automation of the FSW process make it a technically and economically very attractive method to produce these panels.

The aluminium alloys generally used in shipbuilding are the 5000 series aluminium alloys for their good corrosion resistance in a saline environment. For example, Sumitomo Light Metal assembled AA5083-H112 with FSW from extruded panels to manufacture parts for the maritime industry [37, 38].

Figure I.12: Friction stir welded floor panels produced by Sumitomo Light Metal for the 700 Series Shinkansen (see Figure I.13) [39].

Figure I.13: Picture of a 700 Series Shinkansen train [39].

I.2.D.iv Railway industry

In the railway industry, FSW is also used for the assembly of extruded aluminium panels, mainly for the manufacture of wagon walls and floors. On Figure I.12, an example of friction stir welded floor panels in the Shinkansen bullet train (see Figure I.13), Japan's famous high speed train, is visible.

Additionally valuable for this sector, the relatively low (approximately 500°C for FSW aluminium) temperature reached during FSW welding compared to other welding technologies allows for a reduced distortion of the parts during joining and a higher mechanical strength in the heat affected zone. Experimental work comparing MIG and FSW joint performance was carried out by The Welding Institute as part of the EuroStir® project funded by the UK Rail Safety and Standards Board (RSSB), Angel Trains Ltd and HSBC Rail (UK) Ltd. Not only were 3mm thick sheets of AA6005-T6 and AA6082-T6 used in the study, but also extruded profiles of the same materials [40]. Lower side panels for Electrostar trains and for the maintenance parts of the Victoria line of the Bombardier London Underground were assembled by Sapa using FSW. The inner and outer part of

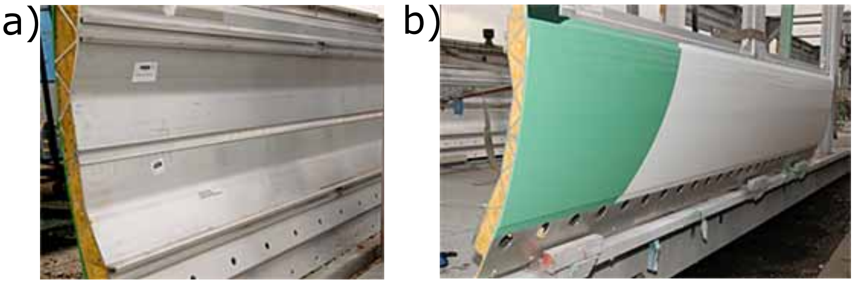

Figure I.14: (a) Inner and (b) outer wall of the Victoria Line Bombardier metro train produced by Sapa using FSW [39].

Figure I.15: Battery tray of the Renault Zoé. The tray is assembled via FSW from extruded aluminium. FSW adds mechanical strength and the guarantee of a sealed joint. [41]

the wagon wall is visible on Figure I.14

I.2.D.v Automotive industry

In the automotive industry, FSW has recently found a place of choice in electric car manufacturing. On Figure I.15, a battery tray of the small electric car Renault Zoé is depicted. The battery trays are assembled by FSW from extruded aluminium parts.

The choice of FSW was mainly for its sealing properties, required in case of battery leakage. Benteler was awarded the contract to manufacture these battery casings in July 2011. At the end of 2012, Benteler was equipped with two FSW machines from Tra-C Industrie. These two machines allow the production of 60,000 to 90,000 parts per year [42]. Other manufacturers such as Tesla or BMW are regularly cited as companies using FSW in the assembly of battery trays.

However, long before the recent popularity of electric cars, FSW was already present in the automotive industry. In 1998, a first study was carried out by The Welding Institute on the manufacture of car doors by stamping, in collaboration with companies such as BMW, DaimlerChrysler, EWI, Ford, General Motors, Rover, Tower Automotive and Volvo [43]. On Figure I.16, a tailored blank is assembled using FSW. This is preceding the final manufacturing of a car door.

In 2015, Hovanski et al. [44] analysed the suitability of using FSW for high volume production, typically associated with the automotive industry. The use of FSW on small series had already been demonstrated by Audi at that time. The conclusion of this

Figure I.16: 6000 series aluminium alloys tailored blanks for door panels [43].

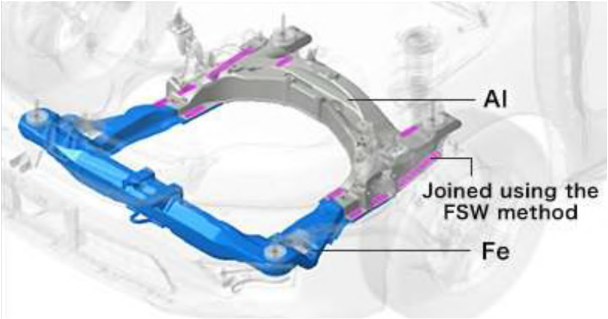

Figure I.17: FSW-assembled Al/Fe engine cradle, 2013 Honda Accord

study focuses on the need to improve the welding speed (less than 1000 mm/min at the time) of FSW compared to other technologies such as laser welding (speed ranging from 6000 mm/min to 10000 mm/min).

Numerous examples of FSW exist in the automotive field and are presented on the Welding Institute's website [43] : the "central tunnel" of the Ford GT (part between the front seats), suspension links for the Lincoln Limousine, rear seats for the Volvo V70 produced by Sapa or rear doors for the Mazda RX-8. Finally, it is in the automotive field that we can also find a case of dissimilar FSW application. Indeed, the engine cradle of the 2013 Honda Accord is composed of anodised aluminium and galvanised steel which are assembled by FSW, as can be seen on Figure I.17. Special assembly precautions are required to avoid galvanic corrosion between these two metals. The solution chosen was to add an elastomer seal between the two parts at the welds **before** the FSW welding. In this way, Honda ensured that the only metallic contact between these metals was at the level of the intermetallic formed during the FSW.

I.2.D.vi Energy sector

In the energy sector, FSW is generally used on copper products for its electrical conductivity and heat dissipation properties.

In Sweden, for example, FSW has been chosen as the joining process for cylindrical copper containers for radioactive waste storage by SKB. These containers are close to 5 m high and have a diameter of around 1 m, with 50 mm thick walls (see Figure I.18). FSW welding of these containers ensures a reliable seal, a critical characteristic for these containers for highly radioactive waste. Other welding methods such as electron beam welding are also being considered by SKB [45]. An example of FSW welding on the top of these containers (during sealing) is visible on Figure I.19.

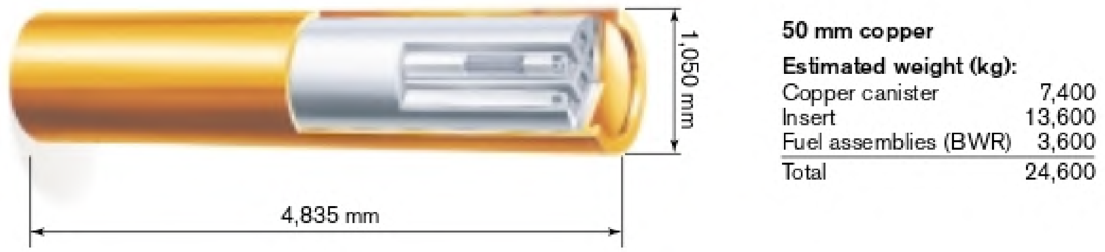

50 mm copper

Estimated weight (kg):

Copper canister	7,400
Insert	13,600
Fuel assemblies (BWR)	3,600
Total	24,600

Figure I.18: Dimensions of storage copper nuclear waste storage cylinder, by SKB. These containers are designed to seal highly dangerous nuclear waste for the foreseeable future.

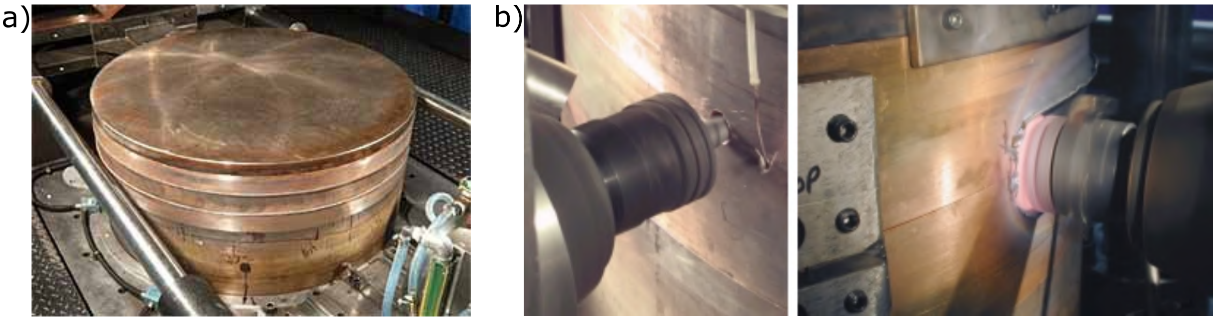

Figure I.19: (a) Unwelded top of a copper canister (b) FSW in progress in joining the top of a copper canister. [46, 47]

I.2.E Welding parameters description

Generally speaking, FSW requires the identification of four key parameters:

- **The rotational speed** of the welding tool, usually expressed in RPM.
- **The axial load** describes the normal reaction force of the weld on the tool, usually expressed in kN.
- **The welding tool** is a parameter in and of itself. Welding tools vary wildly from one another. Some tools have specific features such as tapered pin, grooved and/or concave shoulder, triflutes welding pin, etc [48]. The geometry of the tool also plays an important role in FSW, such as shoulder diameter, pin length, etc. The material in which the tool is made also plays an important role in FSW. The friction coefficient between the tool and the welded material has to be taken into account when designing or choosing a tool for a given manufacturing campaign. Each of these features are welding parameters by themselves, but they are encapsulated in a global "welding tool" parameter.
- **The advancing speed** is the spindle speed of the CNC machine, or robot, along the welded path. This parameter is usually expressed in mm/min. In the case of friction stir spot welding, this parameter is null.

Additional parameters can also be defined such as tool tilt (the angle between the tool's axis and the machine's vertical axis), tool plunging speed, tool dwell time during

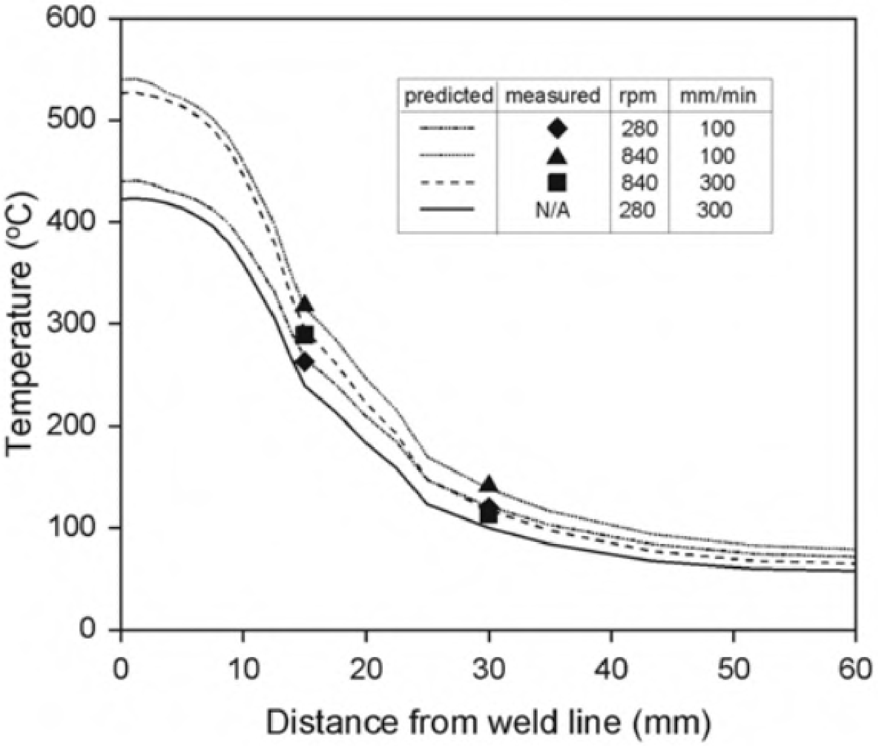

Figure I.20: Modelling and measurements of the maximum temperature at 15 and 30 mm of a dissimilar AA5083/AA6082 FSW weld [51]. Finite element simulation were conducted by Peel et al. [52].

the plunging, etc. However, the four main parameters have a greater impact on the quality of welds compared to the latter ones. Variation of these main parameters will impact weld characteristics in different ways.

I.2.E.i Rotational speed

All other welding parameters being constant, increasing the rotational speed of the tool will increase the temperature of the weld [49–51]. An expression of this phenomenon can be seen on Figure I.20. This is understandable as the heat generated from the welding tool into the weld is friction based. As the rotational speed increases, so does the friction that occurs between the tool and the welded material. Figure I.21 from the work of Tang et al. [50] further corroborates this observation. The temperature elevation generated by an increase in rotational speed is however modest and is not linearly linked to the rotational speed. As the latter increases to higher and higher values, the welding temperature does not increase indefinitely. Tang et al. [50] describe this phenomenon and explain it as such: as the rotational speed increases, so does the temperature, but only up to a certain point, at which the material softening induced by the temperature increase lowers the torque generated by the weld and the material flow stress, which both limit any power generation increase.

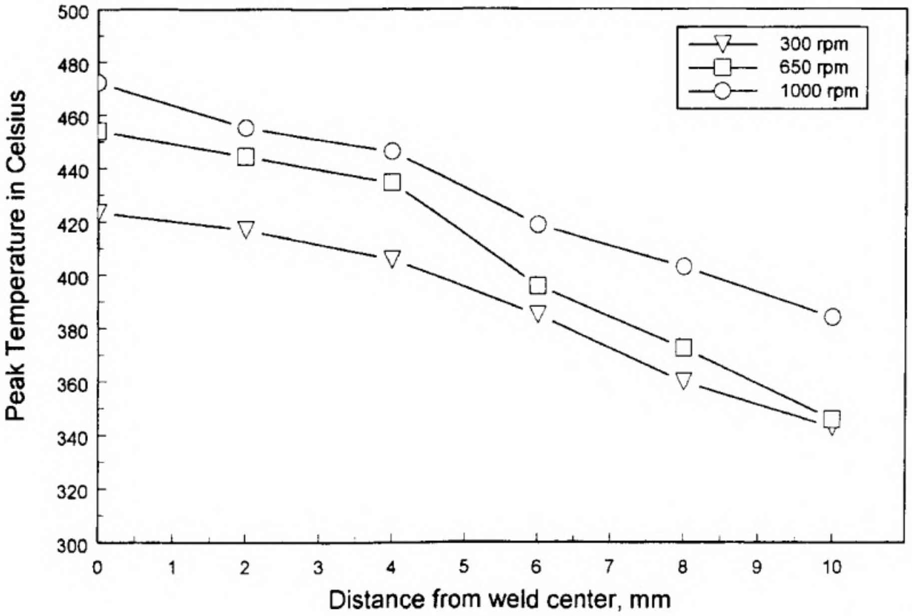

Figure I.21: Temperature profile of multiple FSW joints performed at different rotational speed in AA6061-T6 by Tang et al. [50]. An increase in rotational speed generates an increase in welding temperature.

I.2.E.ii Axial load

During FSW, the axial load is mainly used to drive the CNC machine. While processes such as machining are position controlled, FSW is often force controlled during welding. An example of a force/position control comparison is described in the work of Longhurst et al. [53]. Figure I.22(a) (position control) shows burrs as the weld progresses. The appearance of this defect is amplified here by the fact that the flatness of the plates differs by 1 mm and therefore that the tool sinks into the material during the weld due to the lack of force control. On the other hand, the same weld has been performed on Figure I.22(b), but carried out in force control at around 8 kN. This second weld does not show a similar defect.

This welding control method requires the use of specific machines equipped with load sensors. In its early days, FSW required the use of dedicated, usually expensive, machines. As time went on, the adaptation of CNCs to FSW by adding load sensors allowed the initial cost of FSW technology to be reduced. Nowadays, it is possible to use instrumented robotic arms or FSW "heads" to upgrade CNCs [54].

However, it is possible and sometimes preferable for certain applications to use position control during welding. In both position and force control, the chosen axial load has an impact on heat generation. A higher axial load will lead to an increase in welding temperature [49, 50].

I.2.E.iii FSW tooling

The choice of a FSW tool for a given weld begins with the selection of a tool general design, i.e. geometrical dimensions of the shoulder and the welding pin. On Figure I.23, data provided by K. Colligan (see Appendix) present an empirical relationship between

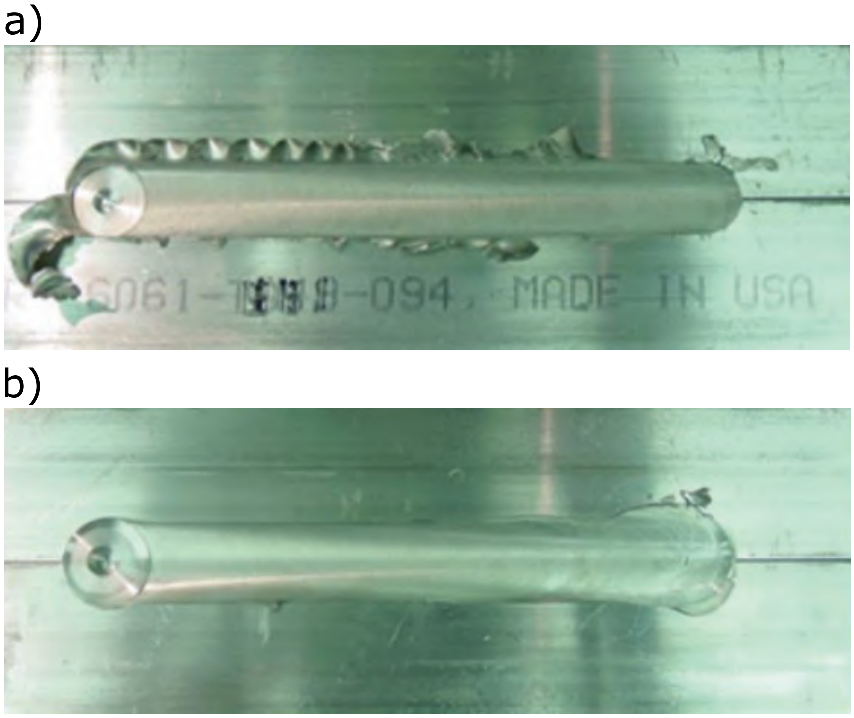

Figure I.22: (a) FSW made via position control. Burrs are visible on the side of the weld and are the result of the intentional unevenness of the plate's surface, making the tool sink into the plate during welding. (b) FSW made via force control . Contrary to the position controlled weld on (a), this weld does not have burrs on the side of the welded joint [53].

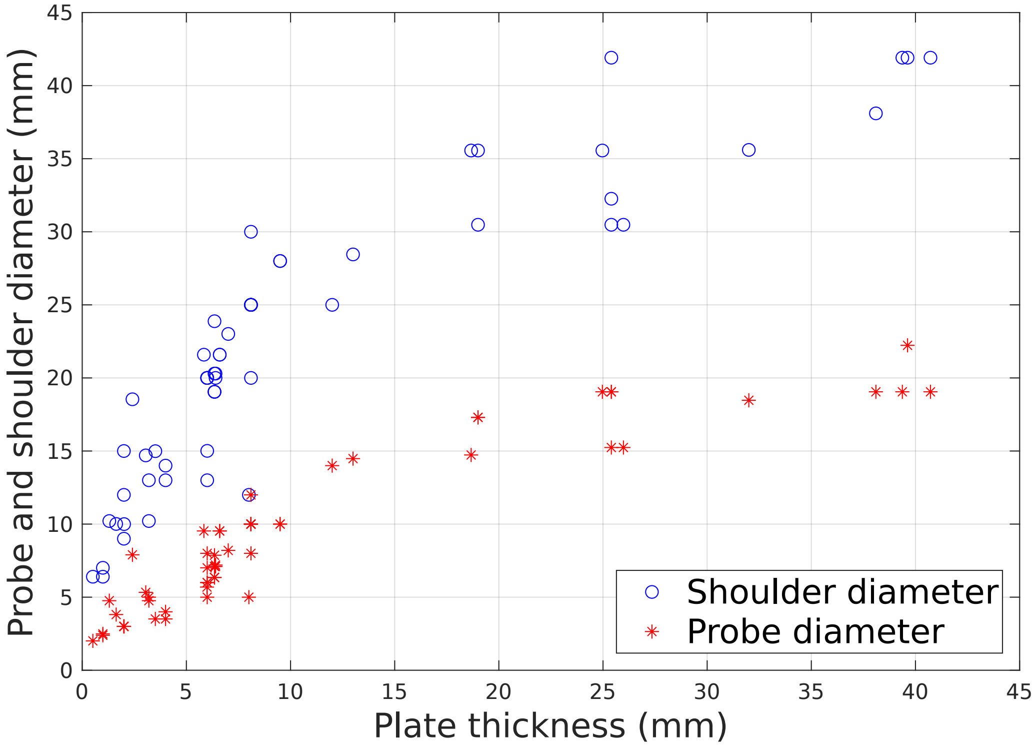

Figure I.23: Empirical analysis of the pin root and shoulder diameters regarding the thickness in an aluminium similar FSW butt joint, based on the data provided by K.Colligan (see Appendix). A bi-linear relationship is noted by the original author.

these geometrical features and plate thickness in the case of aluminium similar FSW butt joint. A bi-linear relationship is observed by the original author. For workpiece below 10 mm, a linear fit ($Tool_D = a \times thickness + b$) conducted by Colligan gave $a = 2.20$ and $b = 6.75$ for the shoulder diameter and $a = 0.92$ and $b = 1.67$ for the pin diameter. These values are close to the ones described by Dubourg and Dacheux [55] early in FSW developments (shoulder $a = 2.26$, $b = 6.99$; pin $a = 0.92$, $b = 1.65$). For workpiece above 10 mm in thicknesses, a different linear relationship is described (shoulder $a = 0.45$, $b = 24.03$; pin $a = 0.18$, $b = 12.84$). The probe and shoulder diameters become less sensitive to a thickness increase. This data and observation could be used to establish a welding procedure for a new workpiece thickness.

Additionally from the tool geometry, attributes such as grooves, flats, etc, and tool material have an influence on the outcome of a FSW joint. While there is no overwhelming design standard for tooling, FSW pins are usually provided with grooves or threads to aid material mixing. The same applies to the shoulder, which is usually provided with grooves. Tool shoulder can also be concave or flat. The depth of these threads or their shapes differ from supplier to supplier. For example, Krasnowski et al. [56] compared different tool shapes (see Figure I.24) and the impact on mechanical properties such as hardness or yield strength when friction stir welding AA6082-T6. They show that threads and grooves on the pin and shoulder facilitate the mixing of the material, which in turn allows for lower temperature FSW.

Regarding the choice of tool material, steel is the preferred choice when welding alu-

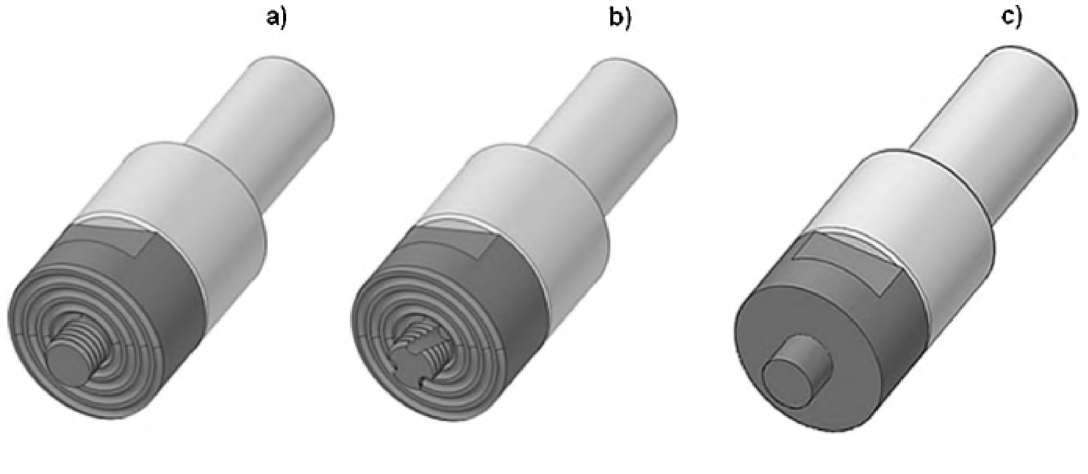

Figure I.24: Different HS6-5-2 steel FSW tools used by Krasnowski et al. [56]: (a) tool with cylindrical threaded probe and a shoulder with a grooved spiral (b) tool with cylindrical threaded probe with three flats, sometimes called triflutes, and a shoulder with a grooved spiral (c) tool with a smooth cylindrical probe without a thread and a flat shoulder.

minium alloys. Tool steel H13/H11 is often mentioned as the preferred alloy for tool manufacturing. Some literature reference simply state "steel", "tool steel" or "high carbon steel" instead of a specific alloy when discussing tool material composition. For more challenging welds (copper, steel, titanium), other materials may be considered such as superalloys, tungsten based carbides, PCBN (Polycrystalline Cubic Boron Nitride), titanium carbides, etc [57–59]. A review by Rai et al. [60] pictures a general overview of tool material choices in multiple welding configurations.

I.2.E.iv Advancing speed

In FSW, the advancing speed parameter plays a double role. On the one hand, it influences the welding's thermal conditions and has to be taken into account when establishing process parameters regarding the weld quality. On the other hand, advancing speed alone dictates the lead manufacturing time of a FSW part in an industrial environment.

Regarding the thermal input of a FSW joint, Figure I.20 shows that at a constant rotational speed, a lower advancing speed results in a higher temperature profile. This phenomenon can be explained by the way heat is generated and distributed in the weld. All other welding parameters being equal for a given joint, a lower advancing speed means a lengthier weld in time. As the heat input of the tool stays the same, being driven by rotational speed and torque, the global amount of energy given to the weld by the tool's friction increases. It results in an increase in welding temperature. For example, at 15 mm from the weld joint, a higher temperature is recorded at 840 RPM and 100 mm/min advancing speed than at 840 RPM and 300 mm/min advancing speed. It is also interesting to note that at 30 mm from the welded joint, Figure I.20 shows that increasing the advancing speed at 840 RPM has a greater cooling potential compared to reducing the rotational speed to 280 RPM.

I.2.F Welding defects

In the ISO 25239-5 standard [61] on FSW welding of aluminium alloys, a table describes a list of existing weld defects for FSW (see Appendix). These defects are inspired from general welding defects defined in the ISO 6520-1 [62] standard. Among these defects, we find:

- **Incomplete penetration/Excess penetration**: Use of a tool that is not suitable (too short/long of a pin) for the intended application. This defect can also occur when the thickness of the edges to be joined varies.
- **Burrs**: Also known as "flash" or "toe flash", this fault appears when the friction of the tool generates too much heat and/or the pressure applied by the tool is too high.
- **Misalignment and lack of metal**: These defects are rarely encountered in FSW. The misalignment may be due to poor placement of the parts in the machine during welding.
- **Extended cavity**: A defect also known as a "wormhole". These defects may not be visible and greatly impact the mechanical performance of the welded joints. Inadequate welding parameters can lead to insufficient material flow in the stir zone of the welded joint. For example, a penetration defect leads to the appearance of these cavities [63]. This defect also appears when the heat input brought in during the welding is insufficient [64].
- **Hooking defect**: This fault only occurs in an overlapping assembly configuration. It occurs when the pressure of the tool pin on the interface between the two plates causes material to rise from the lower plate. Metals often have a thin oxide layer, either passivating or not. The rise and spread of this interface can have significant consequences on the mechanical strength of the weld joint. The shape of the tool's pin can also have an impact on the formation of this defect [65].

I.3 Aluminium to aluminium FSW

I.3.A General overview

Aluminium assemblies are by far the most common in the field of FSW, as shown by the multiple industrial applications presented in Section I.2.D. Contributing to this fact is the low cost of tools to friction stir weld aluminium parts, as well as the high usage of aluminium in today's world. As mentioned in Section I.2.E, H13/H11 tool steel is commonly used to manufacture FSW tooling for aluminium joints. These tools can now be sourced in Europe, Asia and North America, thus making FSW relatively competitive and easy to implement in all the major economic areas.

In Table I.2, a non-exhaustive list of scientific papers on similar and dissimilar aluminium assemblies according to their alloying series is given. In most instances, scientific papers investigate the influence of welding parameters on a wide range of mechanical and microstructural features, such as R_m, $R_{p0.2}$ regarding tensile properties, fatigue strength, hardness, grain size, etc. Overall, AA2024, AA5083, AA6060, AA6061, AA6082 and

Series	1XXX	2XXX	3XXX	4XXX	5XXX	6XXX	7XXX
1XXX	[66]	/	/	/	/	/	/
2XXX		[67–71]	/	/	/	/	/
3XXX			[72]	/	/	/	/
4XXX					/	/	/
5XXX					[73, 74]	/	/
6XXX		[71]			[74, 75]	[71, 74, 76]	/
7XXX		[77, 78]			[79]	[23, 80]	[81]

Table I.2: Summary of publications on aluminium assemblies by FSW

AA7075 are the most popular alloy in the scientific literature. These alloys have a wide range of use in today's industrial sectors.

I.3.B Joint metallurgy

FSW welds can take on two main forms: spot welds and in-line welds. However, disregarding the type of weld choice, FSW joints are composed of 4 distinctive zones. In each of them, the impact of the welding parameters on their respective morphology, grain size, hardness, local mechanical properties, etc, will be different. Figure I.25 shows a general schematic of a welded joint:

- **A**: The base material(s) of the welds.
- **B**: The Heat Affected Zone (HAZ). This zone sees an increase in temperature. It usually leads to a modification of the microstructure, and thus the mechanical properties.
- **C**: The Thermo-Mechanically Affected Zone (TMAZ). This zone also sees a rise in temperature, higher compared to the HAZ (see Figure I.20). The material in this zone also undergoes plastic deformation.
- **D**: The Stir Zone (SZ), or sometimes "Weld nugget". This zone is subjected to the direct stirring and friction of the tool. It sees the highest amount of plastic deformation and material flow.

This weld schematic on Figure I.25 also illustrates another feature of FSW: welded joints are asymmetric in nature. This is illustrated on Figure I.2 with the terms "advancing" and "retreating" side. Depending on the tool's rotation direction, in a butt-joint configuration, each side of the welding path will be labeled in this way. This asymmetric difference has tangible effect on the morphology on FSW joints, as will be discussed in Section I.3.B.i.

Figure I.26 shows the temperature profile obtained during FSW of AA7075 in a butt-joint scenario. Due to the asymmetric nature of the FSW process, the temperature rise on the advancing side is greater than that on the retreating side. This asymmetric temperature rise has to be taken into account when designing FSW butt-joints, as some alloys are more susceptible to degrade their mechanical properties when subjected to

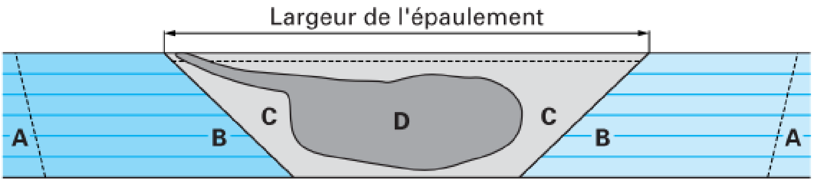

Figure I.25: Cross section of a FSW weld showing the base material (A), the heat affected zone (B), the thermo-mechanically affected zone (C) and the stir zone (D) [82].

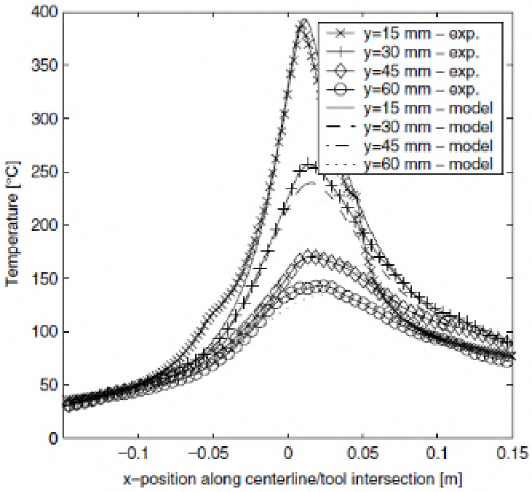

Figure I.26: Temperature profile of a AA7075 welded joint as a function of depth (y) and position relative to the weld line (x) [83].

higher temperature. An example is AA6061 and the hardening β precipitates, which are relatively sensitive to temperature increase. A high temperature can cause coalescence and/or dissolution of these precipitates and alter the alloy's mechanical properties.

I.3.B.i Macrography analysis

Optical microscopy in FSW studies is crucial to evaluate the impact of welding parameters on the morphology of the weld. It is generally performed after etching to better reveal grain boundaries and mixing patterns. Optical microscopy can be performed on similar FSW joints [56], but generally yields limited results. Only grain size and thus, welding zones (stir zone, HAZ, etc), are possibly observed in this way.

Optical microscopy is however particularly interesting in the case of dissimilar welding, as it offers a direct visualization of the mixing that occurs during FSW. Figure I.27 shows 8 different AA2014/AA6061 welds performed at 500 and 1500 RPM. At 500 RPM, the stir zone shows reduced mixing between the two base material. A clear straight line separates the stir zone and at least one of the TMAZ. Both materials appear to be mechanically interlocked, rather than fully mixed. On the contrary, at 1500 RPM, strong mixing occurred in the stir zone, as alternating layers of different colors can be observed. The phenomenon is usually referred to as an "onion ring" pattern. One of the first account of this layering of material in the stir zone in a circular pattern was described by Li et al. [84] on AA2024/AA6061 dissimilar welds. Figure I.28 shows 9 different optical microscopy of dissimilar AA5083/AA6082 welds for various rotational and advancing speed. Once again, the mixing of the stir zone appears to be particularly sensitive to the rotational speed of the tool. The advancing speed's increase or decrease has little to no effect on the stir zone morphology.

Silva et al. [77] went further in the root cause analysis of such mixing pattern by proposing an experimental plan in which the tool is stopped mid-weld. The whole welding tool/welded joint sample is then cut, and material flow is analyzed based on this "frozen state" during welding. Figures I.29 and I.30 originate from this work and respectively show a close up on the onion ring pattern formed in the stir zone of the welded joints and an optical macrograph image of a prematurely stopped weld, with the tool still embedded inside the welded aluminum. Their work also conclude that high rotation speed yields intense onion ring pattern in the stir zone of dissimilar welds. This onion pattern is linked to the threads feature present on the FSW tool pin used in this study. Material from the advancing and retreating side are pushed alternatively towards the bottom of the weld by the threads, thus creating this layering pattern. In Guo et al. [86], AA6061/AA7075 welds have been performed where AA6061 was placed alternatively on the advancing or retreating side. In this specific instance, they concluded that material mixing was significantly more effective when the AA6061 was placed on the advancing side of the weld.

I.3.B.ii Grains and precipitates structure in FSW of Al alloys

Optical microscopy results from the FSW literature show that strong mixing occurs in the stir zone as the rotational speed increases. This effect is particularly visible in dissimilar FSW joints, but such strong mixing also occur in similar welding. This high input of plastic strain around the welding tool in the stir zone/TMAZ of the weld induces dynamic recrystallization.

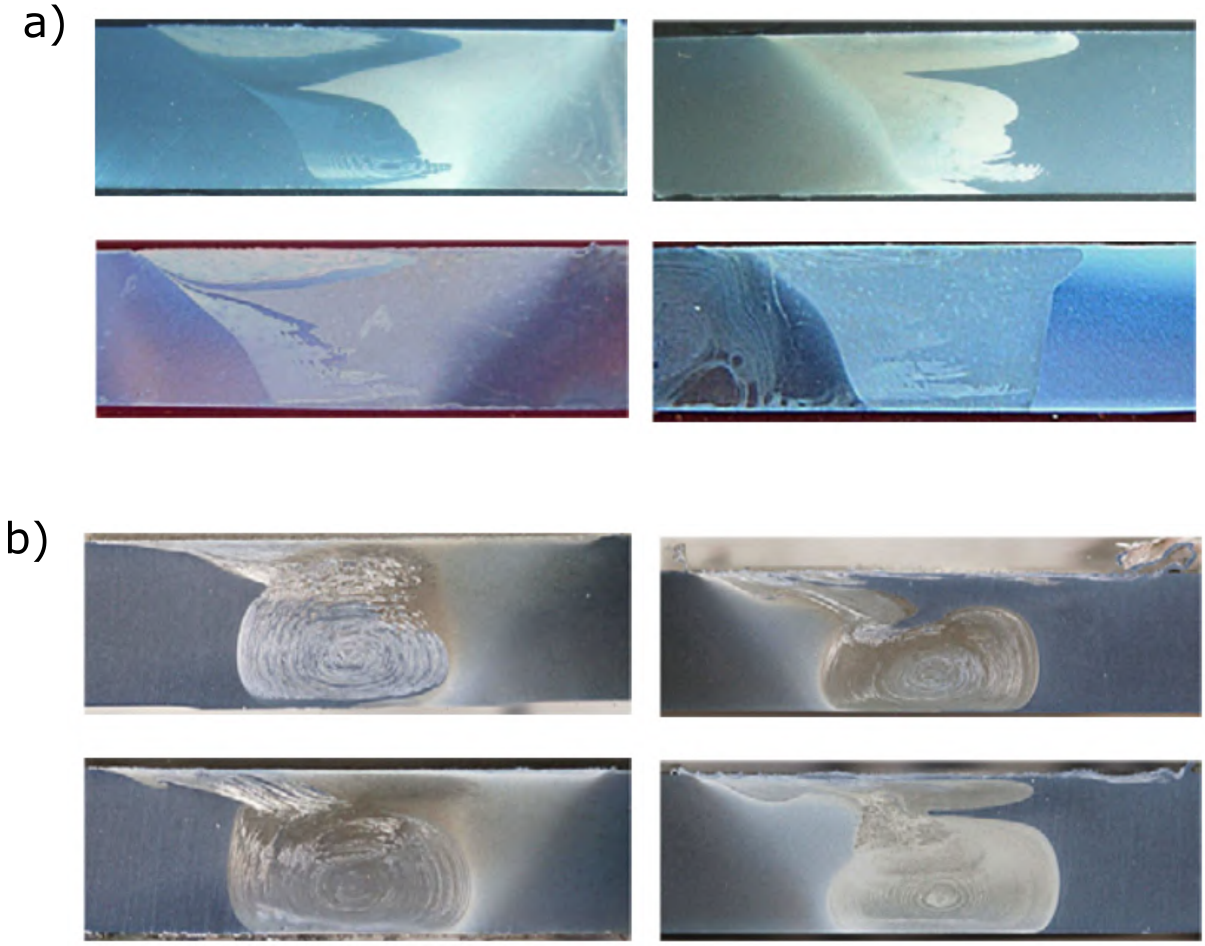

Figure I.27: Optical macrographs of multiple AA2014/AA6061 welded joints at (a) 500 and (b) 1500 RPM. Two distinct stir zone mixing patterns are visible and depend exclusively on the rotational speed of the tool [85].

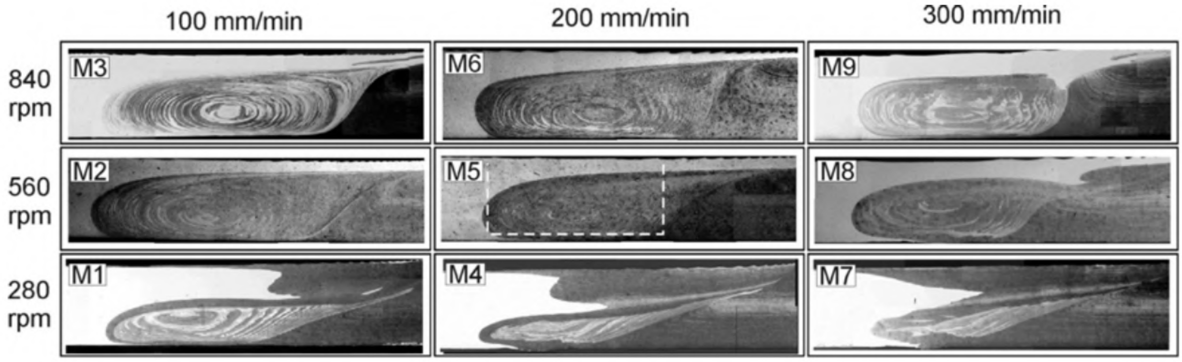

Figure I.28: Macrographs showing the influence of increasing the rotational speed on the mixing of the stir zone in a dissimilar AA5083/AA6082 weld [51].

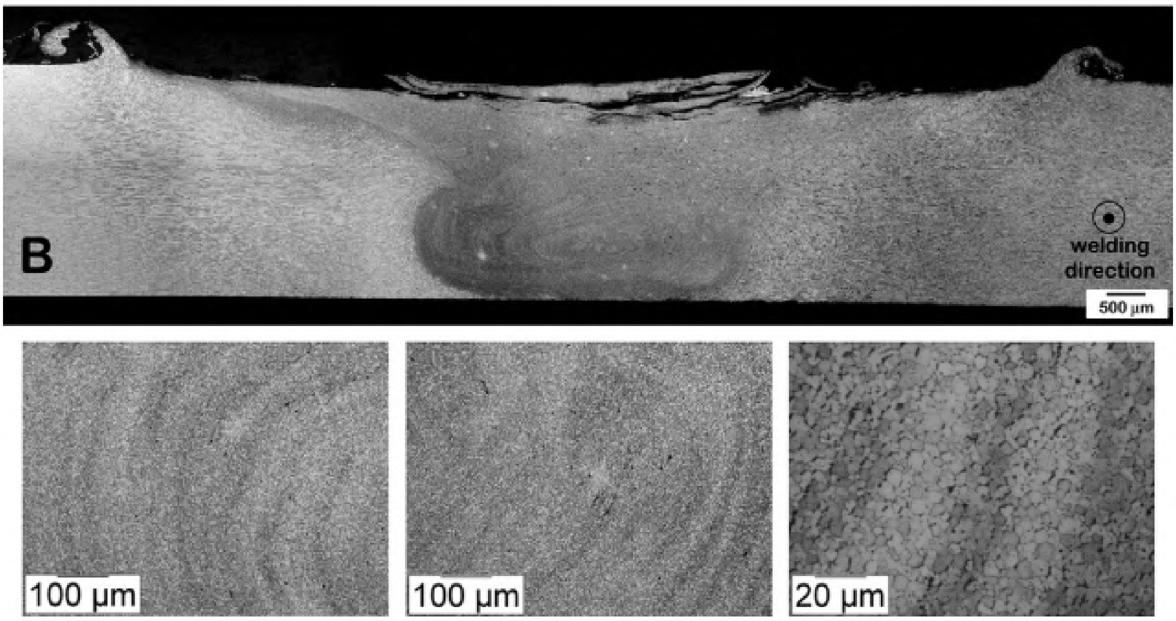

Figure I.29: The "onion rings" phenomenon visible when mixing 2 alloys in FSW, here visualized by a dissimilar joint of AA2024/AA7075 [77].

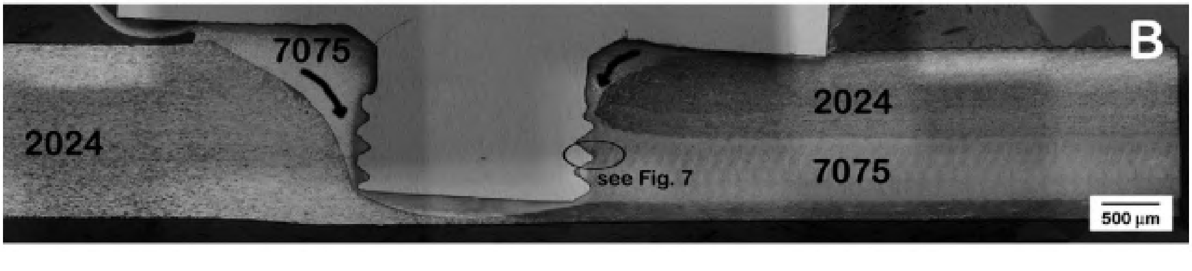

Figure I.30: Macrograph image of a prematurely stopped dissimilar AA2024/AA7075 weld showing the aluminium flux in the welded joint by Silva et al. [77].

Indeed, recrystallization can occur in multiple ways, such as static or dynamic recrystallization. In dynamic recrystallization (DRX), as opposed to static recrystallization, the nucleation and growth of new grains occurs during deformation rather than afterwards as part of a separate heat treatment [87]. As plastic strain is generated through deformation, it accumulates in the grains of the current microstructure, usually along slip planes of crystal orientation of the material. DRX occurs when the amount of stored dislocations reaches a critical amount, triggering the formation of a high angle grain boundary, thus creating a new grain. When DRX takes place, generated microstructure usually exhibit a finer grain size compared to their pre-recrystallization state.

As FSW induces high amount of plastic deformation in the stir zone, studying the impact of the process on recrystallization appears to be crucial. Figure I.31 shows four different images of AA6082. Figure I.31(a) is an optical macroscopic image of the base material. Figure I.31(b) is a SEM (BSE) image of the stir zone after FSW of the same material. A fine equiaxed microstructure is visible. Additionally, Figure I.31(c) and Figure I.31(d) are TEM images of the same base material and welded joint. As described in Section I.1, wrought aluminiums are divided in two main categories: heat-treated alloys and work-hardened alloys. Heat-treated alloys, sometimes referred to as solution hardened alloys, gain their mechanical properties through the nanosized precipitates formed in the matrix during heat treatment. AA6082, being a 6XXX series alloy, has β-type hardening precipitates. Figure I.31(c) shows these precipitates in the base material. Their density is high and distribution in the matrix is uniform. Figure I.31(d) shows the same precipitates in the stir zone after FSW. Here, coalescence has occurred. The distribution is heterogeneous and local density has decreased. As these precipitates dictate the mechanical behaviour of such aluminium alloys, understanding these coalescence mechanisms during welding is critical.

As previously mentioned, DRX occurs in the stir zone of a FSW joint. Figure I.32 from Salih et al. [88] shows 20 different EBSD Euler maps taken in the stir zone of welds manufactured with varying advancing and tool rotation speed. The grain size increases when the welding temperature is raised by either increasing tool rotational speed or decreasing the advancing speed. An increase in welding temperature induces grain growth after DRX [87, 89, 90]. In dissimilar welding, differences in recrystallized grain size can be observed by EBSD mapping as well. Figure I.33 shows the difference in recrystallized grain size in the stir zone, in alternating layers of materials. Here, an additional characterization of the onion ring patterns is unveiled in the form of recrystallized grain size.

I.3.C Mechanical properties

I.3.C.i Hardness

Hardness in general allows the assessment of local mechanical properties. In light of FSW highly heterogeneous nature, either across the entire weld cross section (see Figure I.25) or locally (onion rings phenomenon), microhardness measurements are a valuable tool to characterize FSW joints.

Figure I.34 shows the hardness profiles for three different FSW tools (see Figure I.24) in a AA6082 similar joint, all other welding parameters being equal. The tool that yielded the lowest hardness values (green curve) is a flat shoulder tool with an unthreaded pin. Krasnowski et al. [56] theorizes that the smooth probe and the flat shoulder of the tool on Figure I.24(c) were responsible for supplying a greater amount of heat to the welded

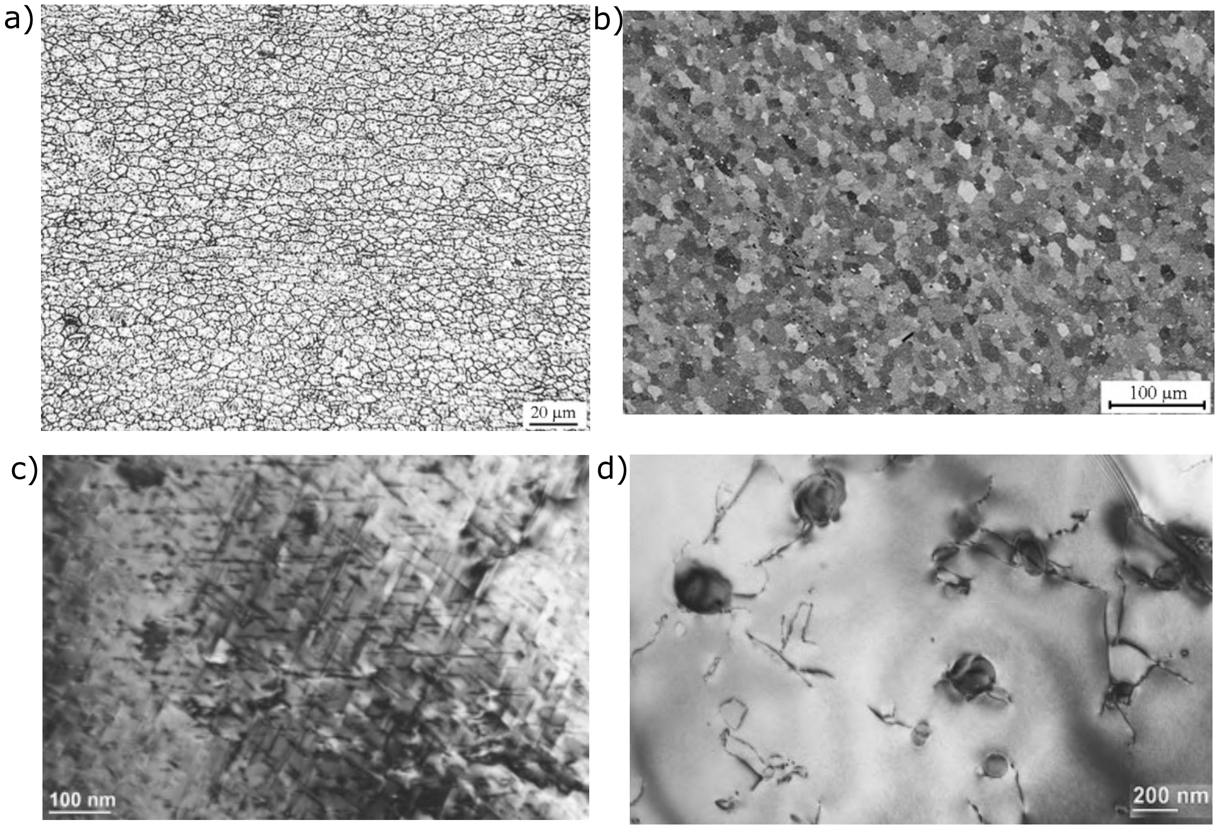

Figure I.31: (a) Optical microscopy of the base material AA6082 (b) BSE (SEM) observation of a recrystallized AA6082 microstructure after FSW (c) TEM image of the strengthening precipitates in AA6082 base material (d) TEM image of the resulting precipitates in the stir zone of a welded joint [56]

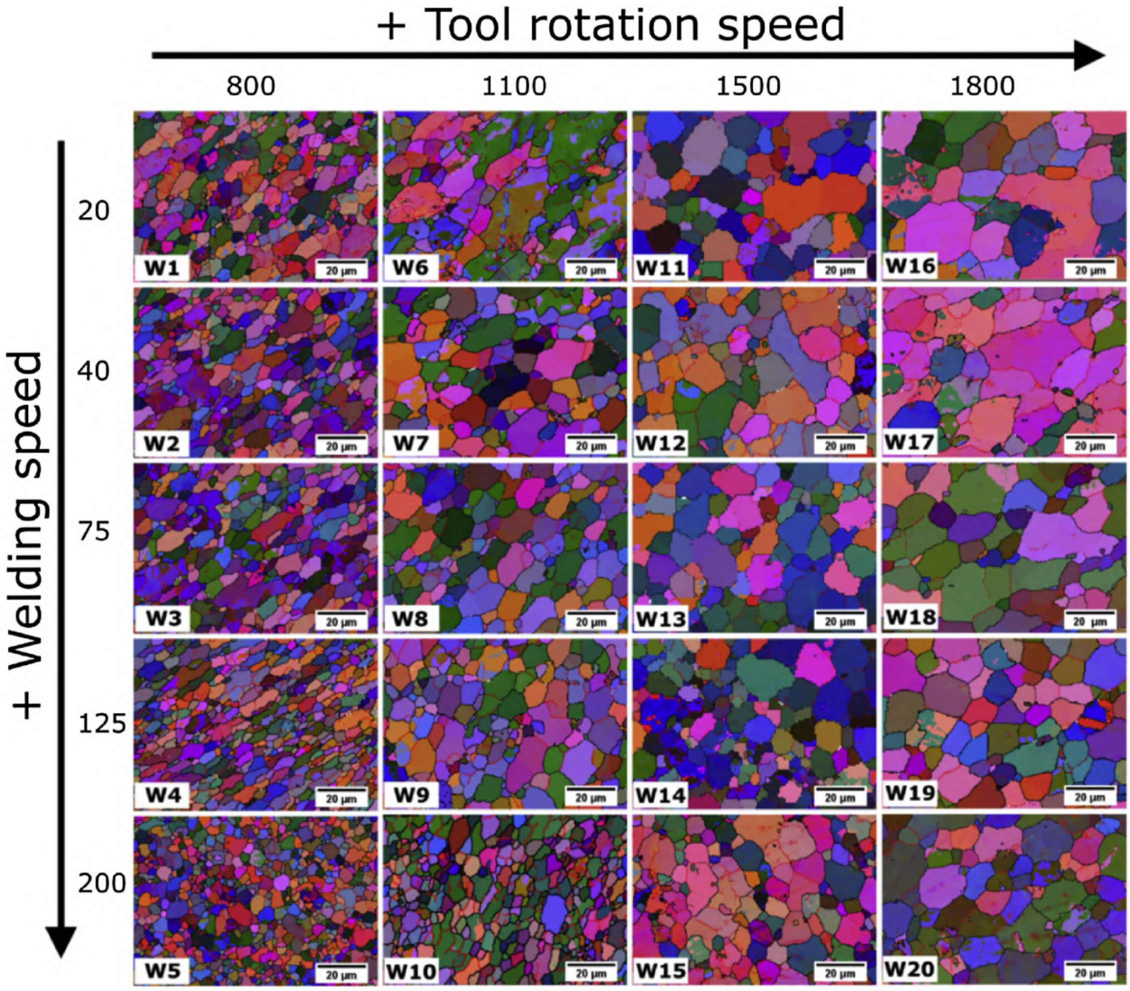

Figure I.32: EBSD Euler maps obtained for different FSW welding conditions. In the maps, LAGBs and HAGBs are depicted by red and black colour, respectively [88]

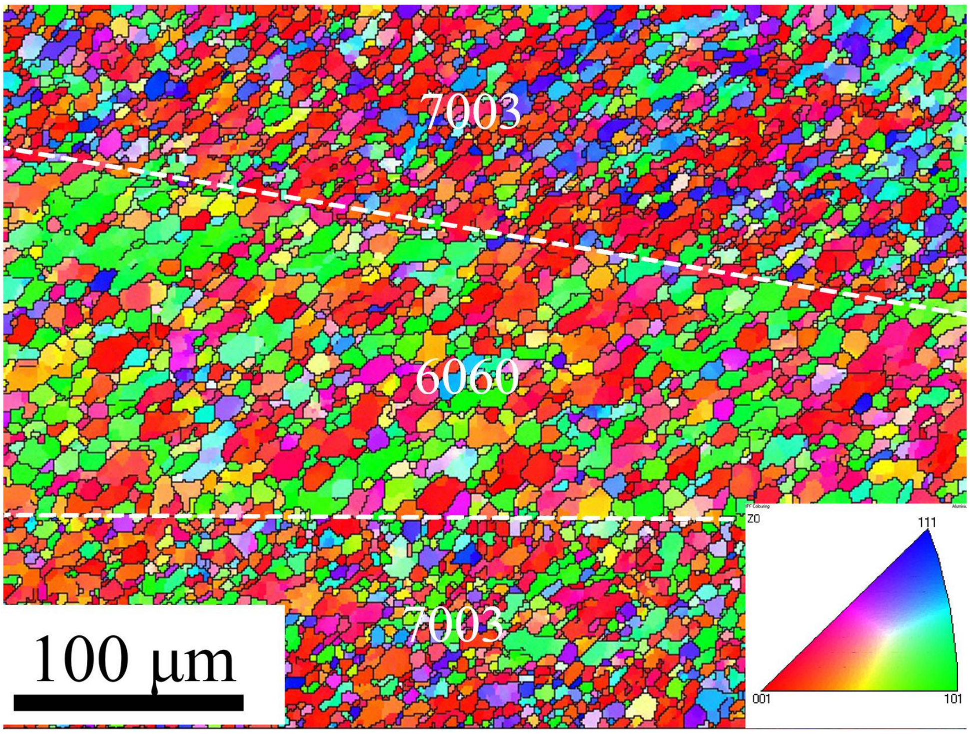

Figure I.33: IPF EBSD map of the stir zone in a dissimilar AA7003 and AA6060 joint. The recrystallized grain size differs depending on the local composition (base material) of the weld [91].

material that resulted in a greater degree of material softening. Tools on Figures I.24(a,b) allowed for a better mixing with a lower heat input thanks to their additional geometrical features, thus preventing further damage on the heat sensitive hardening precipitates of AA6082.

However, for strain hardening alloys such as aluminium alloys from the 5XXX series, Moshwan et al. [73] shows that an increase in hardness can be observed in some areas of the welded joint. Figure I.35 shows five hardness profiles taken at the centerline across the stir zone of a FSW joint. It can be observed that, for all rotational speeds, the hardness peaks are located in the TMAZ of the weld. Moshwan et al. [73] theorizes that the heating and excessive deformation due to tool rotation during FSW resulted in diffusion of magnesium atom from the grain interiors to the grain boundaries to form more β-Mg_2Al_3 in the TMAZ, leading to an increase in hardness. Dissolution of β-Mg_2Al_3 intermetallic phases in the stir zone during the welding process had a considerable effect on the reduction of the joining strength of the welded joints.

Finally, Silva et al. [77] performed microhardness measurements across a dissimilar AA2024/AA7075 FSW joint. These results are plotted on Figure I.36. These hardness profiles are "W" shaped. The hardness values in the stir zone is higher than the AA2024 base material value (137 HV). This observation confirms that strong mixing between the two base materials occurs in the stir zone.

I.3.C.ii Tensile behaviour

Tensile mechanical properties are at the core of material characterization. In the case of FSW, the heterogeneous zones of a given weld will behave differently when mechanically

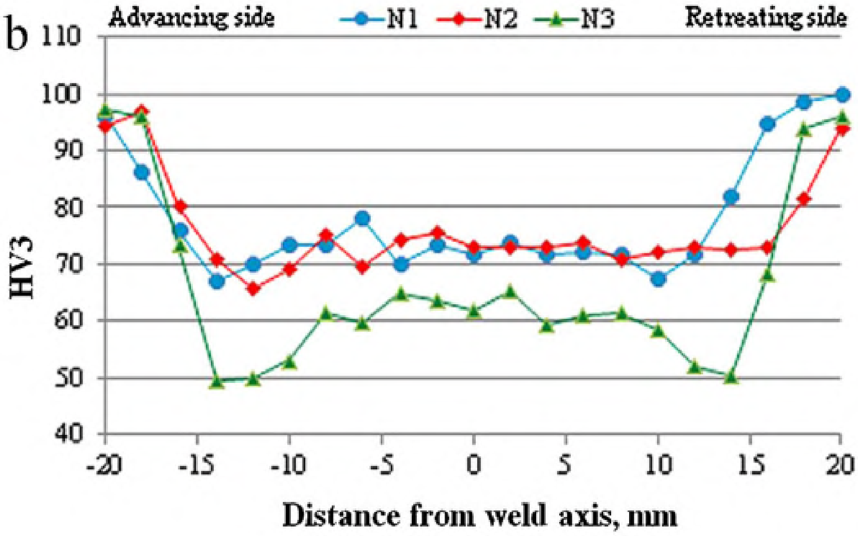

Figure I.34: Hardness profiles for butt joints made of 8 mm thick AA6082-T6 measured 4 mm below the upper surface of the joint for three different FSW tools. N1 corresponds to Figure I.24(a), N2 to Figure I.24(b) and N3 to Figure I.24(c) [56].

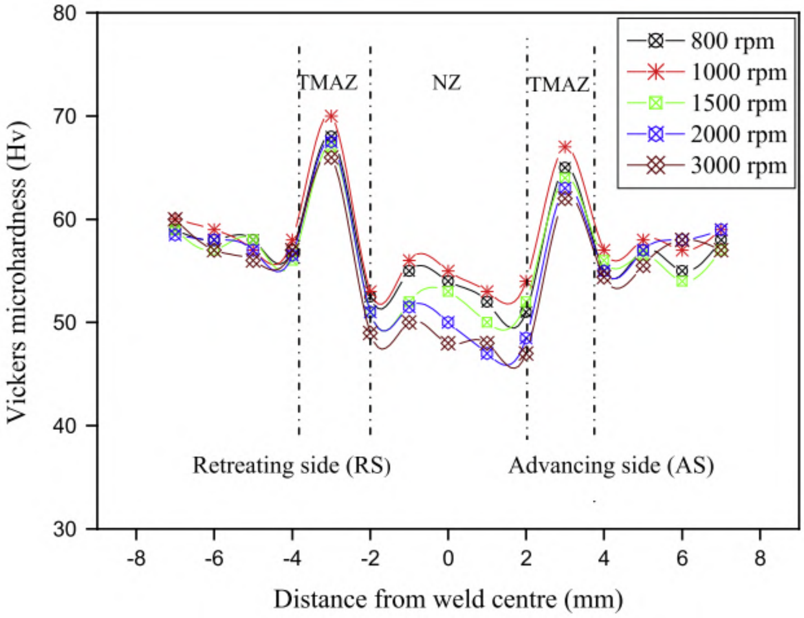

Figure I.35: Vickers microhardness in the stir zone of a friction stir welded AA5052 joint at different tool rotational speeds [73].

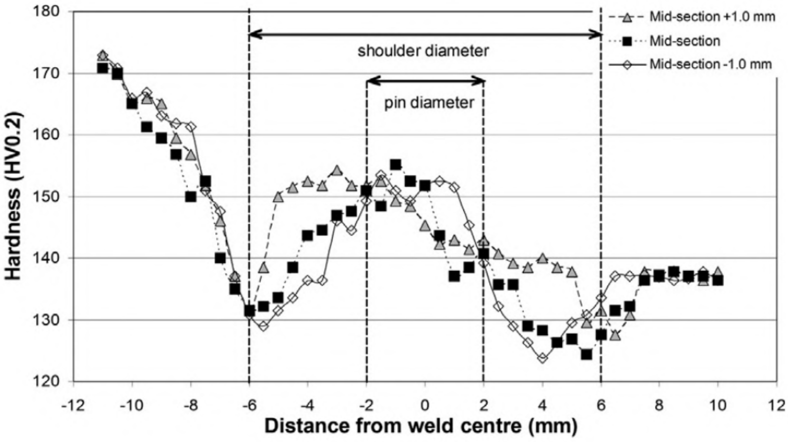

Figure I.36: Microhardness distributions of FSW joints performed at mid-thickness as well as at 1 mm below and above the mid-thickness line in a dissimilar AA2024/AA7075 joint [77].

stressed. As presented, hardness, and thus local mechanical properties, varies widely within the cross section of a welded joint. Figure I.37 present Ultimate Tensile Strength (UTS) and elongation at break for similar AA2024 welded samples. AA2024 is a solution hardening aluminium alloy, and thus its nanoscopic η-phase Al_2Cu precipitates have been affected by FSW, along with its general recrystallized microstructure in the stir zone. Figure I.37(b) present these tensile results with what is called a "joint efficiency", meaning the ratio of the measured tensile properties compared to that of the base material. In this instance, high retention of UTS has been achieved, with some samples having a UTS close to 80% of the base material. However, all samples exhibit quite poor elongation at break compared to the base material. In the vast majority of cases, the samples broke at the interface between the stir zone and the TMAZ, due to the difference in microstructure. Coincidentally, this area is also where the minimum hardness values are usually located within a welded joint of a precipitation hardening aluminium alloy.

On the other side of the aluminium spectrum, Figure I.38 shows tensile results on a AA5052 FSW joints. AA5052 is a strain hardened alloy. The effect of FSW on its hardness properties are different compared to that of a solution hardening aluminium alloy. In this instance, yield strength obtained after FSW in all presented samples is relatively good compared to the base material. On the other hand, UTS values are lower with a maximum joint efficiency of 76%. Elongation at break properties for some joints after FSW are remarkable when compared with the previous AA2024 results.

Table I.3, gives a relatively global overview of the impact of FSW on the UTS of similarly welded aluminium alloys [9]. Once again, the "Joint Efficiency" is the ratio of UTS values before and after FSW. General comments are:

- **FSW of T4 and T6 alloys.** AA6013 welds are here presented in two metallurgical states: T4 and T6. It can be seen that the UTS is identical for both heat treatments after FSW. In the case of AA6013-T4, the joint efficiency is close to 100% meaning no loss of UTS. This observation corroborates an FSW design "rule of thumb": an FSW weld made on an alloy in a T6 state is then comparable to a T4 state locally after natural aging.

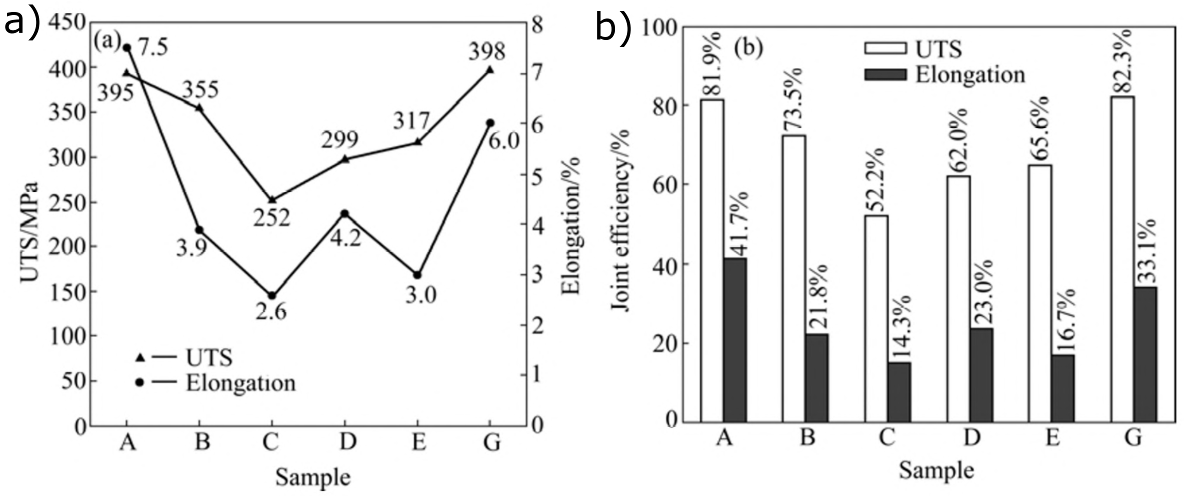

Figure I.37: Summary of the mechanical properties obtained by Radisavljevic et al. [67] in multiple welded samples of AA2024-T352. (a) The absolute value in UTS (MPa) and Elongation (%) are plotted for all samples and, in (b), the joint efficiency of both values is calculated.

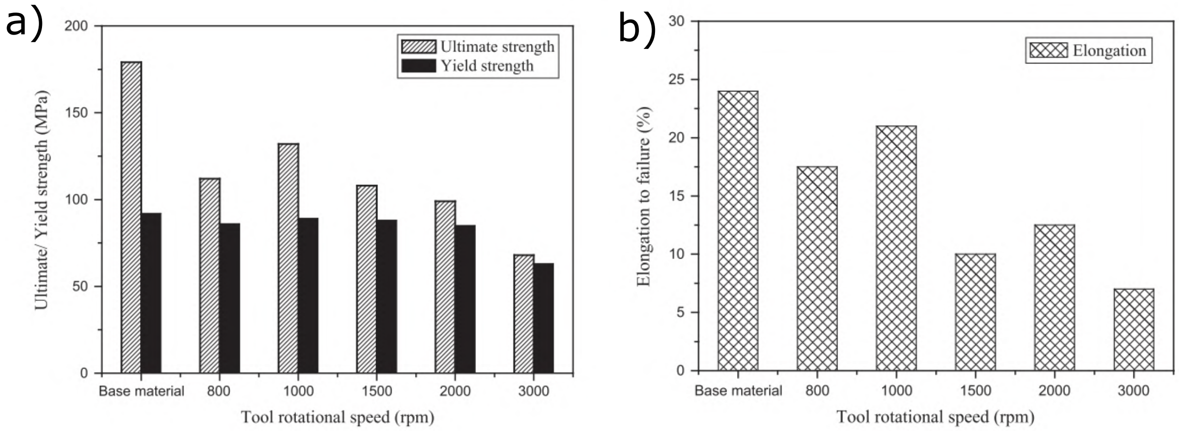

Figure I.38: Yield strength, UTS and elongation at break perpendicular to the welding path of AA5052 after FSW. AA5052 has a yield strength of 89.6 MPa, a UTS of 193 MPa and an elongation at break of 25% [73].

Alloy	R_m (MPa) base material	R_m (MPa) after FSW	Joint Efficiency (%)
AFC458-T8	544.7	362.0	66
2014-T651 (6 mm)	479-483	326-338	68-70
2024-T351 (5 mm)	483-493	410-434	83-90
2024-T3 (4 mm)	478	425-441	89-90
2195-T8	593,0	406,8	69
2219-T87	475,8	310,3	65
2519-T87	480	379	79
5005-H14 (3 mm)	158	118	75
5083-O (6-15 mm)	285-298	271-344	95-119
6013-T4 (4mm)	320	323	94
6013-T6 (4mm)	394-398	295-322	75-81
6056-T78 (6mm)	332	247	74
6061-T6 (5mm)	319-324	217-252	67-79
6063-T5 (4mm)	216	155	72
7020-T6 (5mm)	385	325	84
7050-T7451 (6.4mm)	545-558	427-441	77-81
7075-T651 (6.4 mm)	622	468	75
7075-T7351	472,3	455,1	96
7475-T76	495	465	92

Table I.3: Mechanical characteristics of different wrought aluminium alloys before and after butt joint FSW [9].

- **Lack of additional tensile data.** It should be remembered that this Table does not mention yield strength and elongation at break, two crucial parameters designers usually require in the industry. As seen for two examples of precipitation and strain hardening aluminium alloys, these values can vary widely even as the UTS reduction is of the same order of magnitude.

- **Lack of process parameters identification.** This Table unfortunately does not present the impact of FSW parameters on UTS in general, only for the "optimal" case to obtain the best joint efficiency in each presented alloy. However, all these welds may require multiple tools, widely different welding parameters which may not be obtainable on a single FSW machine, etc.

Finally, in the case of dissimilar aluminium welding, tensile properties of the welded joint becoming intrinsically more complex to characterize. Indeed, as both aluminium alloys can have a large difference in terms of mechanical properties, it is necessary to fully assess how the parent materials mechanical behaviour impact the welded joint.

Table I.4 shows the tensile results of three dissimilar AA7075/AA2024 joints, along with the added mechanical values of both base materials. The average yield strength and UTS of the welded samples are respectively 443 MPa and 229 MPa. Compared to the base materials, these values are closer to those of the AA2024 compared to those of AA7075. This highlights a key feature regarding tensile properties in dissimilar welds: the joint behaves on the basis of the "weakest link" whereas the weakest alloy of the parent materials dictates the mechanical tensile strength of the weld. This phenomenon can also be seen in Guo et al. [86], where AA6061/AA7075 welds have tensile values closest

	R_m (MPa)	$R_{p0,2}$ (MPa)	Elongation (%)	Fracture location
7075 BM	565	491	13	-
2024 BM	458	305	18	-
7075/2024-1	438	269	7.1	HAZ 2024
7075/2024-2	447	224	8.0	HAZ 2024
7075/2024-3	445	253	7.8	HAZ 2024
Average ±	443 ± 4.7	229 ± 22.8	7.6 ± 0.5	-

Table I.4: Tensile data extracted from Silva et al. [77] on dissimilar AA2024/AA7075 welds. Base material tensile values have been added. The joint's tensile properties is defined by the weakest alloy of the parent material.

to the AA6061 alloy. The sample fracture occurred systematically in the HAZ of the AA6061. Additionally, base material positioning (advancing or retreating side) regarding tensile properties has also been assessed, and no significant difference has been observed by placing either AA6061 or AA7075 on the either side of the weld.

I.3.D AA6061-AA7075 dissimilar welding

Dissimilar friction stir welding has been applied to a variety of aluminium couples, as seen in Table I.2. Some results in the literature already report on AA6061 to AA7075 welding.

Cole et al. [92] have set an experimental plan to investigate the specific thermal profile of such welds, and its impact on some mechanical properties. The authors note that AA7075 is known to have the higher hot-strength properties of the two welded alloy. As for AA6061, it has the highest solidus temperature. Spindle power and weld axial force are a relative average value of the two alloys joined at a nominal processing condition, i.e. similar welding, and deviations from these values are attributed to the influence of the material with the largest volume fraction within the stir zone. During tensile testing, welds systematically failed in the HAZ of the AA6061, on the advancing side. The measured joint strength is shown to improve with a decreasing amount of power input to the weld, where the subsequent joint strength is then dictated by the alloy most sensitive to heat input and weld temperature. They achieve a double conclusion on parent material placement as the material with the lowest solidus temperature should be placed on the retreating side of the weld but also the material most susceptible to weakening at elevated temperatures should experience the least amount of power input achievable during the weld process.

As previously mentioned in Section I.3.B, Guo et al. [86] reached a similar conclusion on material placement regarding the mixing of the aluminium alloys in the stir zone. Mixing was found to be more effective when the AA6061 was placed on the advancing side of the weld. When performing dissimilar welds of AA6061 and AA7075 via FSW, the AA6061 should be placed on the advancing side.

Ravikumar et al. [93] documented one of the first large scale mechanical analysis with regards to process parameters of AA6061/AA7075 FSW. 27 different samples have been manufactured using multiples tools and machine process parameters. Ultimate Tensile Strength (UTS), hardness measurements and failure location have been reported. The maximum UTS value obtained on a single sample is 205 MPa with the lower values hovering around 150 MPa. Overall mechanical properties are sometimes significantly worse compared to what Table I.3 has reported. The authors conclude that the higher

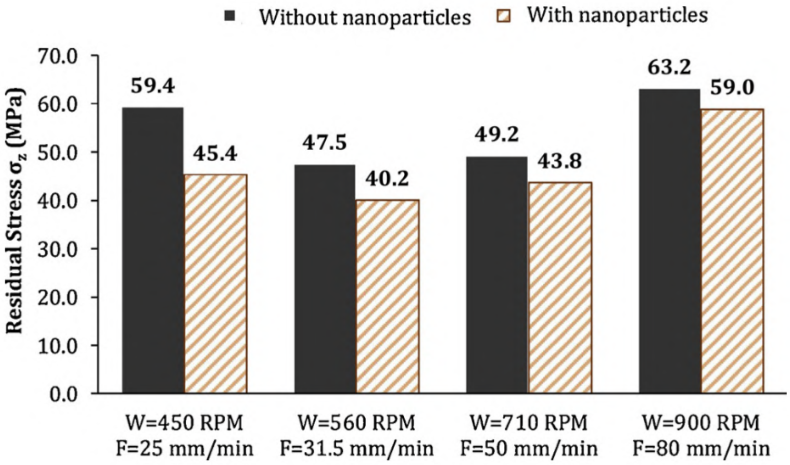

Figure I.39: Maximum amount of residual stress in the midline of the weld thickness for dissimilar AA6061/AA7075 joints, with and without SiO_2 particles [94].

hardness values observed in the stir zone compared to the HAZ and TMAZ are the result of a finer microstructure. However, as previously discussed, dissolution and reprecipitation of hardening precipitates may also play a role in this hardness increase.

Jafari et al. [94] investigated the residual stress distribution of such dissimilar joints, and added SiO_2 particles in the welded joint to alter them. Figure I.39 shows the maximum amount of residual stress on the midline of the joint's thickness. A decrease in residual stress is observed when adding SiO_2 particles. The authors conclude that increasing the advancing and rotational speed increases the residual stresses in the joint.

In conclusion, the data available in literature for AA6061/AA7075 FSW is still limited and no fatigue performance has been reported. As discussed in Section I.4.B, such properties are required for industrial applications, and particularly inside Thales.

I.4 Fatigue life characterization

I.4.A Overview

Fatigue testing is defined as the process of progressive localized permanent structural change occurring in a material subjected to cyclic loading. It may culminate in crack's appearance or complete fracture of the subjected sample after a sufficient number of cycles. In general, crack propagation can be categorized in 3 modes, as seen on Figure I.40. Mode I occurs when the crack is loaded in its opening direction, mode II occurs as this solicitation takes on the form of shearing and finally mode III occurs as the cyclic loading tears the opened crack tip. Two types of fatigue can be distinguished: low cycle fatigue (LCF) and high cycle fatigue (HCF). LCF is characterized by repeated plastic deformation, i.e. in each cycle, and a relatively low number of cycles to failure. On the contrary, HCF usually require more than 10^4 cycles to failure where stress is low and primarily elastic in nature. Fatigue testing is critical to fully mechanically characterise a material. In an industrial environment, mechanically stressing a part in a cyclic way is relatively common.

R is called the stress ratio and is equal to $R = \sigma_{min}/\sigma_{max}$, with σ_{min} and σ_{max} being respectively the minimum and maximum stress experienced by the mechanical part during

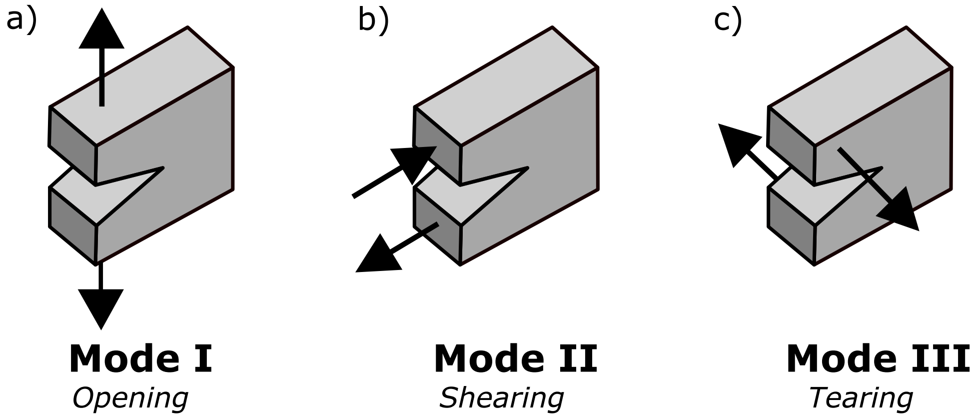

Figure I.40: Fatigue crack solicitation has three mode (a) Mode I where the crack is opened by the cyclic loading, (b) Mode II where shearing occurs and (c) Mode III where tearing occurs. These fatigue crack growth mode can be combined in multi-mode fatigue crack growth [95]

fatigue loading. Figure I.41 visually explains all the variables related to fatigue testing such as stress range $\Delta\sigma$, mean stress σ_m or the stress amplitude σ_a. Figure I.42 visually represents what different R value mean for fatigue testing. For example, for fully reversed loading, $R = -1$. A S-N curve is usually referred to as a Wöhler curve. Fractography refers to the study of the fracture surfaces. Fatigue fracture surfaces have key characteristics that make fractography particularly relevant in this case. It can identify the source of the crack initiation, the crack propagation path, if inclusions played a key role, etc.

I.4.B Fatigue life of FSW joints

Multiple industries and in particular the transportation and aerospace industries have a crucial emphasis to carry out fatigue testing and understand cycling loading. Indeed, catastrophic fatigue failures have occurred in the past, such as the case of the De Havilland Comet aeroplane launched in 1952, one of the first commercial jet engines aircraft, which suffered a fatal flaw in its structural design due to the lack of understanding on metallic fatigue at the time [97].

Fatigue life of FSW joints has been studied through multiple angles. In the review paper by Mishra and Ma [9], early developments in fatigue life of FSW joints are discussed. Multiple comparisons in terms of fatigue life properties are made between FSW and other assembly technologies, mainly fusion based technologies such as laser or MIG welding [98, 99]. Fatigue life of FSW joints is described in those preliminary works as being higher than fusion based assemblies joints. Further studies [100–104] spanning across more than a decade reinforce those early findings. For example, Figure I.43 presents a comparison of fatigue life between FSW and fusion welded samples of AA6061 from Texier et al. [104]. FSW shows better fatigue life compared to Gas Metal Arc Welding (GMAW). In general, fusion based welds have a higher yield strength compared to FSW joints but a significantly lower fatigue life. The difference in fatigue behavior is attributed to the different microstructures created by the two welding techniques. On Figure I.44, cross section views of FSW and GMAW joints are presented. Welding defects are visible in the melting zone of the GMAW sample. Porosities created during MIG welding, or any fusion based welding, in the welded seam is detrimental to fatigue life. On the contrary, FSW

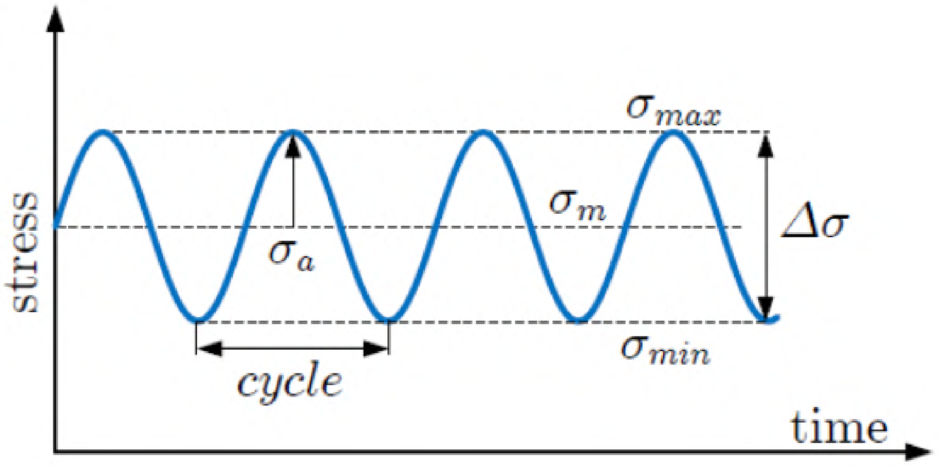

Figure I.41: Visual representation of multiple fatigue-related values such as stress range $\Delta\sigma$, mean stress σ_m, the stress amplitude σ_a, the maximum stress σ_{max} and the minimum stress σ_{min} [96].

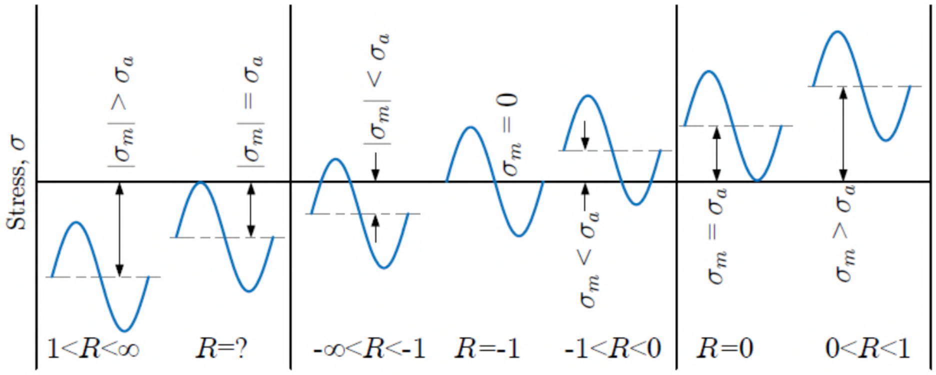

Figure I.42: Visualization of different R value and their meaning in terms of stress amplitude and sign [96].

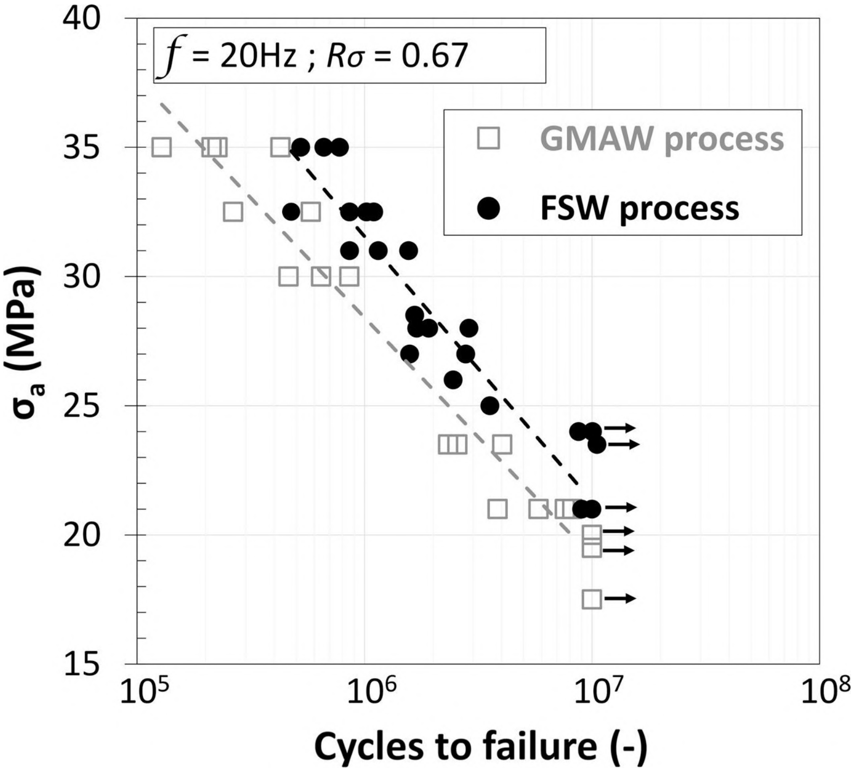

Figure I.43: S-N curves for GMAW (white marks) and FSW (black marks) welded assemblies. FSW joints exhibit higher fatigue life compared to GMAW samples [104].

joints have highly recrystallized, low porosity welded seam, as described in Section I.3.B.ii.

FSW joints presented fatigue properties slightly beneath that of the parent material in multiple studies [105, 106]. Although, in some instances, particular welded joints exhibit lower crack propagation rate and higher fatigue life properties compared to the base material [76, 107, 108]. For example, on Figure I.45, the S-N curve of a double sided AA6061-T6 FSW joint is plotted against the fatigue life of the base material. Surprisingly, the welded joint here exhibit superior fatigue life compared to the parent material. In all three studies of Moreira et al. [107], Vysotskiy et al. [76] and Kim et al. [108], compressive residual stresses from welding are proposed as explanation for this phenomenon. Fatigue crack initiation appears to have multiple origins, depending on the sample preparation [76, 105, 109, 110]. Oftentimes, minor surface defect resulting from tool friction or inadequate welding parameters are responsible for crack initiation and more globally, fatigue life properties. In some instances, cracks nucleate from slip bands in the HAZ of the base material. The pronounced grain refinement present in the stir zone of FSW joints prevents such mechanism from occuring directly in the welded joint.

Industrially speaking, statistical model of fatigue life are often used to design parts and products. One of these statistical model is the part 3 of Eurocode 9. Maggiolini et al. [111] published a review compiling fatigue data for FSW aluminium joints spanning over the last two decades. About 500 sets of data concerning similar FSW butt joints of alloys 2XXX, 5XXX, 6XXX and 7XXX have been aggregated and analyzed. Their main findings are:

- Alloys 2XXX and 6XXX appear to exhibit better post-FSW fatigue properties when naturally aged as compared to artificial aging.

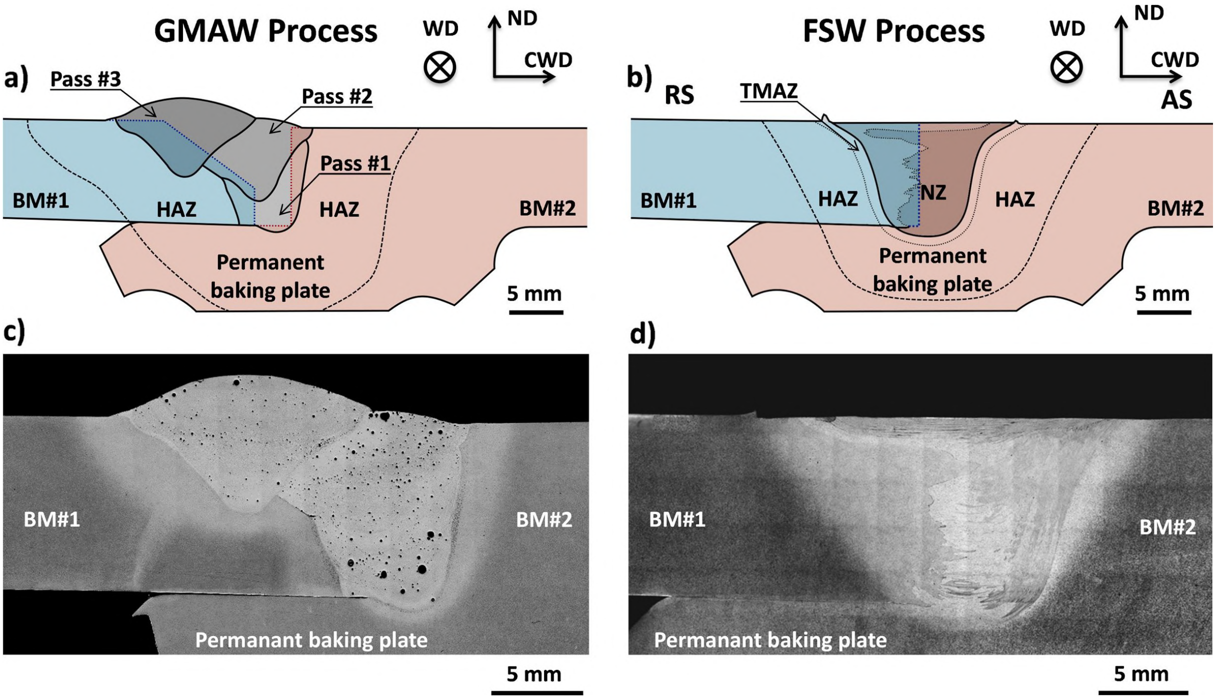

Figure I.44: Cross-section view of the GMAW process and FSW process configurations. (a) Schematic of the GMAW process and its resulting (c) microstruture. Similarly, (b) schematic of the FSW process and the (d) resulting microstructure. Porosities can be seen in the melted zone of the GMAW process [104].

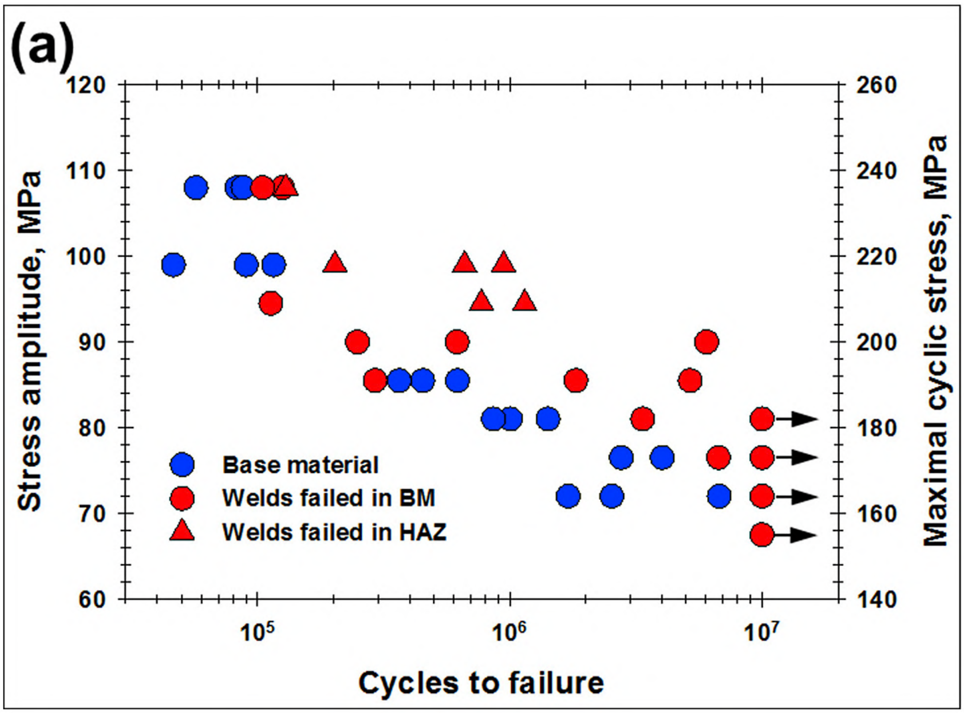

Figure I.45: Fatigue life behaviour of double sided AA6061 FSW joints. The fatigue life of the welded sample is better than the one from the base material [76].

- Post-FSW surfacing appears to increase the fatigue life of the samples
- 7XXX series alloy welded joints appear to have a fatigue life relatively similar to that of the parent material.
- The comparison with the S-N fatigue design curves given in Eurocode 9 shows that the fatigue strength of the welded joints approaches that of the parent plate alloy.

The overall conclusion from this review and statistical analysis of fatigue data for welded joints is that FSW joints have fatigue strength values generally significantly higher than the values recommended by current fusion weld standards.

Finally, some studies have been conducted on the fatigue life of dissimilar aluminium joints [112–114].

Chapter II

Material and methods

As explained in Section I.3, microstructure in the welded joint do not only depend on the specimens features (e.g., alloys and thickness), but also to a large extent on process parameters. Thus, an experimental study enabling to associate process parameters and microstructures has been conducted. In this Chapter, materials and methods are detailed for both the welding process and microstructural characterization.

II.1 Aluminium alloys

II.1.A AA6061: microstructure and mechanical properties

As mentioned in Section I.1, 6*xxx* aluminium alloys contain magnesium and silicon as their main alloying elements. In this study, AA6061 is used in one form: 6 mm thick AA6061 in the T651 state for Al/Al FSW. Its alloying element are measured using inductively coupled plasma (ICP). The chemical composition is provided in Table II.1.

Mechanical properties of AA6061-T651 are described in Table II.2, according to the EN 485-2 standard [115]. $R_{p0.2}$ (MPa) and R_m (MPa) are respectively the yield strength at 0.2% strain and the ultimate tensile strength (UTS). A (%) is the elongation at break during tensile testing. For the bend radius values, t is the thickness of the AA6061 plate considered.

Originally introduced as "Alloy 61S" in 1935 [116], AA6061 is today widely used for its good mechanical properties and ease of machining. As mentioned in Section I.1, AA6061 is a precipitation-hardened alloy. This means that this alloy gains its mechanical properties through precipitation of nanoparticles through heat treatment. The heat treatment of precipitation-hardened alloy happens in two main stages: the solution heat treatment, followed by the precipitation treatment. The T6 heat treatment for AA6061 is visible on Figure II.1.

Alloying elements	Al	Cr	Cu	Fe	Mg	Mn	Ni	Si	Ti
6061-T651	Bal.	0.06	0.17	0.37	0.87	0.08	0.01	0.40	0.07

Table II.1: Chemical composition (%wt) of the AA6061 alloy used in this study. Alloying elements composition were measure using Inductively Coupled Plasma (ICP).

Heat treatment	Thickness range (mm)	Min $R_{p0.2}$ (MPa)	Min R_m (MPa)	Min A (%)	Bend radius (°)	HBS hardness
T6/T651	3 to 6	240	290	10	$4.0 \times t$	88
T6/T651	6 to 12.5	240	290	9	$5.0 \times t$	88

Table II.2: Minimum requirements of T6 and T651 state AA6061 according to the EN 485-2 standard [115].

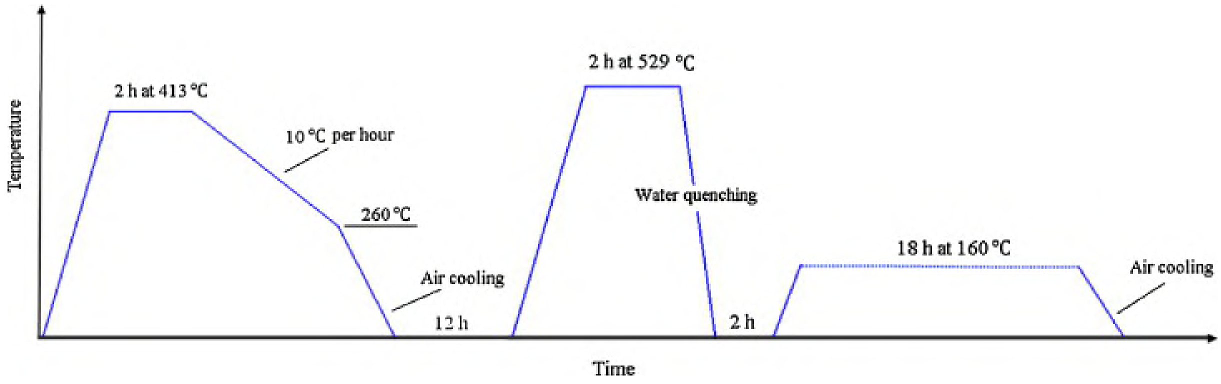

Figure II.1: T6 heat treatment for AA6061 [74].

During this heat treatment, the β precipitates go through multiple precipitation stages [117, 118]:

$$\begin{gathered}\text{Oversaturated solid solution} \rightarrow \text{ Guinier-Preston clusters}\\ (GP) \rightarrow \beta'' \rightarrow \beta' \rightarrow \beta - \text{Mg}_2\text{Si}\end{gathered} \tag{II.1}$$

These precipitates are responsible for the hardness and mechanical properties of AA6061. During the aging treatment of a AA6061-T6 alloy at 160°C (see Figure II.1), first the β'' precipitates form, initially microstructurally coherent with the aluminium matrix. They grow and coalesce to give birth to β' semi-coherent precipitates. These precipitates have a weaker hardening effect compared to β'' precipitates. Finally, the stable, fully matrix incoherent, $\beta - \text{Mg}_2\text{Si}$ phase is formed.

II.1.B AA7075: microstructure and mechanical properties

As mentioned in Section I.1, 7XXX aluminium alloy have primarily zinc as their main alloying element. Other important alloying elements include copper, magnesium, zirconium and chromium. In this study, 6 mm thick AA7075-T651 plates are used in the manufacturing of dissimilar and similar FSW joints. The chemical composition of these plates can be found in Table II.3.

Mechanical properties of AA7075 are described in Table II.4. Similarly to AA6061, the EN 485-2 standard [115] defines minimum mechanical properties required for AA7075-

Alloying elements	Al	Zn	Mg	Cu	Cr	Fe	Si	Ti	Zr	Mn
7075-T651	Bal.	5.29	2.48	1.57	0.20	0.09	0.07	0.05	0.04	0.03

Table II.3: Chemical composition (%wt) of AA7075-T651 used in this study. Alloying elements composition were measure using Inductively Coupled Plasma (ICP).

Heat treatment	Thickness range (mm)	Min $R_{p0.2}$ (MPa)	Min R_m (MPa)	Min A (%)	Bend radius (°)	HBS hardness
T6/T651	6 to 12.5	460	540	8	$12.0 \times t$	160

Table II.4: Minimum requirements of T651 state AA7075 plates according to the EN 485-2 standard [115].

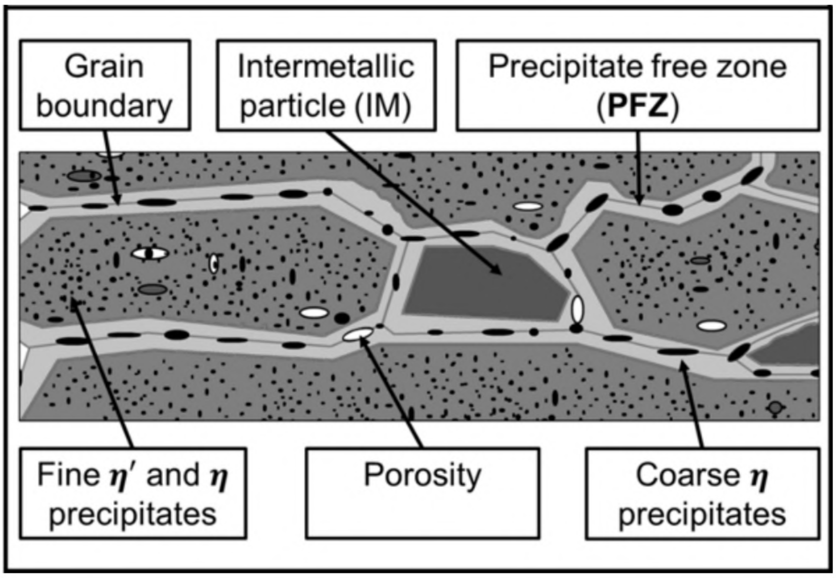

Figure II.2: Schematic of 7XXX rolled microstructure by Lezaack [120].

T651. $R_{p0.2}$ (MPa) and R_m (MPa) are respectively the yield strength at 0.2% strain and the ultimate tensile strength (UTS). A (%) is the elongation at break during tensile testing. For the bend radius value, t is the thickness of the AA7075 considered.

AA7075 is one of the strongest aluminium alloy commercially available. In a similar fashion to AA6061, AA7075 is also a precipitation-hardened aluminium alloy. 7XXX aluminium alloys precipitation mechanisms are far more complex compared to those of AA6061 [119]. A variety of phases with the $Al - Mg - Zn$ ternary composition can occur in these alloys. To maximize their mechanical properties, $MgZn_2$ η phase precipitates are sought after during the manufacturing process. Other critical precipitates such as Cr and Zr based ones can have strong impact on the microstructure of the AA7075. These alloying elements form precipitates called dispersoids and their size and density help in controlling grain size growth during heat treatment at high temperature [120]. These insoluble precipitates have a grain boundary pinning effect.

Figure II.2 shows a schematic of a typical 7XXX series rolled microstructure. Fine intragranular η and η' precipitates contribute to the mechanical strength of a 7XXX alloy. These alloys also exhibit what is called "Precipitate Free Zone" (PFZ) at their grain boundaries. The PFZs are considered weak zones and they facilitate intergranular fracture [121]. These zones appear when Guinier-Preston precipitation occurs and causes a local depletion in alloying element, leading to locally weaker mechanical properties. An example of a AA7075-T651 microstructure is visible on Figure II.3. Coarse η precipitates are visible at the grain boudaries along with large intermetallic particles, similarly to what is visible on the schematic Figure II.2. Finer intergranular η' precipitates can be hinted at inside the grains but are not clearly observable in a SEM.

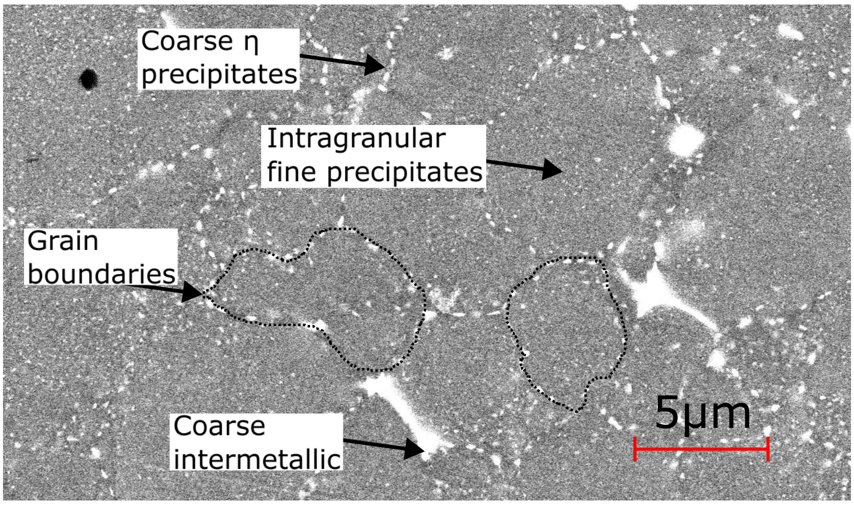

Figure II.3: Example of a AA7075 microstructure after FSW (image acquired with Scanning Electron Microscopy under a Back-Scattered Electron mode). Coarse η precipitates are visible at the grain boundaries as well as coarse intermetallic particles. Finer intragranular η precipitates cannot be observed here due to their size.

During heat treatment, the hardening η precipitates is obtained through the following precipitation path [122]:

$$\begin{aligned}&\text{Oversaturated solid solution} \rightarrow \text{ Guinier-Preston Zone I}\\&(GP)_I \rightarrow \text{ Guinier-Preston Zone II} \rightarrow \eta' \rightarrow \eta - \text{MgZn}_2\end{aligned} \tag{II.2}$$

During cooling of the solution heat treatment, Guinier-Preston (GP) zone precipitate. GP zones are clusters of matrix coherent alloying elements. During either natural of artificial aging, these alloying elements precipitates into the η' semi-coherent phase, before becoming completely matrix incoherent as η precipitates.

II.2 Weld manufacturing

II.2.A Machine and parameters

All the welds have been manufactured at the IMAP laboratory (UCLouvain, Belgium) on the same CNC machine specialised in FSW from TRA-C Industrie[1]. A picture of the experimental setup is provided in Figure II.4. This CNC machine, like many others, uses a scripting language known as G-code to control all movement of the spindle and/or the manufactured part. Three orthogonal directions X, Y and Z are defined to characterize the machine. X corresponds to the welding direction in the horizontal plane, Y to the cross direction in the horizontal plane, and Z to the vertical direction, see Figure II.5.

As described in the state of the art, the weld quality significantly depends on process parameters. Several sensors and actuators are necessary to automatically control the CNC machine during the welding process. For instance, loads sensors on the rotating tool enables the measurement of both the resultant loads (here in kN) along the machine's X, Y and Z axis, and the torque C (N.m) along the Z axis. The machine's characteristics

---

[1] model reference: FSW-LM-AM-16-2D

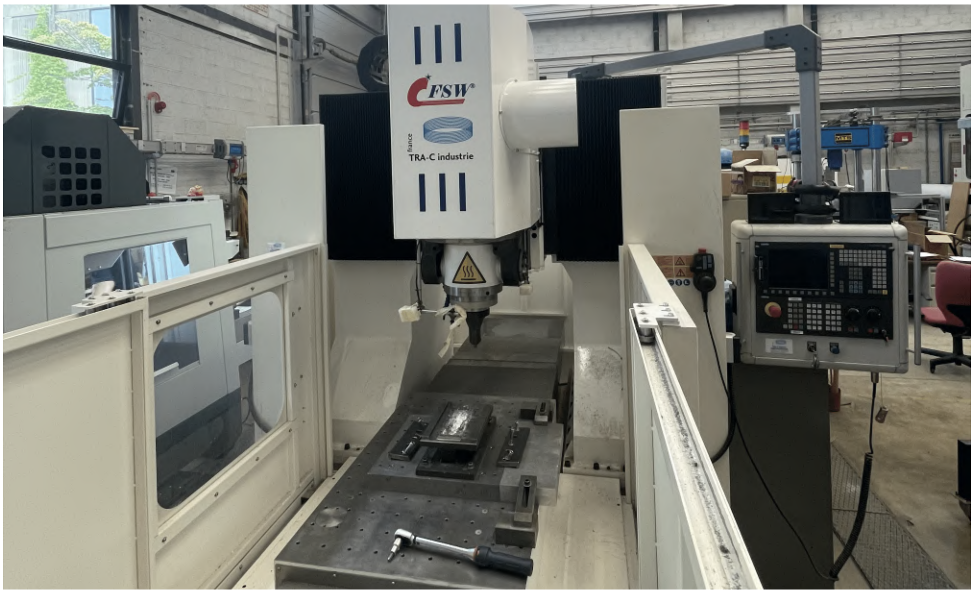

Figure II.4: Experimental setup for sample assembly by FSW.

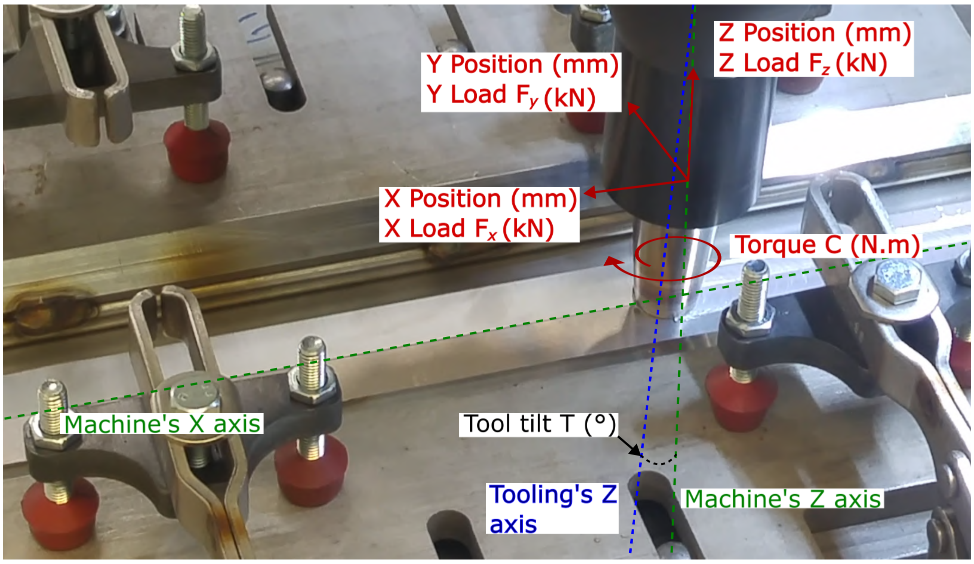

Figure II.5: Close up picture of the tool holder seen on Figure II.4 during welding. Loads and positions along multiple axis are schematized in red. Torque along the Z axis is schematized as well. The machine's X and Z axis are presented with a dotted green line. The tool's vertical axis is in blue. The angle between the machine's Z axis and the tool axis is called the tool tilt.

Value	**Unit**	**Range**
Z axis load	[kN]	0-16
Rotational speed	[RPM]	100-2000
X position	[mm]	0-1000
Y position	[mm]	0-600
Z position	[mm]	0-400
X/Y Advancing speed	[mm/min]	±3000
Z Plunging speed	[mm/min]	±1500
Tool tilt	[°]	±5

Table II.5: Measured data during FSW along with accessible ranges for each of them.

are summarized in Table II.5. The maximum Z axis load is 16 kN. This allows aluminium alloys up to 16 mm thick to be welded, depending on the alloys considered. As the welded joints are straight lines, the X and Y axis measured loads remain relatively low (~2-3 kN at most) and no maximum value has been set. Sensors also include the position along the machine's X, Y and Z axis of the tool head. Tool tilt is the angle between the machine's Z axis and the tooling's Z axis. Figure II.5 shows the complete array of measured values in red along with the visual definition of the tool tilt. Changing the tool tilt allows to slightly modify the way the material is stirred by the tool and alleviate part of the transverse load on the tool into axial load. Changing the tool tilt is a tedious and precise process, requiring the spindle to be turned off. It cannot be changed during welding. Thus, is it set to 1° prior to welding and is not modified thereafter. It should be noted that all the welds are manufactured in force control to avoid common issues listed in subection I.2.F.

As explained in Chapter I, there are four main parameters to characterize a FSW joint: advancing speed, rotational speed, axial load and tool geometry. Variation in these parameters affects the aforementioned values such as loads and torque. The choice of these parameters for each manufacturing campaign is explained in Chapter III.

Furthermore, multiple backing plates of different metals and thicknesses may be used to sink more or less heat during welding and therefore favor targeted thermal environments. This aspect has not been investigated in this study though, and no backing plate were used, leaving the bare steel of the welding apparatus as the sole heat sink.

II.2.B Al/Al welding

While unsecuring the finished plate after a weld, it is common for it to deform and exhibit a slight curve. 44 aluminium assemblies were manufactured, all in a butt-joint configuration, one of the many available welding possibilities presented in subsection I.2.B. A schematic representation of the welding apparatus for Al/Al FSW joint manufacturing is provided in Figure II.6, and a picture of the corresponding experimental setup is presented in Figure II.7. The clamping system used here prevents the plates from sliding side to side and blocks bending resulting from residual stress induced by heat. Two 400×95 mm, 6 mm thick plates were placed on both sides of the clamping system of the FSW machine, as shown in Figure II.6. These plates can be of the same Al alloy (i.e. similar welding) or not (dissimilar welding) . Before welding, the aluminium plates were cleaned with ethanol and paper wipes to remove cutting lubricant residues. The rotating tool is composed of a

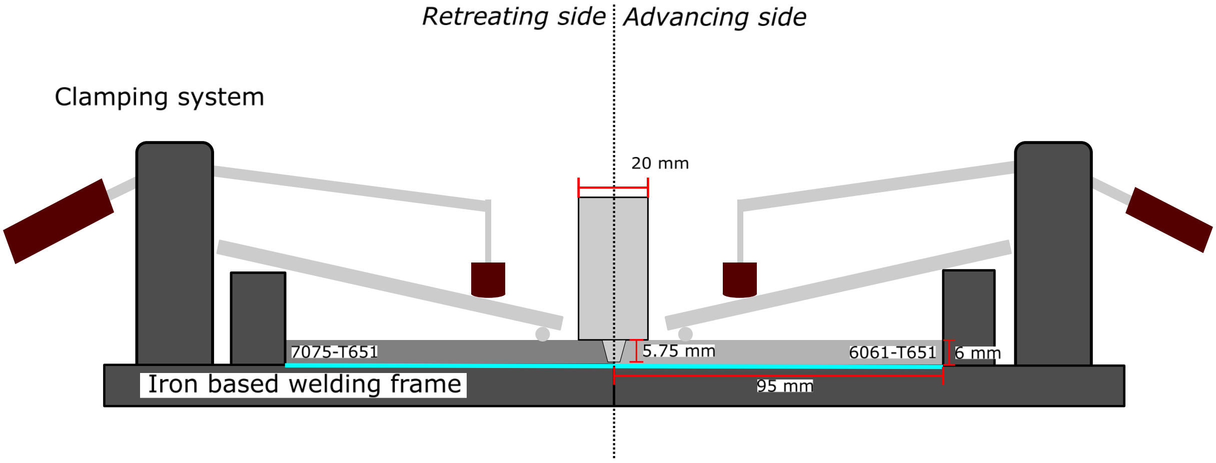

Figure II.6: Schematic of the Al/Al butt-joint welding setup. The blue line signals where a backing plate could be inserted if needed.

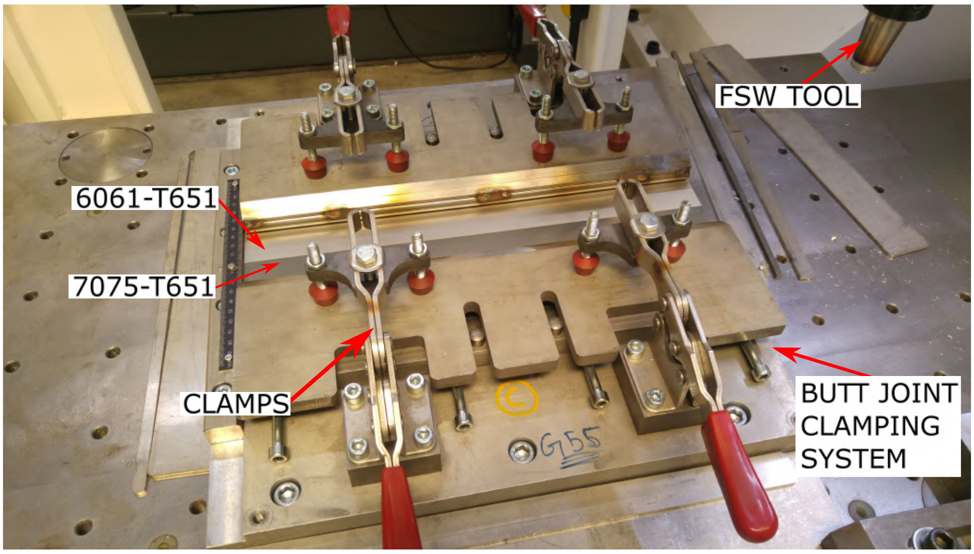

Figure II.7: Welding setup (showing clamps) for a butt joint 6061/7075 (6 mm) on the FSW machine.

threaded 5.75 mm long pin, and a 20 mm diameter grooved shoulder. A picture of a used tool can be seen on Figure II.8(a). A schematic of the tool can be seen on Figure II.8(b). Of course, the friction energy between the tool and the aluminum assembly results in heat dissipation and significant temperature increase of the tool. To ensure similar thermal condition for all the tested assemblies, the tool is air cooled in between successive welds. As discussed in Chapter I, tool geometry depends on the size of the manufactured welds. Data provided by K.Colligan (see Appendix) was presented on Figure I.23. On Figure II.9, the tool used in this study has been added. Its shoulder and pin diameter are well within range of comparable tools.

Two types of assemblies are performed in the case of Al/Al welding, either similar or dissimilar. The first type is shown on Figure II.10(a) as a schematic and on Figure II.11 as a photograph. Three small 100 mm long welds manufactured on a dissimilar assembly are shown. For a given RPM, three welds of 80, 100 and 120 mm/min are performed. These relatively small welds are cut in 10×6×190 mm samples, as the red dotted lines indicates.

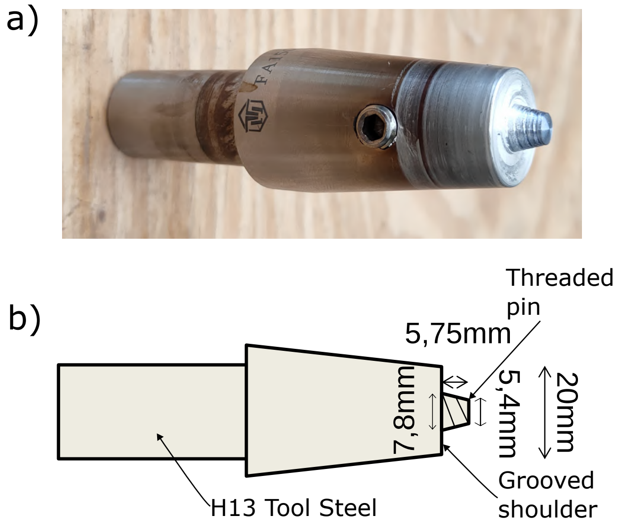

Figure II.8: (a) Picture of the FSW Al/Al tool used (b) Schematic of the steel FSW tool used in the manufacturing of aluminium similar and dissimilar joints.

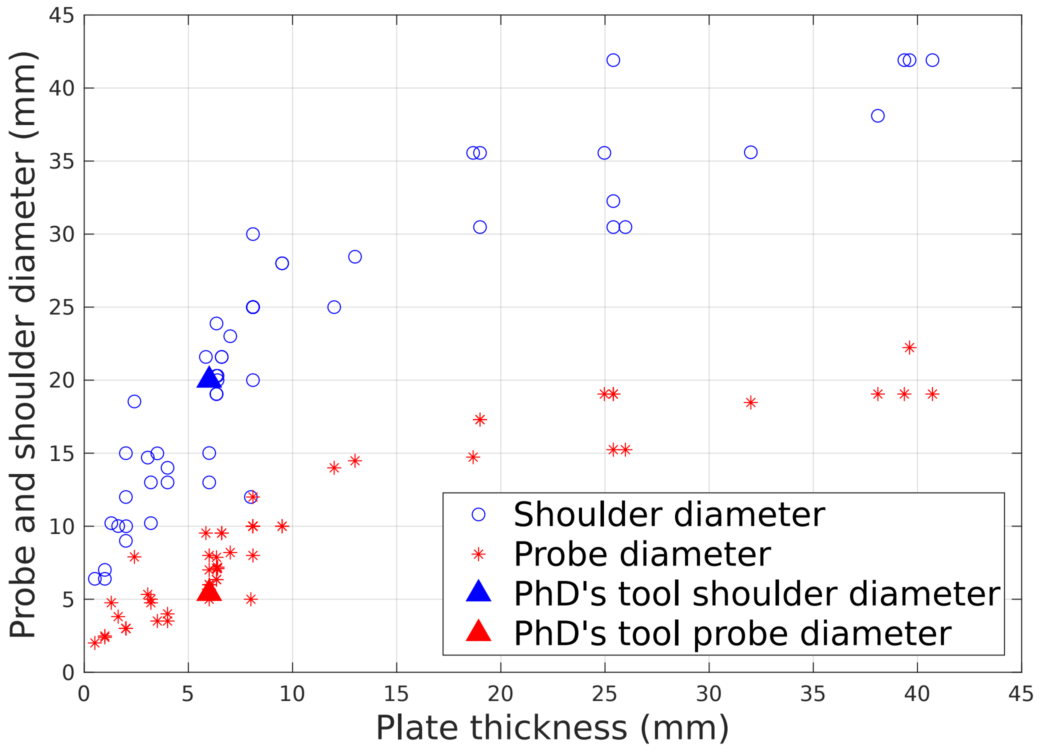

Figure II.9: Shoulder and pin diameter relative to the plate thickness in a butt joint FSW, data provided by K.Colligan. The tool used in the Al/Al joint manufacturing campaign is added.

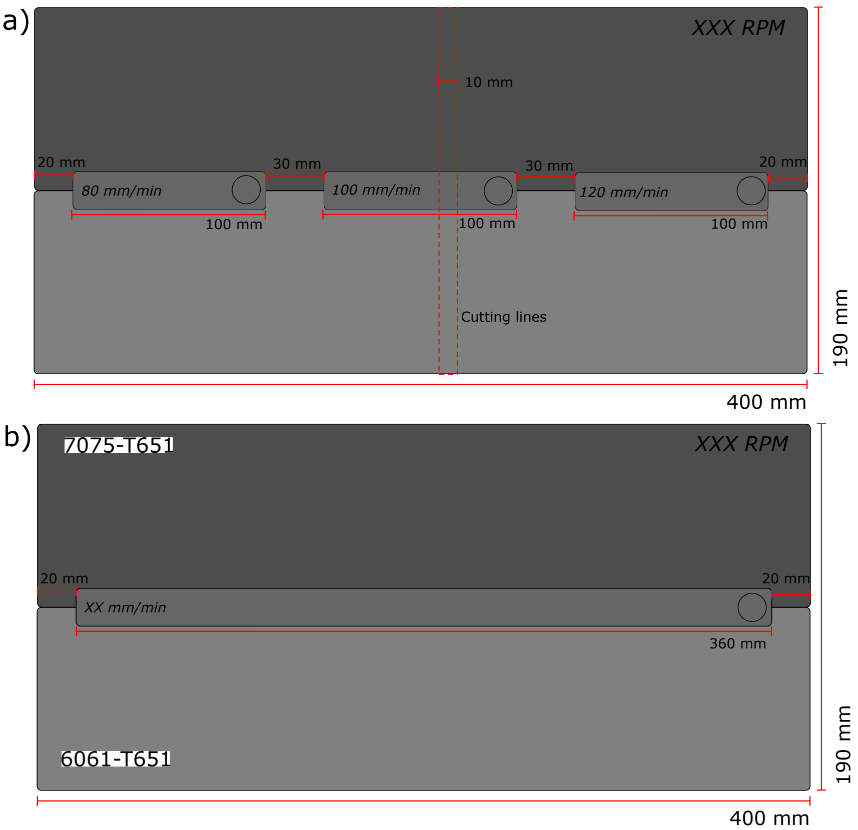

Figure II.10: Schematic of multiple FSW joints on a *butt-joined* dissimilar Al configuration. (a) For microstructural analysis and tensile testing, 10mm wide rectangular shaped sample are extracted. Each plate contains three welds at various advancing speed. (b) 360 mm *butt-joined* weld for fatigue sample manufacturing on a dissimilar and similar Al assembly is done.

These samples can be used for microstructural analysis and mechanical tests, such as tensile testing for example. These multi-advancing speed welded plates are manufactured for practical reasons. Each 100 mm welds is enough to extract at least 5 previously mentioned samples whilst being in the middle of the weld, i.e. in the stable part of the weld. This sample's number is enough for each weld to be fully studied.

The second type of assembly performed is shown on Figure II.10(b). A 360 mm long weld is manufactured in a continuous way along the joint of two base plate. An example of such an assembly can be seen on Figure II.12 between two similar plates of AA7075. For each assembled plate, a single parameter set is chosen. These Al/Al assemblies are specially manufactured with fatigue testing in mind. All fatigue samples for a given experimental parameters set are extracted from a single welded joint. A 360 mm long weld yields 15 fatigue sample. The fatigue sample's shape and extraction plan from these plates are detailed in Section II.4.C along with extraction and polishing method.

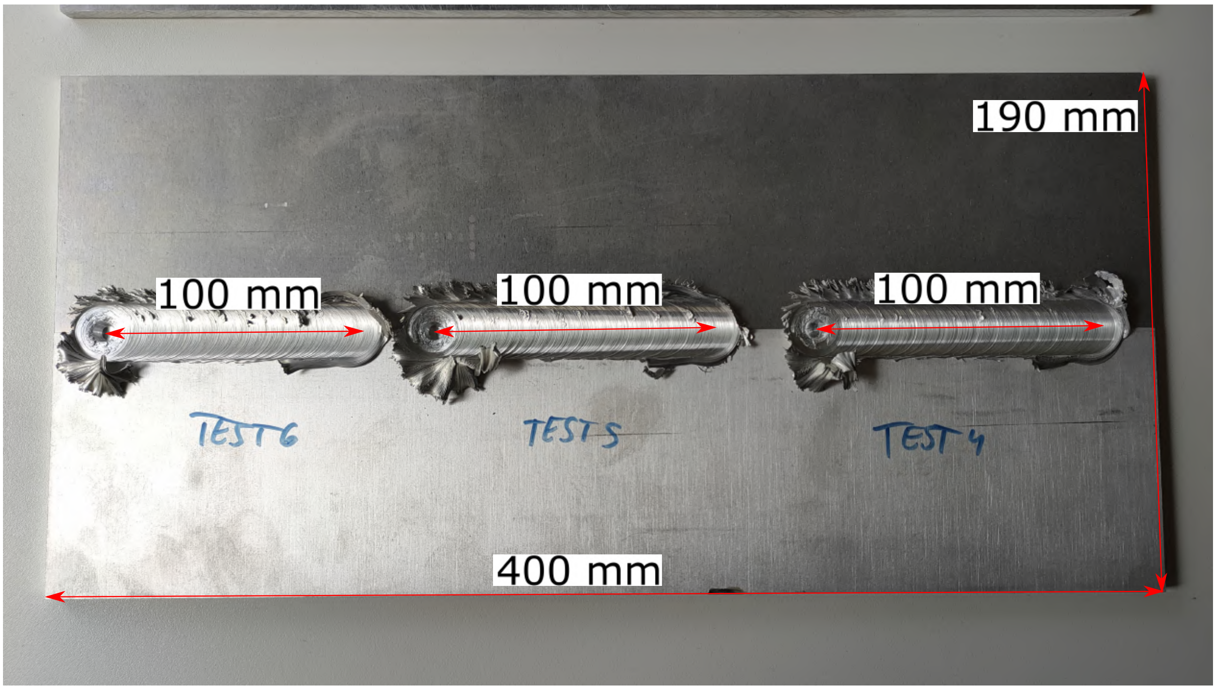

Figure II.11: Example of three 100 mm welds performed on a dissimilar AA6061-AA7075 assembly. The welds exhibit excessive amount of flash. The caption "Test" alongside each weld indicates that they were manufactured as the experimental plan was established.

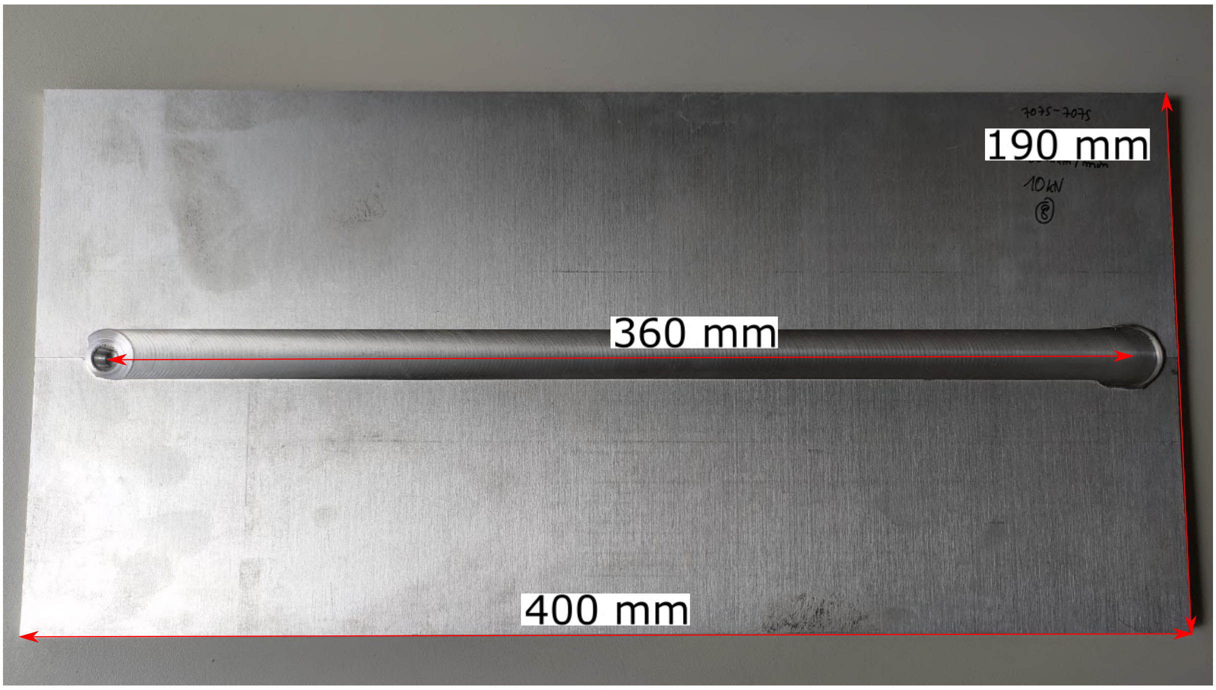

Figure II.12: Example of a long 360 mm weld performed on a similar AA7075 plate. The plate are marked with their respective welding parameter.

II.3 Microstructural characterisation

This part aims at presenting the various experimental techniques used to characterize the microstructure at multiple scale in the welded joints.

II.3.A Optical microscopy and related sample preparation

Optical microscopy can be used to analyze large zones of a specimen: grains, alloy phases, defect, etc. In order to reveal these details, sample preparations are generally necessary. Metallic samples studied using optical microscopy generally require chemical etching beforehand. Indeed, chemical etching is used to identify and analyze the region of interest by taking advantage of one or many chemical reactions to reveal different features of interest. For instance, a chemical reaction may result in a preferential etching of grain boundaries, inclusions or phases, or even crystallographic textures that may all react differently to a reagent. It should be noted that surface polishing of a metallic sample to remove scratches and/or to allow a better etching from a reagent is common practice.

On Figure I.25 in Section I.3.B, the schematic shows different zones in a butt-welded joint (i.e., the HAZ, TMAZ, stir zone and base material), whose size and morphology depend on welding conditions and parameters, and have a significant impact on mechanical properties. It has also been found that different Al alloys are colored differently by a solution of potassium permanganate, which is useful within the context of FSW to identify alloys in the mixing zone. Therefore, within the framework of FSW, the first characterization of the microstructure consists in addressing size and morphology of the different zones. In order to distinguish and characterize different zones of a FSW joing, a Keyence microscope VHX-1000 equipped with a digital camera has been used in this study.

For analyzing dissimilar Al alloys joints with optical microscopy, multiple steps are needed. From the elongated extracted sample presented in Subsection II.2.B on 100 mm welds, polishing is done up to 2400 SiC in preparation for etching. A solution of diluted Weck's reagent, whose formula is 8g $KMnO_4$ + 2g NaOH + 400 mL H_2O [123], is used for the chemical etching. Usually used to characterise casting aluminium by coloration of the dendrites and precipitates, it was found particularly practical for dissimilar Al FSW. On Figure II.13(a), an unetched dissimilar AA6061/AA7075 welded sample can be seen. On the same Figure II.13(b), an etched version of a similarly polished sample can be seen. As each alloy of aluminium is clearly visible, details, especially in the stir zone, are missing compared to the etched surface such as the alternating bands of dissimilar Al alloys also known as "onion rings". The $KMnO_4$ colors each Al phase differently based on alloying elements. In this instance, the AA6061 is observed in a darker tone compared to AA7075.

II.3.B Scanning Electron Microscopy

Scanning Electron Microscopy (SEM) allows to reach a higher spatial resolution than optical microscopy. Thus, observations through SEM are complementary to optical microscopy. Under optimal observation conditions, a FEG SEM is capable of magnification close to x100 000. In this work, a FEI Quanta 650 with a FEG (Field Emission Gun) source was used.

Secondary Electrons (SE) imaging can provide data on grain morphology, inclusions

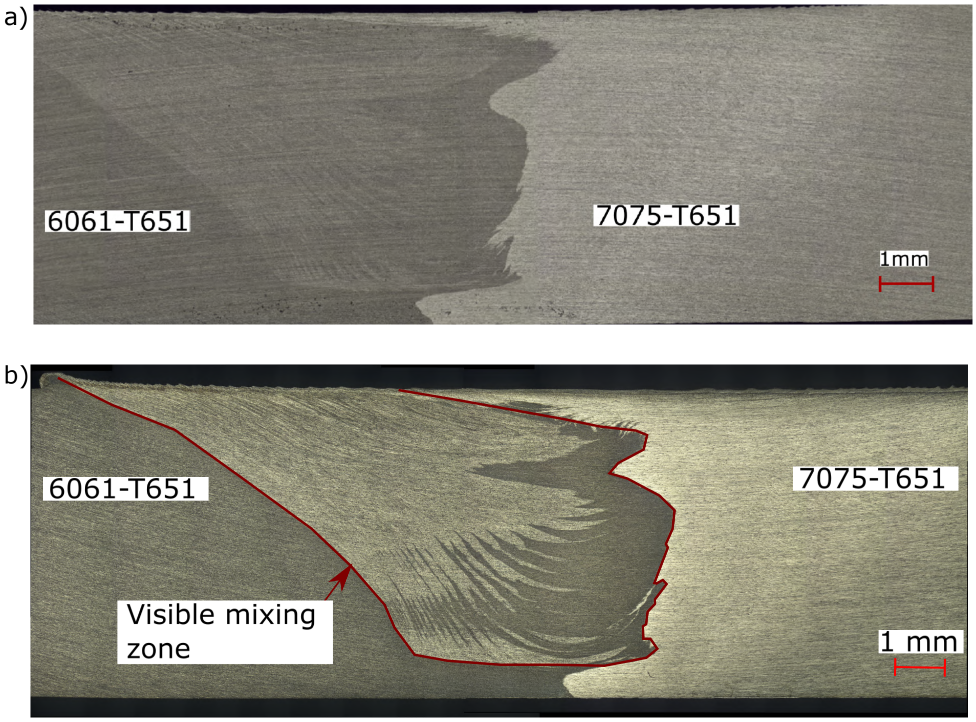

Figure II.13: Macrographs of a FSW dissimilar (a) without and (b) with etching chemical etching.

and porosities within a material. For SE observation, the fundamental principle of optical imaging is used, but substituting photons for electrons. On Figure II.14, it shows that secondary electrons are generated close to the sample's surface. SE observations of the grains, inclusions and porosities require a mirror polishing of the sample. In the case of aluminium, this means a multi-step polishing procedure:

- **Silicon carbide polishing** using dedicated SiC paper. Each polishing step (320 SiC, 600 SiC, 1200 SiC, 2400 SiC) is done for a few minutes on turning polishing tables with water.
- **Diamond polishing** using special cloths and diamond polishing compound up to 1 µm

Within a SEM, electrons from the beam have an accelerating voltage usually ranging from 5 keV up to 30 keV. The inelastic nature of the electron-matter interaction in the case of secondary electrons means that SE have low accelerating voltage (<50 eV). In turn, this makes SE observations particularly suitable for topological analysis such as fracture surfaces as seen in Chapter V on Figure V.11. The depth of field for SE observation is much greater than what can be achievable with optical microscopy. SE observations allow to study the topology of a sample surface, complementary to optical microscopy.

BSE (BackScatter Electrons) are generally used complementary to SE to characterise a microstructure. BSE are generated deeper into the observed material as seen on Figure II.14. BSE interact in a so called elastic way with the observed material. Essentially, BSE have the same accelerating voltage as the incident electrons from the beam. Depending on the atomic number of the observed material, more or less electrons are being re-emitted towards the BSE sensor. Generally, the heavier the element, the more BSE it

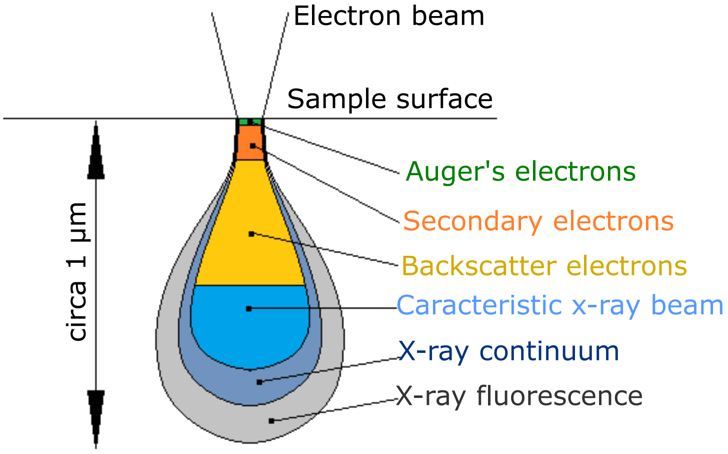

Figure II.14: Pear-shaped electronic interaction volume, showing where each electron type emerges during the electron-matter interaction

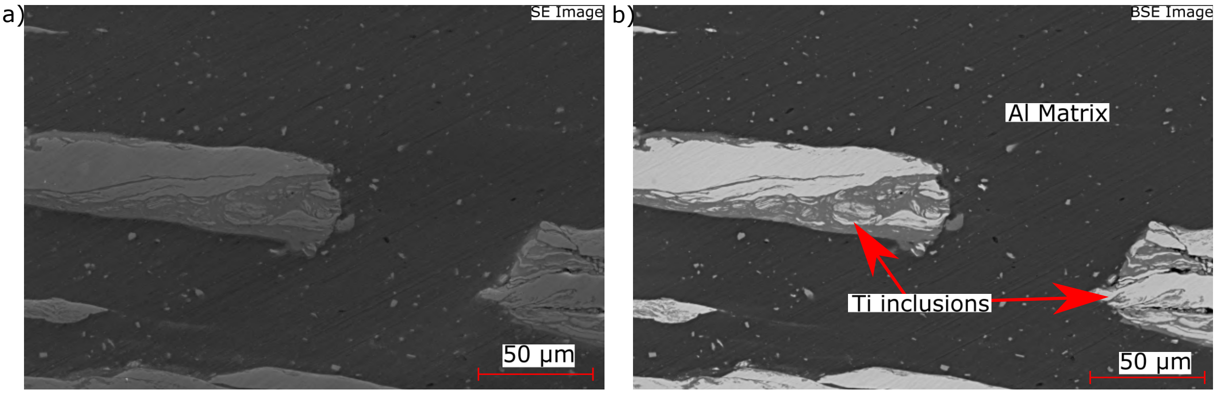

Figure II.15: Comparison of a FSW Ti/Al weld in (a) SE imaging and (b) BSE imaging

will emit when hit by an electron beam. Also, BSE emission coefficient depends slightly on grain orientation.

Sample surface preparation is similar compared to SE observation. On Figure II.15, Ti (atomic number 22) inclusions appear whiter compared to the Al (atomic number 13) matrix as it emits a stronger BSE signal. This defining characteristic of BSE can also help distinguish grains. Such an example is visible on Figure II.3, where grain boundaries are distinguishable thanks to precipitates, with different chemical composition, at the grain boundaries.

EDX (Energy Dispersive X-Ray Spectroscopy) analysis is mainly used in completion to BSE imaging, using another electron-matter interaction. As Figure II.14 shows, part of the incident electron beam is absorbed by the matter and then re-emitted according to the absorption/emission principle. Most of the emitted spectrum falls into the category of X-rays. By analyzing X rays frequencies and amplitude, it is possible to estimate the presence (or absence) of certain elements in the observed sample. Each element of the periodic table re-emits X rays within its own frequencies depending on the accelerating voltage of the incoming electron beam. As mentioned, this observation technique is particularly well suited to BSE observation: the latter makes it possible to quickly and macroscopically identify the presence of various elements, and an EDX analysis can confirm which elements

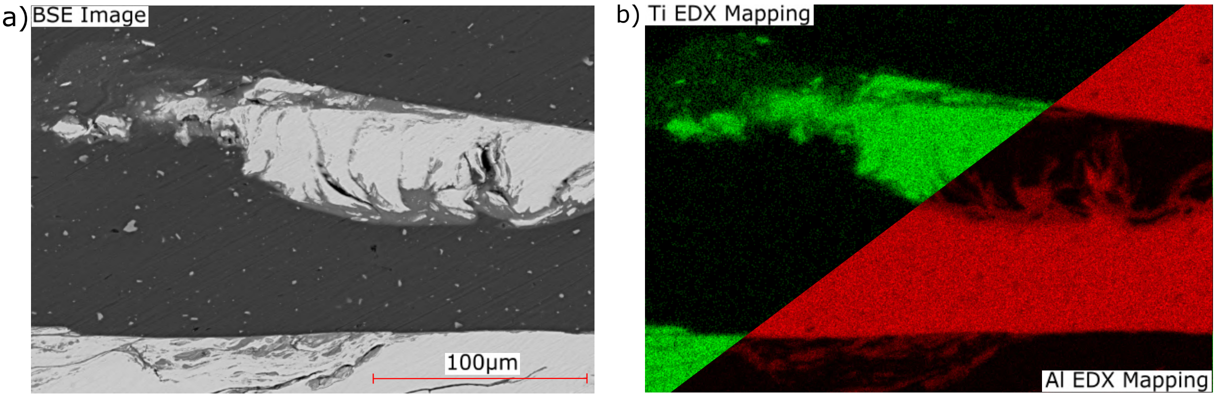

Figure II.16: Relationship between (a) a BSE mapping with (b) an EDX mapping. EDX allows to fully identify which elements create the BSE contrast

are present. Sample preparation is similar to SE and BSE observations. In Figure II.16, an EDX mapping has been carried out on a titanium inclusion within an aluminium matrix, similar to the images presented in figure II.15. The Ti appears brighter than the Al matrix as it emits more BSE. Also, the frontier between the inclusion and the matrix has a gradient of contrast in between the Ti's brightest one and the Al's darkest one. This is explained by the likely presence of AlTi intermetallics with reactivity of both alloys.

The final analysis performed on some samples is called Electron BackScatter Diffraction (EBSD). See [124] for principle details. EBSD is a powerful technique in which, through measurements of diffraction patterns called "Kikuchi lines", it is possible to accurately measure the local crystallographic orientation. For example, measuring the crystallographic orientation allows the drawing of Inverse Pole Figure (IPF) maps. The IPF is generally the image most commonly associated with EBSD. This representation allows, in a rough way, to estimate the distribution of grains in the diffracted area, if particular grain boundaries (twinning for example) exist or to identify potential crystallographic textures. On Figure II.17(a), such a map is shown in the case of a FSW AA6061/AA7075 joint as an example. Difference in recrystallized grain size is visible and can be quantitatively assessed using commercially available software. Other values can be calculated such as the Kernel Average Misorientation (KAM) [124]. KAM is fundamentally the average of crystal orientation from the neighboring pixels. A visualization of KAM calculation is visible on Figure II.18. For each pixel measured using EBSD, a given orientation noted ω is obtained. By averaging this measurement over a circle (or rectangle) with a given radius r, the calculated orientation ω_m is attributed for the pixel. For each pixel, the average KAM is a practical mean of visually assessing local misorientation, which can be linked to multiple causes: high dislocation density, local residual stresses, etc. This tool is highly effective in visualising subgrain structures and lattice bending. A KAM map can be seen on Figure II.17(b) and illustrates how different phases can be identified using KAM. To carry out this type of analysis, sample preparation is crucial. The surface hardening induced by the mechanical polishing is detrimental to the electron diffraction. In the case of polishing FSW aluminium samples, a method known as "vibropolishing" has been used. There are many commercial solutions for vibropolishing, which meet different needs depending on the alloy and the desired effect: use of colloidal silicon, alumina particles, slightly basic, neutral or acidic pH solutions, etc. In many cases, these solutions are mixed with other reagents (hydrochloric acid, hydrogen peroxide for example) or diluted.

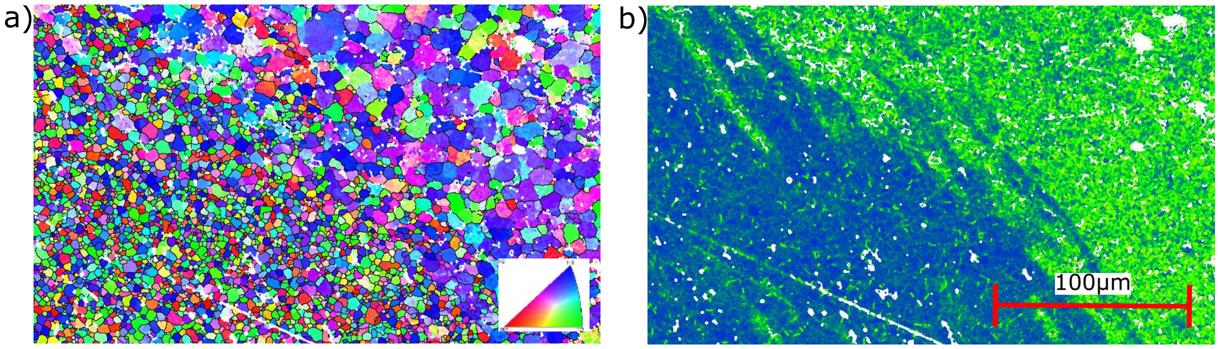

Figure II.17: Two different representation of EBSD results on a 6061/7075 FSW joint: (a) IPF mapping showing crystal orientation and difference in grain size between two apparent phases and (b) KAM mapping showing a difference between each phase

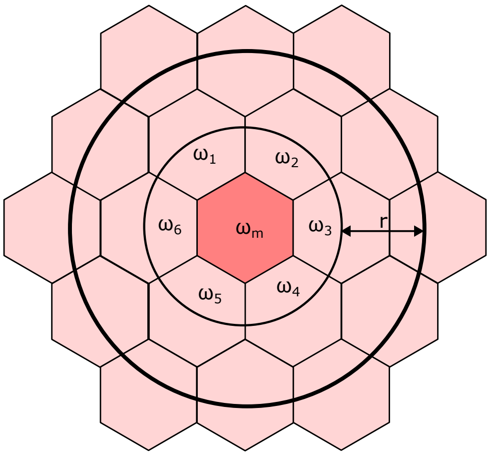

Figure II.18: Visual representation of the KAM calculation process

For aluminium EBSD, it was found that a mixture of 50% demineralised water and 50% commercial OP-AN solution (Struers, Alumina in neutral solution) used on a Buehler Vibromet at 40% power for 2 hours gives the best polishing.

II.4 Mechanical characterisation

In this Section, the multiple experimental techniques used in this study to mechanically characterize the different welds obtained are presented. They are detailed from the more macroscopic one to the finer one.

II.4.A Hardness measurements

Hardness measurements play a role in the mechanical characterization process of this study. In an industrial context, hardness tests are used to quickly characterize a given material or alloy and assess if they meet a given standard for their intended purposes. There exists multiple typed of hardness measurement but they all follow the same procedure, i.e. an indenter is pressed onto the test surface with a given load, for a specified amount of time. Different scale of hardness measurements also exist depending on the size of the indenter and the applied load. Macro hardness machines can go up to 30 kN in applied load. They are generally used in industrial contexts. Micro hardness machines can mechanically load a sample up to a few hundred N of force. Nano indentation uses load going up to a few tens of µN. Depending on the hardness type and scale used, a different value is measured: the diameter of a impressed sphere, diagonal lengths of a diamond-shaped imprint, etc. Both aluminium used in this study are interesting to characterize using micro-hardness values. As explained in Section II.1, mechanical properties of these alloys are induced by nanoscopic precipitates created through various heat treatments. These hardening precipitates are heat sensitive and will start to dissolve and coalescence, given sufficient temperature and time. Hardness measurements allow to characterize the resulting heterogeneities in mechanical properties.

Throughout this work, the Vickers scale is used. A square-shaped diamond indenter is used on an Innovatest Falcon 400 in a micro indentation scenario.

Sample for hardness measurements can be any flat metallic surface. Whether aluminium, titanium or any other metal is considered for this type of analysis, a sample needs to be extracted and polished. For Al joints, both similar and dissimilar, rectangular sample 6×190×10 mm in size (presented on Figure II.10 in Subsection II.2.B) were used to measure cross-section hardness along the welded seam. Samples were extracted using a hacksaw. They are polished with SiC paper up to 2400 grit on one side of the cross section, the other being slightly grinded using low grit SiC paper in order to smooth it and remove cutting marks. An applied force of 200 gr, noted $H_{v0,2}$, with a 12 s dwell time is used. An example of a Vicker's indent can be seen on Figure II.19(a). When performing hardness indentation, it is important to ensure that a previous measurement does not interfere with the next one. According to the ISO 6507 standard [125], the distance between the centres of two adjacent indentations shall be at least six times the mean diagonal length in the case of light metals and their alloys in order for them to not disturb each other. In this case, the diagonals of an indent do not exceed 100 µm and the inter-indent distance is 1 mm when performing hardness profile.

In precipitation hardened aluminium alloys (see Section II.1), hardness measurements give a crucial information regarding the local density and shape of hardening precipitates. As they dictate the mechanical behaviour of their parent material, characterizing them through hardness measurements proves valuable. Hardness measurements characterize the local mechanical properties, as can be seen on Figure II.19(b) where the evolution of the values measured from one alloy to the other is visible. Such evolution can be explained by microstructural analysis and be linked to typical areas (TMAZ, HAZ).

II.4.B Tensile tests

A conventional mechanical test is the uniaxial tensile test extended here to weld testing. A sample is mechanically loaded along a given axis, usually at a given displacement rate. By plotting the calculated stress from a load cell between the sample and the tensile machine along with measured strain, it is possible to obtain a tensile curve. An example of a tensile curve is visible on Figure II.23. From a simple tensile curve, multiple mechanical values can be extracted: Young's elastic modulus, yield strength and ultimate tensile strength (UTS). In the specific case of butt-joint FSW and butt-joint welding in general, this type of mechanical loading allows the calculation of what's called the "joint efficiency". It is the ratio between the lowest of both material's UTS and the measured UTS of the welded joint. In ISO 25239-4 [126], guidelines for Al welding and "joint efficiency" are

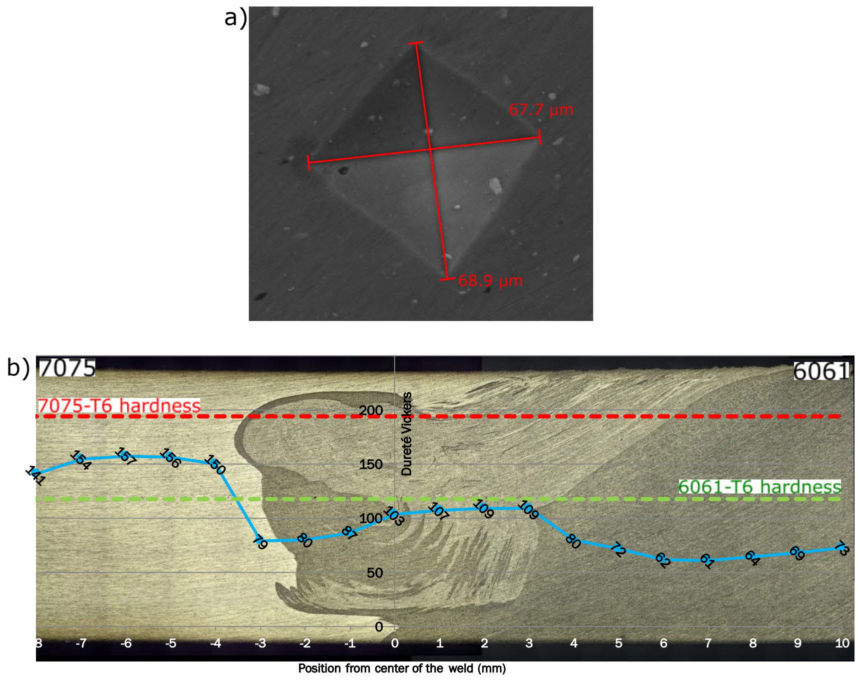

Figure II.19: (a) Hardness indent in a Al matrix seen in SE imaging (b) Hardness profile overlayed on a macrograph of a FSW 6061/7075 joint

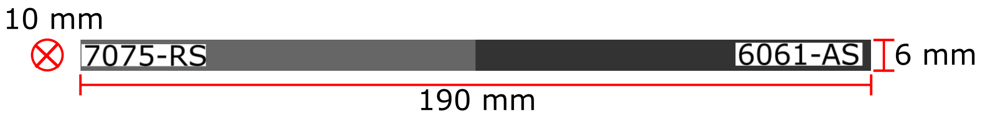

Figure II.20: Illustration of a uniaxial tensile sample from a FSW butt-joint. Alloys differ from one experimental planning to another, but dimensions stay identical.

given based on the metallurgical state of the parent material (T4, T6 etc).For example, a similar AA6061-T6 joint ($R_m = 290MPa$ in T6 state) with a measured UTS of 210 MPa would have a joint efficiency factor of 0.72.

Several machines were used according to their respective availability: an Instron machine with a 30kN load cell, an MTS 100kN machine and an MTS 250kN machine. In each case, the maximum tensile load has been kept well below the maximum authorized load. As such, reasonable assumption is made that the machine's frame did not interfere with the tests.

Tensile samples are extracted from welded Al butt-joined plates in a rectangular shaped 6×190×10 mm piece using a hacksaw, similarly to the way hardness samples are extracted. A schematic of a tensile sample are shown on Figure II.20 as well as a picture on Figure II.21.

Samples are then polished using SiC paper on both cross sections of the weld. Both sides are polished in order to ensure that the failure of the sample during the tensile test will not be result of a surface defect left by the cutting process. Indeed, surface state and especially surface defect can lead to premature failure of a sample. For strain measurements, a black and white speckle is painted on the observed surface. The techniques used for strain calculation is called Digital Image Correlation (DIC) and is detailed in the Subsection II.4.D. The sample is then loaded into the self-tightening clamps of a tensile machine. It is properly aligned with the machine's tensile axis in order to ensure no bend-

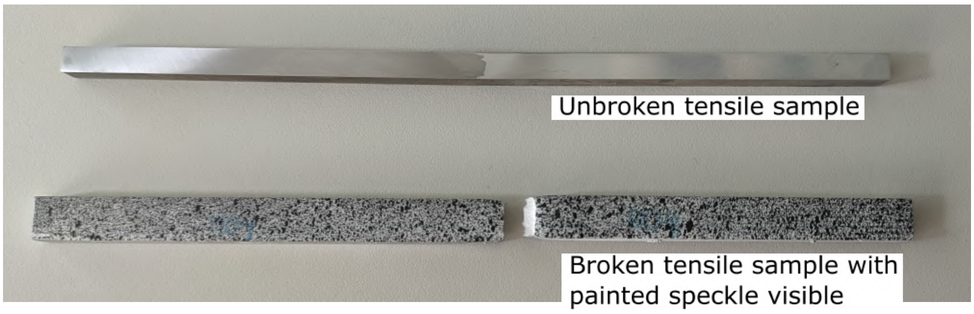

Figure II.21: Photograph of two tensile samples before and after the mechanical test. The paint speckle is visible on the broken sample.

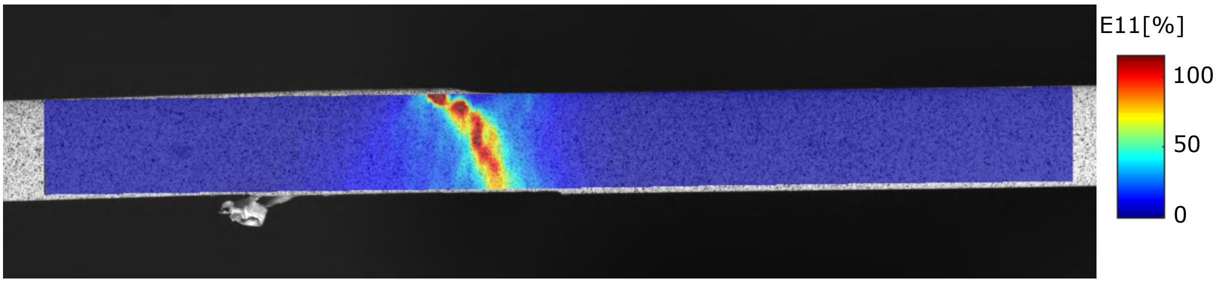

Figure II.22: Example of a DIC-calculated strain map superimposed on an undeformed tensile sample. The strain localization and ensuing fracture is clearly visible and corresponds to a mechanically weaker link in the sample.

ing moment. It is ensured that a sufficient length of the samples' extremities is firmly clamped to minimize slipping of the sample during the tensile test.

The experimental setup is composed of a MTS 250 kN (or sometimes 100 kN) tensile machine along with a MTS acquisition system linked to a computer for data logging. A home-made DIC capture software called *Agnes* is used to capture images and sync up data from the MTS machine (load, position). The sample is deformed at a given rate of 0.6 mm/min. No loading/unloading is performed after sample failure. The overall strain is calculated using a commercially available software called *CMV* and the corresponding (σ, ϵ) curve is drawn. This type of 2D DIC produces strain maps as well. An example of a strain map is visible on Figure II.22. On Figure II.23, the resulting tensile curve is shown.

II.4.C Total fatigue life tests

Fatigue assessment has been performed on aluminium dissimilar FSW joints.

These fatigue tests were carried out by a subcontracted company (Bureau Veritas, Belfort, France) with the following parameters: $R = 0.1$, $25Hz$ frequency with a censoring at $5 * 10^6$ cycles. The machine was regularly tested to ensure conformity. Fractography was performed in a SEM using SE observation mode, described in Subsection II.3.B.

The sample geometry is visible on Figure II.24. It is a flat, dog bone shaped sample. It was designed based on existing plans, inspired from the ASTM E8 / E8M one [127]. The manufacturing of these samples was carried out by water jet cutting in the premises of the Laboratoire Leprince Ringuet (LLR) on the Ecole Polytechnique campus. The choice of waterjet cutting was made for its speed, ease of access and the fact that samples are

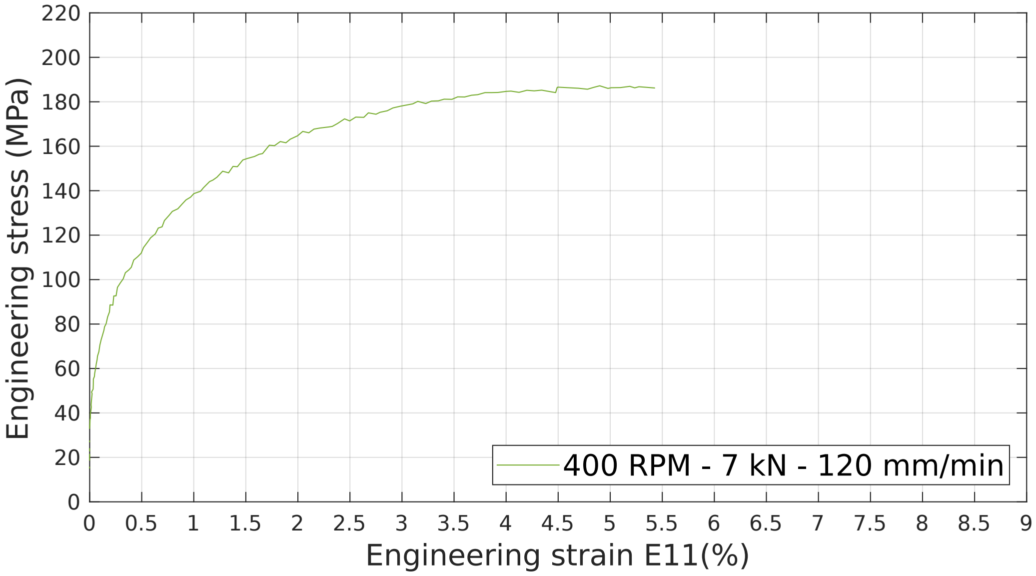

Figure II.23: Tensile curve of ϵ_{11} calculated from the DIC analysis of Figure II.22 in the tensile direction, i.e. the sample longest side.

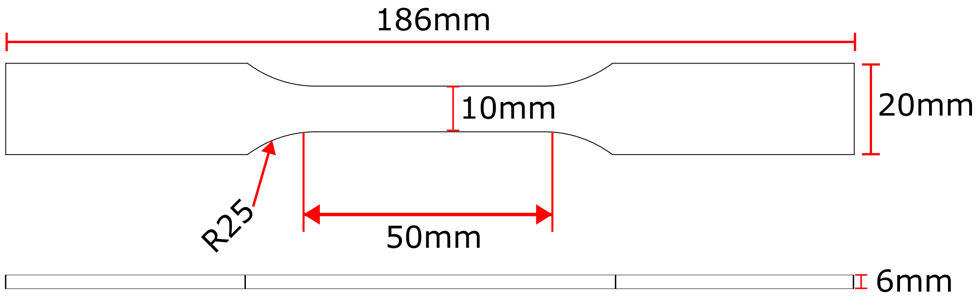

Figure II.24: Fatigue sample for dissimilar Al/Al fatigue.

maintained at room temperature during cutting. The end result along with a schematic of the full plate can be seen on Figure II.25.

Sample preparation then involved multiple steps before being sent for mechanical testing. First, the samples were separated from each other by hand. Then, each individual sample was mechanically stamped for traceability. The stamping has been made as far as possible from the working area as to not interfere with the fatigue results. The samples were then individually hand-polished up to 2400 SiC.

II.4.D Digital Image Correlation

To mechanically characterise a sample, one has to be able to measure strain during the mechanical testing. From strain gauges and Mohr's circle to clip-on extensometers, a wide variety of choice is available, depending on the circumstances and practicality of a given experimental campaign. Digital Image Correlation (DIC) is a popular technique and is extensively used throughout this work. It is defined as a full-field strain measurement method and uses digital capture, i.e. video recording or snapshots, alongside mathematical analysis to calculate strain on an observed surface.

On a domain Ω, I is defined as the reference image and i as the current image.

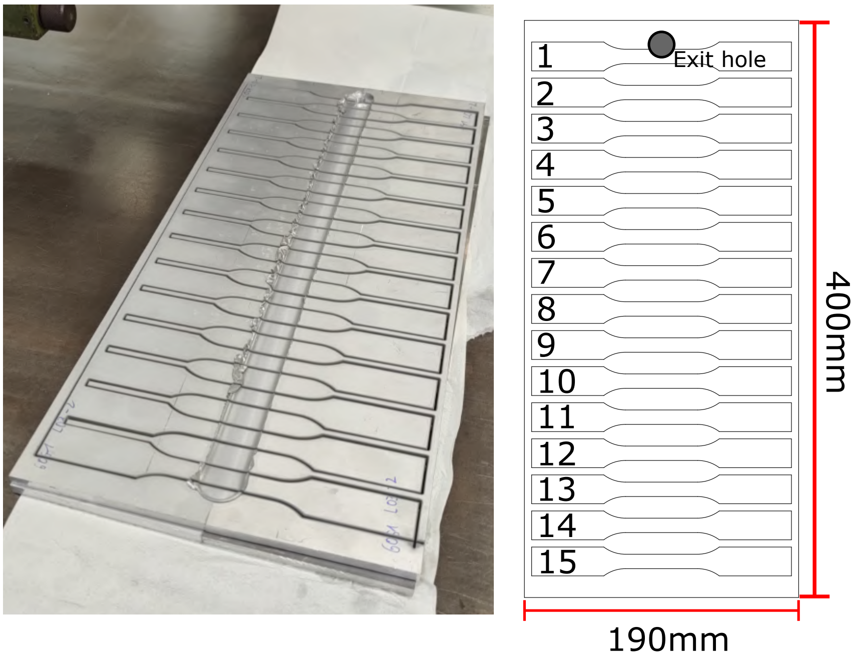

Figure II.25: Fatigue samples after waterjet cutting. The samples are numbered for traceability.

Subsequently, $\underline{X}$ is the reference configuration and $\underline{x}$ the current one. A DIC problem then equates to minimizing $J(\underline{x})$ (II.3) with $\underline{x} = \underline{X} + \underline{u}(\underline{X})$. $\underline{u}$ being here the strain field solving this DIC problem.

$$J(\underline{x}) = \int_{\Omega} [i(\underline{x} - I(\underline{X})]^2 d\Omega \tag{II.3}$$

Out of plane measurements are possible in case of a multiple cameras setup.

At its core, DIC uses contrast within an image to identify nodes and quantify their physical movement during the experiment from previous images or steps. In theory, any surface with enough visible heterogeneity can be used for DIC calculation. Any camera setup can be used to perform DIC as long as the system used is stable and powerful enough to well capture the sample at the desired scale. In practice, surface marking techniques are commonly employed to enhance DIC results. Correlation itself can then be performed on any computer, the computing power of the unit having only an impact on correlation time. Multiple correlation algorithms exist and a good portion of them are either commercially or even freely available.

In this work, multiple marking techniques are used depending on the size and scale of the observed surface: paint speckles for optically measured strains in tensile testing, gold lithography for meso-scale measurements (up to 1 µm) and physical vapor deposition (PVD) of tin for micro-scale analysis in a SEM environment. Figure II.26 showcases each technique's results. The paint marking technique is used to characterize strain at the macroscopic level during macro tensile testing. Gold lithography and tin PVD are exploited in Section IV.5 for measuring local strain during a micro tensile test. On Figure II.27 a BSE image of a deformed microstructure shows the behavior of the marking in extreme strain circumstances. It can be seen that the tin spheres are firmly attached to the surface of the sample as the outline of the damage is visible. The tin layer does not appear to mechanically limit the damage of the underlying aluminium. Thus, the

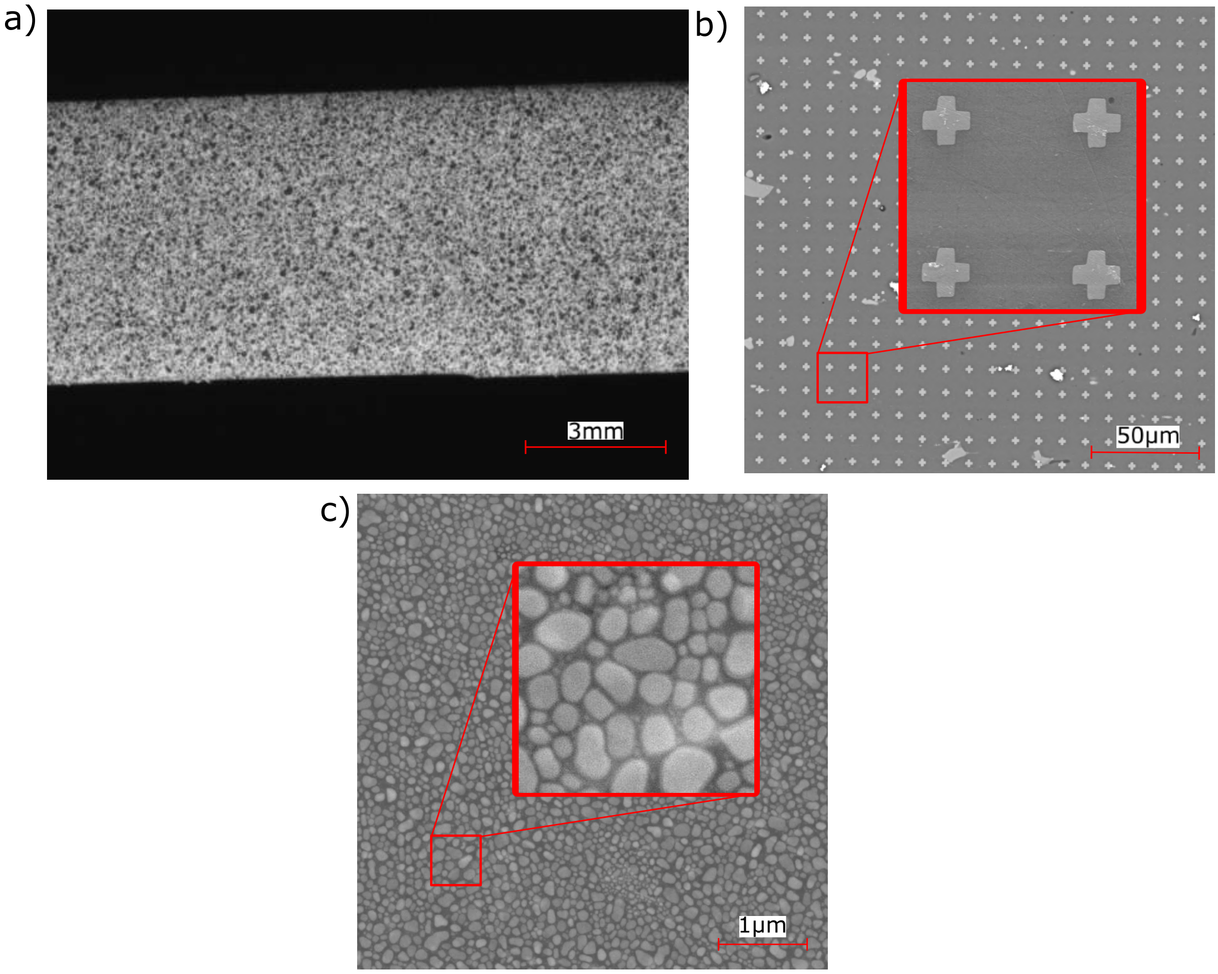

Figure II.26: (a) Paint speckle on a tensile sample (b) Lithographied gold crosses on an Al sample in BSE imaging (c) Tin speckle resulting from PVD on an Al sample in BSE imaging

DIC measured strain are not affected by the tin layer and the sample deformation is well captured.

Strain calculation can be done using commercially available software or using free Python/Matlab code. In this work, the software *Correlation Manual Value* (CMV) is used [128].

During these tensile tests, the strain fields measured are rectangles 6 mm (plate thickness by 50-60 mm in length, depending on the elongation of the sample at fracture. At the chosen resolution and distance between the sample and the camera setup, a pixel is roughly 26 µm in length. From the tensile testing setup, multiple values are measured:

- $Rp_{0.2}$ (MPa) is defined as the stress at 0.2% of apparent plastic strain. The start of yield is considered at the end of the apparent elastic strain behavior of a tested welded joint.
- Ultimate Tensile Strength (UTS, MPa) is the maximum apparent stress during the tensile test
- ϵ_{11} (%) is the overall engineering strain measured on the correlation domain in the tensile axis at sample fracture

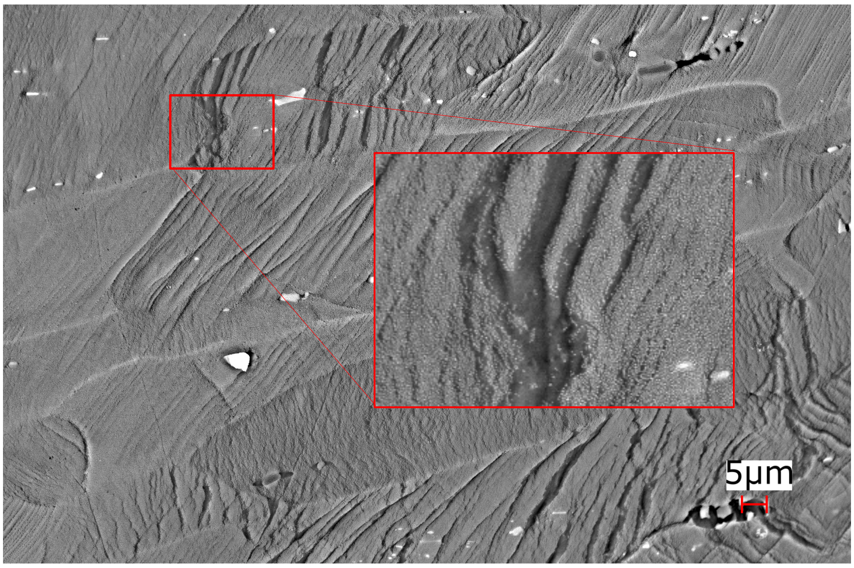

Figure II.27: BSE image of a deformed microstructure after micro mechanical testing. Grain boundaries are visible and extensive damage inside the grains as well. A PVD tin layer has been applied to follow strain using DIC. A close-up on a damaged area is visible, where the tin spheres followed the aluminium's surface even in heavily damaged areas.

Chapter III

Welding parameters optimization

In this Chapter, the procedure for identification of optimal process parameters for Al/Al dissimilar welding, testing and ultimately selection will be discussed. Potential welding parameters need to be identified prior to the manufacturing campaign. Literature studies and discussions with colleagues yielded preliminary parameters. A large parameter window followed by visual inspection, welding load data and basic mechanical testing is explained in Section 1. Subsequently, the various experimental plans are laid out and contextualized to explain their goals they aimed at.

III.1 Dissimilar AA6061/AA7075 welds

III.1.A Identification of visually sound welds

FSW involves multiple welding parameters: tool choice and tilt, axial load, rotational speed, advancing speed, and plunging depth. For Al/Al dissimilar welding, advancing speed, rotational speed of the tool and axial load are modified and form the basis of the experimental plans. The tool choice, tilt and plunging depth are not modified in our study. The tool proposed by the machine manufacturer was deemed satisfactory. This work focuses on the welding parameter selection for that particular tool. As explained in Chapter II.2, changing the tool tilt on the FSW machine is a tedious and lengthy process. It can not realistically be performed in between every other weld. Thus, it was set at 1° at the beginning of this study and not modified afterwards. This value was chosen based on previous studies performed at UCLouvain. The plunging depth is neither modified as it is linked to the selected tool. The initial plunging depth was thus kept at 5.75 mm for all FSW campaigns. The tool rotated in a counter clockwise manner.

Literature is consulted in order to establish a base-line regarding which parameters will be chosen. In most scientific literature, tooling is vaguely discussed. It usually specifies pin length, special features (such as threads) and the shoulder diameter. As such, unless the exact same tooling is used, it is not possible to directly reuse process parameters taken from literature. However, the impact on the weld each parameter variation has is now well documented, as discussed in Chapter I.

Regarding the Al/Al FSW manufacturing campaign, the objective is to establish a process window in terms of axial load, rotational speed and advancing speed for a preselected tool. On Figure II.8 in section II.2, the tool used to manufacture Al/Al dissimilar welds is represented. It is threaded, has grooves on the shoulder and is of a conical shape.

The pin is 5.75 mm in length. The shoulder is 20 mm in diameter.

Dissimilar AA6061/AA7075 butt welding has been identified as more challenging than similar welding, and thus has been used to calibrate the welding parameters prior to similar welding. The AA7075 has been systematically placed on the retreating side. In Guo et al. [86], the impact of base material positioning (advancing or retreating side) for AA6061/AA7075 dissimilar joints have been investigated and the authors report a decrease in hardness in both materials to relatively similar values. The position of the base materials does not change the mechanical behavior of the observed joints, as all samples break in the HAZ of the AA6061, regardless of the welding parameters. They note that the main benefit of having the AA6061 on the advancing side allows a much more effective mixing in the stir zone. Comparable studies on dissimilar butt welding of other materials reach similar conclusions [74, 75].

Dissimilar trial welds are presented on Figure III.1 and also presented in Table III.1. Once manufactured, the trial welds are visually inspected regarding multiple criteria to assess typical defect described in I:

- **The presence of a "wormhole".** This defect can be either seen directly on the surface, such as on Figure III.2(a), or can be hinted by the presence of a small hole at the bottom of the exit hole, see Figure III.2(b). The welding parameters responsible for the weld with a "wormhole" are visually represented by a blue star in the process parameter map of Figure III.1.

- **Amount of flash on a given weld.** Figures III.2(b,d) show two welds, with varying amount of flash. These welds were manufactured using 400 RPM rotational speed and 8 kN axial load. The weld shown on Figure III.2(c) has a 60 mm/min advancing speed and shows an excessive amount of flash compared to the weld on Figure III.2(d), which has been manufactured with an 80 mm/min advancing speed. Although the flash is not extreme in this particular instance, lowering the advancing speed at a given "Rotational Speed/Axial Load" and obtaining a worse surface finish makes no sense in an industrial context aiming at productivity (i.e. speed). Hence, this explains why such low advancing speed where not selected for the experimental plan. As with the wormhole example, the dissatisfactory weld is visually represented on Figure III.1.

Most of the tried welds are however deemed visually satisfactory. On Figure III.1, green surfaces help visualise how the experimental plan covers a wide range of closely related parameters in order to evaluate the impact of each welding parameters. The welds manufactured during the initial analysis of welding parameters on the quality of the weld are marked as "Experimental welds". The subsequent deducted experimental plan lead to the manufacturing of the "Individual welds". Each "Experimental weld" contained within the experimental plan (i.e., the green surfaces) were manufactured a second time to exactly match all aspects of the other welds (weld length, cleaning procedures, etc).

III.1.B Data recording during welding

Additionally during welding, the FSW machine monitors various loads and positions. Such values include:

- **X Position (mm)**: shows the tool head movement along the welded joint. It allows the monitoring of the advancing speed as well as the welded length.

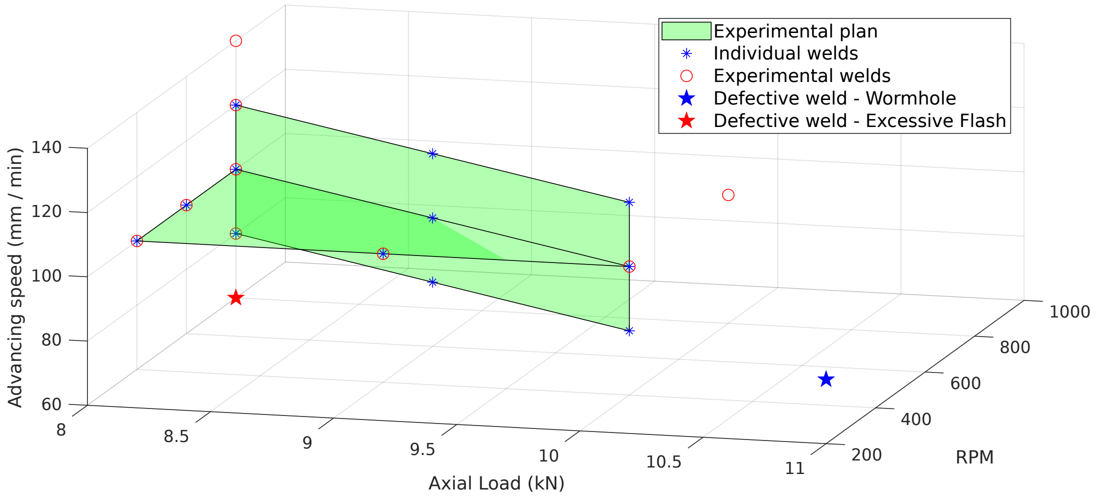

Figure III.1: Spatial visualization of the welded joints. The vertical green surface covers a specific range of welding parameters in which RPM and Axial Load are linearly related. The horizontal surface covers a wider range of parameters at a given advancing speed. The joints used to establish these experimental plans are marked as "Experimental welds". "Individual welds" were deduced and manufactured based on the results of these "experimental welds". Two welds were specifically marked as failed and shown in Figure III.2.

Retreating Side	**Advancing Side**	**Axial load (kN)**	**Rotational Speed (RPM)**	**Advancing Speed (mm / mn)**
7075-T651	6061-T651	8	800	80
				100
				120
		10		100
		9	600	80
				100
				120
		8		100
		10	400	80
				100
				120
		9		100
		8		

Table III.1: Welding parameters of the selected AA6061/AA7075 dissimilar welds.

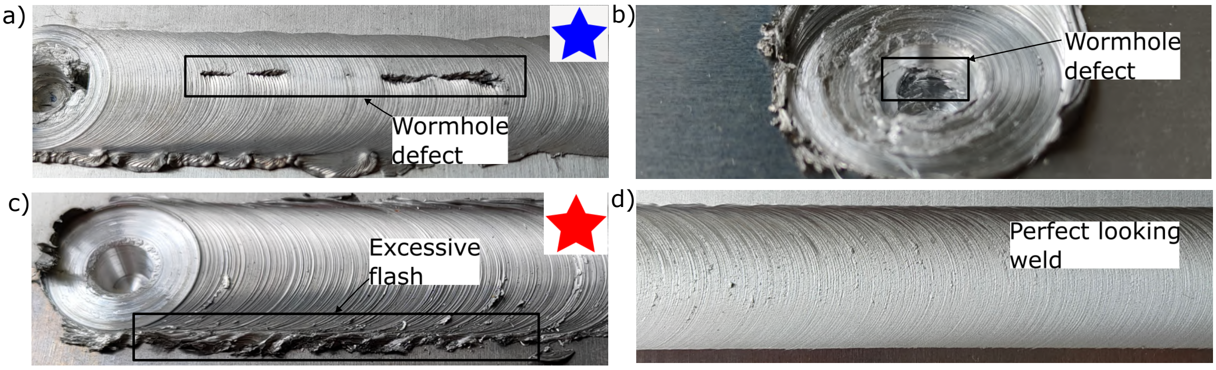

Figure III.2: The symbols shown on welds are tied to Figure III.1. (a) Weld showcasing a clear case of wormhole. (b) Cavity at the bottom of the exit hole, hinting at the presence of a wormhole throughout the weld. (c) Weld exhibiting more flash compared to a similarly manufactured but faster weld. (d) Joint with an appropriate post-weld surface.

- **Y Position (mm)**: registers the tool head position along the transverse side of the welded joint. The position should stay constant throughout all welds presented in this work. Variations of a magnitude of 10^{-3} mm are registered.
- **Z Position (mm)**: Visualizes the plunging depth of the tool, dwell time and depth adjustment during the force controlled section of the weld. It is zeroed when the tip of the tool touches the sample surface.
- **X Axial Load F_x (kN)**: allows to see how changes in advancing speed affect the tool load along the welding direction.
- **Y Axial Load F_y (kN)**: tool load along the transverse direction.
- **Z Axial Load F_z (kN)**: one of the most important value to control during and after a weld. As the welds are force controlled, a stable axial load during welding is a key factor to know if a weld behaved as expected. As the experimental plan is drawn, trial welds are evaluated based on the axial load stability beyond their visual inspection.
- **Torque T (N.m)**: the torque the tool experiences during the weld. This torque is related (with the rotational speed) to the machine power and gives thus a direct feedback on the heat input.

Data extracted from a sound FSW joint is analyzed on Figure III.3. All steps of a typical joint can be described using the annotations on the Figure:

1. **Plugging of the tool tip.** The Z position value decreases but is still positive, meaning that the tool has not entered the plate yet. The tool plunging speed is set to 5 mm/min in this case.
2. **Contact of the tool pin with the welded plate and subsequent plunging to the desired depth.** As the Z position value passes 0 mm, the Z axial load immediately increases. As the tool pin stirs the aluminium and the plate heats up, the axial load stabilize, here between 3 and 4 kN. This stability depends on the

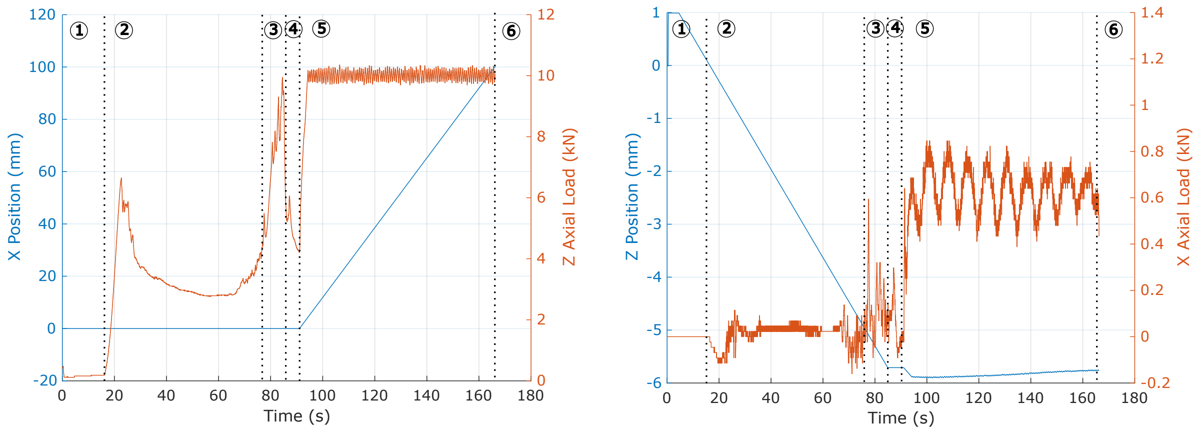

Figure III.3: Steps in a typical FSW joint, here on a dissimilar AA6061/AA7075 joint performed at 400 RPM, 80 mm/min and a load controlled at 10 kN. X/Z loads and positions are provided: (1) Initiation of the tool plunging. (2) Contact of the tool tip with the plate. (3) Contact of the tool shoulder with the plate. (4) Dwell time at maximum plunging depth. (5) Movement of the tool head and welding occurs. (6) Tool removed from the material.

rotational speed of the tool and the fixed plunging speed. A minor change in the X axial load can also be noted.

3. **Contact between the shoulder and the welded plate.** The Z position is approaching the targeted value and an axial load spike is observed.

4. **A few seconds long dwell time is applied once the targeted plunging depth is achieved.** This step allows the plate to heat up slightly, with the full friction of the welding tool. The aim is to reach faster a steady-state regime in the subsequent phases.

5. **The tool moves along the welding axis, X, forming the joint.** The welding speed, here set to 80 mm/min, can be calculated from the X position value if needed. The axial load is stable as the force control mode is enabled and adjustments can be seen on the Z position. The tool moves slightly up as it expends under heat.

6. **The tool exits the material.**

Figure III.4 provides data from another dissimilar weld with a higher rotational speed and a higher advancing speed. The sinusoidal pattern of the X axis load is here more unstable and its absolute value is higher. Both welding data set showcased here display successful welds, i.e. defect free (Figure III.2). On the other hand, Figure III.5 discloses the data generated during a rejected weld of Figure III.1. In this case, the rotational speed of the tool was set to 200 RPM. Compared to both previous welds, the X axis load F_x is abnormally high, i.e. 2.5-3 kN, while in Figures III.3 and III.4 it reaches usually $\sim$ 1kN or lower values. As a lower rotational speed induces a colder welding environment, it is expected but however not to that extent. The colder welding environment also creates a runaway scenario visible here:

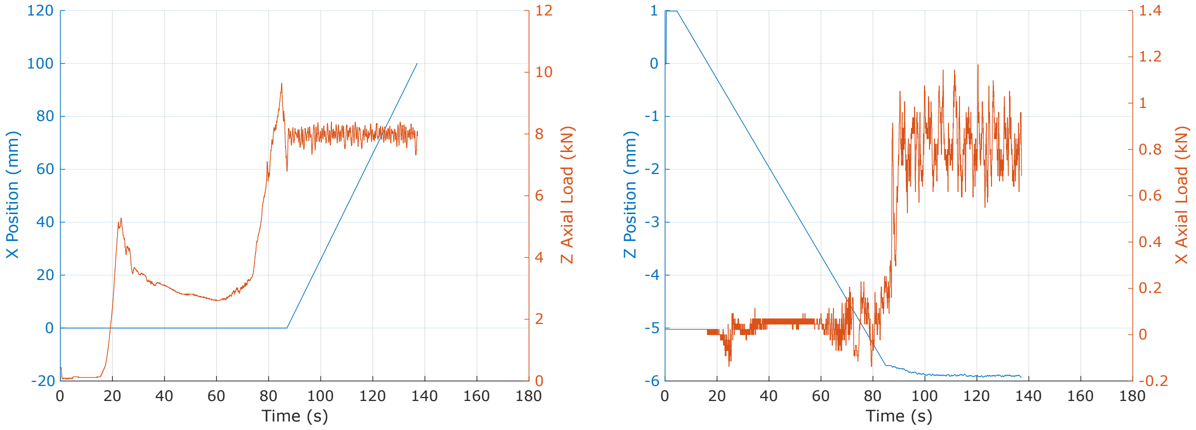

Figure III.4: Data recorded for a FSW dissimilar Al joint performed at 400 RPM, 120 mm/min and 8 kN. Compared to data on Figure III.3, axial load is higher and still stable. The X axial load exhibits excessive oscillating pattern compared to Figure III.3 (with a lower RPM).

1. As the weld is stable in force control mode, the heat generated from friction is too low to maintain the aluminium at a high enough temperature in order to make it malleable.
2. As a result, the aluminium starts to cool down during welding, and its strength properties increase.
3. As this happens, both the Z and X axes loads increase.
4. In order to keep the axial load under control, the tool rises from the weld to alleviate the load on the tool shoulder.
5. However, this creates a negative feedback loop. As the shoulder lifts up, it generates even less heat.
6. This looping cycle goes on until the tool Z position hits the upper boundary set in the welding machine in order to avoid a complete decohesion of the shoulder and the welded plate. If this happens, it would damage the welding pin.

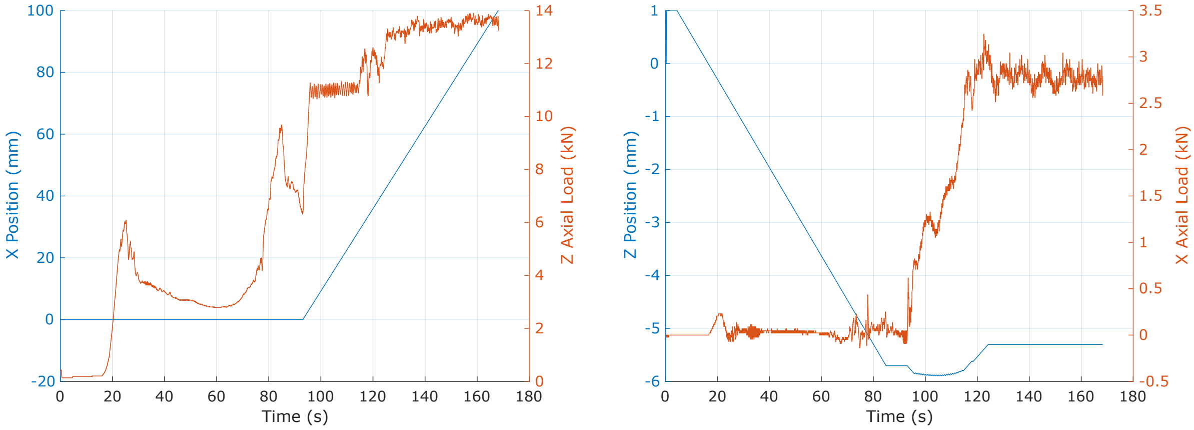

Figure III.5: Data from the trial 200 RPM dissimilar weld exhibiting the wormhole defect seen on Figure III.2(a). Notice the runaway scenario on the axial load as the Z position adjustments reaches its limits.

III.2 AA6061 similar welds

Once dissimilar welding settings are understood, welding parameters for similar welding can be set. However, reusing the same parameters for similar AA6061 welding was not directly successful. The sharp contrast in mechanical properties between the AA6061 (base material yield strength at 240 MPa) and the AA7075 (base material yield strength at 460 MPa) in dissimilar welding implies the use of a lower axial load in the case of AA6061 similar welding. Indeed, the experimental plan for AA6061 similar welding is presented in Figure III.6 and showcases a lower axial load overall compared to dissimilar welds. Table III.2 also provides the tested welding parameters.

Figure III.7 presents the recorded welding data for a similar AA6061 weld manufactured using dissimilar welding parameters. Interestingly, an excessive heat runaway scenario is observed, contrary to the weld on Figure III.5. The axial load lowers as the weld progresses and the tool plunges to increase it. This however, generates excessive heat, thus lowering the mechanical properties of the aluminium, which in turn decreases the axial load. This scenario ends in the same way compared to a lack of heat runaway weld: the tool adjustments hit a displacement limit in its plunging capability, set to ensure that the tool pin does not go through the plate and hit the welding machine's backing plate.

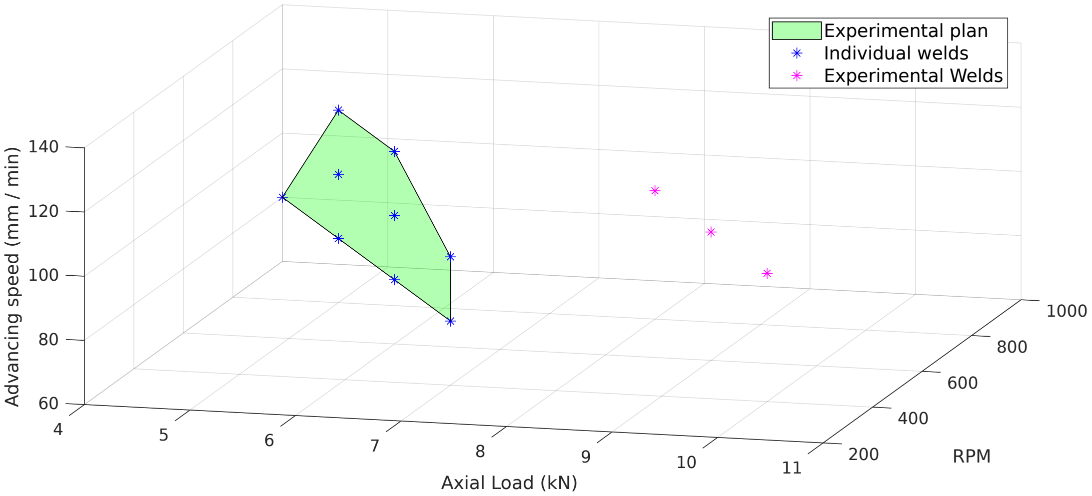

Figure III.6: Spatial visualization of the welding parameters used in the AA6061 similar experiment plan.

Axial load (kN)	**Rotational Speed (RPM)**	**Advancing Speed (mm / min)**
8	800	100
9	600	
10	400	
4	1000	80
		100
		120
5	800	80
		100
		120
6	600	80
		100
		120
7	400	80
		100
		120

Table III.2: Welding parameters of AA6061 similar welds.

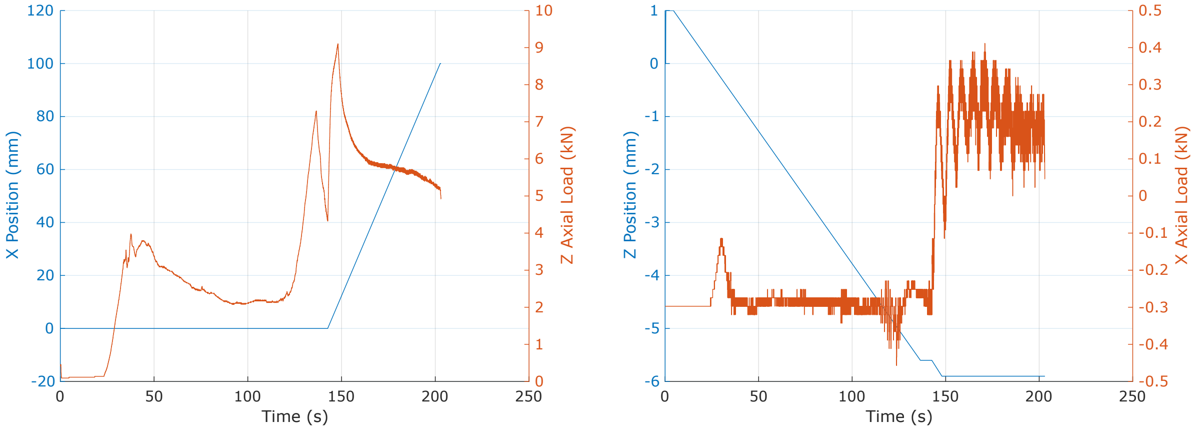

Figure III.7: Welding data of a AA6061 similar weld performed at 400 RPM, 100 mm/min and 10 kN. This weld exhibits an excessive heat runaway scenario.

III.3 AA7075 similar welds

Figure III.8 follows a similar volumetric presentation compared to Figures III.6 and III.1 and presented the experimental parameters used to manufacture the AA7075 similar welds. Similarly, Table III.3 presents the welding parameters used. Contrary to the AA6061 similar welding parameters, in this instance dissimilar welding parameters were successfully used. The welding data of such a weld is provided in Figure III.9. It exhibits all characteristics of a sound weld, as described in Figure III.3. It is understandable that using the same welding parameters yields almost identical welding data as in both instances of dissimilar and AA7075 similar welding, the AA7075 exerts the most resistance on the welding tool. However, the plunging speed is significantly reduced in such welds. A AA7075 similar weld with a higher plunging speed is presented in Figure III.10. A relatively high axial load is obtained ($\sim$ 14kN). Such high loads can be detrimental to the welding machine, and as such are mitigated as much as possible. Lowering the plunging speed is an easy solution to lower the load spiking during plunging. A higher rotational speed also increases friction generated heat and helps in lowering the axial load.

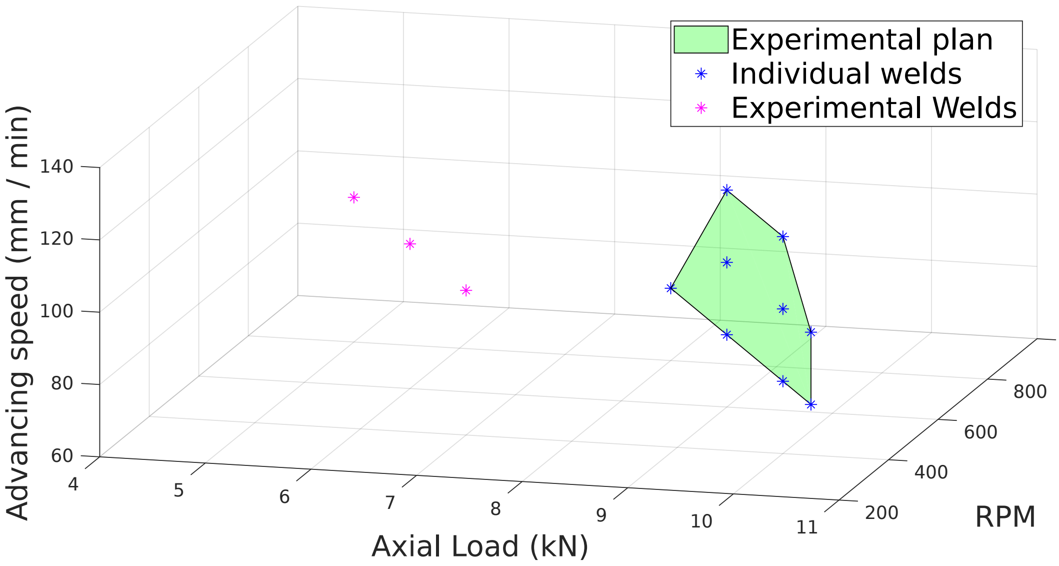

Figure III.8: Spatial visualization of the welding parameters used in the AA7075 similar experiment plan.

Axial load (kN)	**Rotational Speed (RPM)**	**Advancing Speed (mm / mn)**
5	800	100
6	600	
7	400	
8	800	80
		100
		120
9	600	80
		100
		120
10	400	80
		100
		120
10.5	300	80
		100
		120

Table III.3: Welding parameters of AA7075 similar welds.

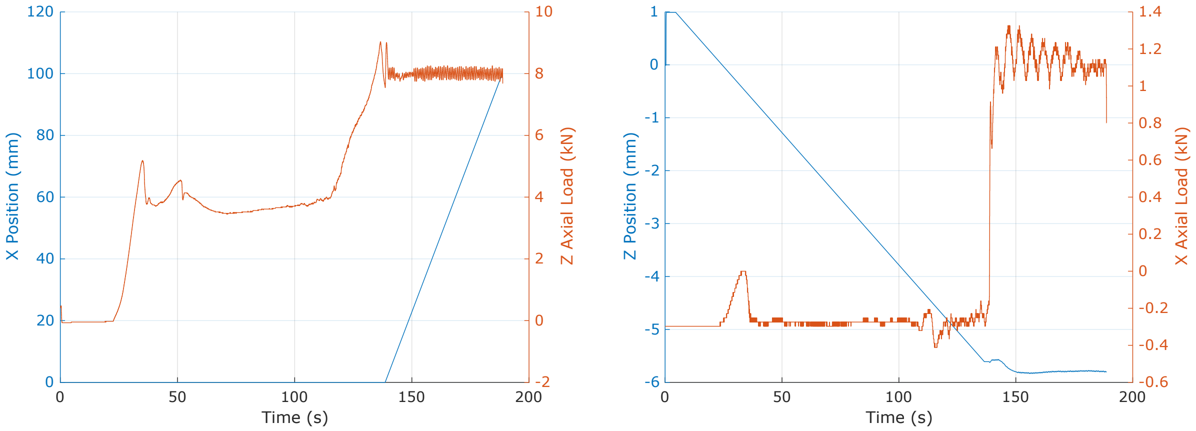

Figure III.9: Welding data of a similar AA7075 weld performed at 800 RPM, 120 mm/min and 8 kN using the same parameters presented on Figure III.4 for a dissimilar weld.

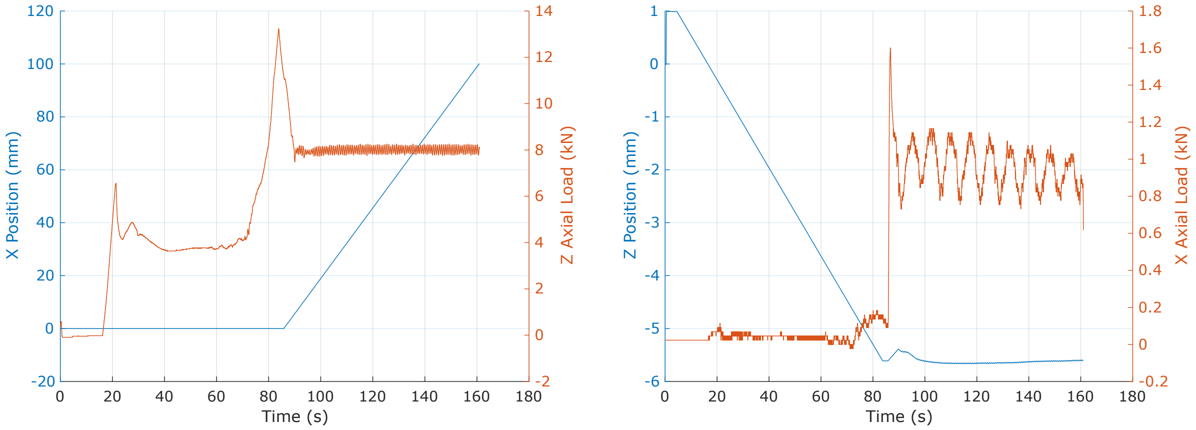

Figure III.10: Welding data of a similar AA7075 weld performed at 800 RPM, 80 mm/min and 8 kN. Welding exhibiting high plunging speed and thus high axial load at the plunging.

III.4 Heat input and torque measurements

In FSW joint manufacturing, heat generation during welding has long interested the academic and industrial sectors. Indeed, heat generation intervenes in multiple key aspects of the weld manufacturing:

- **Tool material choice.** For aluminium FSW, it has been explained that H11/H13 tool steel is the preferred material (see Section I.2.E). However, for higher mechanical properties alloys, such as titanium, steel or superalloys, multiple categories of tool material are available: nickel based super alloy tooling, tungsten (W) based tooling and/or ceramics, such as tungsten carbide (WC) or Polyrystalline Cubic Boron Nitride (PCBN). For example, for WC based tooling, high temperature mechanical properties have been established in the past [129]. Knowing the temperature welds will reach is key in designing tools in the most efficient way possible, as to keep manufacturing costs as low as possible.
- **Welding environment.** In Section I.2.D, an industrial application of FSW in the nuclear sector has been presented. 50 mm thick copper walls are welded in order to produce a nuclear waste canister for long term storage. In this instance, the raw quantity of copper used, and its high thermal conductivity, means that the entire part will experience temperature elevation. In addition, maintaining sufficient heat during welding, as the bulk of the material is essentially acting as a heat pump, is a challenge. Understanding heat generation (location, intensity) can help in minimizing overall heating and lead to eventual process parameters changes (rotational or advancing speed, tools, tool features).
- **Impact on mechanical properties.** Metallic material mechanical properties depend on their microstructure. In the case of FSW, microstructure depends on the welding environment and the process parameters used (see Section I.3.B). Specifically in the case of the aluminium alloys used in this study, AA6061 and AA7075, their mechanical properties is heavily tied with their thermal history (see Sections I.1 and II.1). Understanding heat generation during welding is crucial to understand the mechanical properties of AA6061/AA7075 similar and dissimilar joints.

Early on in FSW research, models were proposed to predict the maximal temperature of welds. In 1998, W. J. Arbegast [130] proposed such a model (see Equation III.1). T is the maximum temperature of the weld, T_m the melting temperature of the alloy, ω the rotational speed and ν the advancing speed. K and α are are both constants that are within the range of 0.65–0.75 and 0.04–0.06, respectively.

$$\frac{T}{T_m} = K\left(\frac{\omega^2}{\nu \times 10^4}\right)^{\alpha} \tag{III.1}$$

Later, further models were established to take into account tool geometry and features. For example, Gadakh and Adepu [131] proposed a model predicting the heat input for FSW tools with cylindrical tapered pin, in Equation III.2. The total heat input Q_{Tot} is divided into three components: $Q_{Tot} = Q_{Shoulder} + Q_{Cone} + Q_{Pin}$. The final mathematical form of energy input into the weld is presented in Equation III.2. ω is the angular rotational speed, $\tau_{contact}$ is the contact shear stress, $R_{shoulder}$ is the tool shoulder radius,

R_{PT} is the tool pin foot radius, H_{probe} is the pin length and α the tool pin taper angle. See [131] for explicit demonstration and hypothesis.

$$\begin{aligned} Q_{Tot} =& \frac{2}{3}\pi\omega\tau_{contact}\Bigg(R_{shoulder}^3 - R_{PT}^3 \\ & + \frac{3}{4}\cdot\frac{H_{probe}}{\cos(\alpha)}(2R_{PT} - H_{probe}\tan(\alpha))^2 \\ & + (R_{PT} - H_{probe}\tan(\alpha))^3\Bigg) \end{aligned} \tag{III.2}$$

However, such models are impractical in an industrial environment, where practical process parameters are discussed, such as rotational and advancing speeds, tool axial load and tool choice.

In this work, a simple heat generation model has been established to compare welds heat input with one another. Some assumptions have been made:

- As all aluminium samples are manufactured using the same tool, tool geometry has been reduced to the tool shoulder radius;
- Other mechanism of heat generation such as deformation was not considered;
- Viscous sliding is ignored, i.e. only dry static friction contributes to the heat generation;
- The welding environment being the same for all welds, the inefficiency of the heat transfer from the tool to the weld is ignored.

The power, in W, transmitted by a rotating axis is:

$$P = \omega \cdot T \tag{III.3}$$

ω is the rotation speed, in rad.s^{-1} and T the torque in N.m. Based on Trancossi and Dumas [132], the stationary torque of a dry sliding rod on a surface can be expressed as:

$$T = \frac{2}{3}\cdot R_{shoulder}\cdot\mu\cdot F_Z \tag{III.4}$$

$R_{shoulder}$ is the radius of the tool shoulder in mm, μ the static coefficient of friction and F_Z the tool axial load in N. By combining Equations III.3 and III.4, Equation III.5 is calculated:

$$P = \omega\cdot\frac{2}{3}\cdot R_{shoulder}\cdot\mu\cdot F_Z \tag{III.5}$$

The power is then divided by the advancing speed V_a, in mm.s^{-1}, of the weld to obtain a linear energy parameter, in J.m^{-1} in Equation III.6:

$$E_l = \frac{2}{3}\cdot R_{shoulder}\cdot\mu\cdot F_Z\frac{\omega}{V_a} \tag{III.6}$$

The obtained Equation III.6 is coherent with trends observed in the literature on the effect of process parameters on the heat generation (see Section I.2.E):

Configuration	F_Z	ω	V_a	E
Dissimilar	8	800	80	1
			100	0.8
			120	0.66
	10		100	1
	9	600	80	0.84
			100	0.67
			120	0.56
	8		100	0.6
	10	400	80	0.62
			100	0.5
			120	0.42
	9		100	0.45
	8			0.4

Table III.4: Welding parameter data for dissimilar AA6061/AA7075 joints with the dimensionless heat parameter.

- $R_{shoulder} \cdot \mu$: increasing the shoulder area and/or changing its material to increase the static coefficient of friction will increase the linear energy of the welding configuration.
- F_z: increasing the axial load of the weld increases the linear energy.
- ω: increasing the rotational speed increases the linear energy.
- V_a: increasing the advancing speed decreases the linear.

Finally, for a given experimental plan, i.e. AA6061, AA7075 similar welds and dissimilar welds, the hottest weld will be assumed as the weld with the highest rotational speed and the lowest advancing speed. The linear energy of such a weld is noted E_{lmax}. Given this information, and by the fact that the same tool is used for all Al/Al FSW welding, we can define the following dimensionless parameter E:

$$E = \frac{E_l}{E_{lmax}} = \frac{F_Z \omega}{V_a} \cdot \frac{V_{amax}}{F_{Zmax} \omega_{max}} \qquad \text{(III.7)}$$

Calculating this value for the process parameters of dissimilar and similar AA6061 and AA7075 yields Tables III.4, III.5 and III.6 respectively.

This criteria offers a practical, yet limited way, of comparing the weld heat input between multiple assemblies of a given experimental plan. However, this criteria is far from perfect. For example, looking at E values in Table III.6 for AA7075 welds, one can see that at a given advancing speed, E is essentially doubled when looking at 300 RPM and 800 RPM welds. On Figure I.20 in Section I.2.E, the weld temperature does not double when the rotational speed goes from 280 RPM to 840 RPM. This limitation of our criteria probably stems from the assumption to ignore viscous shear friction heat.

Finally, an interesting result in heat generation with regard to tool shape is currently a work in progress by K. Colligan from Concurrent Technologies Corporation [133]. In his yet unpublished review he recently presented at the latest FSW international conference, the author has collected multiple welding data for aluminium FSW joints. First, K.

Configuration	F_Z	ω	V_a	E
AA6061	4	1000	80	1
			100	0,8
			120	0,66
	5	800	80	1
			100	0,8
			120	0,66
	6	600	80	0,9
			100	0,72
			120	0,6
	7	400	80	0,7
			100	0,56
			120	0,46

Table III.5: Welding parameter data for similar AA6061 joints with the dimensionless heat parameter.

Configuration	F_Z	ω	V_a	E
AA7075	8	800	80	1
			100	0,8
			120	0,66
	9	600	80	0,84
			100	0,67
			120	0,56
	10	400	80	0,625
			100	0,5
			120	0,41
	10.5	300	80	0,49
			100	0,39
			120	0,32

Table III.6: Welding parameter data for similar AA7075 joints with the dimensionless heat parameter.

Colligan starts by defining the shear yield stress as seen in Equation III.8, i.e. by the ratio of the torque T by the surface integral of the radius of the tool.

$$\tau_{yield} = \frac{T}{\int_S rdA} = \frac{T}{geo} \tag{III.8}$$

The surface integral is referred to as "geo" as it encapsulates the geometry of the tool used. The totality of the tool surface is considered here. To derive "geo", an assumption is made of a concave or flat shoulder, a cylindrical probe and a flat probe tip. The incremental areas for each tool's region are defined in Equation III.9.

$$\begin{aligned} \text{shoulder incremental area} =& \frac{r}{\cos\alpha} drd\theta \\ \text{probe side incremental area} =& \frac{r}{\cos\beta} dzd\theta \\ \text{probe tip incremental area} =& rdrd\theta \end{aligned} \tag{III.9}$$

Substituting the expressions of incremental areas in Equation III.9 for each region of the tool in "geo" in Equation III.8 generates Equation III.10, with $r = (P_R - z \cdot \tan\beta)$ for the probe side:

$$\begin{aligned} geo = \int_S rdA =& \int_0^{2\pi} \int_{P_R}^{S} \frac{r^2}{\cos\alpha} drd\theta \\ &+ \frac{1}{\cos\beta} \int_0^{2\pi} \int_0^{t} (P_R - Z \cdot \tan\beta)^2 dzd\theta \\ &+ \int_0^{2\pi} \int_0^{P_T} r^2 drd\theta \end{aligned} \tag{III.10}$$

α is the shoulder concavity angle, i.e. $\alpha = 0$ for flat shoulder tool, β the frustum probe half angle, i.e. $\beta = 0$ for cylindrical probe, S the shoulder radius, P_R the probe root radius, P_T the probe tip radius and t the probe thickness. Performing the integration of Equation III.10 yields Equation III.11.

$$geo = \frac{2\pi}{3}\left[\frac{S^3 - P_R^3}{\cos\alpha} + \frac{t((P_R + P_T)^2 - P_R \cdot P_T)}{\cos\beta} + P_T^3\right] \tag{III.11}$$

Combining Equations III.8 and III.11 in Equation III.12 leads to the final form of "geo".

$$\tau_{yield} = \frac{T}{\frac{2\pi}{3}\left[\frac{S^3 - P_R^3}{\cos\alpha} + \frac{t((P_R + P_T)^2 - P_R \cdot P_T)}{\cos\beta} + P_T^3\right]} \tag{III.12}$$

Additionally, the normal stress flow is derived from the shear flow stress using the Von Mises criterion in Equation III.13.

$$\sigma_{yield} = \tau_{yield}\sqrt{3} \tag{III.13}$$

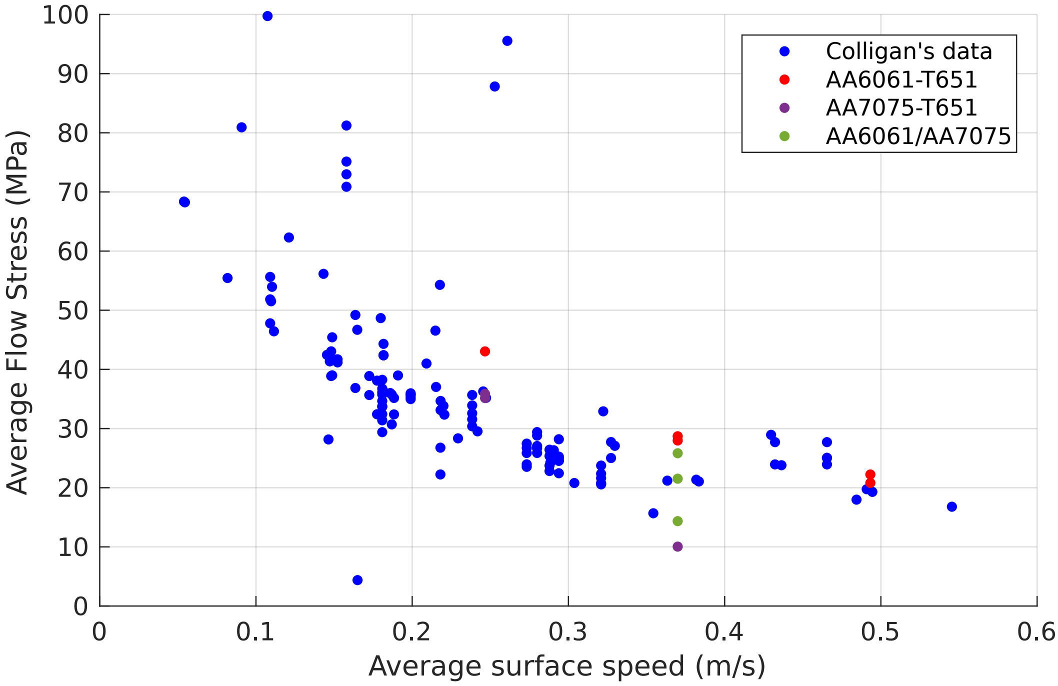

Figure III.11: Flow stress as the function of average surface speed.

Finally, to perform his analysis, the author defines the average surface speed of the tool, i.e. the average of speed seen by individual point in the tool's geometry in the rotating referential of the tool, in Equation III.14, with the help of ω, the rotational speed.

$$\text{Average surface velocity} = \bar{\omega r} = \frac{\omega \int_S r dA}{total\ surface\ area} \tag{III.14}$$

By replacing the numerator of Equation III.14 by geo, the final Equation III.15 is obtained for the average surface velocity of the tool.

$$\bar{\omega r} = \omega \left[\frac{\frac{2}{3}\left[\frac{S^3-P_R^3}{\cos\alpha} + \frac{t((P_R+P_T)^2-P_R\cdot P_T)}{\cos\beta} + P_T^3\right]}{\frac{(S+P_R)(S-P_R)}{\cos\alpha} + \frac{t(P_R+P_T)}{\cos\beta} + P_T^2} \right] \tag{III.15}$$

Based on Equations III.13 and III.15, the author was able to calculate these values for the welding data that had been provided to him. This calculation yielded Figure III.11, where the average flow stress of a welded joint is plotted as a function of average surface speed. The original author notes a bi-linear trend in the data, between samples at 0.3 m/s average surface velocity and above, and those below. The author suggests that this data could be useful in the design of a closed-loop control system. Indeed, for welds that are already performed at 0.3 mm/min for example, increasing the rotational speed would not lead to significant increase in welding temperature.

To compare the present PhD data with K. Colligan's work, values for AA6061, AA7075 and dissimilar welding performed have been added on Figure III.11. Unfortunately, a dysfunctional torque sensor on the welding machine limits the number of data point available in our study. From the limited amount of data available, one can see that the welds manufactured in this study are well within what K. Colligan showed with his approach. Additional torque data on dissimilar joints could be interesting to further analyse the impact of the dissimilar nature of the welds on torque and heat generation.

It is now very interesting to conclude that a large variety of results from different machines, different tools and different materials (similar, and dissimilar welds in our case) can be nicely set in a unique master curve.

III.5 Conclusion

In conclusion, welding parameters for the various FSW Al/Al campaigns have been defined in the following way:

- AA6061/AA7075 dissimilar FSW was used as a benchmark to determine welding parameters. The assumption has been made that dissimilar welding would be more challenging to achieve than AA6061 or AA7075 welding. This approach proved to be successful, as process parameters used in dissimilar welding received little to no adjustments before being used on AA6061 or AA7075 similar welding.

- Process parameters adjustments from dissimilar welding to similar welding had to be done only for AA6061. Generally speaking, our process parameter characterization suggests that for dissimilar Al alloy welding, process parameters for dissimilar joints can be derived from the process parameters required to weld the stronger alloy in a similar welding configuration.

- For a given tool choice, three welding parameters are left for the user to decide: rotational speed, advancing speed and axial load (for force controlled weld). In this regard, process parameters can be drawn in a 3D space with the axes representing the three remaining parameters. This spacial visualization approach, coupled with a "trial and error" method, lead to the establishment of welding parameters able to manufacture sound dissimilar welds in a relatively short time.

- Manufacturing of the welded joints took place in a force controlled environment. Axial load values during welding have been extracted for all samples, and the stability of this axial load during the movement of the welding tool can discriminate between sound welds and welds subjected to either too high or too low of a heat input.

- Finally, heat generation during welding has been modelled with practically in mind, i.e. to derive a model using only process parameters to get a sense of heat generation. This obtained model can generally represent heat input differences between multiple process parameters within a given experiment plan.

- Data provided by K. Colligan on the relationship between torque and rotational speed for various tooling has shown that a bi-linear relationship exists between these values, while taking into account tool geometry. Torque and rotational speed data extracted from this work fit into this observation. This mastercurve, for different tools, machines and alloy choice, is rather nice, especially in an industrial context.

Chapter IV

From micro to macroscopic characterization of Al welds

In this Chapter, the macrographic and mechanical properties at different scales of the Friction Stirred Welds presented in Chapter III are presented. Results are discussed as a function of the selected welding parameters.

IV.1 Mesostructure of the joint observed by optical microscopy

Optical microscopy is a simple characterization tool for mesostructure analysis of friction stir welded joints. In particular, it displays the morphology of the stir zone and size of the thermomechanically affected zone.

IV.1.A Al/Al similar welds

In the case of Al/Al similar friction stir welds, optical microscopy proves to be limited in the case of this study. Reagents using hydrofluoric acid (HF) are often used to characterize aluminium alloy microstructure in optical microscopy. Keller's or Kroll's reagents are often used in that regard [134]. These etchants usually reveal grain boundaries, precipitates and have a slight preferential etching based on crystal orientation. All these characteristics of hydrofluoric acid based reagents make them preferential choices when studying aluminium microstructures. However, due to limitations in the usage of hydrofluoric acid in the laboratory where most of the optical microscopy was carried out, none of these reagents were used. As explained in Section II.3.A in Chapter II, a potassium permanganate based solution along with sodium hydroxyde (NaOH) was used. Here, the permanganate colors the aluminium alloy as it is chemically etched by the NaOH. The coloring speed of the permanganate depends on the alloying elements of the aluminium. Thus, in the case of similar Al/Al welding, this type of etching proves unfortunately quite unsuccessful at analyzing the morphology of a FSW joint, as shown on Figure IV.1 where details in the stir zone are blurred and the frontier between the stir zone and the TMAZ is sometimes invisible. This Figure reveals one of the frontier between the TMAZ and HAZ of the sample. The stir zone is partially visible and an alternating layering pattern of two phases can be distinguished. This morphology will be discussed later in this section, on

Figure IV.1: Example of a similar Al/Al AA7075 joint under optical microscopy, after etching with Weck's reagent.

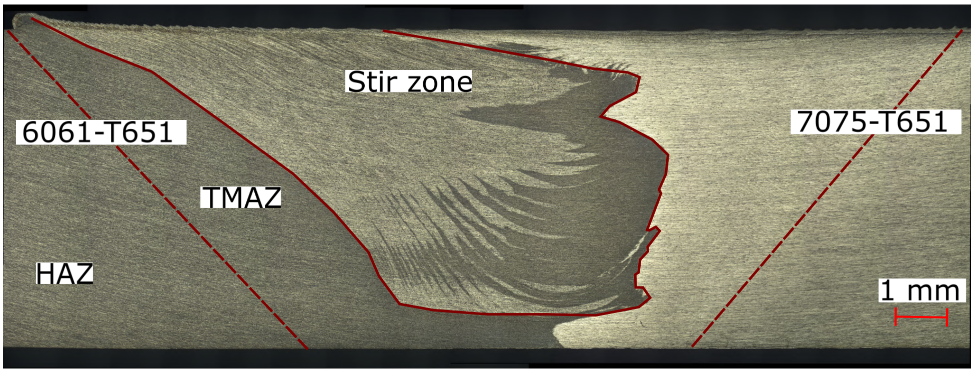

Figure IV.2: Morphology of a FSW joint on a macrograph. The stir zone is clearly identified. The boundaries of the TMAZ and the HAZ are harder to identify visually. The base material is not visible here.

dissimilar welded joints where this stir zone morphology is more contrasted and clearer.

IV.1.B Al/Al dissimilar welds

Figure IV.2 shows the typical morphology of a FSW AA6061-AA7075 dissimilar joint. In section II.3.A of Chapter II, a schematic of a weld cross section is presented on Figure I.25 in Section I.3.B with the typical zones of a FSW joint: stir zone (ST), heat affected zone (HAZ), thermo-mechanically affected zone (TMAZ) and base material (BM). The stir zone is clearly identifiable thanks to the discrepancy in contrast between the two base aluminium.

A partial "onion ring" pattern is visible at the center of the stir zone, at the boundary between the AA6061 and the AA7075. Here, the boundary between the TMAZ and the HAZ is not clearly distinguishable in the AA6061. However, as the weld is relatively symmetrical and the distinction between these two zones is relatively clear in the AA6061, it is possible to fully label this macrograph. The base material is not visible on this macrograph, as it is located further away from the weld stir zone.

Figures IV.3, IV.4 and IV.5 present optical microscopy of the cross section of the welded area for welds performed respectively at 400, 600 and 800 RPM. For each rotational speed, welds were performed at 80, 100 and 120 mm/min. A single axial load value per rotational speed has been used to manufacture 80, 100 and 120 mm/min joints. Multiple axial loads were tested at a given rotational speed, always with a 100 mm/min advancing speed. Macrographs are numbered from 1 to 13 for easier referencing when describing and commenting them.

First of all, the **rotational speed** appears to have a drastic impact on the morphology of the stir zone. From welds 1, 2 and 3 to welds 6, 7 and 8, the mixing pattern is more pronounced in the latter. The stir zone mixing pattern of welds 6, 7 and 8 are closer to an "onion rings" pattern (see subsection I.3.B.i) than the 3, 4 and 5 welds. As the rotational speed increases to 800 RPM, welds 10, 11 and 12 exhibit an even stronger mixing of the stir zone. However, the difference in stir zone morphology is more drastic when going from 400 RPM welds to 600 RPM welds, than when going from 600 RPM welds to 800 RPM welds. Additionally, a "bulb shaped" feature (marked on weld 6 by a dotted red circle) appears when rotational speed are at 600 RPM and higher. This feature along with the intensification of the "onion rings" pattern testify of a stronger mixing of both alloys. To better understand these alternating layers of contrast, Figure IV.6 displays EDX results taken from the stir zone of a dissimilar AA6061/AA7075 weld. As presented in Table II.1 in Section II.1, the highest difference in chemical composition between the two alloys is found in Zn content. With the help of an EDX analysis, this difference in Zn concentration is high enough to allow for differentiation of the parent material at a local level in the stir zone. Consequently, optical microscopy imaging is enough to distinguish the parent material present in each "band" of the onion ring pattern. This SEM observation completes what Figure IV.2 hints at regarding the composition of each band in the stir zone of an Al dissimilar weld. The contrast in optical microscopy between the two aluminium alloys is sufficient to distinguish both alloys in each band of the onion ring structure. Lastly, the rotational speed variation does not change the bottom part of the weld.

Secondly, the impact of the **advancing speed** at a given rotational speed appears to be negligible compared to the impact of the rotational speed. Indeed, the difference in stir zone mixing between welds 1, 2 and 3, welds 6, 7 and 8, and welds 10, 11 and 12 appears to be minimal when compared to the previous described effect of rotational speed change. On welds 1, 2 and 3, the increase in advancing speed does not appear to have any kind of effect on the stir zone mixing pattern. However, the top region of the stir zone, along the shoulder contact area of the tool, has a stronger onion ring pattern, with alternating layers of AA6061 and AA7075 becoming more and more visible as the rotational speed increases. A similar behaviour of the top part of the stir zone can be observed on welds 6, 7 and 8, and 10, 11 and 12. In general, an increase in advancing speed modifies the mixing pattern along the shoulder contact area, at the top of the weld. Additionally, a small wormhole defect can be observed in the mixing zone of weld 12. As the heat input of FSW decreases as the advancing speed increases (see subsection I.2.F), this kind of defect is more prone to appear. Lastly, the bottom part of the weld is not affected either by the advancing speed increase or decrease.

Finally, the effect of the **axial load** can be studied on some welds. At 400 RPM, welds 2, 4 and 5 show that a decrease in welding force leads to a more heterogeneous boundary between the stir zone and the TMAZ of the AA7075. However, this behavior does not appear at 600 RPM, with regards to welds 7 and 9. Here, no significant difference is observed between the two samples. Lastly, at 800 RPM, the increase of axial load from 8 kN to 10 kN, respectively evidenced by welds 11 and 13, leads to the emergence of a

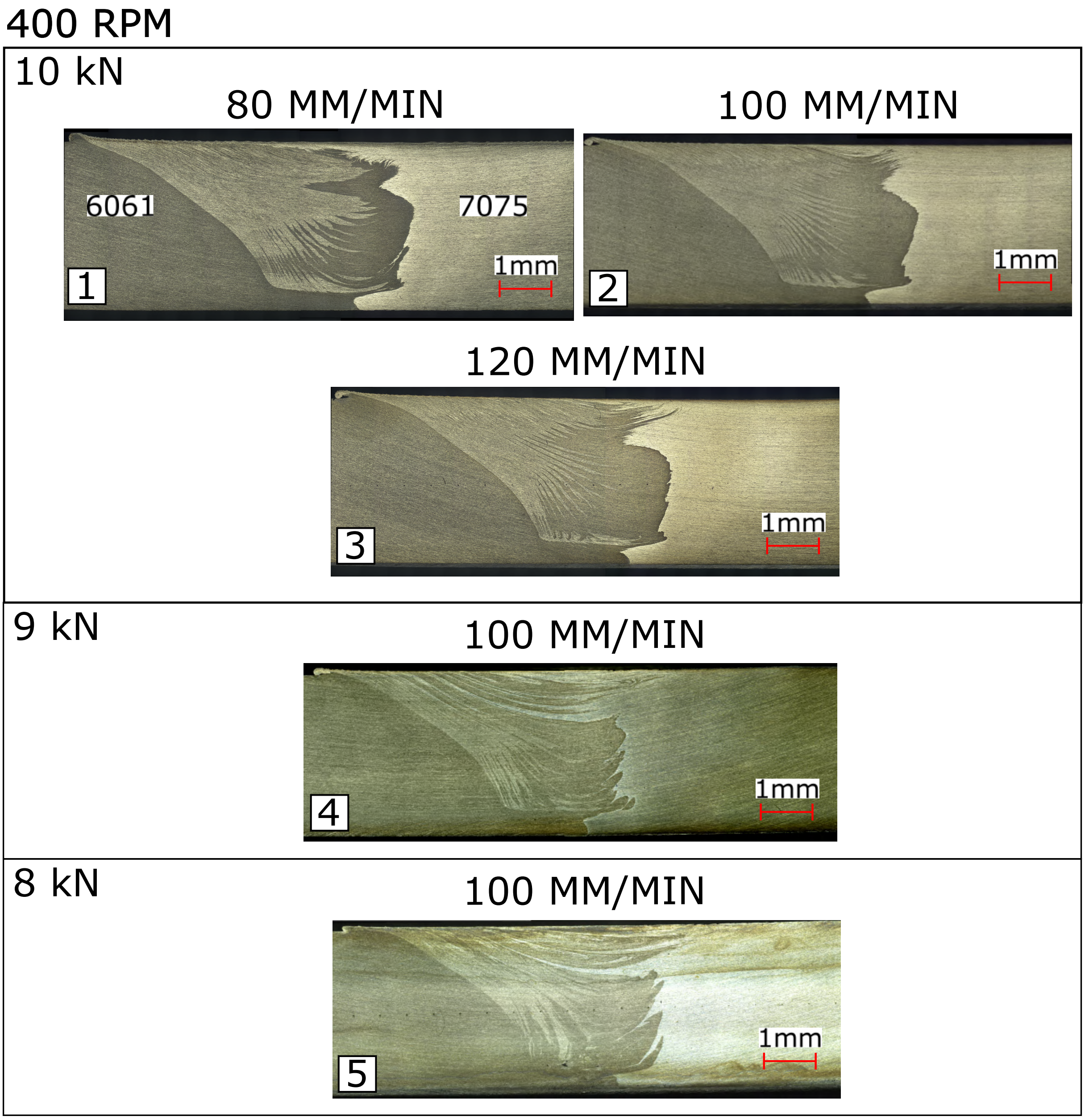

Figure IV.3: Macrographs of dissimilar AA6061/AA7075 FSW joints performed at 400 RPM. Three different axial loads have been tested.

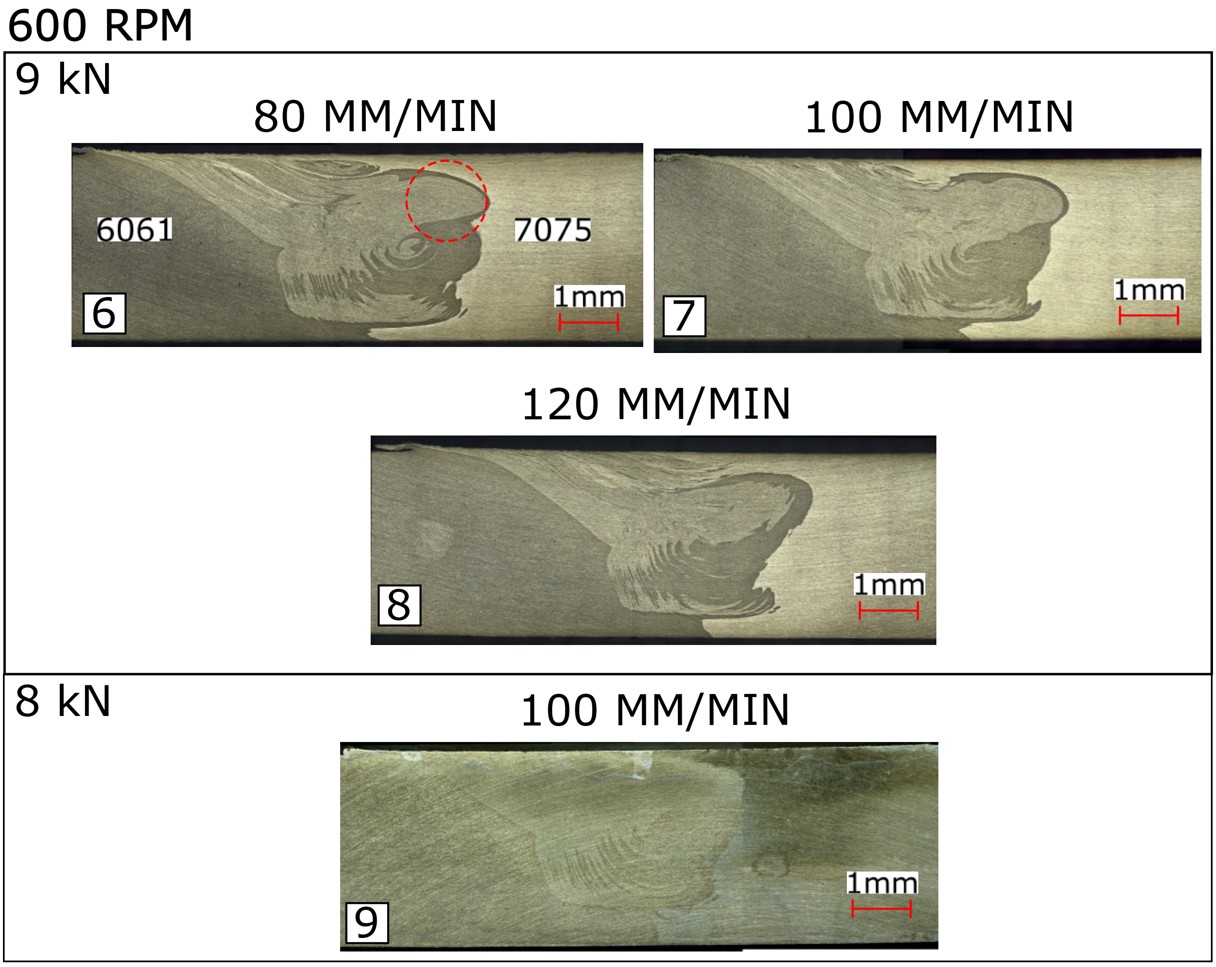

Figure IV.4: Macrographs of dissimilar AA6061/AA7075 FSW joints performed at 600 RPM. Two different axial loads have been tested. On weld 6, the dotted red circle shows a "bulbous" area of the stir zone that differs from welds shown on Figure IV.3 (i.e. 400 RPM).

new stir zone mixing pattern. A "double vortex" pattern, with a clear boundary between the stir zone and the TMAZ of the AA7075 is visible. Additionally, weld 13 is the only one exhibiting a significantly different microstructure in the bottom part of the stir zone, with a smaller thickness of, at a first glance, "unwelded" material.

Generally speaking, these optical macrographs lead to the following conclusions that will now be discussed in relation to the literature of dissimilar Al/Al FSW:

- The **rotational speed** has the highest impact on stir zone mixing compared to all other welding parameters. This result is coherent with previous observation cited in Steuwer et al. [51] for AA5083 welded to AA6082 by FSW. On Figure I.28 in Chapter I, a similar evolution of stir zone mixing is visible. Similarly, mixing improves more substantially between two rotational speeds when reaching particularly low RPM in absolute value (i.e here 400 RPM). Other literature work reach similar conclusion, see [77, 85] for respectively AA2024/AA7075 and AA2024/AA6061 FSW. So this seems to be a general conclusion when welding alloys presenting very different strength.

- The **axial load** does not have a strong impact on the stir zone mixing. However, a

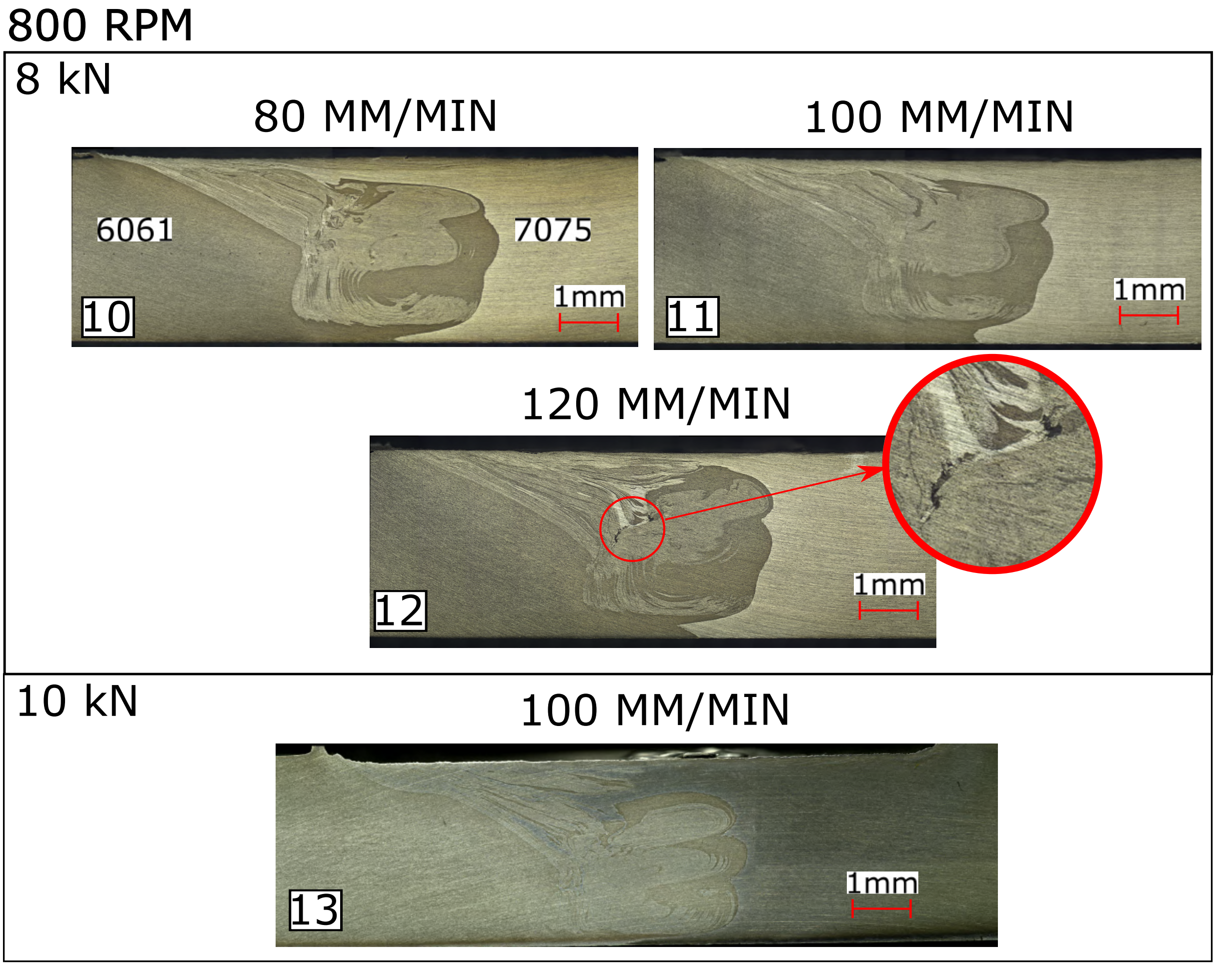

Figure IV.5: Macrographs of dissimilar AA6061/AA7075 FSW joints performed at 800 RPM. Two different axial loads have been tested. On weld 12, a red circle highlights a small defect known as "wormhole".

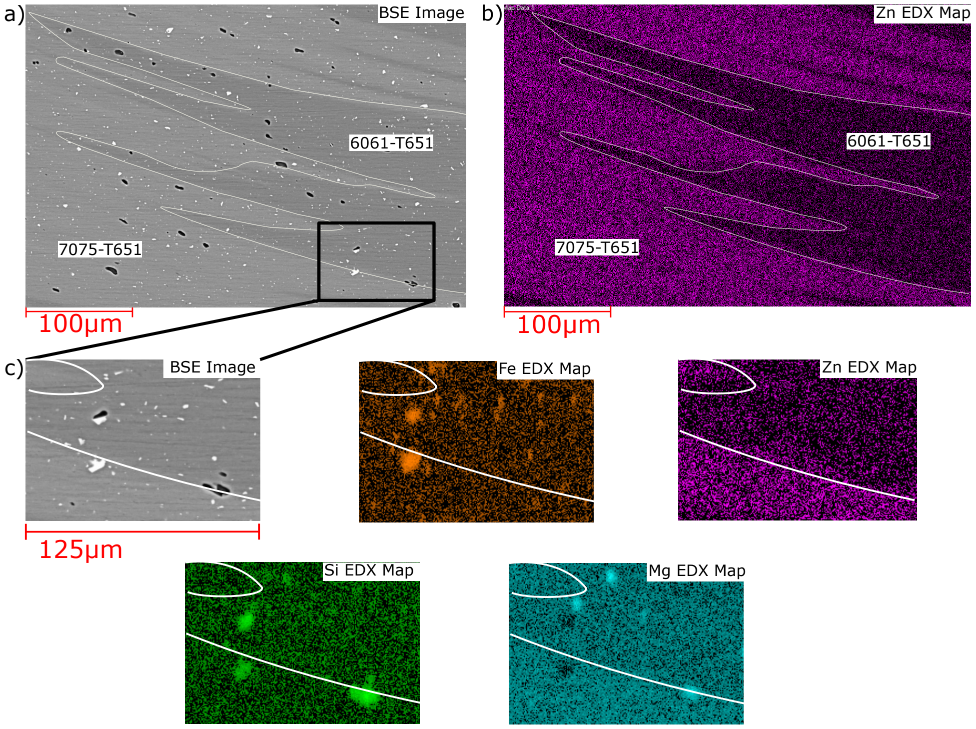

Figure IV.6: (a) BSE image taken in the center of a 400 RPM FSW stir zone between AA6061 and AA7075 alongside with (b) EDX showing the Zn distribution map which enables to differentiate the corresponding light and dark grey areas in BSE identified as AA7075 and AA6061 respectively. A white contour outlines the border between AA6061 and AA7075. (c) A magnified zone from (a) showing 2 types of inclusions: Fe rich (white on BSE) and Mg-Si rich (black on BSE) identified on corresponding EDX maps.

single case of a higher axial load at high rotational speed creates a double vortex. This structure has already been observed in the literature [86]. Accounts of single layered vortex are more commonly observed [75, 135]. Guo et al. [86] attributes these vortices to the three flats present on their tools. Here no flats are present of the FSW tool. This higher axial load combined with a high rotational speed also decreased the size of the clear boundary at the bottom of the weld between the AA6061 and the AA7075. An explanation could be that, as both advancing speed and RPM are high compared to the other welds, the heat input is higher in this weld (see subsection III.4). This could lead to a significant material softening, allowing the shoulder to plunge deeper inside the weld, thus reducing the size of the joint line remnant at the bottom of the stir zone. Similarly, this higher heat input and subsequent softening could also explain the observed double vortex structure, despite the absence of flats on the tool.

- The **advancing speed** does not either have a strong effect on the mixing in the stir zone for the samples considered, with the exception of a single weld exhibiting what appears to be a wormhole defect. This defect has not been observed at identical advancing speed and lower rotational speed, i.e. colder welds. Mishra et al. [136] described wormhole formation on the advancing side of similar 7XXX and 5XXX joints. However, these defects were observed in lap welded joints and at double the rotational speed observed in this study. Their material combination also involves a lower strength 5XXX alloy compared to the 6XXX alloy used in this study. However at high welding temperatures these alloys could exhibit similar strength, which might explain the similar behaviour.

IV.2 Hardness measurements

The methodology used for hardness measurements has been explained in Section II.4.A. Hardness measurements present the advantage of being a fast and practical mean to compare the heterogeneities of the weld mechanical properties for different welding conditions. All the hardness profiles in this study are arranged in a similar way: the X axis is zeroed at the center of the weld, positive values on the X axis are on the advancing side, and thus negative values on the X-axis are on the retreating side.

IV.2.A Al/Al similar welds

IV.2.A.i AA6061 similar joints

Figures IV.7(a,b,c) show the hardness profiles taken at the center line of similar AA6061 welds respectively manufactured at 80, 100 and 120 mm/min. Thus, the impact of the **rotational speeds** on hardness measurements can be assessed. As described in Chapter I and additionally detailed in Section III.4, an increase in rotational speed at a given advancing speed leads to an increase in heat generation and overall temperature of the weld. This temperature elevation can have a detrimental effect on hardness values via hardening precipitates dissolution.

On Figure IV.7(a), i.e. at an advancing speed of 80 mm/min, the rotational speed does not appear to have a significant impact on the hardness profiles. Note that, however for each plotted curve, a different value in axial load was selected to manufacture the weld. This experimental choice complicates the establishment of a conclusive assertion of rotational speed effect on hardness values in this case. The 1000 RPM curve at 4 kN has substantially higher hardness values on the advancing side compared to the weld manufactured at 600 RPM and 6 kN. A similar observation can be made on the retreating side of the weld, where both 1000 RPM and 400 RPM joints have the same hardness profiles. At 80 mm/min, the center of the weld, i.e. the stir zone, does not show significant difference between all samples, ranging from 400 RPM to 1000 RPM.

On Figure IV.7(b), i.e. at an advancing speed of 100 mm/min, a somewhat similar conclusion can be drawn for the **lower axial load** welds presented. Hence, between the 1000 RPM and 4 kN, and 400 RPM and 7 kN hardness profiles, minute differences are noted and no substantial effect of RPM increase is observed. However, at **higher axial load**, a clear difference can be established between the 400, 600 and 800 RPM welds. The minimum hardness in the HAZ is rather similar for all those welds. However, the 400 RPM and 10 kN weld has the lowest width of HAZ, followed by the 600 RPM and 9 kN weld, and then the 800 RPM and 8 kN joint. In this "high axial load" scenario, an increase in rotational speed leads to a decrease in hardness values both on the advancing and retreating sides. Additionally, contrary to hardness profiles described at 80 mm/min, here the stir zone exhibits two distinguishable behavior: 400 RPM welds have a clearly lower hardness plateau in the stir zone compared to 600, 800 and 1000 RPM joints, and the 800 RPM and 8 kN weld appears to have a larger stir zone hardness plateau compared to the other samples.

Finally, on Figure IV.7(c), i.e. at an advancing speed of 120 mm/min, the effect of RPM increase at the highest advancing speed of this experimental plan can be assessed. The minimum hardness value in the HAZ is little influenced by the rotational speed. However, in the stir zone, the 400 RPM weld has significantly lower hardness values compared to the other joints. The increase in width of the HAZ with increasing rotational speed in much clearer for this high advancing speed. It seems that this phenomenon is more evidenced as the rotational speed increases.

These observations will now be discussed in relation to previous data and relevant literature. At relatively low axial load values, the effect of the rotational speed on hardness values appears to be limited. As previously mentioned, for these AA6061 similar welds, the true effect of RPM variation is hard to assess on the hardness measurements as, experimentally, a variation in RPM value is always accompanied by a variation in axial load. In Chapter III, the reasoning behind these experimental choices has been explained. For a given base material, an increase in axial load is generally associated with an increase in heat generation (see Sections I.2.E and III.4). As the rotational speed stays the same, additional heat is generated by a higher subsequent torque. In Long et al. [137], the torque for three different aluminium alloys is shown to decrease as the rotational speed increases, for a given plunging depth. In that study, the required axial load is found inversely proportional to the rotational speed. As the general heat input from the tool decreases along with the rotational speed, at low axial load values this effect is counter balanced by the gradual increase in axial load.

The hardness measurements in AA6061-T6 are affected by the volume fraction and size of the β precipitates formed in the T6 temper (see Section II.1). These precipitates are affected by the temperatures reached during FSW. In the TMAZ and HAZ, these precipitates coalesce (i.e. grow) and/or partly dissolve [138, 139]. This leads to a decrease

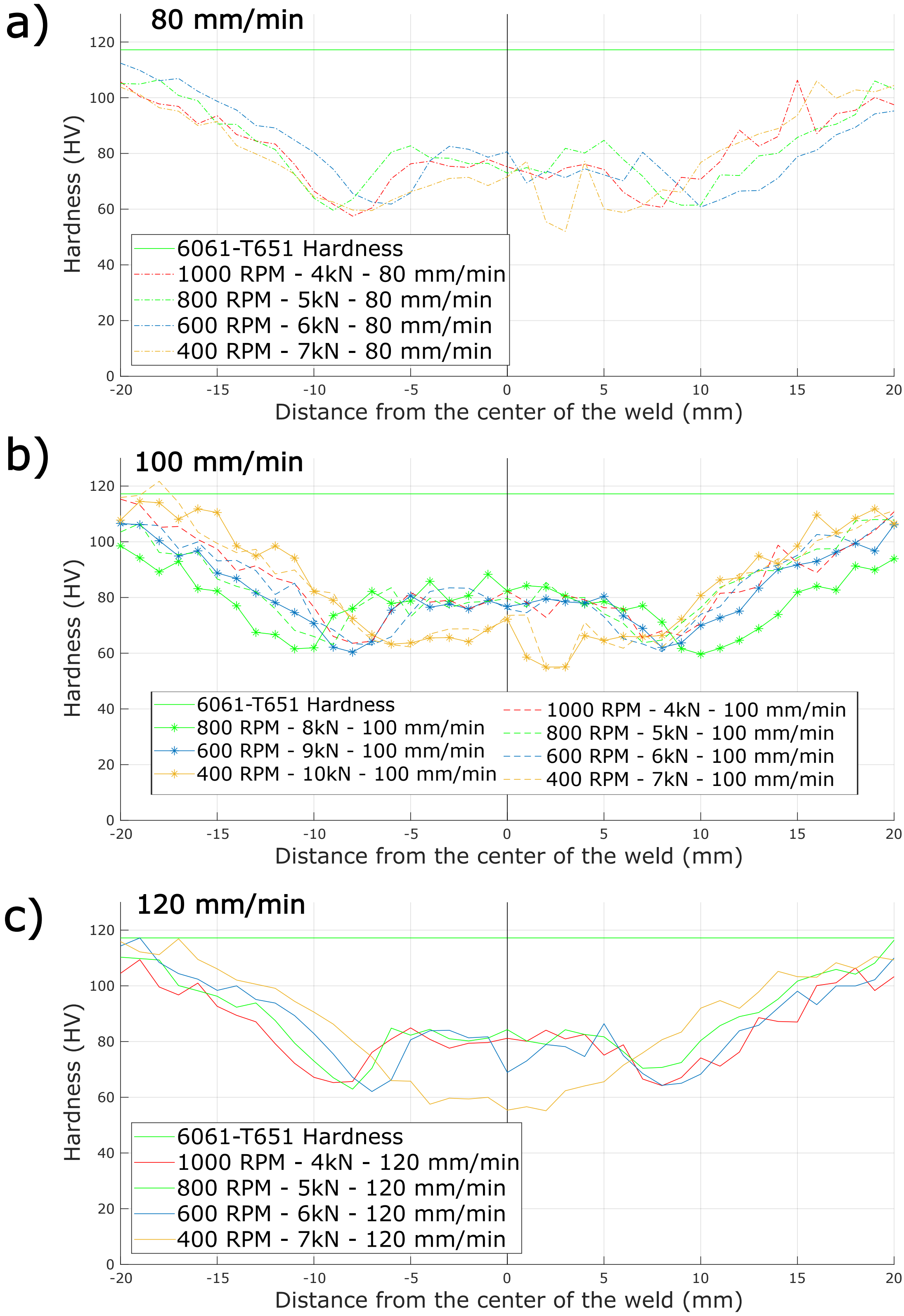

Figure IV.7: Hardness measurements for AA6061 similar joints at (a) 80, (b) 100 and (c) 120 mm/min. For each advancing speed value, multiple rotational speeds and axial loads are plotted. Positives values are the advancing side.

in hardness compared to the base material. In the stir zone, the temperature has reached up to 80% of the melting temperature of the alloy [83] usually causing the full dissolution of precipitates. Following natural aging, the welds reach the hardness of the T4 state. The hardness measurements presented lead to the conclusion that for these parameters, the size of the TMAZ and HAZ are the same in joints manufactured at low axial load, with a near perfect counter balancing effect on temperature, and thus hardness, between an increase in axial load and a decrease in rotational speed.

However, at higher axial load values for otherwise identically welded samples (same RPM, same advancing speed), the rotational speed appears to have an effect on the width of the HAZ (i.e. it increases if the rotational speed increases) as shown in [140] for position controlled welds. The effect of the axial load is however interesting here. As explained, the hardness is here closely related to the precipitation of β phase in light of the thermal environment it is subjected to during welding. At these higher axial loads, and ensuing torques, the impact on heat generation of the axial load appears to hit a limit. At this point, only rotational speed changes appear to have an effect on heat generation, thus affecting the hardness measurements. On Figure III.7 in Chapter III, these AA6061 similar welds with high axial load exhibit a "heat runaway scenario" in which the material softens so much that the CNC machine is unable to fully compensate in plunging depth to maintain a sufficiently high axial load. This "heat cap" result is coherent with the data provided in the Appendix on the work of Colligan, K. In his work, the author shows that the shear flow stress (a value linearly linked to torque) and the average surface velocity (a value linearly linked to rotational speed) have a bi-linear relationship, with a minimum threshold at which, the torque values reach a limit after which only an increase in rotational speed will lead to an increase in temperature. Our hardness measurements at high axial load corroborate well with these results.

At 400 RPM and 100-120 mm/min (Figures IV.7(b,c)), which are the coldest of all welds, the hardness of the central part of the weld is not increasing compared to the HAZ. The maximum temperature in the stir zone was probably too low here. The hardness profile suggests that the dissolution of β precipitates is only partial in these welds. This lack of Mg and Si dissolution will indeed impede the formation of GP zones through natural aging and lead to lower hardness. It might even be the sign that stable β precipitates are formed in these stir zones as the temperature is not sufficient to lead to their dissolution.

A peculiar hardness profile is noted for 800 RPM, 8 kN and 100 mm/min welds on Figure IV.7(b) where the central hardness plateau associated with the stir zone is much larger compared to the other weld. In Section IV.1.B, this sample showed a double vortex stir zone along with a deep penetration of the FSW tool. The high axial load used to manufacture this joint has enlarged the stir zone of this weld. This phenomenon only occurred at 800 RPM. High material softening associated with high rotational speed, i.e. high heat input, could explain such behaviour.

Figures IV.8(a,b,c,d) show the hardness profiles taken at the center line of similar AA6061 welds respectively manufactured at 400, 600 and 800 and 1000 RPM for various advancing speeds and two different axial loads. This way the impact of **advancing speed** and **axial load** on hardness measurements will be further assessed. As described in Chapter I and additionally detailed in Section III.4, an increase in advancing speed at a given RPM leads to a decrease in heat input and overall temperature of the weld. An increase in advancing speed also causes a faster cooling down after the tool passes at a given location. An increase in axial load leads to an increase in heat input.

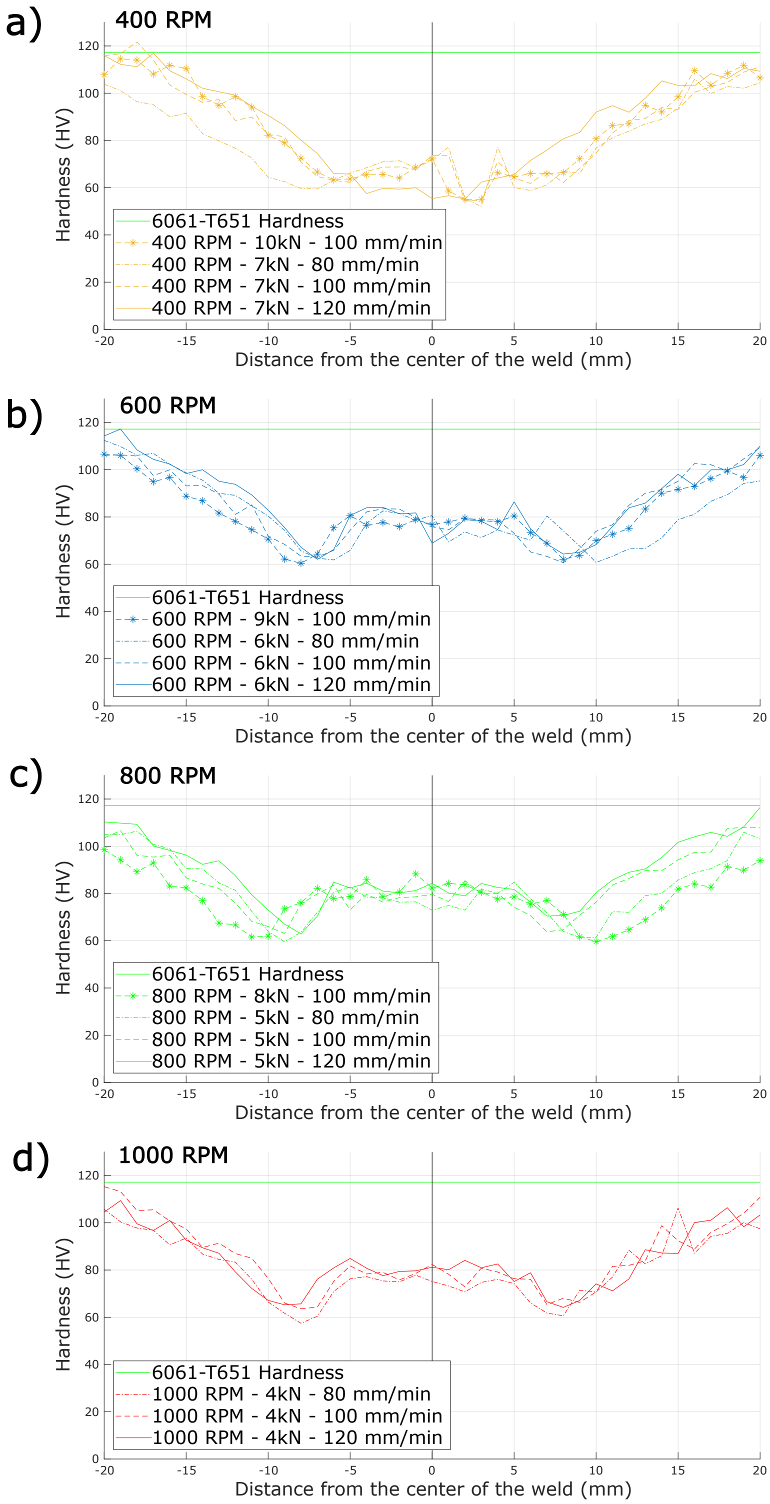

Figure IV.8: Hardness measurement for AA6061 similar joints at (a) 400, (b) 600, (c) 800 and (d) 1000 RPM are presented. For each rotational speed, multiple advancing speeds and axial loads are plotted. Positives values are the advancing side.

On Figure IV.8(a), i.e. at a rotational speed of 400 RPM, the lower hardness value of the stir zone previously discussed is clearly visible. At such low RPM, different advancing speeds have quite unclear effect on the width of the HAZ. One may see however that the lowest hardness values are attributed to the coldest 400 RPM weld, i.e. 120 mm/min. An increase in axial load does not have any effect on the hardness on these joints.

Figure IV.8(b), i.e. at a rotational speed of 600 RPM, the hardness of the stir zone is higher than the TMAZ/HAZ hardness. Beyond that, either on the retreating or advancing side, the advancing speed appears to have moderate effect on hardness profiles. The 600 RPM, 6 kN and 80 mm/min has the lowest hardness of the advancing side, but is similar to other joints when analyzing the retreating side. The higher axial load weld does not yield significant difference in hardness profile.

Figure IV.8(c), i.e. at a rotational speed of 800 RPM, a similar hardness plateau is found in the stir zone. In this case however, on both the advancing and retreating side, the hardness profile of these joints exhibit a symmetrical pattern. At 5 kN, the coldest 800 RPM welds, i.e. 120 mm/min, exhibits the smallest width of its HAZ, followed by the 100 mm/min joint and finally the 80 mm/min joint, the hottest joint. Additionally, an increase in axial load to 8 kN at 100 mm/min yielded an even lower hardness profile compared to any 5 kN joints. At 800 RPM, the welded joints are particularly sensitive to heat input.

Finally, Figure IV.8(d), show the hardness profiles for 1000 RPM and 4 kN welds at three advancing speeds. Contrary to 800 RPM joints, the hardness profiles do not show significant differences among one another. No additional axial force have been tested at this rotational speed.

A difference in stir zone hardness previously noted while describing the impact of rotational speed is here clearly visible between the 400 RPM hardness curves and the curves at higher rotational speed. On the other hand, the advancing speed does not have a significant impact on hardness at 400 and 600 RPM. A strong influence pattern has only been observed at 800 RPM. It could be speculated that at 600 RPM and below, the rotational speed is not high enough that differences in time at high temperature, i.e. advancing speed, would generate enough difference to have different dissolution and coarsening behaviour of β precipitates. In Section III.4, the normalized linear heat input of welding parameters show that at low rotational speed, advancing speed has a lower impact on heat input compared to higher rotational speed. Steuwer et al. [51] show that the difference in temperature profile for low and high rotational speed (280 and 840 RPM) when treating the effect of the advancing speed is relatively small compared to the difference generated by low and high rotational speed themselves. This can probably be mitigated depending on the difference in advancing and rotational speeds considered. In our case the significantly higher thermal transfer of 800 RPM welds would generate stronger differences between low and high advancing speeds in terms of weld temperature, generating concurring hardness profiles. However, 1000 RPM welds show no significant impact of the advancing speed on hardness profiles. The higher rotational speed may have softened the AA6061 to a point where heat generation is capped and the advancing speed ceases to have an effect on total heat absorption.

Similarly, the axial load does not have a significant impact on hardness profiles at 400 and 600 RPM. At 800 RPM however, the additional heat generated by the higher axial load is notable. However, a lack of higher axial load measurements at 1000 RPM renders a definite conclusion impossible.

IV.2.A.ii AA7075 similar joints

Figures IV.9(a,b,c) present the hardness values of AA7075 welded joints for respectively 80, 100 and 120 mm/min. Thus, the influence of the **rotational speed** on hardness values can be assessed on this specific aluminium alloy compared to AA6061.

Figure IV.9(a), i.e. 80 mm/min welded joints, shows a hardness plateau in the stir zone, comparable to the one observed in AA6061 samples. Apart from two outlying hardness indent in the stir zone respectively for 400 and 800 RPM, the hardness values for all rotational speed are similar in the stir zone. No clear effect of the rotational speed can be established.

Figure IV.9(b), i.e. 100 mm/min welded joints, shows that for higher axial load, there is limited effect of the rotational speed on the stir zone hardness. However, at lower axial load, the stir zone hardness increases if the rotational speed increases. Additionally, hardness distribution across the stir zone is wider at lower axial load compared to higher axial load.

Figure IV.9(c), i.e. 120 mm/min welded joints, shows interesting results in the stir zone. Indeed, apart from an outlying indent in the 800 RPM joint, the general hardness plateau in the stir zone is linked to the rotational speed. Especially notable on the retreating side of the stir zone, an increase in rotational speed yields an increase in hardness values. However, in the HAZ and TMAZ, no effect of the rotational speed can be evidenced. One may eventually see a small increase in the HAZ when the RPM increases but this is not totally consistent between all rotational speed conditions.

For AA7075 joints, the effect of the rotational speed at low or moderate advancing speed appears to be quite insignificant. No substantial difference in hardness values or profiles throughout the weld is seen at 80 or 100 mm/min. However, at 120 mm/min, a difference in the stir zone hardness values is noted, with higher rotational speed having higher hardness values. Similarly to what has been described in AA6061 welds, there is a possibility that, as the rotational speed increases and thus, the welding temperature of the stir zone, some η precipitates, if not all, are dissolved again inside the aluminium matrix (see Section II.1). If true, the welded joint underwent natural aging while awaiting to be mechanically tested, and the slight difference in heat input yielded different T4 like metallurgical state after welding and aging. M. Lezaack [120], a colleague at UCLouvain, has studied the η precipitation in Friction Stir Processing (FSP) of AA7075 (just bead-on-plate processing but would lead to similar precipitation as FSW). He has however shown that η stable and µm sized precipitates form after FSP in the stir zone. The formation of η precipitates rather than the dissolution of Mg and Zn elements is probably favored at low heat input, which he did not study. Such coarse η precipitates, formed at grain boundaries, are not offering much strengthening in the stir zone. Indeed, as discussed for the AA6061, a good dissolution of alloying elements favors the formation of GP zones during natural aging. To conclude, cold welds (e.g. 300-400 RPM) could actually present low stir zone strength due to an incomplete dissolution in the stir zone as well as the formation of stable η precipitates that contribute little to the strengthening.

Figure IV.10(a,b,c,d) present respectively hardness profiles measured at 300, 400, 600 and 800 RPM for various advancing speeds. Presented in this fashion, the effect of the **advancing speed** and **axial load** at a given rotational speed can be described for AA7075 similar joints.

Figure IV.10(a) shows hardness profiles in AA7075 joints performed at 300 RPM. At lower advancing speed, i.e. higher temperature input and mostly slower cooling rate for

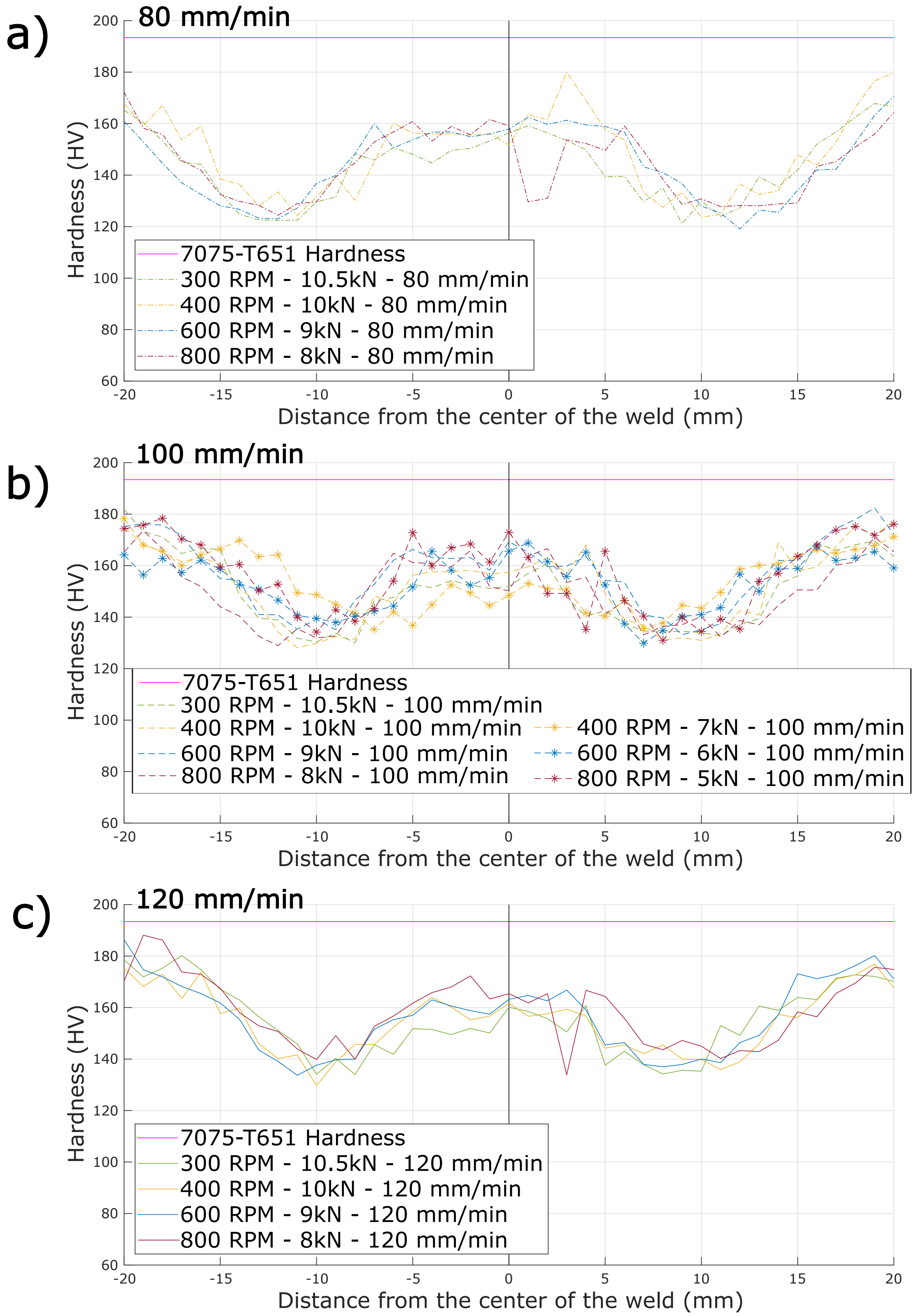

Figure IV.9: Hardness measurements for AA7075 similar joints at (a) 80, (b) 100 and (c) 120 mm/min. For each advancing speed value, multiple rotational speeds and axial loads are plotted. Positives values are the advancing side.

a given RPM value, the hardness is lower in the HAZ compared with higher advancing speed and the HAZ is clearly much wider. However, no significant difference in stir zone hardness is noticed.

Figure IV.10(b) plots hardness values across the 400 RPM welded joints. Once again, the lowest advancing speed yields the lowest minimum hardness values and widest HAZ. The difference between 100 and 120 mm/min is however not as strong compared to 300 RPM welds. At 10 kN, no difference of stir zone hardness is noted. Additionnaly, lowering the axial load improved HAZ hardness but degraded the stir zone hardness values.

Figure IV.10(c) presents hardness values across the 600 RPM welded joints. The 80 mm/min weld has a substantially lower minimum hardness and the widest HAZ compared with 100 and 120 mm/min, whose hardness profiles have blended together and are almost indistinguishable. It appears that, as the rotational speed increases, two behaviours are unveiled. Stir zone hardness values are similar across all 600 RPM samples. Lowering the axial load in this case does not affect the stir zone hardness value similarly to 400 RPM welds, the HAZ hardness exhibits a more gradual increase towards the base material.

Finally, Figure IV.10(d) plots the hardness values of AA7075 similar joints welded at 800 RPM. This time, for the 8 kN welds, the 80 mm/min as well as the 100 mm/min show low minimum hardness properties and a very wide HAZ compared with the 120 mm/min welds. It can also be noted that the stir zone hardness values appear to be generally more erratic at this rotational speed. At 800 RPM, the lower axial load did not change the overall shape of the hardness profile, as described for 400 and 600 RPM welds. The decrease in axial load at 100 mm/min resulted in higher minimum hardness and a narrower HAZ at such high rotational speeds.

In AA7075 welded joints, similarly to AA6061, changing the advancing speed has an influence on the hardness profile. However, this effect is much more pronounced in AA7075 compared to AA6061. When lowering the advancing speed, the temperature of the weld increases (see Section III.4). The η precipitates present in AA7075 appear to be more sensitive to the cooling rate (i.e. the advancing speed) compared with the β precipitates of AA6061. Particularly, hardness profiles from 600 and 800 RPM lead to the conclusion that some threshold temperature exists, at which point the hardness drops significantly. Hardness values of AA7075 is closely linked to η phase precipitates. As described in Section I.3.D, the solidus of AA7075 is lower than AA6061. This could explain the difference in hardness behaviour between AA6061 and AA7075 welds at high temperature. Now the difference in behavior of β and η precipitates should be studied at a fine scale to really understand why the rotational speed (i.e. the maximum temperature) has more effect in AA6061 welds while the advancing speed (i.e. the cooling rate and maximum temperature) has more effect on AA7075 hardness.

IV.2.B Al/Al dissimilar welding

Hardness measurements from dissimilar aluminium joints are now presented in this Section. Figures IV.11(a,b,c) are plotted hardness values along the centerline of the cross section of the welds for 80, 100 and 120 mm/min. Thus the influence of the **rotational speed** on hardness of dissimilar welds will be assessed. The AA7075 is on the retreating side for all Figures, i.e. the x negative side on the graphs. Straight horizontal lines on all

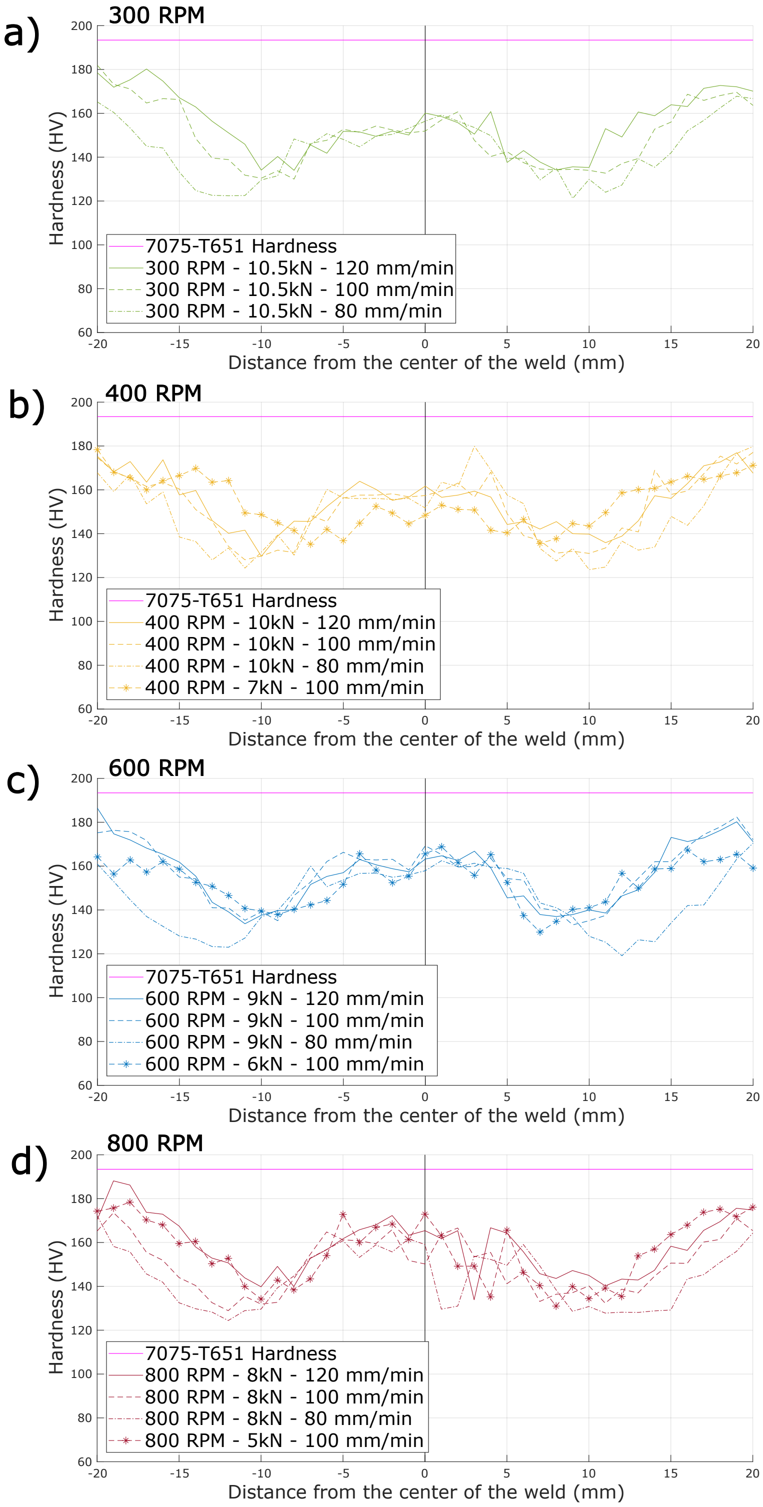

Figure IV.10: Hardness measurement for AA7075 similar joints at (a) 300, (b) 400, (c) 600 and (d) 800 RPM are presented. For each rotational speed, multiple advancing speeds and axial loads are plotted. Positives values are the advancing side.

Figures show an average of the two base material's hardness.

Figure IV.11(a), i.e. 80 mm/min welded joints, shows a higher hardness value in the stir zone as the rotational speed increases, reaching values close to the AA6061 base material. The transition between the stir zone and the TMAZ of the AA7075 is clearly visible and its position is linked to the rotational speed. As the latter increases, the ST/TMAZ boundary is located further away on the AA7075 side. The width of the HAZ in the AA7075 is slightly affected by the rotational speed, i.e. it increases as the rotational speed increases. On the other hand, the AA6061 HAZ has the same size for all rotational speeds.

Figure IV.11(b), i.e. 100 mm/min welded joints shows, similarly to 80 mm/min welds, a higher hardness value in the stir zone as the rotational speed increases is noted. The boundary between the stir zone and the TMAZ of the AA7075 is located further away into to AA7075 as the rotational speed increases, similarly to 80 mm/min welds. Note that, the 800 RPM, 10 kN and 100 mm/min sample, which has a peculiar double vortices stir zone, exhibit a larger TMAZ in both advancing and retreating side. However, here the size of the HAZ in both Al alloys is linked to the rotational speed. A rotational speed increase leads to an increase in the width of the HAZ.

Figure IV.11(c), i.e. 120 mm/min welded joints shows once again a higher hardness value in the stir zone as the rotational speed increases. Although in this case, the difference between the 600 and 800 RPM curves are minimal. The 400 RPM has a ST/TMAZ boundary in the AA7075 located the closest to the center of the weld. The width of the HAZ for the AA7075 shows a slight correlation with the rotational speed as it increases during a RPM increase. On the other hand, the 800 RPM weld has the widest HAZ but only marginally compared to 400 and 600 RPM, both of which have similar HAZ size.

As the rotational speed of the weld increases, the hardness value of the stir zone increases. As described in Section II.3.A and clearly visible on Figures IV.3, IV.4 and IV.5, an increase in rotational speed favors strong mixing in the stir zone of dissimilar joints. On those macrographs, it can be seen that the stir zone is separated in two. The boundary between the AA6061 TMAZ and the stir zone has a strong AA7075 contrast, and inversely for the boundary of the AA7075 TMAZ and the stir zone. Looking at the hardness curves, the locally high hardness values in the stir zone are located on the AA6061 side. This result is coherent with the previous observations in the stir zone contrast observed by optical microscopy. Additionally, as hardness in both AA6061 and AA7075 alloys are related to their respective hardening precipitates (see Section II.1), the hardness elevation in the stir zone is also related to the precipitation mechanism happening during and after FSW. One could speculate that the η precipitates from the AA7075 has transferred to the stir zone during mixing and thus, lead to a local increase in hardness. A better mixing as the rotational speed increases would support such an idea. This is probably true to a certain degree, but it should be noted that the local stir zone maximum is lower than any hardness value in the AA7075 on the retreating side. On the one hand, compared to AA7075 similar welds hardness curves, the absolute value is much lower in dissimilar welds in the stir zone with 65-120 HV, compared to 140-170 HV. But on the other hand, compared to the AA6061, the local hardness absolute value is higher, with hardness values in the stir zone of AA6061 similar welds being equal to 60-80 HV. The higher temperatures of high rotational speed welds probably lead to the dissolution of hardening precipitates and subsequent GP zone strengthening in the stir zone in both aluminium alloys. As the mixing is stronger at high rotational speed, diffusion from one

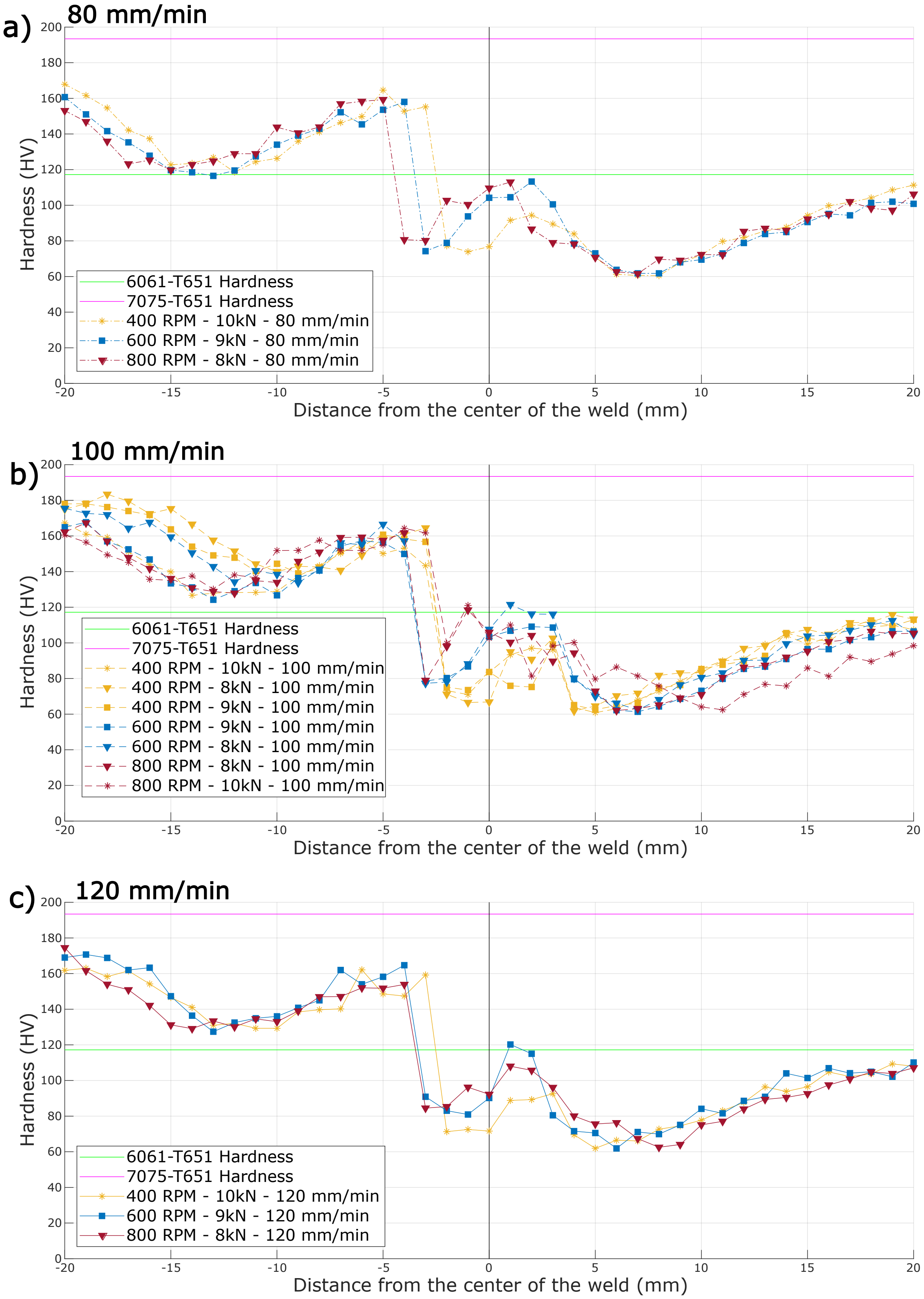

Figure IV.11: Hardness measurements for AA6061/AA7075 dissimilar joints at (a) 80, (b) 100 and (c) 120 mm/min. For each advancing speed value, multiple rotational speeds and axial loads are plotted. Positives values are the advancing side.

AA6061 "ring" to a AA7075 one would be facilitated.

The size of the HAZ in both Al alloys is related to the rotational speed, and thus to the heat input. This result is coherent with the HAZ size change in similar AA6061 and AA7075 welds previously discussed, although this effect has only been noted at high advancing speed for AA7075. One can observe that the AA7075 in dissimilar welding appears to be more sensitive to the change in rotational speed, which was not very evident in the similar AA7075 welds.

Figures IV.12(a,b,c) show the hardness values across the welded joints of dissimilar AA6061/AA7075 welds for 400, 600 and 800 RPM at varying **advancing speeds** and **tool axial loads**. Thus, the influence of both these parameters on hardness can be further described.

Figure IV.12(a), i.e. 400 RPM welds, show low absolute hardness values in the stir zone. The HAZ size on the AA7075 retreating side is greatly affected by the tool axial load. A higher axial load induces a much larger HAZ. This is not the case in the HAZ of the AA6061. An increase in advancing speed reduces the size of the HAZ in both alloys, albeit this effect is more pronounced in the AA7075.

Figure IV.12(b), i.e. 600 RPM welds, shows an increase in hardness values in the stir zone. This effect was already noted on Figure IV.11 but is here more clearly visible. All joints have hardness values close to the AA6061 base material value. The advancing speed influences the HAZ of the AA7075, as for the 80 mm/min joint (the hottest 600 RPM welds) has the widest AA7075 HAZ of all. 100 and 120 mm/min HAZ are smaller. In the AA6061, once again, the advancing speed has little influence on the HAZ. The 80 mm/min is noted to have the widest of them all, but only by a slight margin. Lowering the axial load from 9 kN to 8 kN has a strong influence on the size of the AA7075 HAZ as well, with the highest load having a larger HAZ. Similarly to the advancing speed influence on the AA6061, the axial load also has a very slight effect on the HAZ size, with the 8 kN joint having a barely smaller HAZ compared to 9 kN.

On Figure IV.12(c), the 800 RPM joints are presented. Hardness profiles and values in the stir zone are different from 400 and 600 RPM. The local maximum is here wider. The hottest 80 mm/min joint has the lowest AA7075 side hardness and the widest HAZ on the AA7075 side. 100 and 120 mm/min do not appear to have different hardness values in the AA7075. In the AA6061, the advancing speed alone does not appear to have any clear influence. Axial load, on the other hand, does. The 10 kN high joint has the widest HAZ of the AA6061. Interestingly, this is not the case in the AA7075 HAZ, where the axial load does not appear to have any influence.

Overall, the influence of advancing speed and axial load in the HAZ of the AA6061 seems to be limited, as noted on the AA6061 similar welds. Some influence of the advancing speed are observed, for example with the HAZ width in the 400 RPM, 10 kN and 80 mm/min weld of the 600 RPM, 9 kN and 80 mm/min. These joint are the hottest 400 and 600 RPM joints and have the widest HAZ in the AA6061 for a given axial load. In Section IV.2.A, we explained the role of the heat input on β precipitation. This observation, albeit limited, tends to assert that high heat joint have wider HAZ. Similarly, axial load increase tends to have wider HAZ, but the effect appears to be limited. 400 RPM joints have the widest range of axial loads, and the influence of that parameter appears to be limited as well. The 8 kN has the smallest HAZ of all, but only by a small margin. Although, at 800 RPM, the high 10 kN load has the widest AA6061 HAZ.

In contrast, the HAZ of the AA7075 appears to be more sensitive to either advancing speed or axial load changes, as noted in the AA7075 similar welds, as noted in AA7075 similar welds. Higher axial loads lead to noticeably larger HAZ. Faster advancing speeds lead to smaller HAZ, with the caution that 800 RPM welds appear to be less sensitive for slow advancing speeds. These observations are coherent with the η precipitate sensitiveness to temperature increase.

Assembly	Parameter	Effect on hardness	Explanation
AA6061	Rotational speed	Larger HAZ when increased at high load. Threshold effect between 400 and 600 RPM welds in the stir zone.	Heat input dissolves and coarsen β'' hardening precipitates of the T6 state. It increases with load and RPM. It leads to GP zone formation during natural aging in the stir at high RPM.
	Advancing speed	Distinct larger HAZ on both AS and RS at 800 RPM only.	Stronger influence at high RPM as the heat ratio between the coldest and hottest weld decreases.
	Axial load	Larger HAZ at 800 RPM.	A higher axial load lead to more heat input.
AA7075	Rotational speed	Higher stir zone value at high RPM and fastest advancing speed.	Different heat input lead to different η dissolution and precipitation rate. Low heat input lead to coarsening of the precipitates at the expense of their dissolution.
	Advancing speed	Slow advancing speed lead to larger HAZ. Existence of a thermal threshold.	A slow cooling rate leads to excessive η precipitate coarsening.
	Axial load	Larger HAZ.	Higher heat input thus more η precipitates dissolution and coarsening in the HAZ.
Dissimilar	Rotational speed	Larger HAZ in both alloys, but stronger influence on AA7075, higher stir zone values on the AA6061 side.	Behaviour close to hardness in similar welds.
	Advancing speed	HAZ width of AA6061 and AA7075 increases when advancing speed decreases, but more substantially for AA7075.	Coherent with the behaviour of the base materials in similar welds.
	Axial load	HAZ width of AA6061 and AA7075 increases when axial load increases, but more substantially for AA7075	Coherent with the behavior of the base materials in similar welds.

Table IV.1: Synthesis of the hardness behaviour in similar and dissimilar welding of AA6061 and AA7075.

Table IV.1 summarizes the effect of process parameters on hardness. In general, the effect of the welding parameters on the hardness of dissimilar welds closely resemble

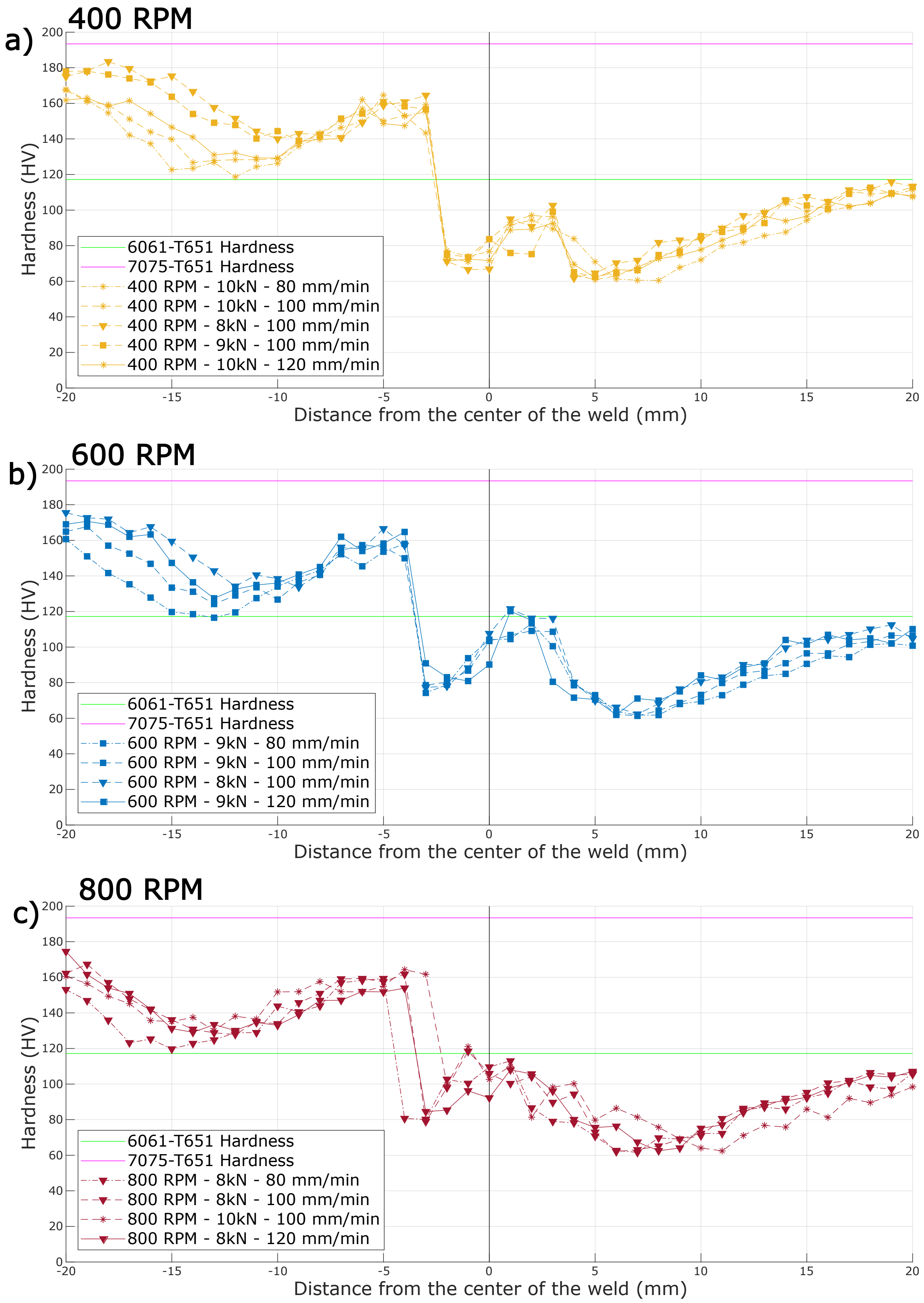

Figure IV.12: Hardness measurements for AA6061/AA7075 dissimilar joints at (a) 400, (b) 600 and (c) 800 RPM. For each rotational speed value, multiple advancing speeds and axial loads are plotted. Positives values are the advancing side.

that of the base materials in similar welding configuration, especially in their respective HAZ. This result is coherent as each HAZ only sees heat input. Diffusion on alloying elements from the other aluminium alloy might not occur, and only the dissolution of hardening precipitates thanks to the thermal profile of the welds has an influence on the local hardness.

However, the stir zone of such welds exhibit an interesting pattern. As the rotational speed increases, so does the hardness value and the size of the high hardness value zone inside the welded stir zone. This result closely match the observations made on the macrographs of dissimilar welds (see Section IV.1.B), where stronger mixing has been detailed as the rotational speed increases possibly due to AA7075 mixing. The hardness values inside the stir zones even go as high as the value for the AA6061 base material. But on the other hand, this local maximum is well below the lowest hardness value of the AA7075 HAZ. A possible explanation could be the diffusion of alloying elements between the AA7075 and AA6061. As the rotational speed increases, the stronger mixing and higher heat input allows such diffusion to occur. Finally, rotational and advancing speed have been found to influence each alloy differently in dissimilar joints. The rotational speed has a strong influence in the width of the HAZ in AA6061 welds. The advancing speed on the other hand, greatly influences the HAZ width in AA7075.

IV.3 Tensile properties

In this study, all Al/Al samples presented in Chapter III are mechanically tested using tensile testing. As presented in Chapter II, Digital Image Correlation (DIC) is interesting to measure local strain heterogeneities in tensile samples. Indeed, as presented beforehand in this Chapter, FSW joints are highly heterogeneous, and dissimilar FSW joints present yet another layer of difference in the joint structure. 2D DIC allows to capture the full mechanical discrepancy these heterogeneous welds offer during tensile testing. As a reminder, the DIC strain maps picture the weld upside down (tool shoulder friction path is located at the bottom of DIC maps), with the advancing side on the right of the image.

IV.3.A Al/Al similar welding

IV.3.A.i AA6061 tensile results

For AA6061 similar welding, tensile values for all samples are provided in Table IV.2.

The AA6061 similar welding samples cover a wide range of welding parameters. According to the standard EN 485-2 [115], the yield strength and UTS of a 6 mm thick AA6061-T651 alloy are respectively 240 MPa and 290 MPa. Its elongation at failure is 9%.

Figures IV.13(a) and (b) respectively show the start of yielding (also called "apparent yield strength") for AA6061 similar friction stir welded joints as a function of RPM and advancing speed. Variation in rotational speed does not appear to have a substantial influence on the apparent yield strength of such samples. An optimum for all advancing speeds appears between 600 and 800 RPM. However, 1000 RPM is only substantially detrimental to the 80 mm/min sample. On the other hand, a higher advancing speed for a given RPM/axial load value increases yield strength. With the exception of the

Axial load (kN)	**Rotational Speed (RPM)**	**Advancing Speed (mm / min)**	$Rp_{0.2}$ **(MPa)**	**UTS (MPa)**	ϵ_{11} **(%)**
8	800	100	126	196	6.9
9	600		128	198	5.6
10	400		86	190	7.9
4	1000	80	107	193	5.7
		100	117	202	5.1
		120	122	197	3.3
5	800	80	125	195	5.6
		100	116	200	5.2
		120	122	205	5.5
6	600	80	116	198	5.3
		100	121	202	5.4
		120	123	205	5.2
7	400	80	111	191	8.2
		100	115	192	7.9
		120	89	187	5.2

Table IV.2: Weld parameters of AA6061 similar welding along with global tensile properties.

400 RPM, 7 kN, 120 mm/min sample, i.e. the coldest weld in this experimental planning, the yield strength increases for all rotational speeds as the advancing speed increases.

Figures IV.13(c) and (d) respectively plot the UTS for the AA6061 welded joints in function of the rotational speed and the advancing speed. Similarly to the apparent yield strength on Figure IV.13(a), all advancing speeds benefit from faster rotational speeds. However, at 1000 RPM, a slight decrease can be noted for all advancing speeds. This effect can be noted on IV.13(d) as well. Generally speaking, 100 mm/min advancing speed seems to be a good middle ground for all rotational speed. However, for 400 and 600 RPM welds, increasing the rotational speed increases the UTS.

Finally, Figures IV.13(e) and (d) both draw a similar conclusion: an increase in either the rotational speed or the advancing speed is detrimental for the elongation at failure. It can be noted that 400 RPM samples have the highest elongation at failure of all the presented samples.

To further understand how these welded joints behave in tensile testing, Figure IV.14 plots the tensile curves of the 400 RPM AA6061 similar samples. Two distinct tensile behaviour are observed at this rotational speed. The 10 kN, 100 mm/min sample along with the 7 kN, 120 mm/min appear to have a lower apparent yield strength, compared to the other plotted curves. To better understand this discrepancy, DIC obtained strain maps for these two vastly different curves are shown on Figures IV.15(a,b,c) (i.e. high apparent yield strength case) and IV.16(a,b,c) (i.e. low apparent yield strength case). On both these Figures, the strain maps have been plotted during apparent elastic loading, at the apparent start of yield and the UTS. For the 400 RPM, 7 kN and 120 mm/min sample on Figure IV.16(c) has much higher and localized strain in its TMAZ before failure compared to Figure IV.15(c). However, Figures IV.16(b) and IV.15(b) do not show significant

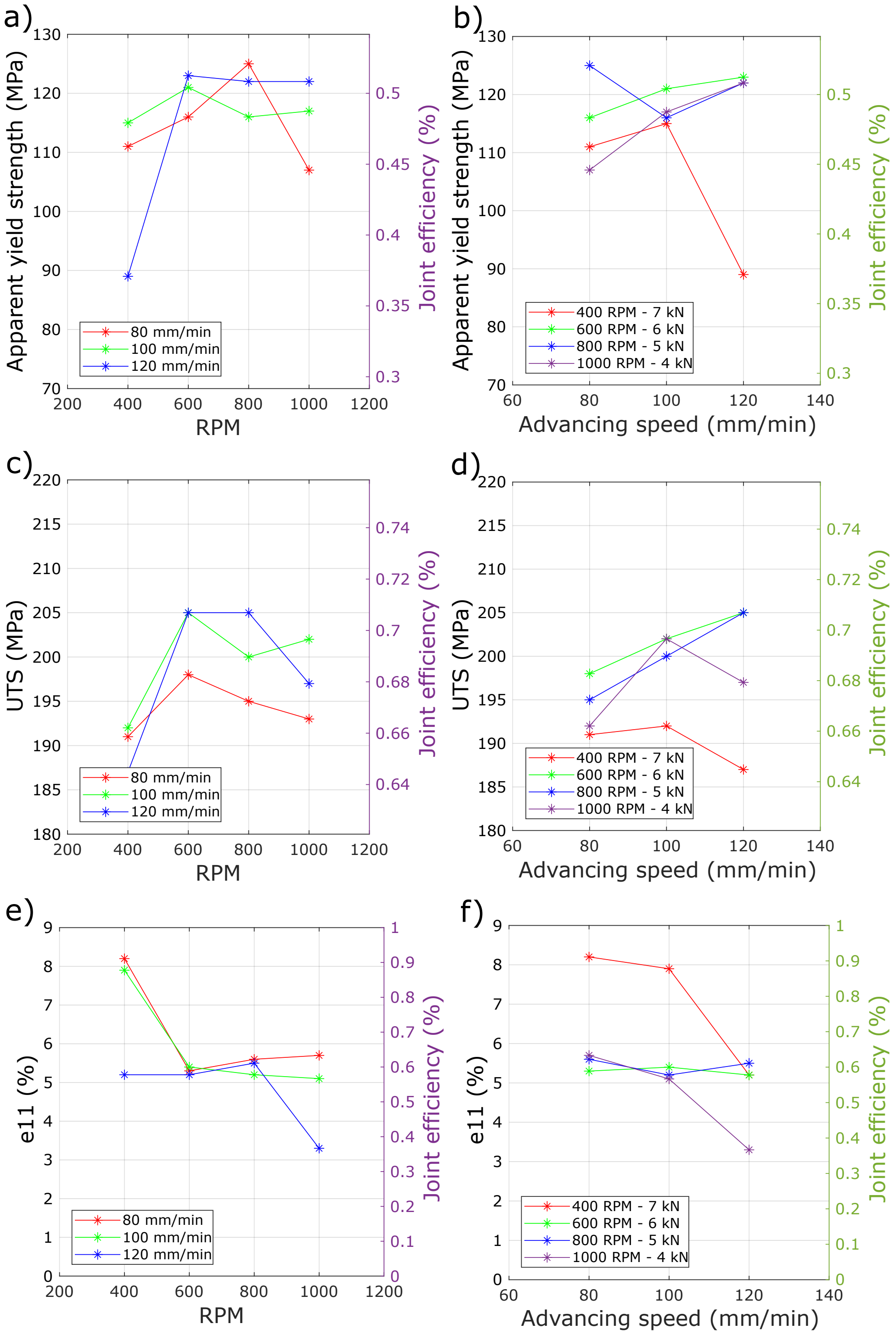

Figure IV.13: Tensile properties of friction stir welded similar AA6061 joints. Apparent yield strength as a function of RPM (a) and advancing speed (b). UTS as a function of RPM (c) and advancing speed (d). Elongation at failure as a function of RPM (e) and advancing speed (f). For a given RPM value, the axial load is identical. On all Figures, the joint efficiency is the ratio with the base material's mechanical properties.

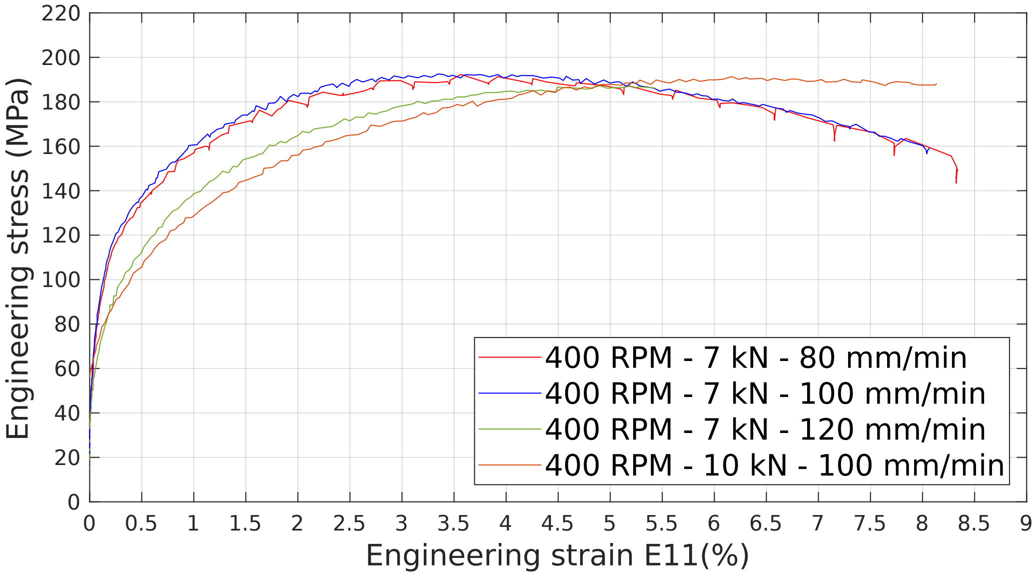

Figure IV.14: Tensile curves of 400 RPM samples in AA6061 in a similar welded joint. Two different tensile behaviours can be visible.

difference at the start of yielding. In the previous Section, hardness properties of these samples were investigated. To fully understand the relationship between hardness profiles and strain distribution, DIC maps have been generated for every mechanically tested welds.

On Figure IV.17, the DIC strain maps in the stir zone for 400 RPM welds have been plotted. Figure IV.13(b) has indicated that increasing the advancing speed at 400 RPM leads to a decrease in apparent yield strength at 120 mm/min. Figures IV.17(a,b,c) show three different strain distribution at 10 kN for varying advancing speed. At 80 and 100 mm/min, the strain is located in the TMAZ/HAZ of the welds, mostly in the HAZ. However, at 120 mm/min, strain concentration occurs in the stir zone. On Figure IV.8(a), this welded joint exhibited the lowest stir zone hardness causing this very early strain concentration in the stir zone. On Figure IV.13(f), this welded joint shows the highest elongation at failure of all AA6061 joints. This is probably the consequence of less strain localization, i.e. a lower notch effect. Indeed, a strong notch is known to be detrimental to ductility [141]. Figure IV.17(d) exhibits an even larger stir zone strain concentration than in Figure IV.17(c), and similarly it appear to be detrimental to its apparent yield strength (see Table IV.2). However, the corresponding hardness profile on Figure IV.13(a) is not similar to the one related to the strain maps of Figure IV.17(c).

Figure IV.18(a,b,c) draws the strain maps of 600 RPM welded samples at the start of yielding for 6 kN and varying advancing speeds. In this instance, one can observe no significant difference between the welded joints. The strain appears to localize in the TMAZ/HAZ of the retreating and advancing side. No severe asymmetry can be noted. Observing their respective hardness profiles in Figure IV.8(b) reveals similar hardness profile in the stir zone and HAZ for these welded joints. The 9 kN welded joint of Figure IV.18(d) shows more strain localization in its HAZ/TMAZ. Additionally, the affected area appears to be slightly larger. This would coincide with its hardness profiles on Figure IV.8(b), where a slightly larger stir zone hardness plateau can be noted for this

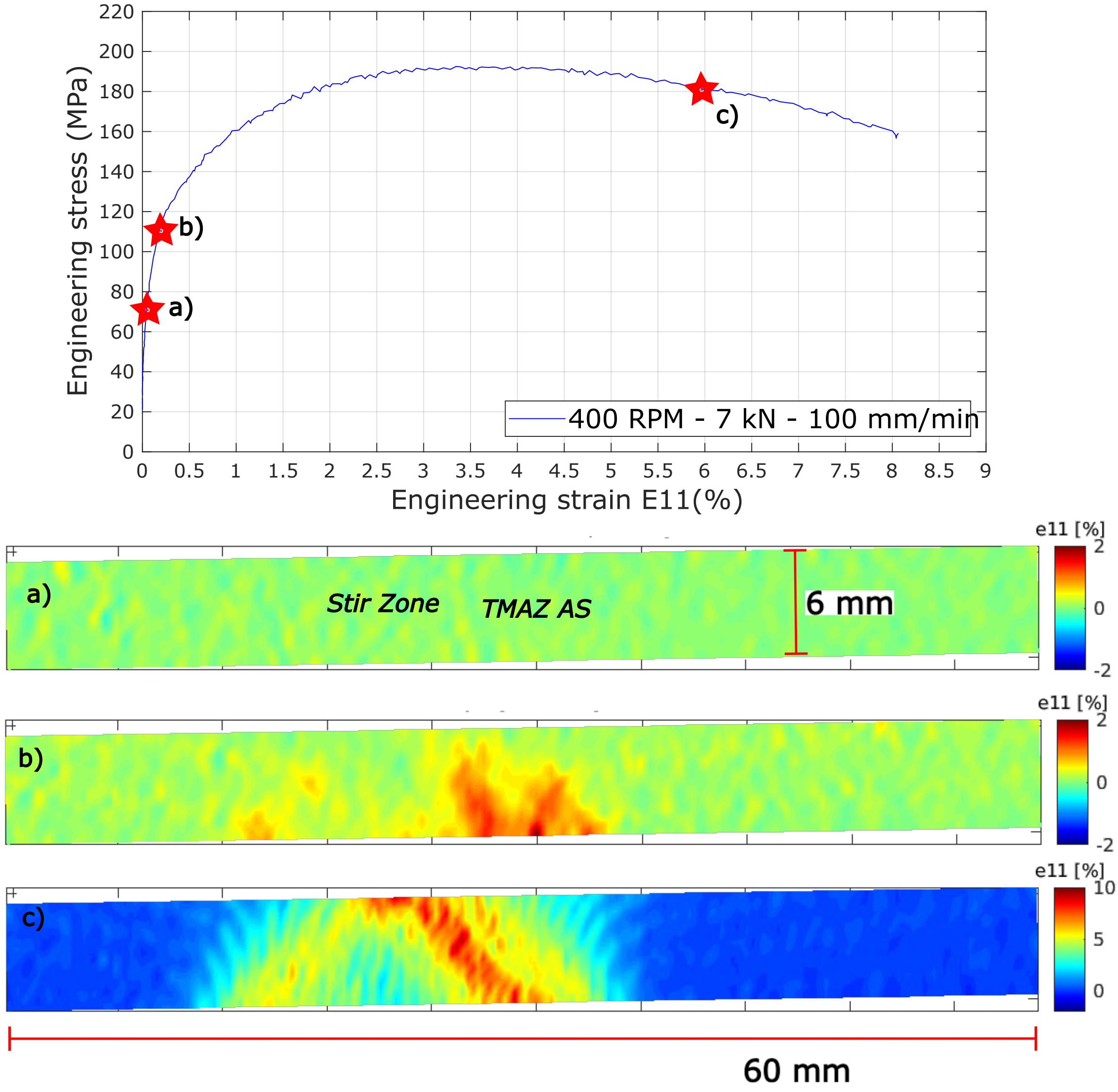

Figure IV.15: Strain/stress curve for the 400 RPM, 7 kN, 100 mm/min similar AA6061 sample along with DIC stress maps at different step of the tensile test: (a) during the elastic phase, (b) at the beginning yielding and (c) when necking has set in. A significant amount of strain localizes in the stir zone, even though the sample eventually broke in the AS TMAZ.

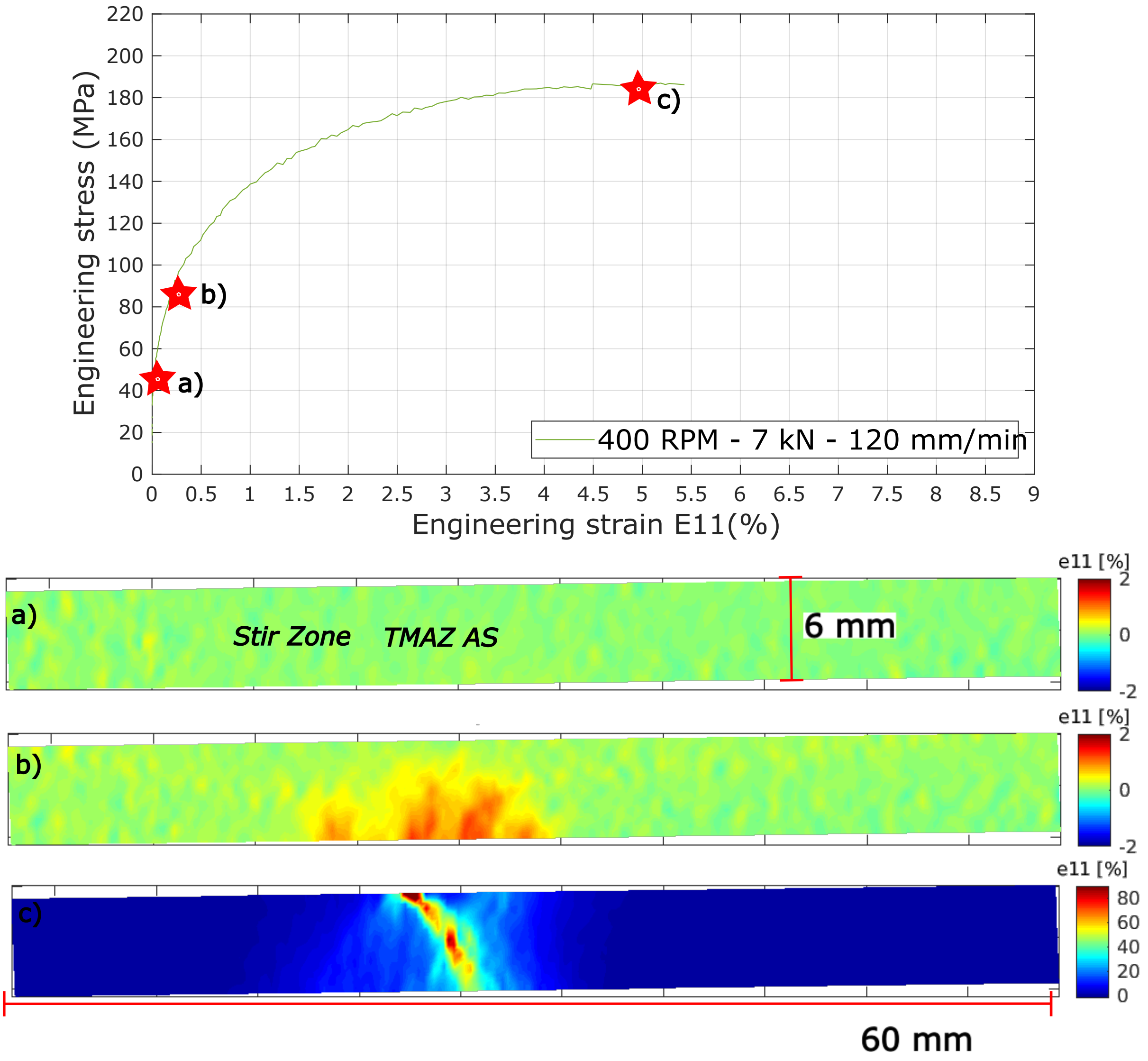

Figure IV.16: Strain/stress curve for the 400 RPM, 7 kN, 120 mm/min similar AA6061 sample along with DIC stress maps at different step of the tensile test: (a) during the elastic phase, (b) at the beginning yielding and (c) when necking has set in. The stir zone has a minimal amount of strain and the fracture area sees enormous amount of plastic deformation.

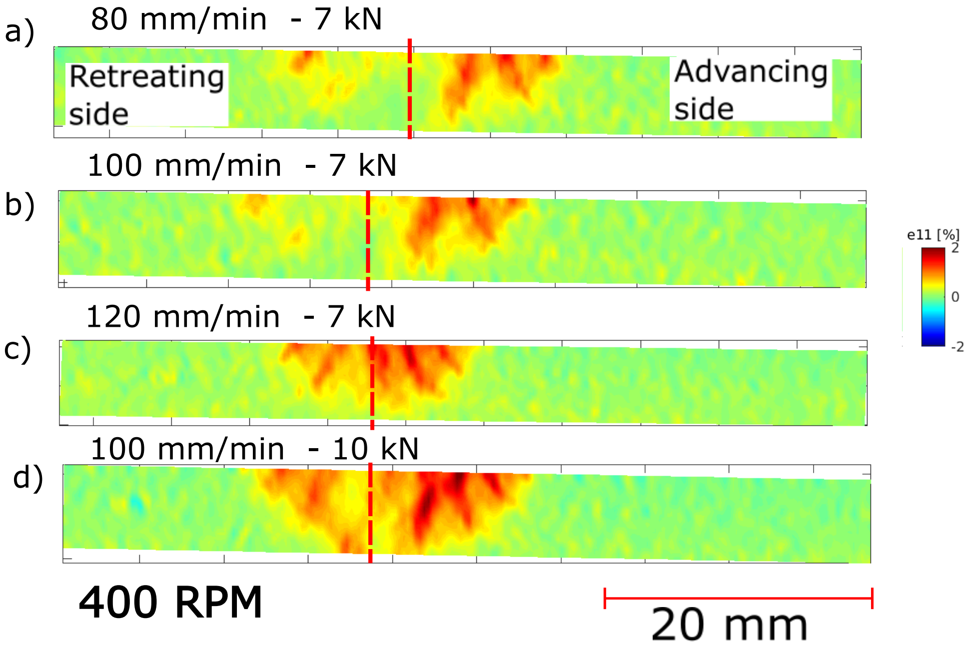

Figure IV.17: DIC strain maps of $e_{11}(\%)$ at reach of the apparent yield strength in the stir zone of AA6061 400 RPM welds with the following welding parameters: (a) 80 mm/min and 7 kN, (b) 100 mm/min and 7 kN, (c) 120 mm/min and 7 kN and (d) 100 mm/min and 10 kN.

sample.

Figures IV.19(a,b,c) plot the strain maps for 800 RPM and 5 kN welded joints, for various values of advancing speed. As the advancing speed increases, the size of the strain localization area at the boundary between the HAZ and the TMAZ decreases. Once again, this decrease in strain area localization size is linked with the measured apparent yield strength for 800 RPM in Figure IV.13(b). On the plotted hardness profiles for such welds (see Figure IV.8(c)), the 120 mm/min and 5 kN weld exhibit a narrower HAZ compared with the 80 and 100 mm/min welds. The high axial load welded joint, here on Figure IV.19(d), appears to have a larger uniformly strained stir zone, along with higher strain localization in its AS and RS TMAZ. This welded sample was described as having a double vortices and a larger stir zone in Section IV.1.B, along with a larger hardness stir zone plateau in Section IV.2.A. These results perfectly match the strain localization observed here. However, this weld does not exhibit a low apparent yield strength.

Finally, Figure IV.20(a,b,c) plots the strain maps of 1000 RPM manufactured welded joints. No significant difference are noted between Figures IV.20(a) and (b), i.e. 80 and 100 mm/min. However, the Figure IV.20(c) shows a more heterogeneous strain distribution, although in this instance, this does not translate to lower mechanical properties or hardness values, as Figures IV.13(b) and IV.8(d) attest.

Overall, for a given rotational speed, increasing the advancing speed is beneficial for the apparent yield strength in most cases. One notable exception happens at 400 RPM. As has been explained in details in Sections II.1 and IV.2.A, a higher heat input is detrimental for the weld's mechanical properties, mainly due to the dissolution of β precipitates in the HAZ of AA6061 during FSW. Increasing the advancing speed lowers the overall heat input of the weld at a given RPM (see Sections I.2.E and III.4) and thus, as the hardening precipitates dictate the mechanical properties of the AA6061 alloy, the apparent yield

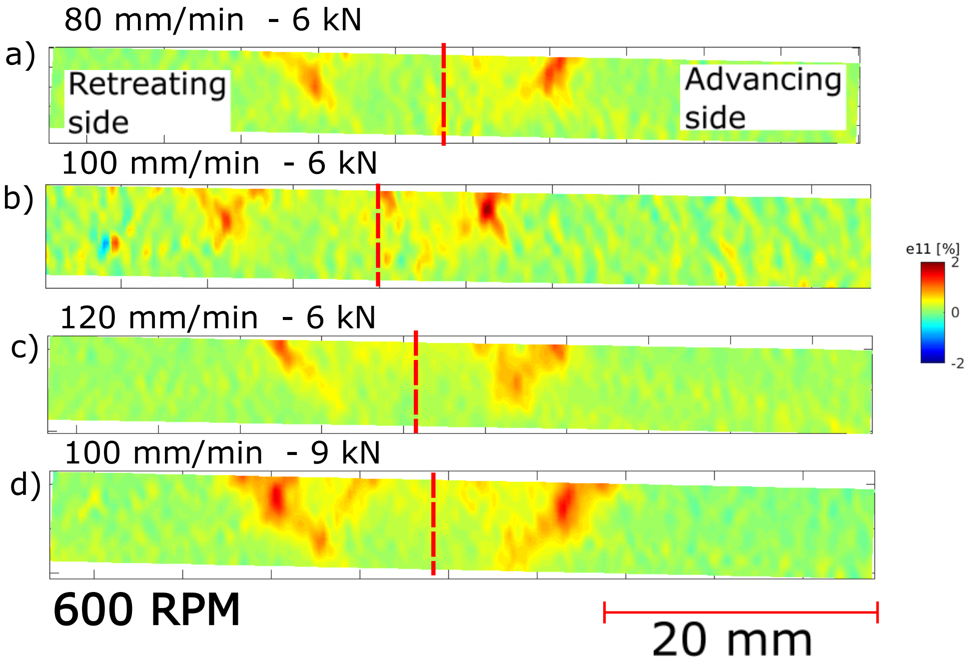

Figure IV.18: DIC maps of $e_{11}(\%)$ at reach of the apparent yield strength in the stir zone of AA6061 600 RPM welds with the following welding parameters: (a) 80 mm/min and 6 kN, (b) 100 mm/min and 6 kN, (c) 120 mm/min and 6 kN and (d) 100 mm/min and 9 kN.

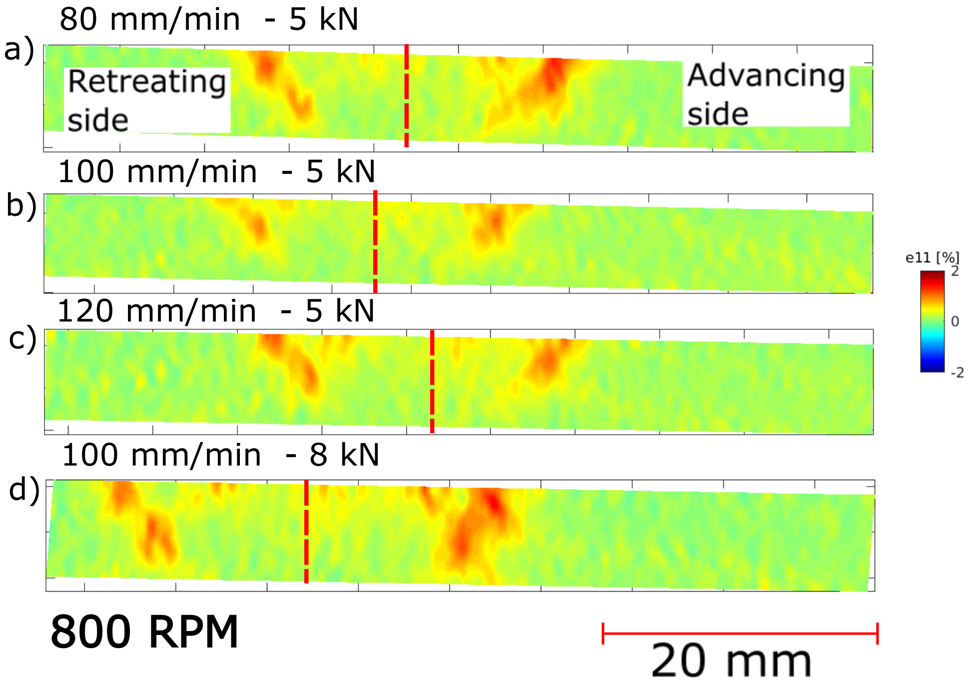

Figure IV.19: DIC maps of $e_{11}(\%)$ at reach of the apparent yield strength in the stir zone of AA6061 800 RPM welds with the following welding parameters: (a) 80 mm/min and 5 kN, (b) 100 mm/min and 5 kN, (c) 120 mm/min and 5 kN and (d) 100 mm/min and 8 kN.

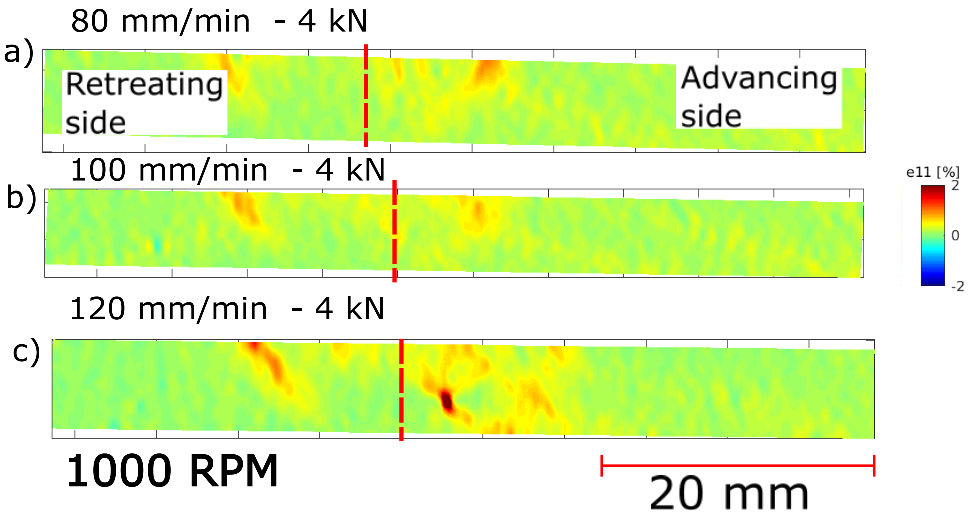

Figure IV.20: DIC maps of $e_{11}(\%)$ at reach of the apparent yield strength in the stir zone of AA6061 1000 RPM welds with the following welding parameters: (a) 80 mm/min and 4 kN, (b) 100 mm/min and 4 kN and (c) 120 mm/min and 4 kN.

strength increases. This effect has already been described when applied to hardness measurements, but here this hypothesis is further verified as the apparent yield strength shows correlation with the heat input of a welded joint. Thanks to DIC measurements, our results show that there is a clear correlation of strain localization at apparent yield strength and hardness profiles (values, size of the HAZ). A general observation can also be made: the strain tends to localize on the top of the welded joint, where the tool shoulder was in contact. This is certainly the hottest spot of the weld and thus possibly the weakest part of the joint (except if a good Mg and Si alloying element dissolution favors GP zone formation). Lastly, one effect that has been noted in hardness measurements is the higher hardness values the stir zone reaches in AA6061 at higher rotational speed. Here this effect is visually confirmed by the 400 RPM samples on Figures IV.17(a,d), as they have strain localization inside their respective stir zone. It was hypothesized that the higher weld heat generated by the high rotational speed was sufficient enough to completely dissolve the alloying elements of AA6061 and reform GP zones that would then naturally age to a T4 state. The strain maps between low and high rotational speed tend to support this conclusion.

Based on the previous analysis and what Figures IV.13(d,f) show, it is only logical to further analyze the effect of advancing speed on the UTS and the elongation at failure.

Figures IV.21(a,b,c) show strain maps when reaching the UTS measured in the stir zone of 400 RPM welds at 7 kN for various advancing speeds. On all three welds, the failure occurred at the boundary between the TMAZ and the HAZ, where previously strain localization has been observed at the apparent yield strength. On Figure IV.13(d), the UTS for 400 RPM welds is shown to be lower than other rotational speeds. Localization in the AS HAZ is relatively strong for Figures IV.21(a,b) and significantly higher for Figures IV.21(c). At 80 and 100mm/min, the stir zone appears to have plasticized under the load. However it is clear that an increase in advancing speed leads to a stronger strain localization in the HAZ and thus, a lower plastic strain in the stir zone. Interestingly, Figure IV.13(f) shows that these welded joints have the highest elongation at failure of all the tested samples, for their respective advancing speed. As explained with the tensile

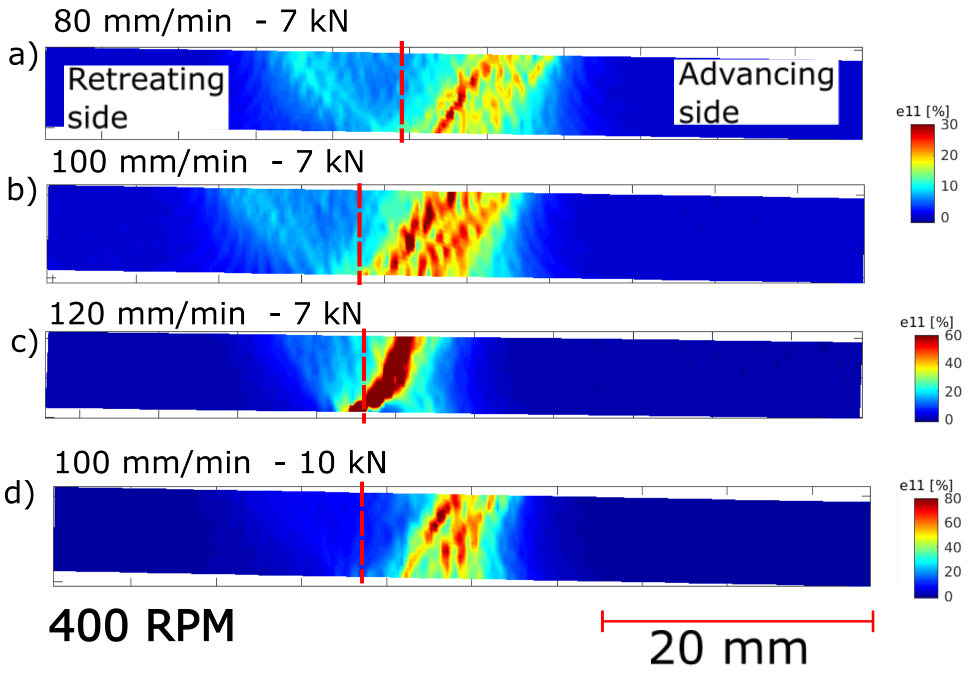

Figure IV.21: DIC maps of $e_{11}(\%)$ at the UTS in the stir zone of AA6061 400 RPM welds with the following welding parameters: (a) 80 mm/min and 7 kN, (b) 100 mm/min and 7 kN, (c) 120 mm/min and 7 kN and (d) 100 mm/min and 10 kN.

DIC maps at reach of the apparent yield strength, this effect could be explained by a larger notch in the plasticaly deformed zone. Overall, an increase in advancing speed generates a decrease in elongation at failure. The Figure IV.21(d) of a 10 kN welded joint shows a strongly heterogeneous strain localization with the HAZ of the joint. Table IV.2 shows that this sample has the lowest UTS of all the tested joints.

Figures IV.22(a,b,c) present the strain maps at the UTS of 600 RPM AA6061 joints at 6 kN for various advancing speeds. On Figure IV.22(a), one can notice that the strain localized on the boundary of the TMAZ/HAZ on the retreating side, contrary to the welds presented in Figures IV.22(b,c). The stir zone between the samples has accumulated plastic deformation to comparable absolute values. The main difference between the presented welds appears to be the absolute strain value the fracture area reached. Figure IV.13(d) shows that 600 RPM welds increase their UTS as the rotational speed increases. On Figure IV.22(a), the fracture occurred in the RS. Hardness measurements plotted in Figure IV.8(b) show that the 600 RPM, 6 kN and 80 mm/mn weld has an asymmetrical hardness profiles, where the hardness minimum value of the RS is reached 5 mm into the RS, compared to 10 mm in the AS. The narrow hardness minimum in the RS of the HAZ appear to be linked to the fracture localization observed here. Finally, the high axial load used in the manufacturing of Figure IV.22(d) does not appear to have an effect on its mechanical properties or strain distribution.

Figures IV.23(a,b,c) show the strain maps obtained during the tensile testing of 800 RPM welds at 5 kN for various advancing speeds. First, it can be noted that the sample depicted on Figure IV.23(c) broke in the RS of the weld. However, when comparing its hardness curves with other 800 RPM samples (see Figure IV.8(c)), it is not possible to reach any conclusion on the failure location relative to the hardness. Similarly to 400 and 600 RPM samples, the UTS increases as the advancing speed increases. The elongation

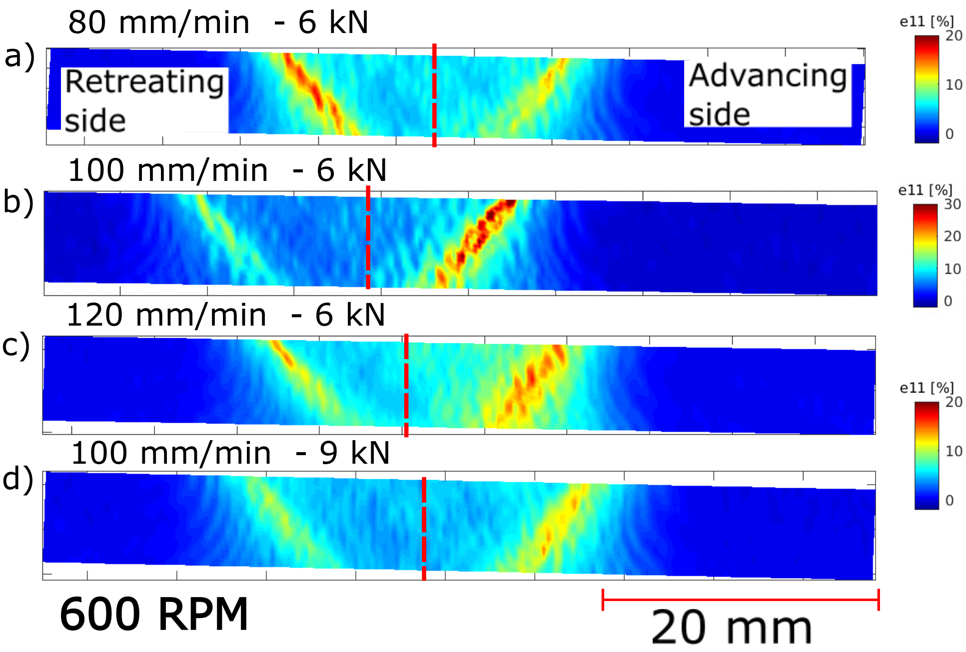

Figure IV.22: DIC maps of $e_{11}(\%)$ at the UTS in the stir zone of AA6061 600 RPM welds with the following welding parameters: (a) 80 mm/min and 6 kN, (b) 100 mm/min and 6 kN, (c) 120 mm/min and 6 kN and (d) 100 mm/min and 9 kN.

at failure across the 800 RPM welds is not affected by the advancing speed.

Finally, on Figures IV.24(a,b,c), three strain maps of 1000 RPM welds are shown. The strain map on Figure IV.24(a) has broken on its retreating side. However, in this case, this fracture location in the HAZ of the RS coincides perfectly with the lowest hardness value of this welded sample, as can be seen on Figure IV.8(d). A rather uncommon localization phenomena occurs in the 120 mm/min sample. However, it is explained by the Figure IV.25 showing a wormhole defect present in this weld. However, interestingly, this welded joint has a similar UTS compared to the other welds, as can be seen on Table IV.2.

The UTS value and elongation at failure for AA6061 similar welds appears to be influenced by the advancing speed. As it increases the UTS increases as well, but the elongation at failure decreases. One explanation could be a relationship with the HAZ width observed in the hardness measurements. It is thought that wider HAZ will have a larger notch effect on the plastic strain compared to a narrower one. Larger HAZ will be able to accommodate more overall strain. This would lead to poorer mechanical properties, but an increase in ductility. It is thought that such a phenomenon is responsible for the observed behavior in Figure IV.21, where the elongation at failure decreases with the advancing speed increase, i.e. smaller HAZ. Similarly, at 600 RPM, the 80 mm/min samples appears to have a similar behavior, whereas the local narrow area of minium hardness in the RS leads to the sample fracture in this area. Overall, a relationship between AA6061 mechanical tensile properties, strain localization and hardness profiles can be established. The precipitation mechanism explained during hardness testing is the same here, whereas the β precipitates dissolve due to heat in the HAZ and process parameters influence its precipitation in GP zone/coarsening after FSW.

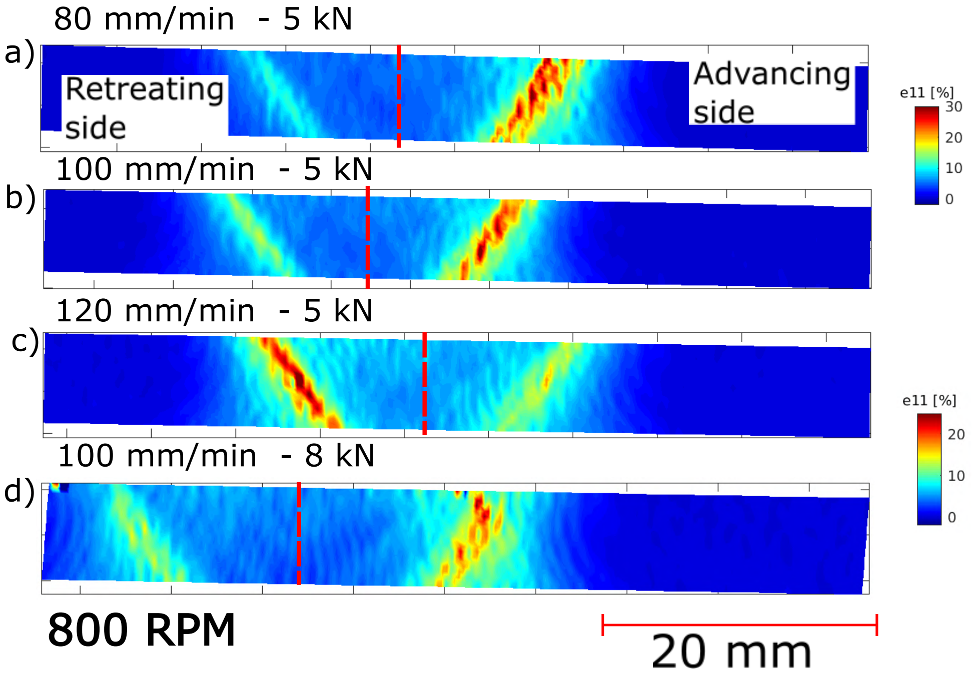

Figure IV.23: DIC maps of $e_{11}(\%)$ at the UTS in the stir zone of AA6061 800 RPM welds with the following welding parameters: (a) 80 mm/min and 5 kN, (b) 100 mm/min and 5 kN, (c) 120 mm/min and 5 kN and (d) 100 mm/min and 8 kN.

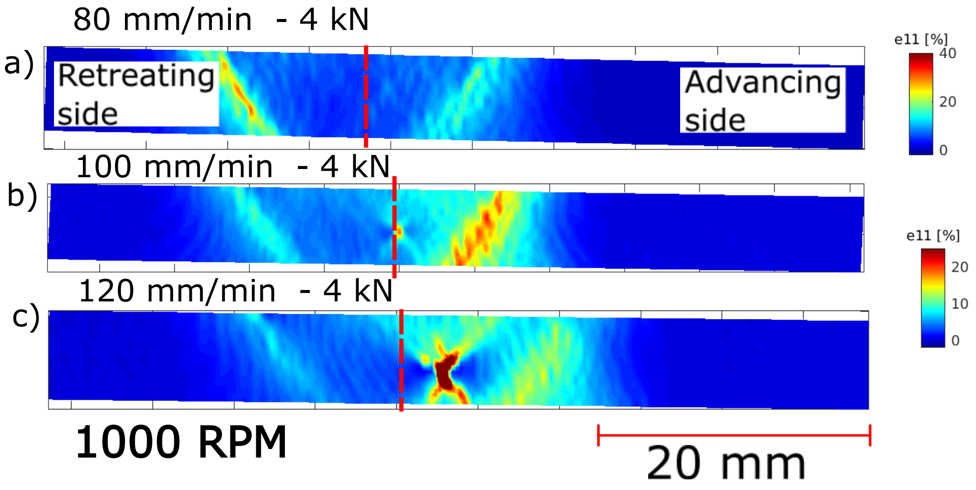

Figure IV.24: DIC maps of $e_{11}(\%)$ at the UTS in the stir zone of AA6061 1000 RPM welds with the following welding parameters: (a) 80 mm/min and 4 kN, (b) 100 mm/min and 4 kN and (c) 120 mm/min and 4 kN.

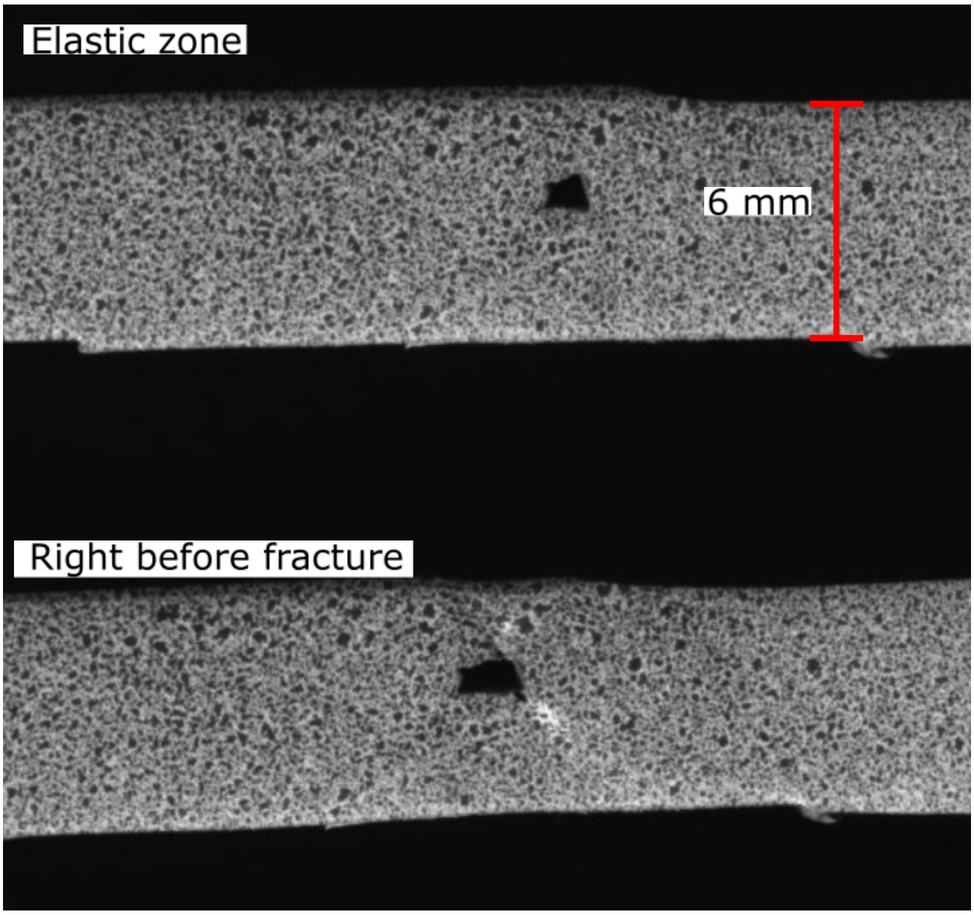

Figure IV.25: Pictures of the AA6061 similar 1000 RPM, 4 kN and 120 mm/min tensile sample. A wormhole defect if observed before and after the tensile test.

Axial load (kN)	**Rotational Speed (RPM)**	**Advancing Speed (mm / min)**	$Rp_{0.2}$ **(MPa)**	**UTS (MPa)**	ϵ_{11} **(%)**
5	800	100	/	115	8
6	600		/	63	/
7	400		/	61	/
8	800	80	316	333	0.6
		100	302	302	0.2
		120	/	74	/
9	600	80	300	435	4.1
		100	333	432	2.5
		120	334	349	0.2
10	400	80	316	435	4.1
		100	314	461	5.9
		120	344	383	0.5
10.5	300	80	299	432	5.3
		100	326	459	5.3
		120	326	326	0.1

Table IV.3: Weld parameters for AA7075 similar welding along with tensile results.

IV.3.A.ii AA7075 tensile results

For AA7075 similar welded samples, all tensile values are provided in Table IV.3.

Similarly to AA6061 tensile testing, the AA7075 samples cover a wide range of welding parameters. According to the same standard EN 485-2 [115] used for AA6061, the yield strength and UTS of a 6 mm thick AA7075-T6 plate are respectively 460 and 540 MPa. Its elongation at failure is 8%.

Figures IV.26(a,b) respectively show the start of yielding for AA7075 similar friction stir welded joints as a function of RPM and advancing speed. Variation in rotational speed does not have a strong influence on the apparent yield strength of such joints. For example, 80 mm/min joints on Figure IV.26(a) have an apparent yield strength ranging from 300 to 320 MPa, but overall the increase or decrease in rotational speed has no effect. On the other hand, Figure IV.26(b) shows a clear influence of the advancing speed on the apparent yield strength. Tensile data here shows that an increase in advancing speed, i.e. colder welds, leads to an increase in apparent yield strength, with the exception of 800 RPM welds.

Figures IV.26(c,d) respectively show the UTS values for AA7075 similar FSW joints, as a function of RPM and advancing speed. Contrary to what has been observed for the apparent yield strength, RPM has an influence here on the UTS of such joints. Indeed, an increase in rotational speed, i.e, hotter welds, leads to a decrease in UTS. However, interestingly, an inverse effect is noted for the influence of advancing speed on UTS. An increase in advancing speed, i.e. colder welds and narrower HAZ, leads to a decrease of UTS as well, seemingly in a contradictory way compared with the influence of rotational speed on the UTS.

Finally, Figures IV.26(e,f) respectively show the elongation at failure of AA7075 similar welded joints, as a function of rotational and advancing speed. Similarly to the influence of rotational speed on UTS, an increase in RPM, i.e. hotter welds, leads to a sharp decrease in elongation at failure. Additionally, the 120 mm/min samples have the overall lowest elongation at failure of all the welded samples, no matter the rotational speed of the welded joint. Regarding advancing speed, a similar contradictory description as with UTS can be made. As the advancing speed increases, i.e. colder welds and narrower HAZ, the elongation at failure decreases sharply. It can noted that no matter the advancing speed, the 800 RPM welds have overall low elongation at failure values compared with the other samples.

A similar approach as for AA6061 welded joints will be carried out in this Section. Tensile results with DIC strain maps at the reach of yielding and the UTS for various rotational speeds are provided for all the mechanically tested joints.

Figures IV.27(a,b,c) show the DIC strain maps at the start of yielding of 300 RPM and 10.5 kN AA7075 similar welds for 80, 100 and 120 mm/min advancing speed respectively. Localization of strain is visible in the TMAZ/HAZ of all samples, no matter the advancing speed. However, strain localizes in a "banding" pattern. It is unclear what phenomenon is causing this strain localization pattern. This kind of fringe pattern is reminiscent of a Moiré fringe interferometry pattern [142]. It can occur in DIC measurements when the marking used shows sign of regular pattern. However, AA6061 and AA7075 tensile samples were prepared in the exact same way, with the exact same paint application method, tested on the exact same tensile machine and using the exact same camera setup for image capture, and this kind of pattern has not been observed on the DIC strain maps of AA6061 welded joints. Ultimately, the global strain localization of these strain maps is coherent with the morphology of FSW joints and all low elongation strain maps show similar banding, thus, this effect is ignored when commenting strain localization regarding process parameters. Figure IV.26(b) showed an increase in yield strength for an advancing speed increase. DIC strain maps suggest that an increase in advancing speed leads to strain localizing closer to the middle of the weld. Coincidentally, hardness measurements for 300 RPM welds on Figure IV.12(a) show a significantly narrower HAZ for 120 mm/min welds, i.e. the coldest weld here. Generally speaking, the HAZ for AA7075 welds at 300 RPM is narrower for the coldest weld, and inversely the largest for the hottest weld. The strain map of this sample, on Figures IV.27(c), show similar strain localization pattern. However, the difference between 80 and 100 mm/min strain maps is minimal.

Figures IV.28(a,b,c) show the DIC strain maps at the start of yielding of 400 RPM and 10 kN AA7075 similar welds for 80, 100 and 120 mm/min advancing speed respectively. The 400 RPM, 100 mm/min and 7 kN sample is not shown here, as the data in Table IV.3 show that this sample broke almost immediately during tensile testing. The same banding effect as described on Figure IV.27 is visible here. Strain localizes in the HAZ/TMAZ in all samples, i.e. for all the advancing speed, in a similar way as described for 300 RPM welds. As the advancing speed increases, strain localized closer to the center of the weld. This phenomenon is noticeable when comparing the 80 and 120 mm/min samples. Similarly to 300 RPM welds, a wider HAZ for the 80 mm/min joint has been observed on the hardness profile of this joint on Figure IV.12(b). Again, these strain maps suggest that strain localizes in the HAZ of the sample at the start of yielding.

Figures IV.29(a,b,c) show the DIC strain maps at the start of yielding of 600 RPM and 9 kN AA7075 similar welds for 80, 100 and 120 mm/min advancing speed respectively. Similarly to 400 RPM joints, the 600 RPM, 100 mm/min and 6 kN joint is not shown here,

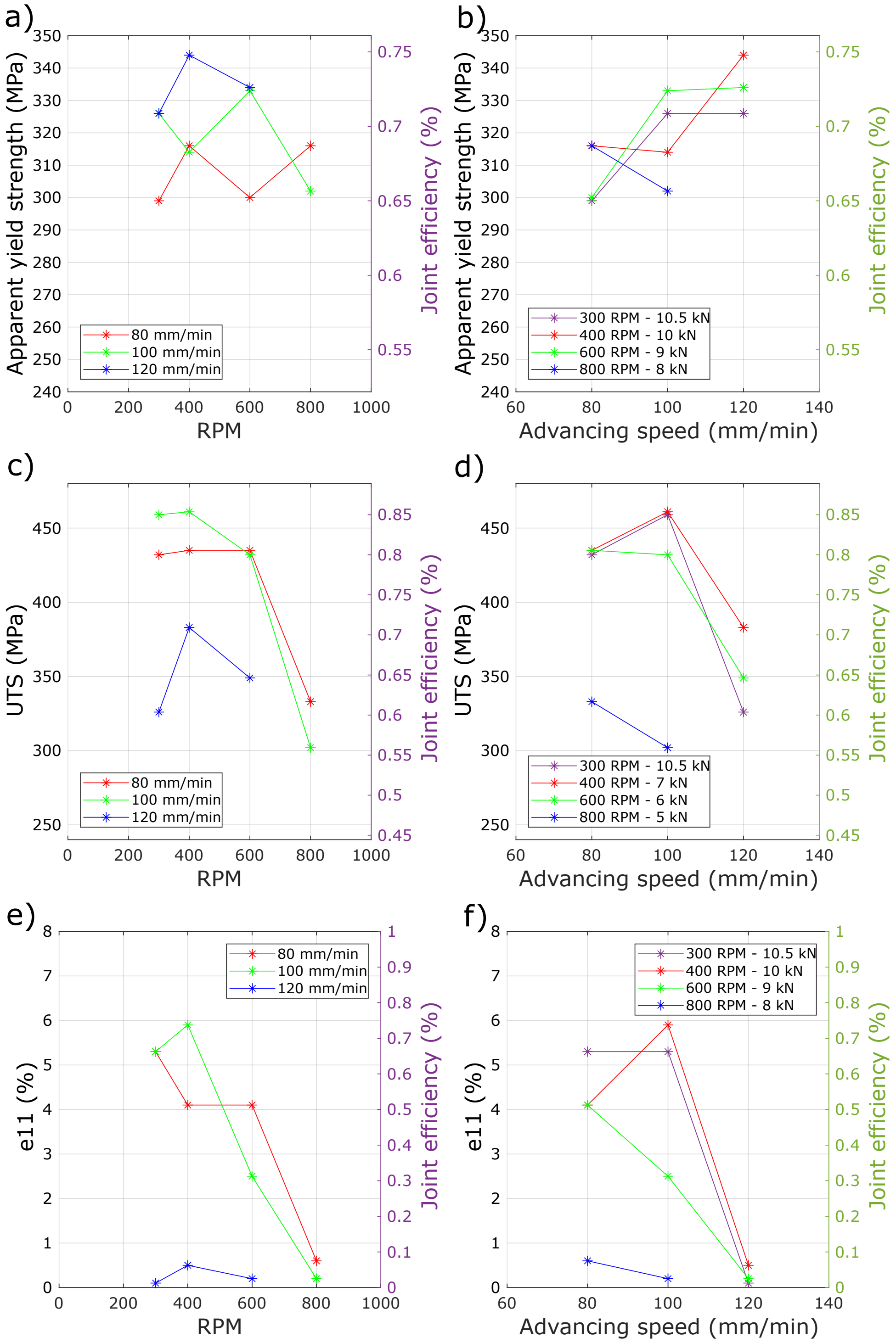

Figure IV.26: Tensile properties of friction stir welded similar AA7075 joints. Apparent yield strength as a function of RPM (a) and advancing speed (b). UTS as a function of RPM (c) and advancing speed (d). Elongation at failure as a function of RPM (e) and advancing speed (f). For a given RPM value, the axial load is identical. On all Figures, the joint efficiency is the ratio with the base material's mechanical properties.

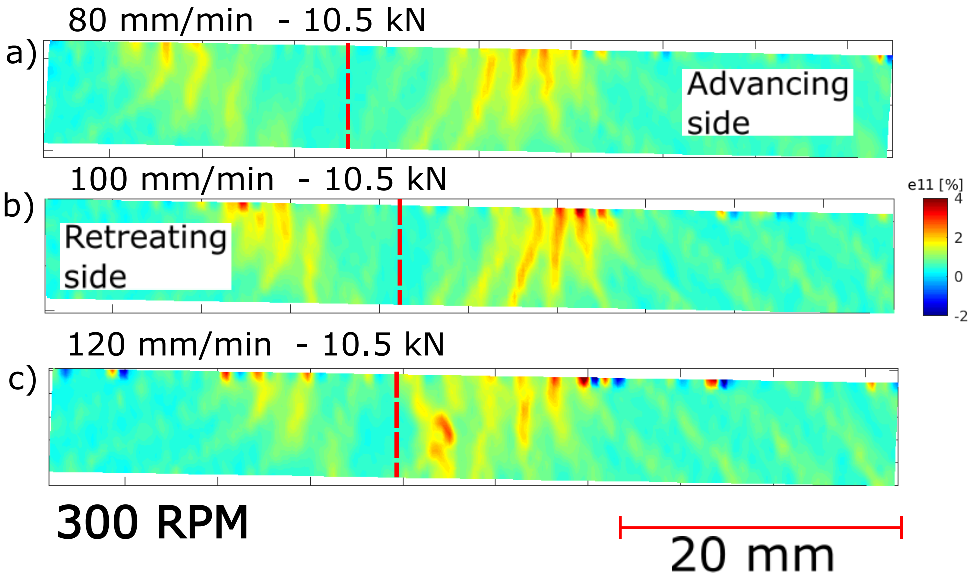

Figure IV.27: DIC strain maps of $e_{11}(\%)$ at reach of the apparent yield strength in the stir zone of AA7075 300 RPM welds with the following welding parameters: (a) 80 mm/min and 10.5 kN, (b) 100 mm/min and 10.5 kN and (c) 120 mm/min and 10.5 kN.

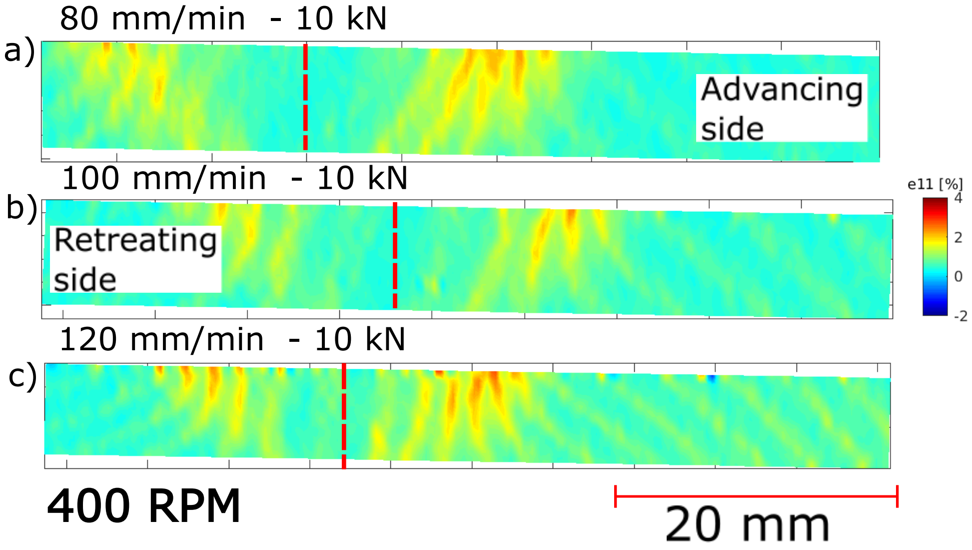

Figure IV.28: DIC strain maps of $e_{11}(\%)$ at reach of the apparent yield strength in the stir zone of AA7075 400 RPM welds with the following welding parameters: (a) 80 mm/min and 10 kN, (b) 100 mm/min and 10 kN and (c) 120 mm/min and 10 kN. The 400 RPM, 7 kN and 100 mm/min is not shown here as it broke instantly.

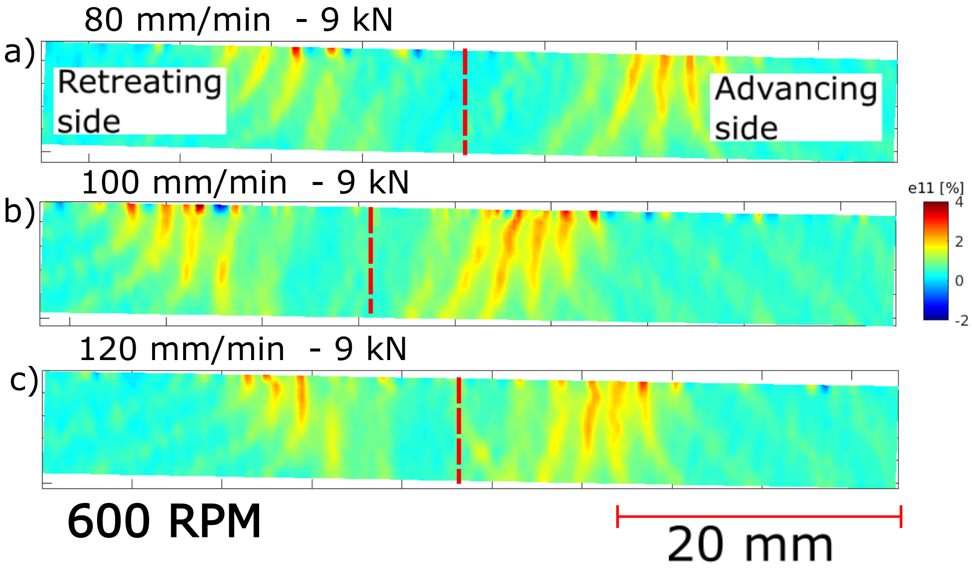

Figure IV.29: DIC strain maps of $e_{11}(\%)$ at reach of the apparent yield strength in the stir zone of AA7075 600 RPM welds with the following welding parameters: (a) 80 mm/min and 9 kN, (b) 100 mm/min and 9 kN and (c) 120 mm/min and 9 kN. The 600 RPM, 6 kN and 100 mm/min is not shown here as it broke instantly.

as tensile data in Table IV.3 show early failure during tensile testing. Similarly to 300 and 400 RPM samples, the DIC strain maps show strain localization closer to the center of the weld as the advancing speed increases. The hardness measurements for 600 RPM joints, presented on Figure IV.12(c), show a significantly wider HAZ for the 80 mm/min sample compared with 100 and 120 mm/min samples. Additionally, Figure IV.26(b) show that the 80 mm/min, i.e. the hottest weld of 600 RPM joints, has one of the lowest yield strength of all the AA7075 FSW joints. The strain localization on Figure IV.29(a) is located the furthest from the center of the weld. Coincidentally, the same pattern is observed for hardness measurements.

Finally, Figures IV.30(a,b) show the DIC strain maps at the start of yielding of 800 RPM AA7075 similar welds for 80 and 100 mm/min advancing speed respectively. Two 800 RPM samples (100 mm/min and 5 kN, 120 mm/min and 8 kN) are not shown here, as tensile data in Table IV.3 shows early failure during tensile testing. The strain maps of the two 800 RPM samples are relatively similar. The only visible difference is the higher apparent strain values in the 80 mm/min sample compared to the 100 mm/min sample. However, hardness measurements on Figure IV.12(d) show that these two different samples have similarly sized HAZ, with comparable hardness value. Figure IV.26(b) shows a slight decrease in apparent yield strength as the advancing speed increases. The strain distribution evolution with the advancing speed could be tied with this decrease in apparent yield strength. However, 300 RPM and 10.5 kN and 600 RPM and 9 kN samples have lower absolute apparent yield strength at 80 mm/min compared to the 800 RPM and 8 kN sample, and do not show similar strain localization value in their respective strain maps.

Overall, strain localization at the start of yield in AA7075 FSW joints occurs at the location of the minimum hardness value, in the HAZ. For all samples, strain localization has been observed in both HAZ, i.e. advancing and retreating side. Contrary to AA6061 FSW joints, no localization has been observed in the stir zone. Hardness profiles for these

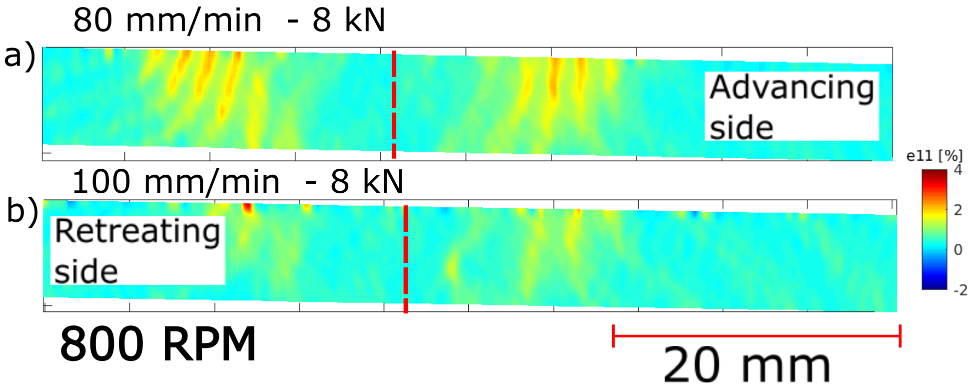

Figure IV.30: DIC strain maps of $e_{11}(\%)$ at reach of the apparent yield strength in the stir zone of AA7075 800 RPM welds with the following welding parameters: (a) 80 mm/min and 8 kN and (b) 100 mm/min and 8 kN. The 800 RPM, 5 kN and 100 mm/min and 8 kN and 120 mm/min samples are not shown here as they broke instantly.

joints on Figure IV.12 show clear correlation between the hardness minimum point, the HAZ width and strain localization area in all samples. In Section IV.2.A, the influence of the η hardening precipitates on the local hardness of AA7075 has been explained. Generally speaking, this hardening precipitate is highly sensitive to temperature and especially cooling rate, i.e. advancing speed. As these precipitates are major contributors in mechanical properties and in turn, local hardness values, the strain localization pattern observed is coherent with this explanation.

Figures IV.31(a,b,c) show strain maps when reaching the UTS measured in the stir zone of 300 RPM welds at 10.5 kN for various advancing speeds for AA7075 joints. The three strain maps shown here have widely different strain distribution. On Figure IV.31(a), the strain localized in the HAZ of both the AS and RS to similar strain values. The stir zone has accumulated some plastic deformation. On Figure IV.31(b), the stir zone reached a higher plastic strain value compared to the 80 mm/min weld and the HAZ of the AS shows the maximum strain. Finally, Figure IV.31(c) shows overall low plastic deformation and no significant difference is noted with the strain map obtained at the apparent yield strength, which in turn is logically explained by data in Table IV.3 that indicates that the apparent yield strength and UTS for this sample are identical. Between Figure IV.31(a) and Figure IV.31(b), UTS value increases with the advancing speed, and the elongation at failure is almost identical. The higher UTS be related with the higher plastic strain values in the AS HAZ of the 100 mm/min sample. Regarding hardness measurements on Figure IV.12(a), the strain localization at UTS in the HAZ of both samples is clearly visible.

Figures IV.32(a,b,c) show strain maps when reaching the UTS measured in the stir zone of 400 RPM welds at 10 kN for various advancing speeds for AA7075 joints. Similarly to 300 RPM joints, three widely different strain maps are obtained. However, interestingly, Figure IV.32(b) shows stronger strain localization in both the HAZ of the 100 mm/min sample compared with the strain maps of the 80 mm/min sample on Figure IV.32(a). Figures IV.26(d,f) shows an increase in UTS value when increasing the advancing speed as well as a significant increase in elongation at failure. Similarly to 300 RPM samples, high strain localization in the HAZ is seemingly related to higher UTS values and in this

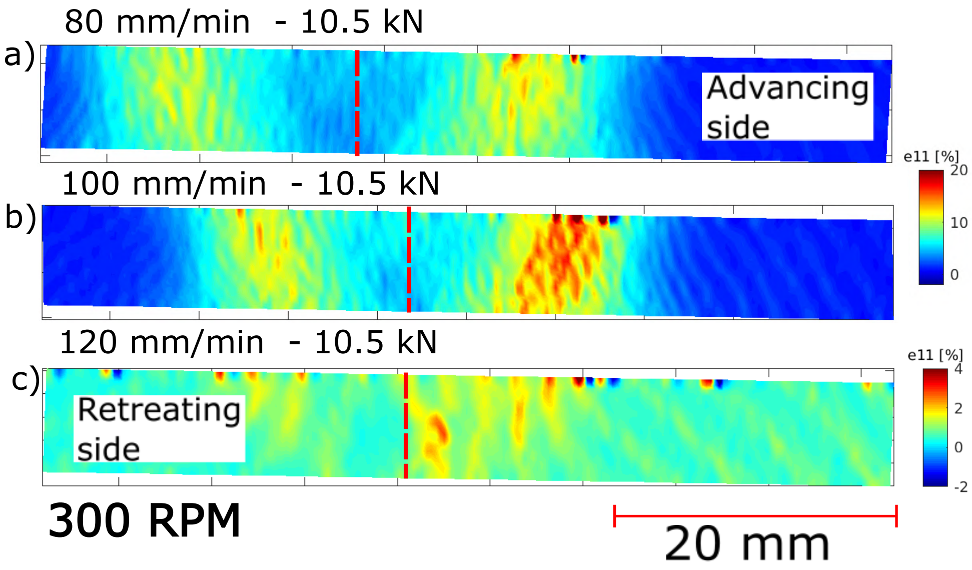

Figure IV.31: DIC strain maps of $e_{11}(\%)$ at the UTS in the stir zone of AA7075 300 RPM welds with the following welding parameters: (a) 80 mm/min and 10.5 kN, (b) 100 mm/min and 10.5 kN and (c) 120 mm/min and 10.5 kN.

case, higher elongation at failure.

Figures IV.33(a,b,c) show strain maps when reaching the UTS measured in the stir zone of 600 RPM welds at 9 kN for various advancing speeds for AA7075 joints. In this instance, Figure IV.26 shows a slightly lower UTS value for 100 mm/min compared with 80 mm/min sample, as well as a sharply lower elongation at failure. Interestingly, the elongation at failure appears to be related to a strong strain localization phenomenon in the HAZ, similarly to what has been described for 300 and 400 RPM samples.

Figures IV.34(a,b) show strain maps when reaching the UTS measured in the stir zone of 600 RPM welds at 9 kN for various two speeds for AA7075 joints. The strain maps of 800 RPM welds at UTS show little to no difference with those at the apparent yield strength on Figure IV.30. Figure IV.26(e) shows particularly poor elongation at failure for 800 RPM samples. These samples have a fragile tensile behavior. Figure IV.34(a) only shows a slight increase in strain localization value when compared with the strain maps at apparent yield strength.

Overall, it appears that tensile behavior of AA7075 joints are more heterogeneous in nature compared to AA6061 joints. Hardness measurements analysis performed on AA7075 similar welds in Section IV.2.A yielded that advancing speed increase, i.e. faster cooling rate, resulted in a narrower HAZ width along with the probable coarsening of η precipitates in the HAZ of these joints, based on the research of M. Lezaack [120]. Interestingly, this narrower HAZ is here related to lower values of UTS as well as a stronger strain localization phenomenon in the HAZ of 300 and 400 RPM welds. In turn, similarly to what has been described in AA6061 welds tensile behavior, a narrower HAZ leads to a stronger notch effect and a lower ductility.

IV.3.B Al/Al dissimilar welding

Finally, AA6061/AA7075 dissimilar joints tensile properties have been determined, similarly to AA6061 and AA7075 similar welding. Table IV.4 shows the raw data from tensile

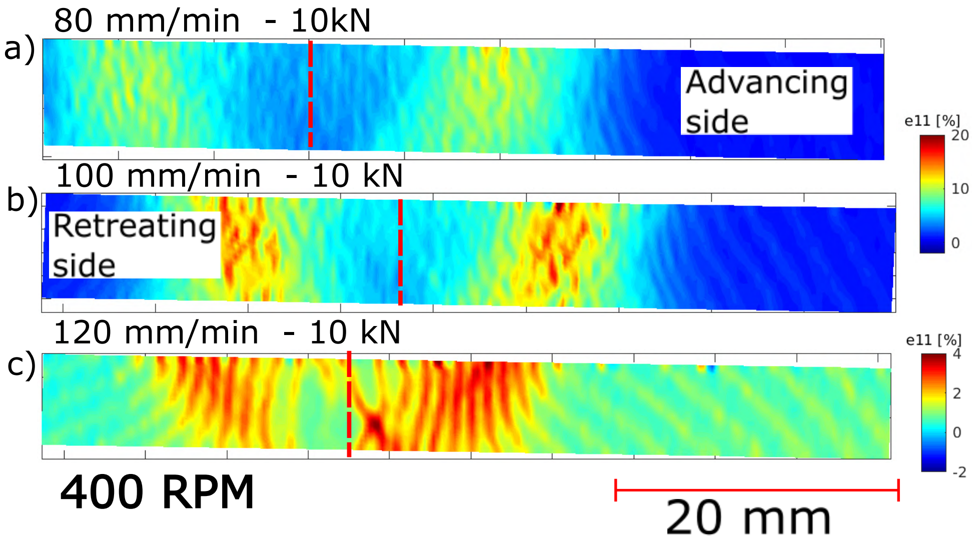

Figure IV.32: DIC strain maps of $e_{11}(\%)$ at the UTS in the stir zone of AA7075 400 RPM welds with the following welding parameters: (a) 80 mm/min and 10 kN, (b) 100 mm/min and 10 kN and (c) 120 mm/min and 10 kN. The 400 RPM, 7 kN and 100 mm/min is not shown here as it broke instantly.

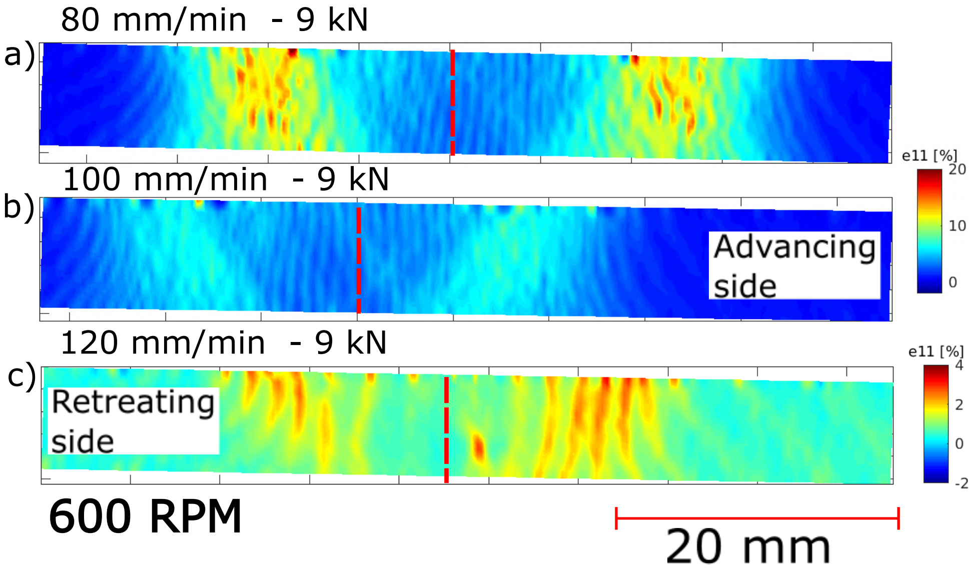

Figure IV.33: DIC strain maps of $e_{11}(\%)$ at the UTS in the stir zone of AA7075 600 RPM welds with the following welding parameters: (a) 80 mm/min and 9 kN, (b) 100 mm/min and 9 kN and (c) 120 mm/min and 9 kN. The 600 RPM, 6 kN and 100 mm/min is not shown here as it broke instantly.

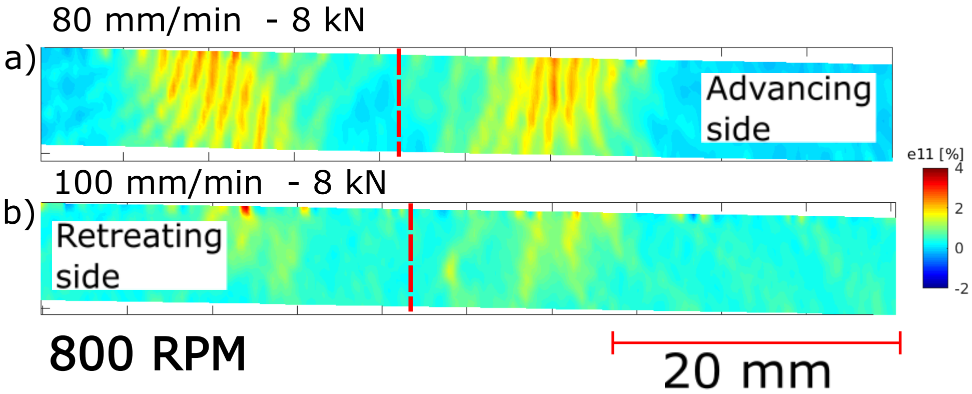

Figure IV.34: DIC strain maps of $e_{11}(\%)$ at the UTS in the stir zone of AA7075 800 RPM welds with the following welding parameters: (a) 80 mm/min and 8 kN and (b) 100 mm/min and 8 kN. The 800 RPM, 5 kN and 100 mm/min and 8 kN and 120 mm/min samples are not shown here as they broke instantly.

testing on dissimilar FSW joints.

Figures IV.35(a,b) respectively show the apparent yield strength of the dissimilar welded joints, as a function of rotational and advancing speed. In both cases, no clear influence from either parameters can be noted on the apparent yield strength. In both instances of AA6061 and AA7075 welding, no clear influence of process parameters on apparent yield strength has been noted on Figures IV.13(a,b) and Figure IV.26(a,b) for AA6061 and AA7075 respectively.

Figures IV.35(c,d) show the UTS of these dissimilar joints regarding rotational and advancing speed, respectively. No significant effect of the rotational speed on UTS can be noted. For example, an increase in rotational speed on 80 mm/min samples from 400 RPM to 600 RPM yielded a slight increase in UTS, whereas all other variations are either constant, or minute increases or decreases from one rotational speed to the other. For similar AA6061 welds, a slight decreasing trend can be noted on Figure IV.13(c) for high rotational speed. On the other hand, Figure IV.26(c) regarding similar AA7075 welds show a clear decrease of UTS with an increase in rotational speed. The dissimilar joint does not appear to have similar trends compared to its base materials regarding the impact of RPM on UTS. On the other hand, Figure IV.35(d) shows a clear effect of advancing speed increase on the UTS, i.e. an increase in advancing speeds yields an increase in UTS. Similarly, the same effect can be observed for AA6061 similar welds in Figure IV.13(d). However, regarding AA7075 similar welds, Figure IV.26(d) shows a clear decrease of UTS for high advancing speeds.

Finally, Figure IV.13(e,f) shows the elongation at failure for AA6061/AA7075 dissimilar welds, as a function of rotational and advancing speeds. Both rotational and advancing speeds increases seemingly lead to a minute increase in elongation at failure. In AA6061 similar welding, Figures IV.13(e,f) show a downward trend in elongation at failure as both rotational and advancing speeds increase. However, the absolute value of elongation at failure is much higher at low RPM for similar AA6061 joints compared to dissimilar joints. On the other hand, as for AA7075 similar welding, Figures IV.26(e,f) show a clear degradation of elongation at failure for either a rotational of advancing speed increase.

Overall, the global tensile behavior of dissimilar AA6061/AA7075 joints appears to be primarily related to that of the AA6061. This result is coherent with previous observations

Axial load (kN)	**Rotational Speed (RPM)**	**Advancing Speed (mm / min)**	$Rp_{0.2}$ **(MPa)**	**UTS (MPa)**	ϵ_{11} **(%)**
10	400	80	153	192	4.1
		100	153	209	4
		120	140	212	5.1
9	600	80	139	199	4
		100	145	205	4
		120	145	210	5.4
8	800	80	149	199	5.3
		100	137	208	4.8
		120	126	211	5.6
9	400	100	170	208	2.3
8			161	205	1.9
8	600		183	211	2.6
10	800		171	192	3.5

Table IV.4: Aluminium dissimilar welding parameters and tensile results.

from the literature, specifically regarding AA6061/AA7075 assemblies [86, 93]. Guo et al. [86] reach similar joint efficiency values in their dissimilar assemblies, while considering a slightly high UTS value for their base material. This tensile behavior is rather logical, as the clearly weakest material dictates the tensile properties of the welded joint. The assembly then has a "weakest link" behavior regarding this dissimilar weld. Similarly to what has been carried out for both similar AA6061 and AA7075 joints, DIC strain maps have been obtained for all samples at two specific moment during a tensile test: at reaching of the apparent start of yielding and at the UTS.

Figures IV.36(a,b,c,d,e) show the DIC strain maps at the start of yielding of 400 RPM dissimilar welds for 80, 100 and 120 mm/min advancing speed and various axial load. Clearly, all samples show a similar behavior, where the strain localizes in the HAZ of the AA6061, on the advancing side. At 10 kN, plastic strain can also be noted inside the stir zone. Interestingly, the plastic strain value of the stir zone decreases as the advancing speed increases. On Figure IV.35(b), no significant difference in apparent start of yield value was observed relative to the advancing speed. Generally speaking, the overall strain concentration values appear to decrease as the rotational speed increases. Indeed, the strain value in the HAZ of Figure IV.36(a) is lower compared to that of Figure IV.36(c). Additionally, the absolute value of the strain in Figure IV.36(a) is rather high by itself, at almost 4%. Finally, at a constant advancing speed, Figures IV.36(b,d,e) appear to show a decrease in strain concentration when the axial load decreases. All the observations here tend to lead to the conclusion that a lower heat input would lead to less strain concentration in the HAZ of the AA6061.

Figures IV.37(a,b,c,d) show the DIC strain maps at the start of yielding of 600 RPM dissimilar welds for 80, 100 and 120 mm/min advancing speed and various axial load. On Figure IV.37(c), the stir zone is absent from the DIC strain maps as a misplacement of the tensile sample occurred. Generally, no significant difference between the Figures IV.37(a,b,c) can be noted. The strain localization in the HAZ of the AA6061

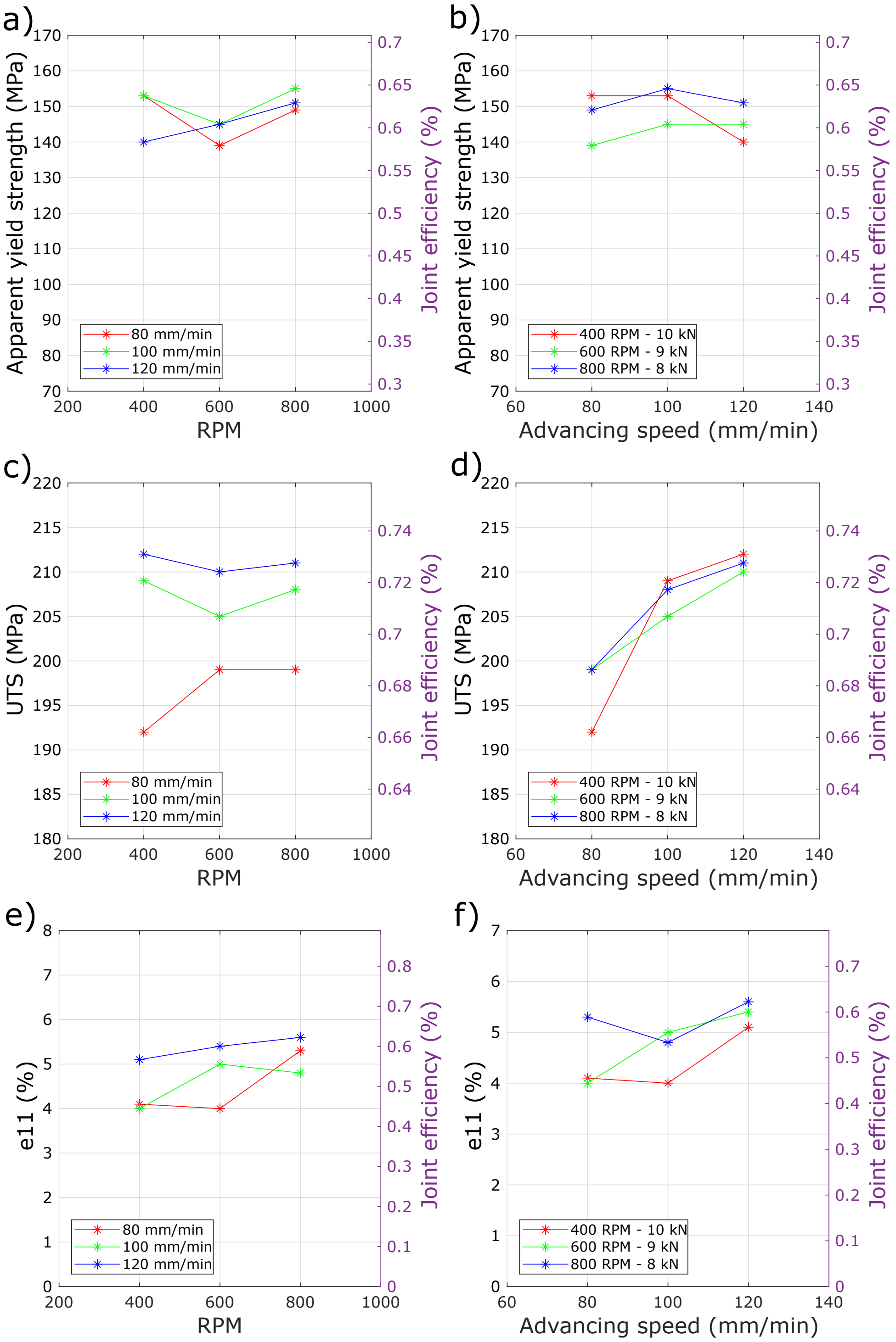

Figure IV.35: Tensile properties of friction stir welded dissimilar AA6061-AA7075 joints. Apparent yield strength as a function of RPM (a) and advancing speed (b). UTS as a function of RPM (c) and advancing speed (d). Elongation at failure as a function of RPM (e) and advancing speed (f). For a given RPM value, the axial load is identical. On all Figures, the joint efficiency is the ratio with the AA6061's mechanical properties.

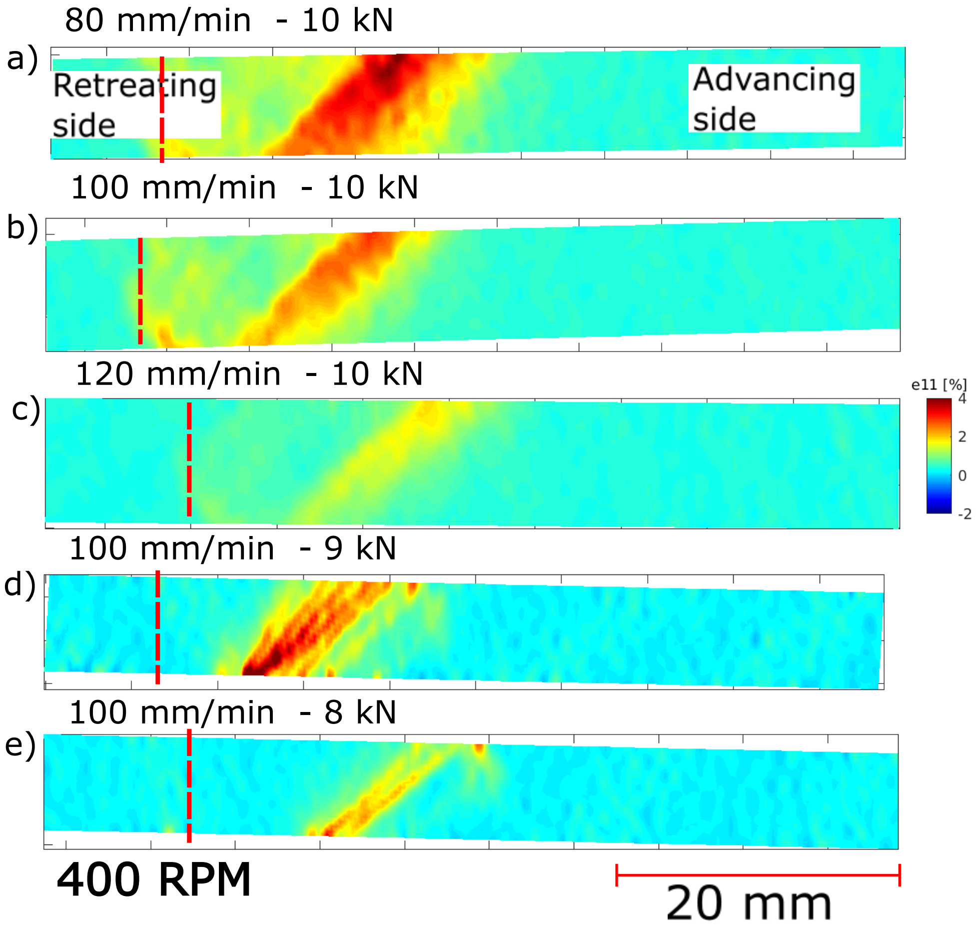

Figure IV.36: DIC strain maps of $e_{11}(\%)$ at the apparent yield strength in the stir zone of AA7075/AA6061 dissimilar welds at 400 RPM welds with the following welding parameters: (a) 80 mm/min and 10 kN, (b) 100 mm/min and 10 kN, (c) 120 mm/min and 10 kN, (d) 100 mm/min and 9 kN and (e) 100mm/min and 8 kN.

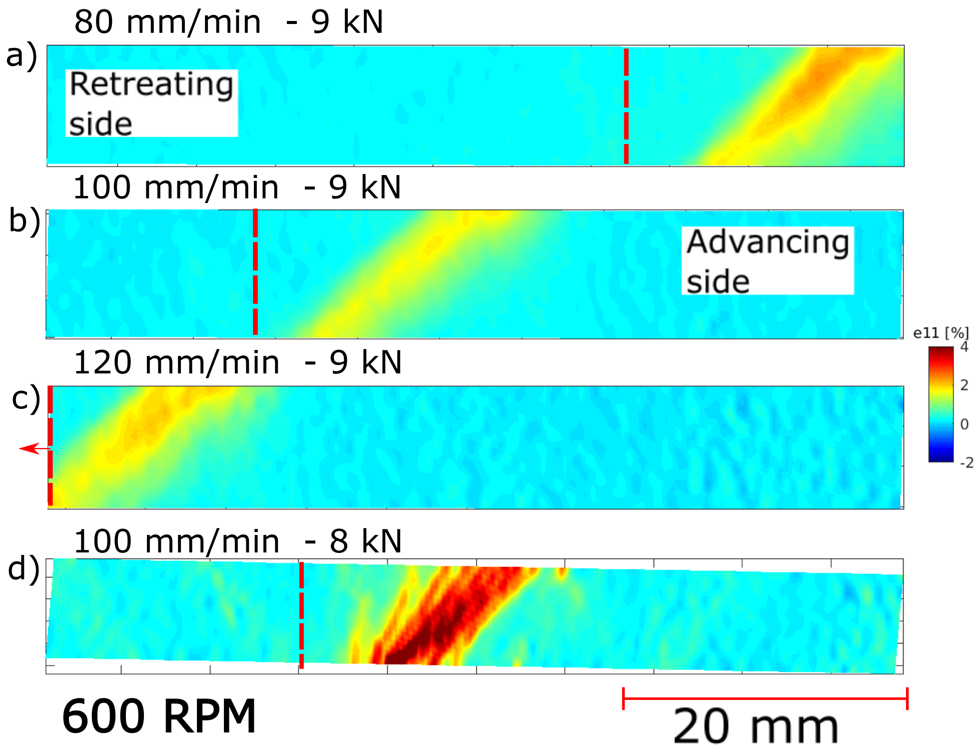

Figure IV.37: DIC strain maps of e_{11}(%) at the apparent yield strength in the stir zone of AA7075/AA6061 dissimilar welds at 600 RPM welds with the following welding parameters: (a) 80 mm/min and 9 kN, (b) 100 mm/min and 9 kN, (c) 120 mm/min and 9 kN and (d) 100 mm/min and 8 kN. Sample (c) was misplaced and this, the information on stir zone plastic deformation is missing.

is generally similar, and lower when compared with strain values of 400 RPM samples. Additionally, stir zone strain values decrease between 400 and 600 RPM sample. This observation is rather interesting. Indeed, hardness measurements on Figure IV.11 show the impact of RPM increase in dissimilar welds. It has been shown that an increase in rotational speed leads to an increase in stir zone hardness for all advancing speeds. The decrease in stir zone strain values from 400 to 600 RPM is correlated to the increase in hardness value inside the stir zone. Finally, lowering the axial load at a constant advancing speed of 100 mm/min lead to higher strain in the HAZ of the AA6061. However in this case, no clear relationship between HAZ hardness values and strain HAZ values have been noted.

Figures IV.38(a,b,c,d) show the DIC strain maps at the start of yielding of 800 RPM dissimilar welds for 80, 100 and 120 mm/min advancing speed and various axial load. For all strain maps shown here, the strain localizes in the HAZ of the AA6061. For a given axial load of 8 kN, an increase in advancing speed lead to a decrease in strain localization value in the HAZ, similarly to what has been observed on Figure IV.36 for 400 RPM dissimilar welds. Similarly to what has been observed on 600 RPM samples on Figure IV.37, the strain value inside the stir zone is lower when compared to 400 RPM samples. Again, hardness measurements on Figure IV.11 show a clear increase in stir zone hardness as the rotational speed increases. Finally, an axial load increase from 8 kN to 10 kN at 100 mm/mn appears to lead to a higher strain localization value in the stir zone, contrary to what has been observed on 600 RPM samples.

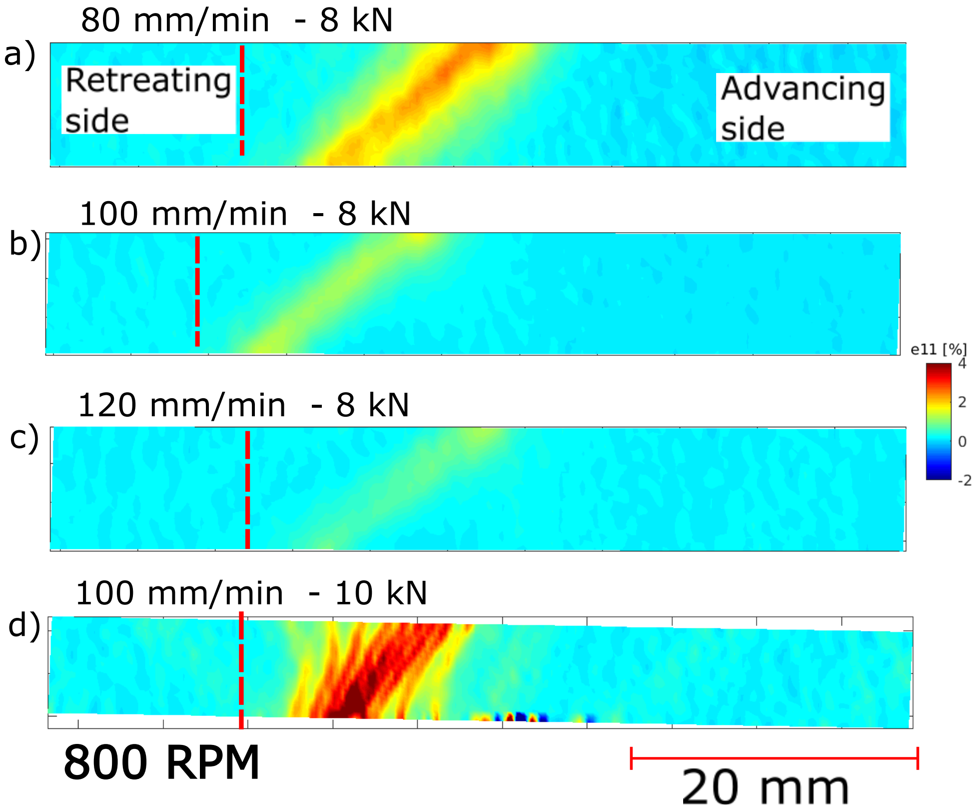

Figure IV.38: DIC strain maps of $e_{11}(\%)$ at the apparent yield strength in the stir zone of AA7075/AA6061 dissimilar welds at 800 RPM welds with the following welding parameters: (a) 80 mm/min and 8 kN, (b) 100 mm/min and 8 kN, (c) 120 mm/min and 8 kN and (d) 100 mm/min and 10 kN.

Overall, at the reach of apparent start of yield, all samples show strain localization in the HAZ of the AA6061, placed here on the advancing side. Hardness measurements for all samples have shown a minimum hardness value in said HAZ of the AA6061. The strain localization is here related to the local hardness minimum value. When discussing hardness measurements for dissimilar welding and AA6061 similar welding, this hardness minimum was explained by the coarsening of the β hardening precipitates of AA6061 in the HAZ. Additionally, strain also localizes in the stir zone of 400 RPM samples, which have been shown to have lower hardness values in their stir zones on Figure IV.11 compared to other rotational speed. This was explained by the maximum temperature reached inside the welded joint. As the temperature increases with the rotational speed, some β hardening precipitates are dissolved back inside the Al matrix instead of coarsening, leading to formation of GP zones and subsequent increase in hardness values. No significant difference in apparent yield strength have been shown on Figure IV.35(b). However, a strong relationship between an increase in advancing speed and UTS has been noted on Figure IV.35(d). The heterogeneous strain localization values observed here, at the apparent start of yield, could already explain trends later observed in UTS. To investigate this phenomenon further, strain maps at UTS for all dissimilar samples are described.

Figures IV.39(a,b,c,d,e) show the DIC strain maps at the UTS of 400 RPM dissimilar welds for 80, 100 and 120 mm/min advancing speed at various axial load. All samples exhibit strong strain localization in the HAZ of the AA6061, and some stir zone strain localization as well. No significant difference can be observed as the advancing speed increases. Lower axial loads do not appear to have a significant influence on the strain localization in the HAZ of the AA6061, but show lower stir zone strain values.

Figures IV.39(a,b,c,d) show the DIC strain maps at the UTS of 600 RPM dissimilar welds for 80, 100 and 120 mm/min advancing speed and various axial load. Similarly to what has been observed for 400 RPM dissimilar welds, no significant difference in HAZ strain values are noted across the various advancing speeds. However, the strain value in the stir zone appears to be lower when compared with strain zone values of 400 RPM dissimilar welds. This stir zone strain decrease was noted at the apparent start of yield between 400 and 600 RPM samples as well. Higher hardness values in the stir zone once again appear to be related to this decrease in stir zone strain.

Finally, Figures IV.39(a,b,c,d) show the DIC strain maps at the UTS of 800 RPM dissimilar welds for 80, 100 and 120 mm/min advancing speed and various axial load. Similarly to what has been described for 400 and 600 RPM samples, increase in advancing speed do not appear to have a noticeable effect on strain localization. However, similarly to what has been described in 600 RPM samples regarding the stir zone strain value, the lower stir zone strain value when compared with the 400 RPM samples on Figure IV.39 were already observed at reach of the apparent yield strength and related to hardness measurements.

Generally speaking, the strain localization at UTS in dissimilar joints appears to be the continuation of phenomenon observed at the apparent start of yield. The stir zone localization at low rotational speed has been linked to lower hardness measurements, in turn related to the β hardening precipitation and coarsening. Strain localized in the HAZ of the AA6061, the lowest hardness value in all samples. Interestingly, the increase in UTS related to an increase in advancing speed was not particularly visible on UTS strain maps. However, a clear relationship between HAZ strain localization values and an increase in advancing speed when reaching the apparent start of yield has been shown previously.

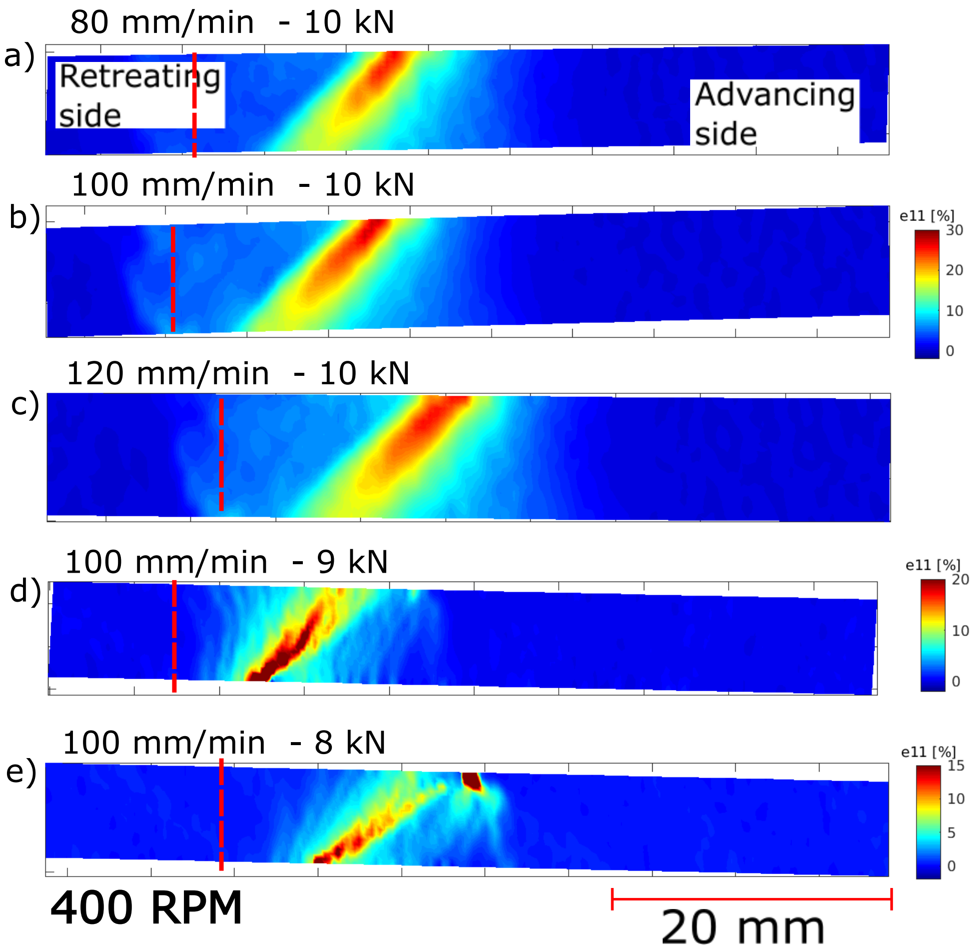

Figure IV.39: DIC strain maps of $e_{11}(\%)$ at the UTS in the stir zone of AA7075/AA6061 dissimilar welds at 400 RPM welds with the following welding parameters: (a) 80 mm/min and 10 kN, (b) 100 mm/min and 10 kN, (c) 120 mm/min and 10 kN, (d) 100 mm/min and 9 kN and (e) 100mm/min and 8 kN.

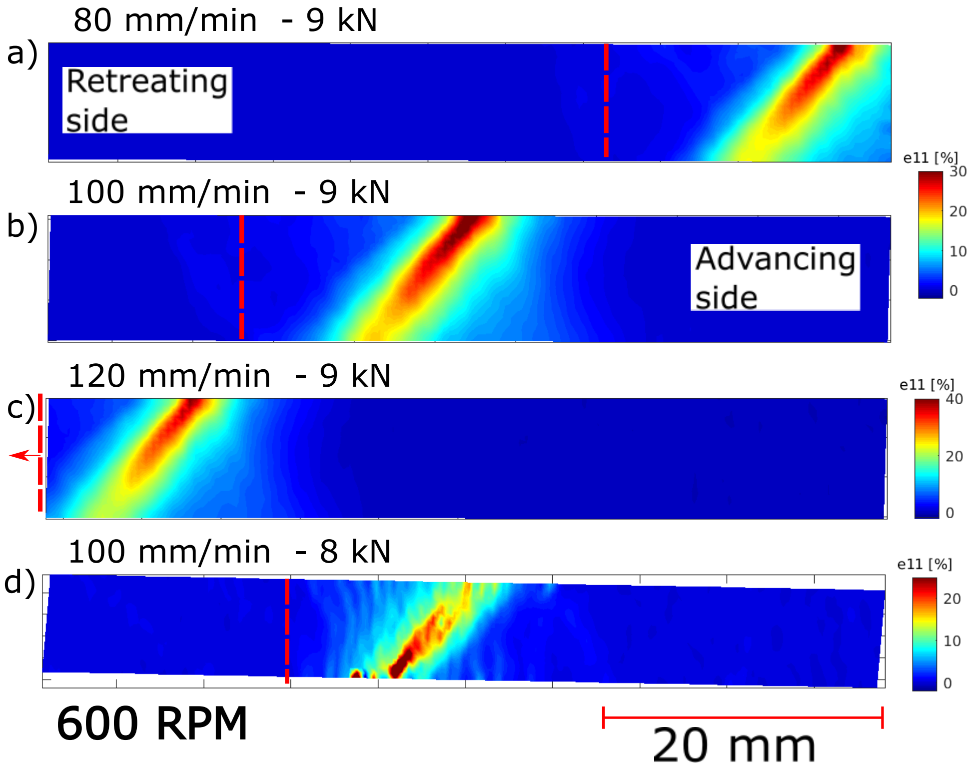

Figure IV.40: DIC strain maps of $e_{11}(\%)$ at the UTS in the stir zone of AA7075/AA6061 dissimilar welds at 600 RPM welds with the following welding parameters: (a) 80 mm/min and 9 kN, (b) 100 mm/min and 9 kN, (c) 120 mm/min and 9 kN and (d) 100 mm/min and 8 kN. Sample (c) was misplaced and this, the information on stir zone plastic deformation is missing.

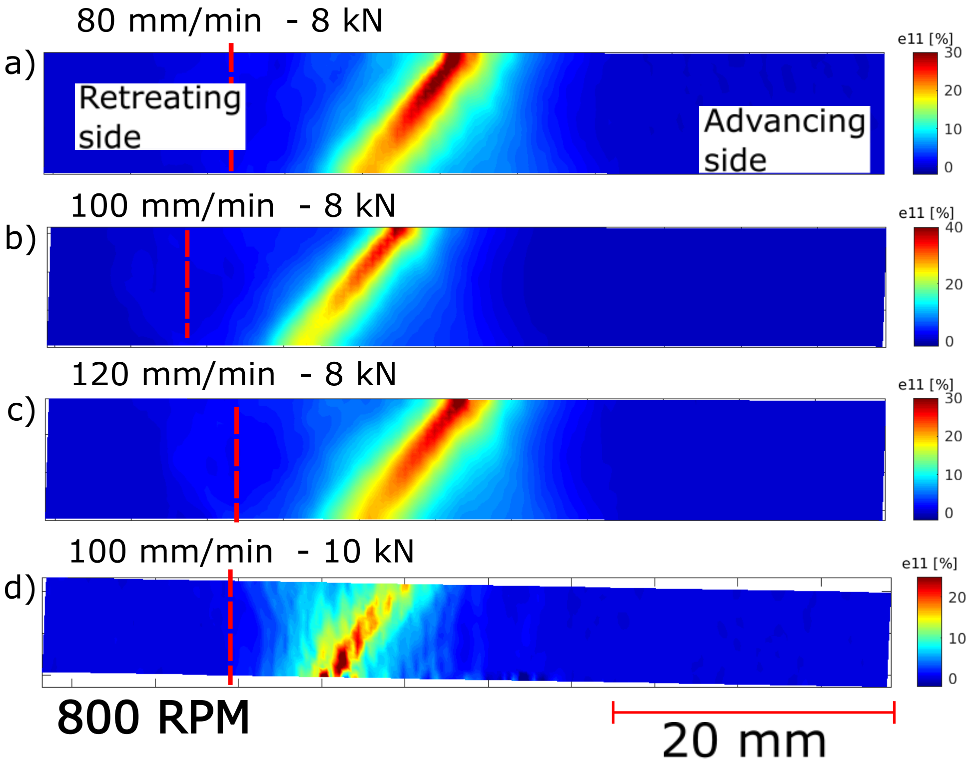

Figure IV.41: DIC strain maps of $e_{11}(\%)$ at the UTS in the stir zone of AA7075/AA6061 dissimilar welds at 800 RPM welds with the following welding parameters: (a) 80 mm/min and 8 kN, (b) 100 mm/min and 8 kN, (c) 120 mm/min and 8 kN and (d) 100 mm/min and 10 kN.

The UTS behavior of such welds would then depend on the HAZ strain localization at the apparent start of yielding, while at the same time showing no influence of advancing speed variation on said values of the apparent yield strength.

IV.4 Conclusion

Tensile behavior of a wide range of AA6061 and AA7075 similar and dissimilar joints have been studied with the help of DIC strain maps. Some general observations can be drawn from these results:

- The minimum of hardness has been related to local strain localization in AA6061 and AA7075 similar and dissimilar welding. These hardness values are located in the HAZ of the welds and thus, sample failure occurred in the HAZ of either the advancing or retreating side. Relationship between HAZ width and location in hardness measurements were established concerning β and η precipitates of respectively AA6061 and AA7075.
- Variation in ductility for AA6061 and AA7075 similar welded joints were explained by the width of the HAZ, in turn differently related to welding parameters of both AA6061 and AA7075 similar welds. It has been found that wider HAZ lead to a weaker notch effect during tensile testing, leading in turn to higher ductility.
- The apparent yield strength and ultimate tensile strength of dissimilar AA6061/AA7075 welded joints depend heavily on the tensile properties of similar AA6061 joints. Dissimilar welded joints behave on the basis of the "weakest link" where the weakest alloy, i.e. AA6061 in this case, dictates the tensile behavior of the welded joints. This result is further emphasized by systematic sample failure in the HAZ of the AA6061.

IV.5 Local strain and damage analysis

This section is from a scientific paper currently under revision after reviewing.

IV.5.A Introduction

In dissimilar FSW of aluminium alloys, the stir zone exhibits strong heterogeneous alloy mixing from both base materials (see e.g. [143] for 2024-7075 welds). Dissimilar FSW has promising applications especially in the aerospace industry [87]. Extensive research has been conducted in the FSW literature to asses basic mechanical properties (hardness, yield strength, ultimate tensile strength, etc.) and sometimes studying fatigue properties[25, 87, 144]. However, especially in the case of dissimilar FSW Al joints, some of those mechanical tests have the potential of studying more closely the heterogeneity of those welds. In that regard, capturing strain maps on the entire sample could be of interest.

Generally, digital image correlation (DIC) based techniques are employed to assess heterogeneous strain distribution under tension. Using a paint based marking techniques and an optical camera setup, it is possible to generate strain maps at the macroscopic scale on the cross section of tensile samples of welded joints [145–166]. Suthar et al. [160]

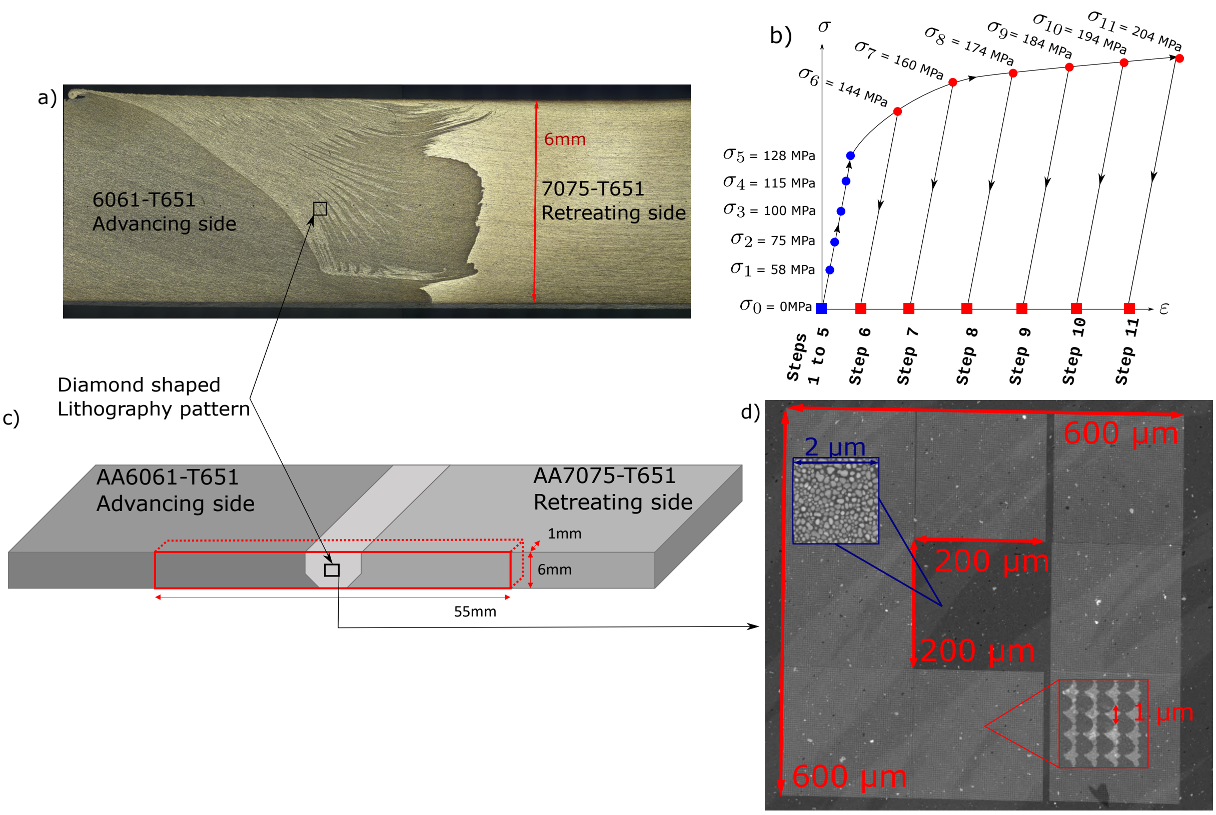

Figure IV.42: (a) Cross section of the weld and the selected DIC area. (b) Loading path with macroscopic stress/strain curve and imaging steps. (c) Sample extraction from the weld. (d) Gold micro-grid and tin random pattern (blue square).

specifically studied strain localization in similar AA6061-AA6061 and dissimilar AA6061-AA7075 welds using optical camera DIC. In general, researches exploiting macroscopic scale DIC evidence the significant effect of strain localisation in the heat affected zone (HAZ), often the weak zone (e.g. in AA6061 alloy [160]), on the tensile response. Hiscocks et al. [166] performed dissimilar magnesium FSW welds and were able to reach slightly better resolution ($>$ 240 µm) using improved optical cameras. This allowed them to evidence some heterogeneous deformations inside the nugget zone of their dissimilar welds but with large zones of uncaptured strain localisation. The research studies in [167, 168] exploited a higher resolution DIC performed using optical cameras than can reach a resolution of typically 20 µm. However, no results are available at the scale of bands of dissimilar materials that are typically observed in the stir zone of dissimilar friction stir welds nor at the scale of damage. This requires a DIC resolution below 1 m or even below 100 nm and is the aim of the present paper.

To reach such a resolution, some micro or even nano-scale digital image correlation (DIC) experiments have been developed using scanning electron microscopy (SEM) rather than optical cameras [169–171]. Such high resolution analysis (called HR-DIC) is of great interest for studying localized strain distribution and damage mechanisms.

Our study investigates the local strain and damage distribution in a dissimilar aluminium AA6061-AA7075 FSW joint and the effect of the mechanical properties and alloying elements of the base metals. To the best of the author's knowledge, high resolution

SEM based DIC has never been performed on dissimilar FSW joints.

IV.5.B Material and methods

A dissimilar weld 160 mm long composed of 6 mm thick AA6061-T651 and AA7075-T651 rolled plates are manufactured using a dedicated FSW machine. AA7075 is richer in Zn (5.29 wt%) than AA6061 (0.06 wt%). FSW parameters are optimized to avoid any major defects such as wormholes or kissing bonds, both being common in dissimilar FSW joints [172]. Pin length, rotational speed, advancing speed and vertical force are controlled to reach 5.75 mm, 400 RPM, 120 mm/min, and 10 kN respectively. Vickers hardness measurements were performed at mid-thickness of that weld on the transverse section with 1 mm distance between indents and using a 200 g load. As depicted in Figure IV.42(a,c), a single 55×6×1 mm^3 sample is extracted from the weld stir zone using a micro-cutting machine and has been polished up to 1 µm using a classical polishing routine. The analyzed area has been selected to study strain partitioning between the two mixed alloys inside the stir zone. The sample is extracted from the cross-section orthogonal to the welding direction (Figure IV.42(c)). Different marking techniques are employed to perform the HR-DIC at two different scales, to capture strain at various scales, in between bands of aluminium alloys and at the scale of intermetallic particles.

1) In the central region of the weld, a gold pattern (Figure IV.42(d)) is deposited on a 600 µm×600 µm region using lithography. Diamond shaped markings spaced by 1 µm are used to form the pattern. A central 200 µm×200 µm square region is left empty.

2) The 200 µm×200 µm central region of the micro-grid is studied at a finer scale (Figure IV.42(d), zoom in blue square) using another pattern composed of randomly scattered 50 to 100 nm diameter tin speckles, and carried out via metal vacuum evaporation [173].

The in situ tensile test is carried by using a tensile machine inside a SEM. The measured macroscopic stress/strain curve is presented in Figure IV.42(b). SEM is used to acquire a total of 12 Back-Scattered Electron (BSE) images at different targeted steps of the deformation process. The BSE images are acquired in the cross section of the welded joint (Figure IV.42(c,d)) before applying the DIC markings. To minimize electronic noise generated by the tensile machine during the image acquisition process, the sample is elastically unloaded (Figure IV.42(b)). The gear mechanism used to apply the tensile machine cannot be shut down during sample loading. However, the electrical current in the tensile machine generates noise on the BSE images. Consequently, the samples must be unloaded to properly power off the tensile machine and acquire quality images. High resolution strain fields are computed by using a custom made Correlation Manual Value (CMV) HR-DIC software [128]. The acquired BSE images are overlapped to the identified strain fields in order to associate strain and alloys distributions.

Figure IV.43(a,b) shows the Zn energy-dispersive X-ray spectroscopy (EDX) map in the stir zone. On EDX maps, the contrast gives an information on the local element composition. A brighter spot means more analyzed element is present. Figure IV.43(b) shows how BSE contrast (Figure IV.43(a)) allows to qualitatively assess the local Zn content, and is sufficient to differentiate between AA6061 and AA7075 phases locally. Moreover Figure IV.43(c) shows a magnification of an area exhibiting both types of intermetallic particles present in AA6061 inside the stir zone: Mg-Si rich and Fe rich in black and white respectively in the BSE image.

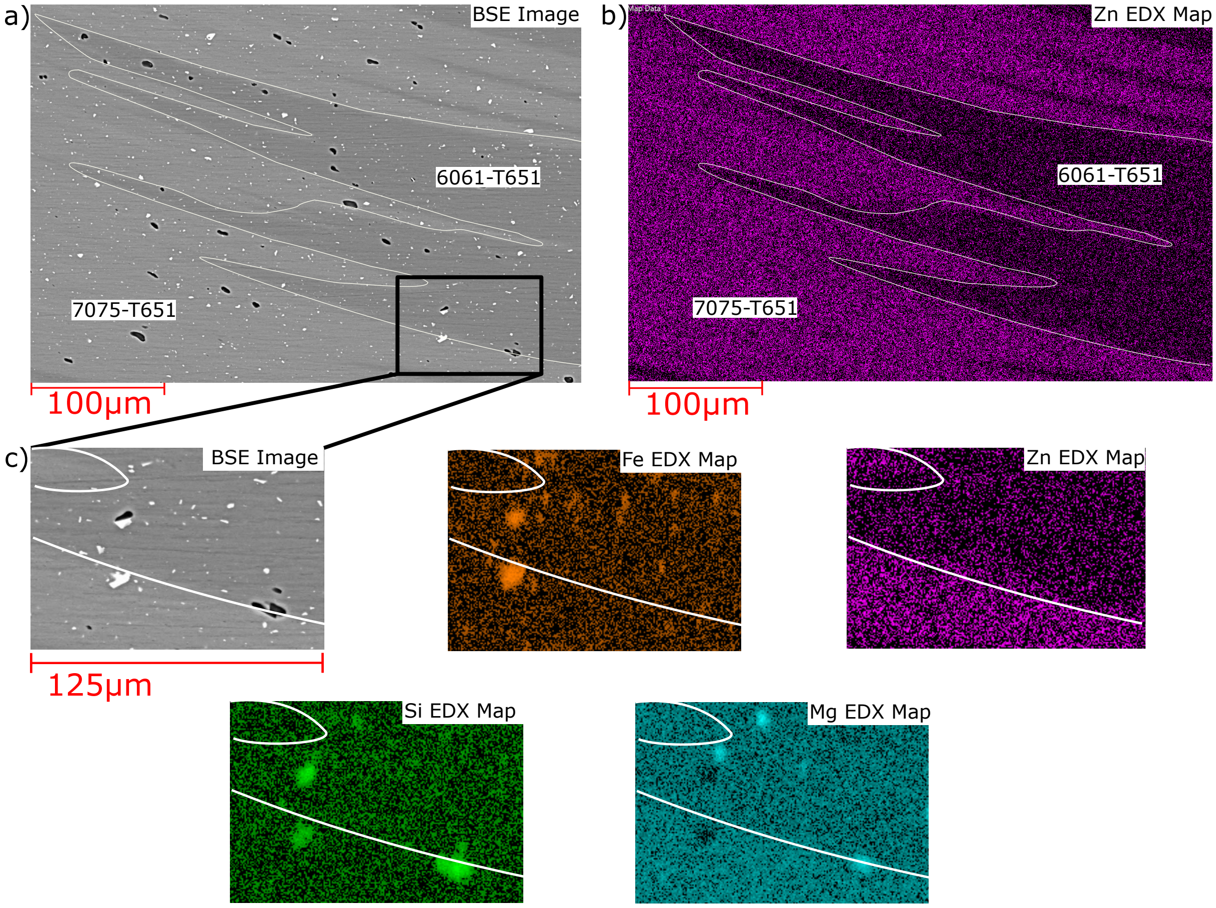

Figure IV.43: (a) BSE image taken in the center of the stir zone between AA6061 and AA7075 and (b) EDX map showing the Zn distribution which enable to differentiate the AA7075 and AA6061 alloys. (c) A magnified zone from (a) showing two types of inclusions: Fe rich (white) and Mg-Si rich (black) identified by the corresponding EDX maps.

IV.5.C Results and discussion

IV.5.C.i Phase pattern and microstructure

Figure IV.44 shows the hardness profile of the sample taken at the centerline of the cross section of the welded joint. A sharp difference in hardness values between the AA6061 (right) and AA7075 (left) side of the welded joint is highlighted by a red circle. In the stir zone (evidenced by two vertical red lines), a local maximum is observed at a "distance from the center of the weld" equal to 3 mm. This is the location where the HR-DIC sample was extracted. This hardness local maximum, coupled with the mixing of aluminium alloys on Figure IV.42(a), is the motivation to study local strain localization in that zone.

BSE contrast in Figure IV.43(a) shows the AA6061 in a darker grey compared to the lighter AA7075, which reveals a mixing phase pattern composed of alternating layers of AA6061 and AA7075. This contrast allows the phase identification of Figure IV.45(a). A pattern with 1 µm spaced diamond shaped markings is well adapted to capture strain in both alloys while the finest speckle pattern in the central area is used to capture the local strain field at the micro Mg-Si and Fe rich particles scale.

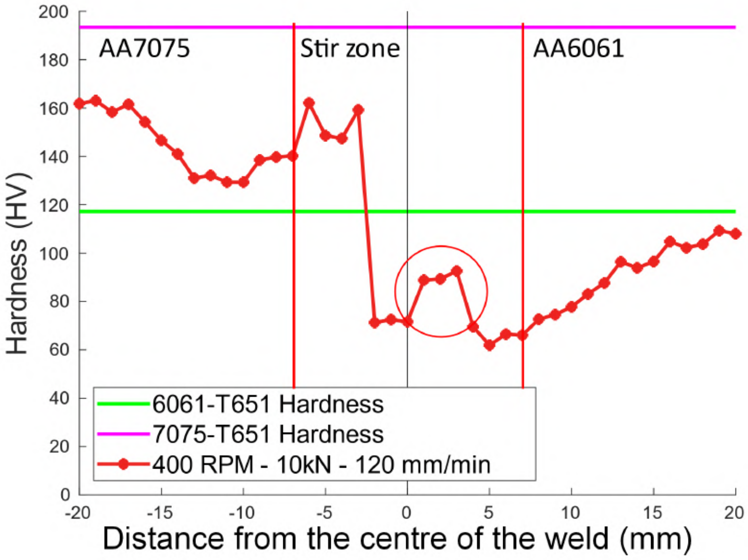

Figure IV.44: Hardness profile taken at the centre line of the studied AA6061-AA7075 FSW joint. The HR-DIC sample has been extracted in the red-circle zone.

Figure IV.45(a) shows the phase identification resulting from grey scale thresholding made with ImageJ software (AA6061 in red and AA7075 in blue. Using the diamond pattern, macroscopic strain fields in the stir zone are first measured (Figure IV.45(b)). Using Figure IV.45(a) an alloy composition can be attributed to each pixel of the image. A plastic strain value was also attributed to this pixel, using the DIC software. Figure IV.45(b) shows that the strain distribution is associated to the alloy's distribution pattern of Figure IV.45(a). A statistical analysis complements this observation, and box-plots representing plastic strain distribution for each alloy at each loading step are provided in Figure IV.45(c). In the T651 state, yield strength (and ultimate tensile strength) are 240 MPa (290 MPa) and 460 MPa (540 MPa) for AA6061 and AA7075 respectively. As the yield strength of AA6061 is lower than the yield strength of AA7075, the AA6061 exhibits a higher mean value of plastic deformation for a given applied strain compared to the AA7075 when reaching the onset of plasticity (Figure IV.45(c). This justifies the qualitative association between Figures IV.45(a) and (b). In addition, first and third quartiles enables to quantify in each alloy the statistical dispersion of plastic strain. As shown in Figure IV.45(c), this dispersion is qualitatively associated with the alloy distribution pattern as it clearly increases with the applied stress for both alloys, but more significantly for the alloy with the lowest yield stress (i.e. AA6061). However, the significant strain heterogeneity taking place inside each alloy (and not only between both alloys) suggests that strain localization arises at a lower scale in each alloy. To support this impression more quantitatively, a simple variance decomposition of the plastic strain distribution is presented in Figure IV.45(d) to measure to what extend the alloy phases explain the strain dispersion. During elastic loading (i.e. steps 1 to 5), with similar elastic properties in both alloys, strain distribution is unaffected by the phase pattern (explained variance of 0%). Then, plastic strain gradually increases (i.e. steps 6 to 11), and tends to localize in the softest alloy. Consequently, the phase pattern explains an increasing part on the variation of strain accommodation, but partially as it only reaches 7% before fracture. Thus, most of the strain dispersion is due to strain localization among each phase,

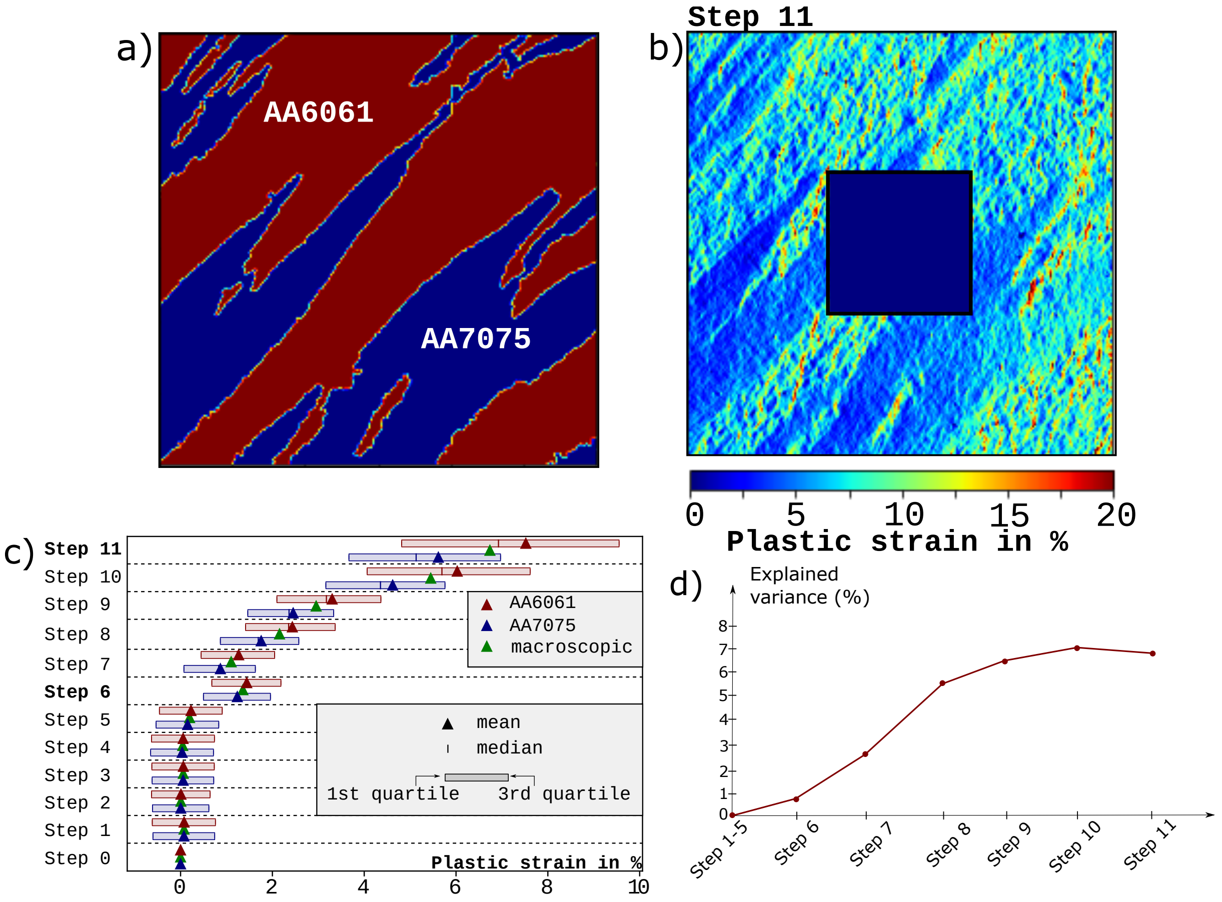

Figure IV.45: (a) Alloy distribution in the diamond shaped lithography area obtained by image segmentation. (b) Plastic strain field at step 11 in the diamond shape area. (c) Box-plots of plastic strain for each grade and for each loading step. (d) Percentage of the strain distribution variance explained by the phase pattern.

while only 7% of the strain dispersion occured due to the fact that one alloy is softer than the other. Thus, local intragranular mechanisms likely explain the remaining part of the strain distribution variance. This is demonstrated here by the finer scale analysis within the AA6061 using the finer HR-DIC central grid (Figure IV.42(d)). Mg-Si and Fe rich inclusions are identified in the stir zone as shown in Figures IV.43(c) and IV.46(a,c). Local strain heterogeneities reported in Figures IV.46(b,d) are clearly associated to intermetallic particles. On the basis of Figure IV.46, multiple deformation and damage mechanisms may explain the strain distribution are identified: 1) decohesion between Mg-Si rich inclusions and the Al matrix, and 2) fracture of Mg-Si rich inclusions (highest strain values being located where decohesion and cracks appear), 3) strong plastic strain localization surrounding intermetallic particles, 4) unbroken hard Fe inclusion inducing a strong localization in the Al matrix, and 5) areas of relatively low plastic strain within clusters of Fe rich particles. Additionally, high plastic strain values are also observed in areas without large intermetallic particles. Most likely, these plastic strain localization patterns may be the result of the underlying microstructure, and particularly grain orientation and size [174]. However, no Electron BackScatter Diffraction (EBSD) data is available for this sample to make more than a hypothesis that grain size and orientation could explain this phenomenon.

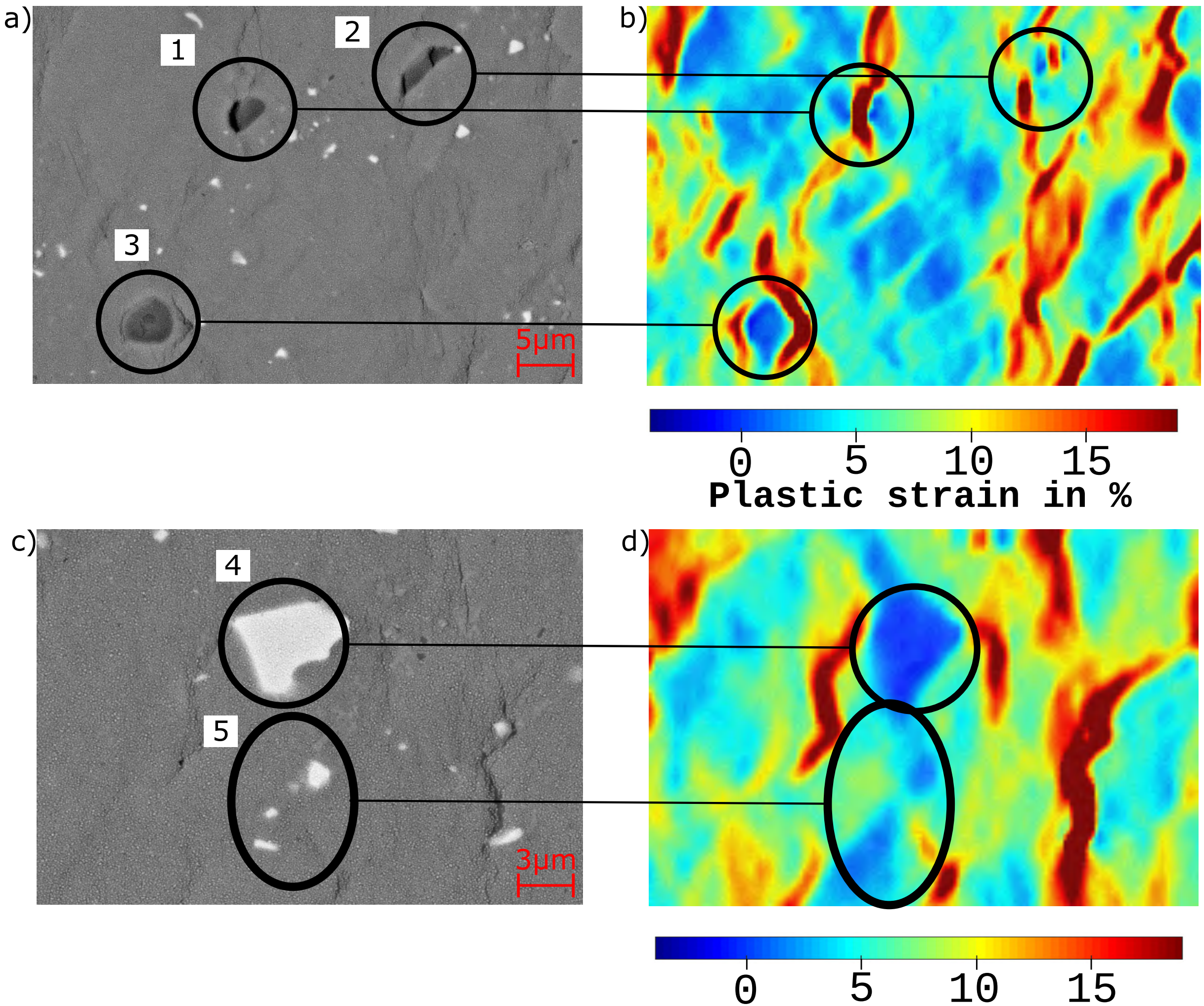

Figure IV.46: BSE imaging of Mg-Si (a) and Fe rich inclusions (c) along with their respective local strain maps (b,d). Multiple damage behaviour are identified and numbered: 1) Mg-Si rich inclusion decohesion from the Al matrix, 2) Mg-Si rich inclusion fracture, 3) Strong plastic strain localization, 4) Unbroken Fe inclusion, 5) Low plastic strain within a cluster of Fe rich inclusions.

IV.5.D Conclusion

A SEM in-situ tensile experiment conducted on a dissimilar AA6061-AA7075 assembly obtained by FSW is presented. High resolution digital image correlation has been performed at two different scales in the weld to characterise strain localization as a function of microstructural features. Mixing patterns of both Al alloys were quantitatively correlated with observed strain distribution and localization. However, this distribution explains only up to 7% of the variance just before failure. Thus, as the local AA6061 and AA7075 distribution is not sufficient to explain strain distribution, a finer scale damage analysis in the softest alloy revealed local damage and strain localization mechanisms, associated to Mg-Si and Fe rich particles.

Chapter V

Fatigue properties

In this Chapter, fatigue results obtained on friction stir welded aluminium joints will be discussed for various welding parameters. The first section of this Chapter will present the raw fatigue data obtained during the experimental campaign. Sample selection for fatigue will be explained. Each tested sample aims at analyzing the impact of a single welding parameter on fatigue life.

The second section of this Chapter will analyze the fatigue data in the form of S-N curve. Comparison will be made with the literature.

The third and final section of this Chapter will analyze the fracture surfaces of broken fatigue sample in order to further explain the fatigue life properties described in the previous section.

V.1 Fatigue testing and data

Fatigue testing protocol is detailed in the subsection II.4.C in Chapter II. The fatigue samples are dog-bone shaped and have been designed based on flat specimen following the ASTM E8 / E8M standard [127]. The fatigue life of aluminium FSW joints has been tested on four different welding parameter sets. The base material AA6061-T6 has also been tested within the same experimental plan, using the same machines, sample definition and preparation.

V.1.A Sample selection

In Section IV.3 of Chapter IV, tensile properties of the welded joints were presented. Based on the results of Figure IV.35 in Section IV.3.B, AA7075-T6 has not been included in the fatigue experimental plan following dissimilar tensile results obtained and presented in Section IV.3.B. These results show that when tensile properties are concerned, dissimilar joint will behave on the basis of the "weakest link" and mechanical properties are defined by the alloy with the weakest mechanical properties, i.e. AA6061. Strain maps shown in Section IV.3.B for dissimilar welds show strong strain localization in the Heat Affected Zone (HAZ) of AA6061. All dissimilar FSW samples break in the HAZ of the AA6061. Hence, this alloy has been the only base material included in this study.

A useful metric often used to present welded joint mechanical properties is called the "joint efficiency". This factor is defined by the ratio of a welded joint mechanical property with its base material value, or in this case with its weakest base material mechanical property value. On Figure IV.35 in Section IV.3.B, joint efficiencies for all the apparent yield strength, UTS and elongation at break are presented. Hence, the chosen samples for fatigue testing are:

- **AA6061-AA7075 dissimilar weld, 400 RPM, 120 mm/min and 10 kN**: this sample was selected as it has the slowest rotational speed along with the fastest advancing speed out of all the dissimilar FSW joints, i.e. the coldest dissimilar FSW joint of the experimental plan, as seen in Table III.4. The UTS of this sample was reported to be the highest of the dissimilar joints during tensile testing, albeit with a lower yield strength compared to other samples at the same advancing speed but with different rotational speeds. The combination of these mechanical properties along with the unique thermal aspect of this weld make it a suitable candidate for fatigue testing.
- **AA6061-AA7075 dissimilar weld, 400 RPM, 80 mm/min and 10 kN**: this sample has a **slower advancing speed** compared to the previously described sample but the same rotational speed. In this regard, the welded joint was subsequently realized at a higher welding temperature (see Table III.4), while keeping the same rotational speed. As seen in Section IV.1.B, the rotational speed greatly influences the morphology of the stir zone, with higher rotational speed creating stronger "onion rings" pattern [51]. The identical rotational speed between these two samples gives them almost identical stir zone mixing morphology, as can be seen on Figure IV.3 in Section IV.1.B. Additionally, hardness measurements presented on Figure IV.11(a) show a difference in HAZ width both in the AA6061 and AA7075.
- **AA6061-AA7075 dissimilar weld, 600 RPM, 120 mm/min and 9 kN**: this sample has a **higher rotational speed** but identical advancing speed compared the first described sample, therefore was manufactured at a higher welding temperature, as seen in Table III.4. However, the main difference with the previous 400 RPM, 80 mm/min sample concerns the stir zone morphology of this sample. As described in Section IV.1.B and on Figure IV.4, the stir zone morphology varies greatly compared to the previous sample manufactured at 400 RPM. Fatigue results from this sample compared to the first 400 RPM, 120 mm/min sample will draw conclusions on the effect of higher heat input along with a change in stir zone morphology. This change could have an effect on fatigue crack initiation and growth.
- **AA6061-AA6061 similar weld, 400 RPM, 120 mm/min and 10 kN**: This **similar** FSW joints has been manufactured using the same process parameters compared with the first described sample. The stir zone size is assumed to be somewhat similar, but as described in Section IV.1.A on Figure IV.1, the affirmation has not be verified due to the similar nature of the weld, rendering chemical etching non conclusive. By using identical process parameters, the heat input in the weld is assumed to be similar. Based on these assumptions, the fatigue results from this welded joint will draw conclusions on the difference in fatigue life, at a given set of welding parameters, between dissimilar AA6061/AA7075 welding and AA6061 similar welding, i.e. the assembly with the closest macroscopic mechanical properties.

V.1.B Fatigue life results

This fatigue experimental plan had a $R = 0.1$ and a $25Hz$ frequency with a censoring at $5 * 10^6$ cycles, i.e. all fatigue testing was halted at this number of cycle, with the exception of a single sample. As a reminder, the samples were hand polished up to 2400 SiC grit paper and has a gage section of 50 by 10 by 6 mm. The fatigue tests have been subcontracted and carried out by Bureau Veritas. This was to ensure compliance with international standards in fatigue testing, a key requirement for Thales.

The fatigue life results regarding the base material is provided in Table V.1. The base material fatigue data originates from the experimental plan as well as from Vysotskiy et al. [76]. The experimental procedure of the literature based base material data is similar to the one used in this study. Fatigue samples are flat dog-boned shaped specimens machined with their length perpendicular to the welding direction. In Table V.2, the fatigue parameters used in both studies are presented.

Fatigue life results for the dissimilar AA6061/AA7075 400 RPM and 80mm/min, 400 RPM and 120 mm/min, similar AA6061 welding at 400 RPM and 120 mm/min, and dissimilar AA6061/AA7075 600 RPM and 120 mm/min are described respectively in Tables V.3, V.4, V.5 and V.6. In each Table, a row represents a single fatigue sample. A maximum applied stress, a number of cycle to failure (or censoring) and a weld failure location is attributed to each fatigue sample. The failure location has the following nomenclature: ST for Stir Zone, TMAZ for Thermo-Mechanically Affected Zone, HAZ for Heat Affected Zone and BM for Base Material. For the HAZ, TMAZ and BM the location of weld failure in noted with regard of the alloy in which it occurred for dissimilar welds, and either advancing side (AS) or retreating (RS) for the single similar welds. As a reminder, in dissimilar welded joints, the AA6061 is placed on the advancing side, and the AA7075 on the retreating side. These results will be discussed in the next Section with appropriate data representation.

Experimental plan		Extracted from the literature [76]	
Maximum applied stress σ_{max}	Cycle to failure	Maximum applied stress σ_{max}	Cycle to failure
175	5 000 000	160	1 704 748
175	242 295	160	2 538 856
183	5 000 000	160	6 764 240
190	5 000 000	170	2 763 392
205	562 496	170	4 020 179
205	5 000 000	180	861 513
205	5 000 000	180	1 006 680
212	271 424	180	1 417 184
212	1 587 585	190	364 845
220	1 130 562	190	452 393
220	482 421	190	620 615
		220	46 472
		220	90 369
		220	115 993
		240	57 046
		240	83 048
		240	87 718

Table V.1: Fatigue date for AA6061-T651 base material. A set of sample was tested alongside welds in the experimental plan, the other was extracted from Vysotskiy et al. [76].

	Bureau Veritas	Literature referece[76]
Polishing grit (SiC)	2400	2400
Gage section (mm.mm.mm)	50×10×6	30×8×1.5~2.5
Censoring (number of cycle)	$5 * 10^6$	10^7
Testing frequency (Hz)	25	50
R value	0.1	0.1

Table V.2: Comparison of the fatigue testing parameters between this study and a literature point of reference. [76]

Maximum applied stress σ_{max}	Cycle to failure	Weld failure location
153	5 000 000	$\emptyset$
160	810 702	TMAZ AA6061
160	894 238	BM AA7075
167	5 000 000	$\emptyset$
167	5 000 000	$\emptyset$
175	173 052	TMAZ AA6061
175	241 576	TMAZ AA7075
175	5 000 000	$\emptyset$
175	5 000 000	$\emptyset$
183	222 445	TMAZ AA6061
183	308 531	ST
183	426 196	TMAZ AA7075

Table V.3: Fatigue data for AA6061-AA7075 400 RPM, 80 mm/min, 10 kN samples.

Maximum applied stress σ_{max}	Cycle to failure	Weld failure location
102	5 000 000	$\emptyset$
102	5 000 000	$\emptyset$
109	5 000 000	$\emptyset$
116	5 000 000	$\emptyset$
123	130 258	ST
130	182 806	ST
146	183 662	ST
146	115 868	ST
153	57 582	ST
153	201 078	ST
175	17 930	ST
175	37 795	ST

Table V.4: Fatigue data for AA6061-AA7075 400 RPM, 120 mm/min, 10 kN samples.

Maximum applied stress σ_{max}	Cycle to failure	Weld failure location
175	5 000 000	∅
175	5 000 000	∅
183	668 087	HAZ AS
183	5 000 000	∅
183	2 263 207	BM AS
190	618 697	TMAZ AS
190	296 231	TMAZ AS
197	616	TMAZ RS
197	101 997	TMAZ RS
197	497	TMAZ RS
205	256	TMAZ AS
205	296	TMAZ RS

Table V.5: Fatigue data for AA6061-AA6061 400 RPM, 120 mm/min, 10 kN samples.

Maximum applied stress σ_{max}	Cycle to failure	Weld failure location
100	5 000 000	∅
130	5 000 000	∅
167	5 000 000	∅
167	673 724	TMAZ AA6061
175	848 079	BM AA6061
175	611 245	ST
175	10 000 000	∅
183	361 371	TMAZ AA6061
190	266 292	TMAZ AA7075
190	332 219	TMAZ AA7075
197	300 364	TMAZ AA7075
197	311 644	TMAZ AA6061
205	199 361	TMAZ AA6061
205	139	TMAZ AA6061

Table V.6: Fatigue data for AA6061-AA7075 600 RPM, 120 mm/min, 9 kN samples.

V.2 S-N curve analysis

From the fatigue life results presented in the previous Section, S-N curves are plotted. All S-N curves in Figures throughout this section have a color matching fitting curve, modelled on a power law, as seen on Equation V.1. σ_{max} is the maximum applied stress in MPa and N the number of cycle.

$$\sigma_{max} = a \times N^b \tag{V.1}$$

V.2.A Base material and literature fatigue life

Figure V.1 presents the resulting S-N curves from fatigue testing of the base material in two different cases: one base material configuration obtained through the experimental plan along with a S-N curve out of Vysotskiy et al. [76]. The base material used in this study appears to have slightly better fatigue properties compared to the literature reference. One explanation could reside in the polishing method used. In this study, fatigue samples were polished entirely by hand up to 2400 SiC grit. In the literature reference, the term "mechanically polished" is used. Difference in polishing techniques could explain the discrepancy observed in the base material values, all other fatigue parameters being relatively similar. Small variation in polishing and surface condition can lead to widely different results in fatigue testing [175]. Additionally, base material yield strength slight variation from one batch to another could explain these different results. In any case, our base material reference appears to be suited for comparison with the different welds, as its strength is even higher than what has been found in the literature. For further reference to a base material, data obtained during our study will solely be used.

Figure V.2 additionally draws fatigue results from Vysotskiy et al. [76] on a double sided AA6061-T6 FSW joint. In this paper, the double sided FSW joint is described as having better fatigue life properties compared to its base material. In their study, the authors attribute the increased fatigue life of their sample to compressive residual stress, along with the double sided nature of their welded joints, which ensures the total absence of certain welding defects, such as lack of penetration or hooking. However, this kind of fatigue results in aluminium FSW joints is quite unusual, as the authors mention. Most aluminium FSW joints have lower fatigue life compared to their base material [105, 106].

V.2.B Base materials and AA6061 similar welding fatigue life

Figure V.3 shows the fatigue data for the similar AA6061 joint manufactured using 400 RPM, 120 mm/min and 10 kN and for the base material. The AA6061 similar joint exhibits lower fatigue life when compared with the base material. In Section IV.3.A, the effect of the varying process parameters on the tensile mechanical properties are described. Figures IV.13(a,b) show the apparent yield strength of such similar welds, relative to the varying welding parameters. In general, the maximum apparent yield strength for all the AA6061 welds are well below 130 MPa. However, specifically in the case of low rotational speed welds, i.e. 400 RPM joints, an additional decrease in apparent yield strength was observed at high advancing speeds. The DIC strain maps when reaching the apparent yield strength (Figure IV.17 in Section IV.3.A) lead to the conclusion that higher advancing speed and axial load, both features of the AA6061 similar joint tested here in fatigue,

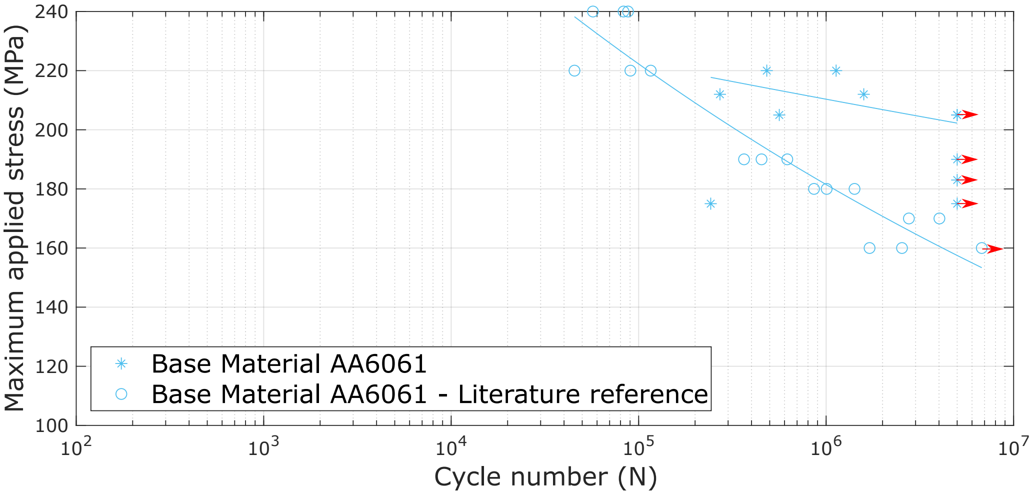

Figure V.1: Two S-N curves of the AA6061 fatigue life. The experimental campaign yielded one curve and literature review the other [76].

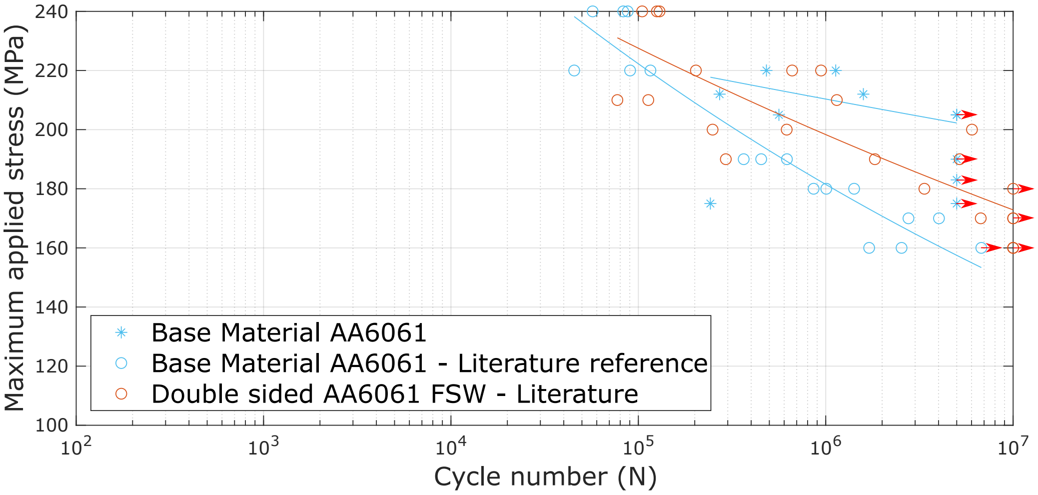

Figure V.2: S-N curves of the base material, a AA6061-T6 fatigue testing from the literature and a double-sided FSW joint from Vysotskiy et al. [76]. The double sided FSW welds exhibit higher fatigue life when compared with their base material.

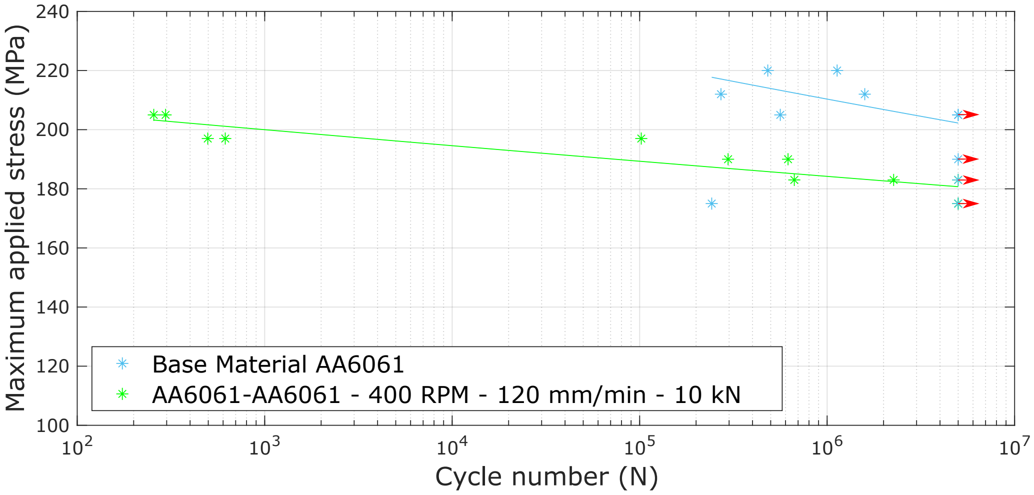

Figure V.3: S-N curves of the similar AA6061 joint manufactured with 400 RPM, 120 mm/min, and 10 kN along with this study's base material.

lead to a decrease in apparent yield strength, with a clear strain localization observed directly in the stir zone. However, fatigue data shown here are quite remarkable when compared with these results. Indeed, apart from 4 data points at LCF, the HCF properties of this welded joint are particularly strong regarding the yield strength measurement during tensile testing. The DIC strain maps at the ultimate tensile strength (UTS) of these welds were described on Figure IV.21, with clear strain localization in the HAZ on the advancing side. However, fatigue results presented in Table V.5 shows failure location in the TMAZ on the retreating side. Local strain hardening of the aluminium during fatigue testing lead to a totally different fracture mechanism when compared with tensile testing.

V.2.C Comparing similar and dissimilar welding fatigue life

Figure V.4 shows the S-N curves of joints manufactured using 400 RPM, 120 mm/min and 10 kN process parameters for an AA6061 similar and an AA6061/AA7075 dissimilar joint, along with the base material curve. The dissimilar welded joints exhibit significantly lower fatigue life compared to both the similar AA6061 joint and the base material. Additionally, Table V.4 show that all the dissimilar samples broke in their stir zone, without exception. The welding parameters of these two welds being identical, the only explanation for such a behavior resides in the dissimilar nature of the welded joint. In Section IV.1.B, dissimilar macrographs were described for various rotational speed and particularly, a relatively minimal mixing in the stir zone of the two aluminium alloys was noted at 400 RPM. Nevertheless, no significant welding defects (such as wormhole, lack of penetration) were observed. Additionally, the tensile properties of 400 RPM dissimilar welds were described in Figure IV.35(b,d) and no significant impact of the rotational speed on apparent yield strength or UTS has been described. In turn, the dissimilar nature of mixing in the stir zone remains as the only explanation for this fatigue behavior, but with the added particularity that, whatever the defect present in this specific stir zone, it does not appear to have an effect on static tensile properties. The influence of hardening β and η precipitates has been described in details when discussing hardness

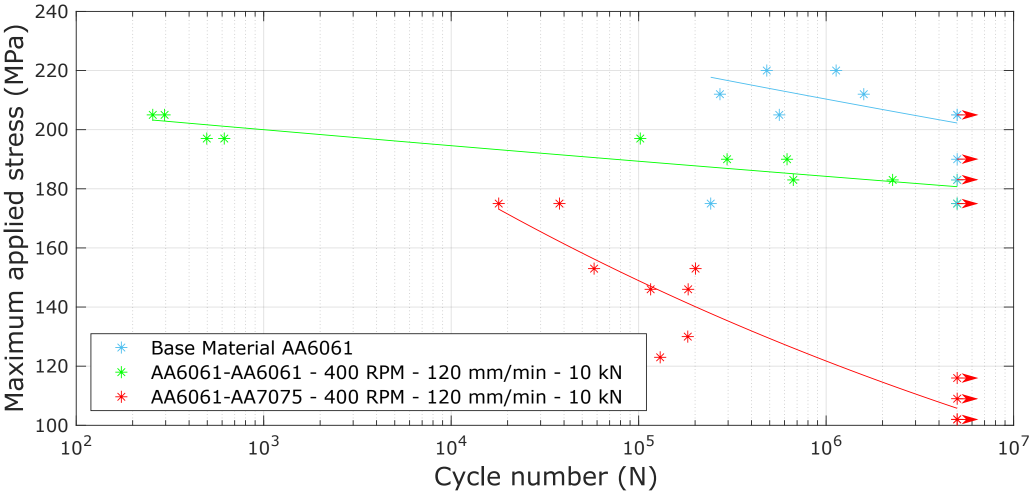

Figure V.4: S-N curves of the joints manufactured with 400 RPM, 120 mm/min, 10 kN both in a similar and dissimilar fashion. The dissimilar nature of the weld appears to significantly lower its fatigue properties.

and tensile results in Sections IV.2.A and IV.3.A. The dissimilar nature of the considered joint, along with its low RPM (400 RPM) and high advancing speed (120 mm/min), i.e. the coldest weld of the experimental plan, could have played a role in particular on β and η coarsening/dissolution mechanism in the stir zone. However, hardness measurements in said the stir zone on Figure IV.12(a) at 120 mm/min does not corroborate this hypothesis. To better understand the underlying mechanism responsible for such fatigue behavior, additional samples at different rotational and advancing speeds are presented.

V.2.D Impact of heat input in dissimilar welding on fatigue life

V.2.D.i Increase of heat input by rotational speed increase

Figure V.5 shows four different S-N curves: the base material, the AA6061 similar joint (400 RPM, 120 mm/min, 10 kN) and two dissimilar AA6061/AA7075 joint for 120 mm/min, 10 kN and two rotational speeds: 400 and 600 RPM. By increasing the rotational speed for one dissimilar joints, the influence of **increased heat and stir zone morphology change** can be assessed. The fatigue life of dissimilar AA6061/AA7075 600 RPM, 120 mm/min and 9 kN is better than the 400 RPM dissimilar joint and as good as the similar 400 RPM joint. As discussed when analyzing Figure V.4, the poor fatigue properties of the 400 RPM dissimilar joints could have multiple root causes, mainly the low mixing stir zone of 400 RPM samples along with the relatively low welding temperature of this joint. In this instance, the 600 RPM, 120 mm/min and 9 kN dissimilar joint has the best alloy mixing in its stir zone (as evidenced by Figure IV.4 of Section IV.1.B) along with a higher rotational speed. Either way, an increase in heat input and/or a better mixing of the stir zone is beneficial for fatigue life in dissimilar joints.

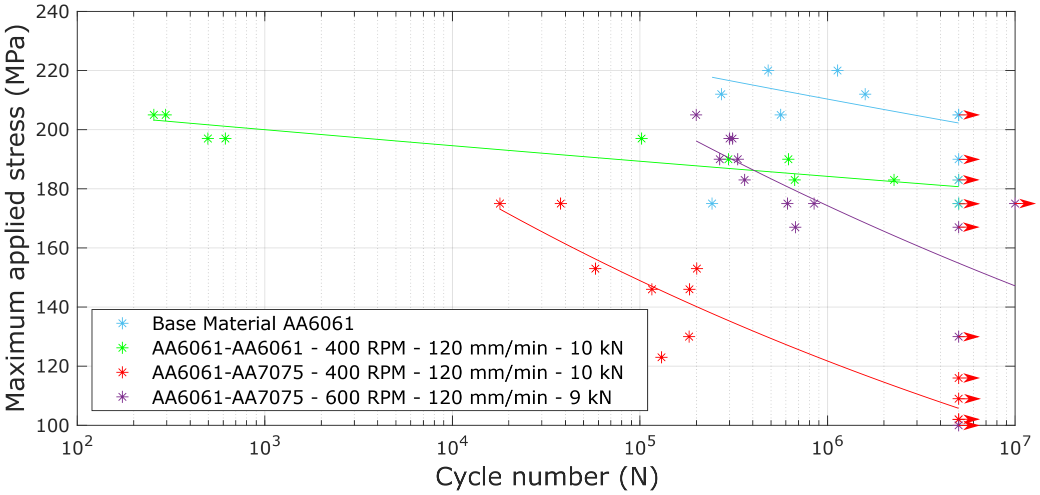

Figure V.5: S-N curves of the base material, the AA6061 similar 400 RPM, 120 mm/min and 10 kN joint, along with two dissimilar AA6061/AA7075 joints performed at 120 mm/min for two different rotational speeds (400 and 600 mm/min).

V.2.D.ii Increase of heat input by advancing speed decrease

Finally, Figure V.6 shows four different S-N curves: the base material, the AA6061 similar joint (400 RPM, 120 mm/min, 10 kN) and two dissimilar AA6061/AA7075 joint for 400 RPM, 10 kN and two advancing speeds: 80 and 120 mm/min. Figure V.5 shows that the fatigue properties of the 600 RPM dissimilar joints were better, but no conclusive evidence could be drawn on whether this better fatigue life could be attributed to stir zone mixing or heat input. On this last dissimilar sample, the fatigue life shown for the 400 RPM, 80 mm/min sample is slightly worse compared to the AA6061 similar joint or the 600 RPM dissimilar AA6061/AA7075 joint from the previous Section, but far better compared to the 400 RPM, 120 mm/min sample. In turn, this observation concludes that at 400 RPM, the heat input of the welding parameters plays a primary role in defining the fatigue life properties of dissimilar joints. Additionally, the 600 RPM dissimilar curve had still better fatigue properties, comparable with those of the AA6061 similar joint. Material mixing in the stir zone influences the fatigue life, but its influence on fatigue life appears to be weaker than the influence of heat input.

In conclusion, all the fatigue data of FSW joints at HCF appear to have relatively close fatigue properties, except for a notable exception with a substantially lower fatigue life. By comparing samples manufactured with a range of process parameters, our data leads to the conclusion that heat input in dissimilar welded joints plays a key role in assuring good fatigue life, where an increase in heat input leads to better fatigue life. Additionally, stir zone mixing appears to also play a role, albeit to a lesser degree. This result is quite interesting, as it appears to be almost contradictory to the conclusions drawn from tensile data in dissimilar joints in Figure IV.35, where rotational speed appeared to have little to no effect on apparent yield strength and UTS and an increase in advancing speed (i.e. decrease in heat input and HAZ narrowing) lead to better UTS values for these dissimilar joints. However, hardness measurements presented in Section IV.2.B showed that an increase in heat input by either a higher rotational speed or a lower advancing speed induces a larger HAZ in both Al alloys, with the AA7075 showing stronger hardness

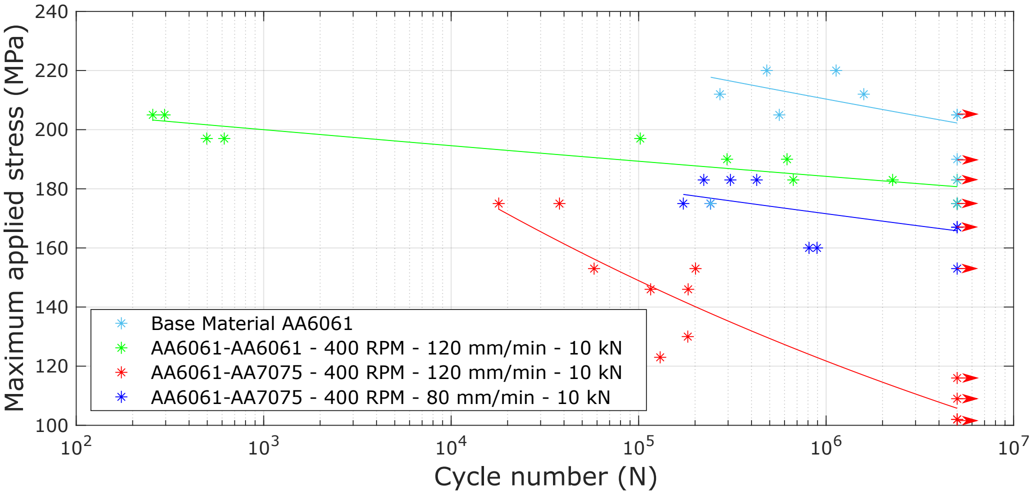

Figure V.6: S-N curves of the base material, the AA6061 similar 400 RPM, 120 mm/min and 10 kN joint, along with two dissimilar AA6061/AA7075 joints performed at 400 RPM and 10 kN for two different advancing speeds (80 and 120 mm/min).

differences compared to the AA6061. This larger HAZ in an high heat environment would create a larger, high ductility zone where a notch would appear during mechanical testing in general. Finally, Figure IV.35(e) shows that the elongation at break in dissimilar FSW joints benefits slightly from a rotational speed increase, but Figure IV.35(f) shows that an advancing speed decrease leads to worse ductility. Both of these evolution leading to temperature weld increase. This, combined with the relatively high stress fatigue life (higher than the apparent yield strength) of dissimilar joints make little use of tensile data to predict the fatigue life properties of dissimilar joints.

V.3 Fatigue fractography

In the previous Section, a substantially lower fatigue life has been shown for a dissimilar AA6061/AA7075 FSW joint. Data lead to the conclusion that heat input plays an important role in fatigue life properties of these joints. With the help of fractography, this Section will investigate the microstructural feature responsible for such poor fatigue life.

SEM fractography has been performed on broken fatigue samples in order to analyse the failure mechanism and understand the difference in fatigue properties between the welded joint of the experimental plan.

Figure V.7 shows an SE image of a fracture surface. Fatigue striations are clearly visible, thus confirming that fatigue did indeed occur.

For all fatigue samples, except those from the 400 RPM, 120 mm/min dissimilar joints with poor fatigue life, the fractography looks similar. Figure V.8 depicts such a typical fracture surface. The fracture surface has the following features:

- **Crack initiation area:** the zone in which the crack nucleates and start to propagate from. Similarly to Vysotskiy et al. [76], cracks in this study nucleated from the surface and not from slip bands system of the aluminium matrix. A detailed image of a typical surface crack nucleation site is visible on Figure V.9. A large inclusion is distinguishable from the Al matrix, close to the surface. Fatigue crack initiation

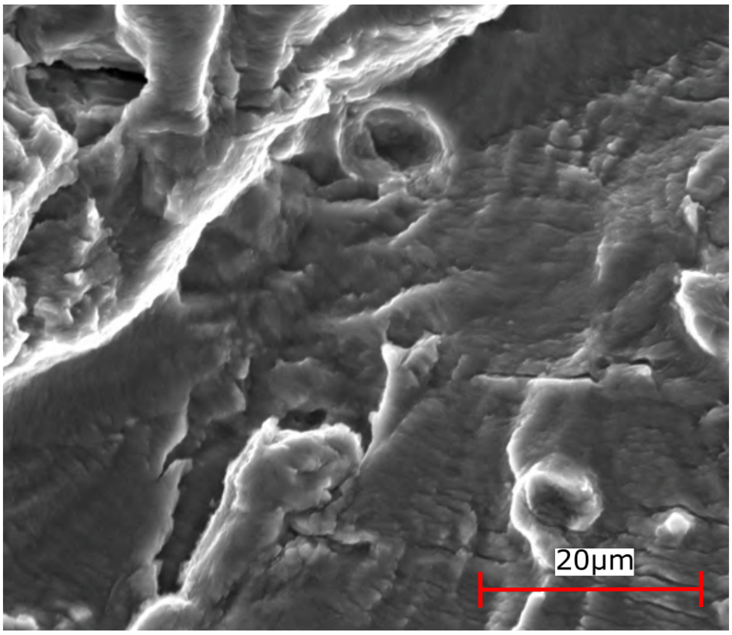

Figure V.7: Fatigue striation visible in SE imaging on the AA6061-AA7075 400RPM, 80 mm/min, 10 kN sample.

occurred on this inclusion. The latter appears to have attributes characteristically associated with melting pools, such as small round bumps.

- **Crack propagation:** as the crack is initiated either on a slip plane or, in this case, on the sample's surface, it then propagates during cycling loading. As explained in Chapter I.4.A, fatigue crack growth has multiple stress intensity factor, described as modes depending on how the crack tip is being loaded. In the case of FSW joints tested perpendicularly to the welding direction, all the samples exhibit a mode I crack propagation path, i.e. the crack tips are opened by the cyclic loading.
- **Ductile fracture:** as the crack grows during the propagation phase, the stress applied to the remaining surface of the sample increases as the total amount of gauge surface decreases. Once the stress in this remaining plane exceeds the ultimate tensile strength of the material, the sample breaks in a similar way to a tensile test. For AA6061 particularly, this surface is identified by the multiple dimples on the fracture surface, as can be seen on Figure V.10. This fracture surface is typical of ductile fracture.

All samples tested in this experimental fatigue plan, except for the AA6061-AA7075 400 RPM, 120 mm/min, 10 kN sample, exhibit this fracture behavior. Figure V.11 shows the change of fracture mechanism between fatigue crack growth and ductile failure.

As mentioned in the previous section, the AA6061-AA7075 400 RPM, 120 mm/min, 10 kN welded joints has a subpar fatigue life compared to the base materials and even all the other welded joint considered. Figure V.13 shows the fracture of a fatigue sample with these process parameters. This fracture surface has some unusual features:

- **Both Al alloys are visible** meaning that the sample broke exactly at the junction between the two aluminium plates. This is illustrated in Figure V.12, where the line failure of the sample is visible. A small portion of the AA7075 alloy crosses the

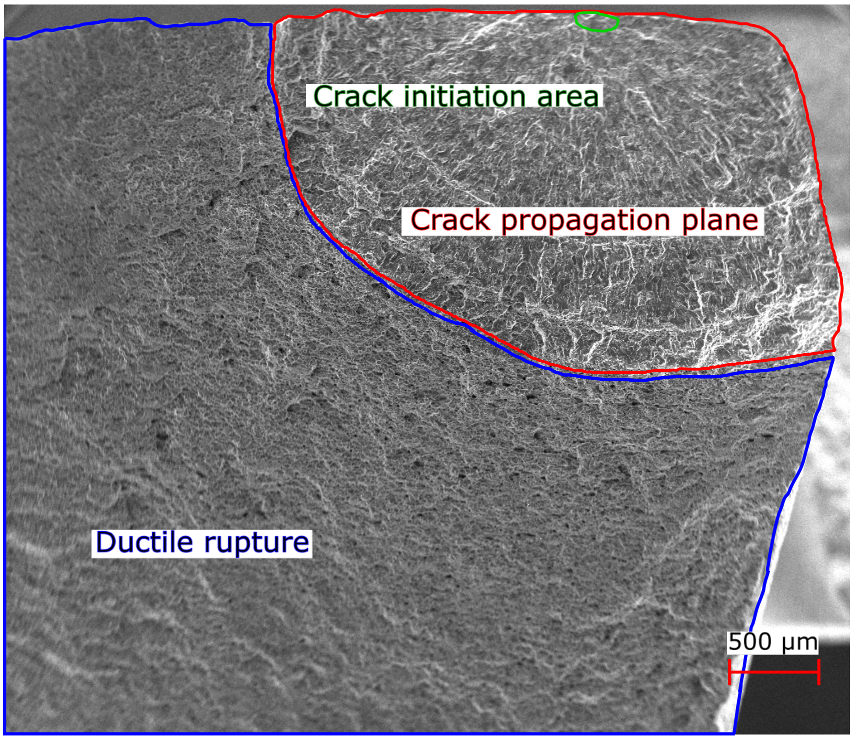

Figure V.8: SE imaging of a fracture surface of a 600 RPM, 120 mm/min, 9 kN sample. The crack originated from the surface, like all other observed welds. Three main areas are visible: the crack initiation, the fatigue crack propagation plane and the ductile fracture.

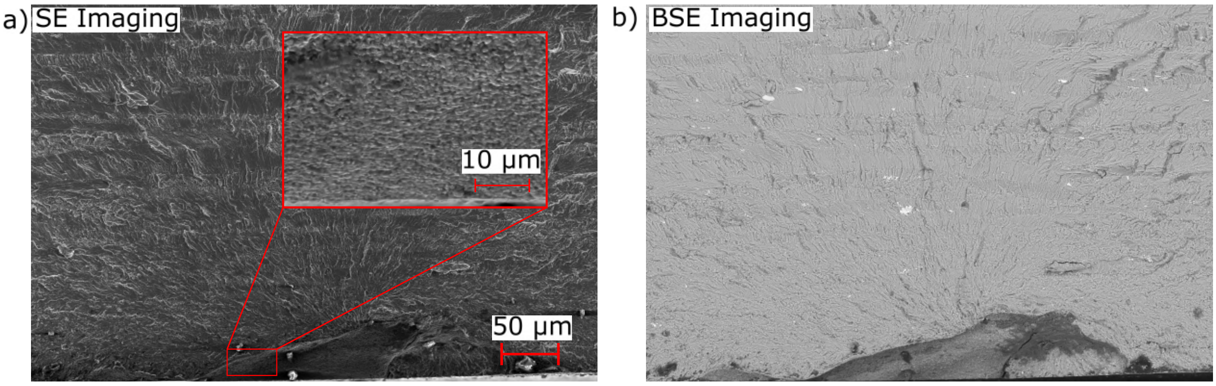

Figure V.9: SE and BSE imaging of a surface crack initiation site in a AA6061-AA7075 600 RPM, 120 mm/min, 9 kN fatigue sample at $\sigma_{max} = 197 MPa$. The crack initiation site appears to have a small dimpled area, which could be reminiscent of a local melting of the Al matrix.

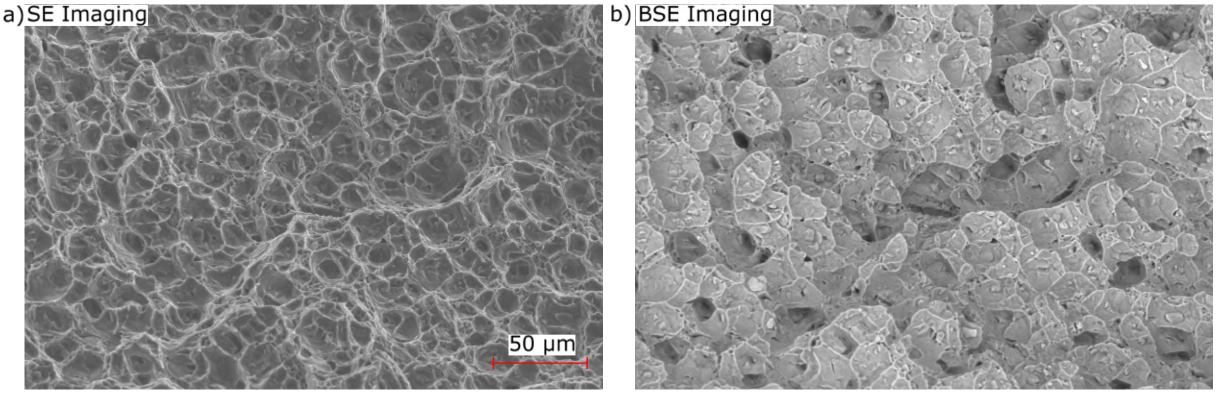

Figure V.10: (a) SE and (b) BSE imaging of a ductile fracture surface. Dimples are visible and are typical of ductile fracture surfaces [76, 101, 106, 114, 176]. The BSE imaging suggest the presence of coarse inclusions in the dimples.

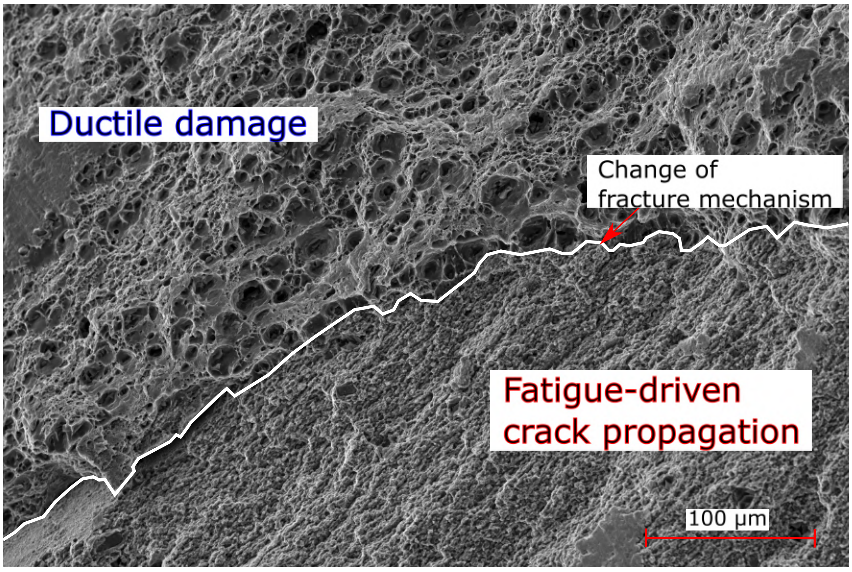

Figure V.11: SE imaging of an AA6061-AA7075 400 RPM, 120 mm/min, 10 kN sample showcasing the change of fracture mechanism between the fatigue driven crack propagation and the ductile rupture of the sample.

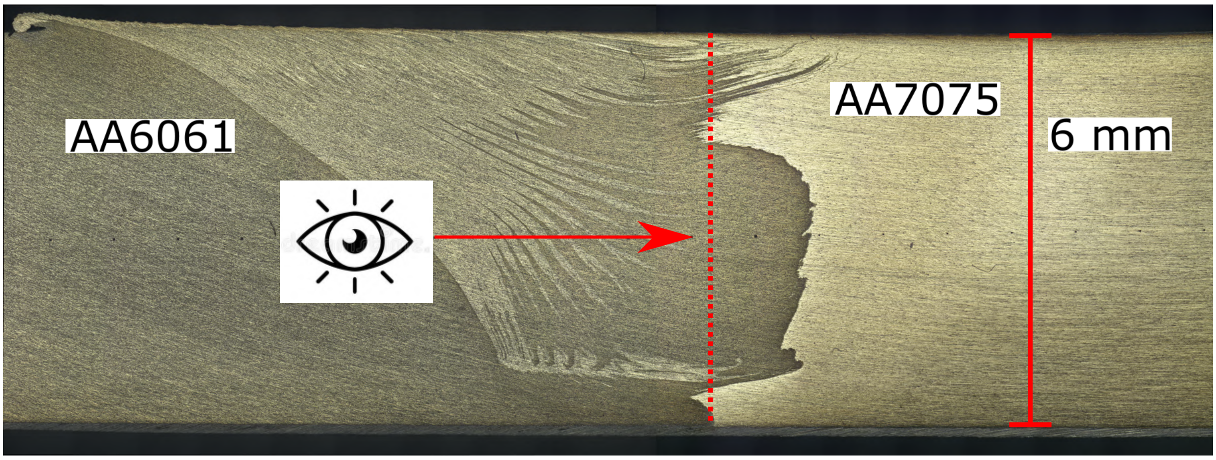

Figure V.12: Macrograph illustrating the point of view from which the unusual fracture surface is extracted, see Figure V.13. The sample has broken exactly at the middle on the weld, in line with the remnant observed at the bottom of the weld.

failure line at the bottom of the weld. This can also be observed on Figure V.13 in the zoomed inset figure highlighting that zone. This could be the result of a welding defect such as lack of penetration of the welding tool. However, this defect was not observed on the corresponding optical macrographs presented in Section II.3.A. Similarly, the good tensile testing result from this welded joint, with a fracture in the HAZ of the AA6061 along with a 209 MPa UTS, did not lead to conclude that such a defect could be present within this welded joint.

- **The crack propagation plane extends on the whole gauge section**. The crack originated from the bottom of the weld along the entire welded seam, as the ductile fracture is visible at the top of the figure and appears to have propagated along the entire surface of the welded joint, contrary to the other fatigue samples where the crack initiation appears to have originated from a single point on the surface sample. On this crack propagation plane, diagonal lines are visible that are reminiscent of the tool pin mixing action.

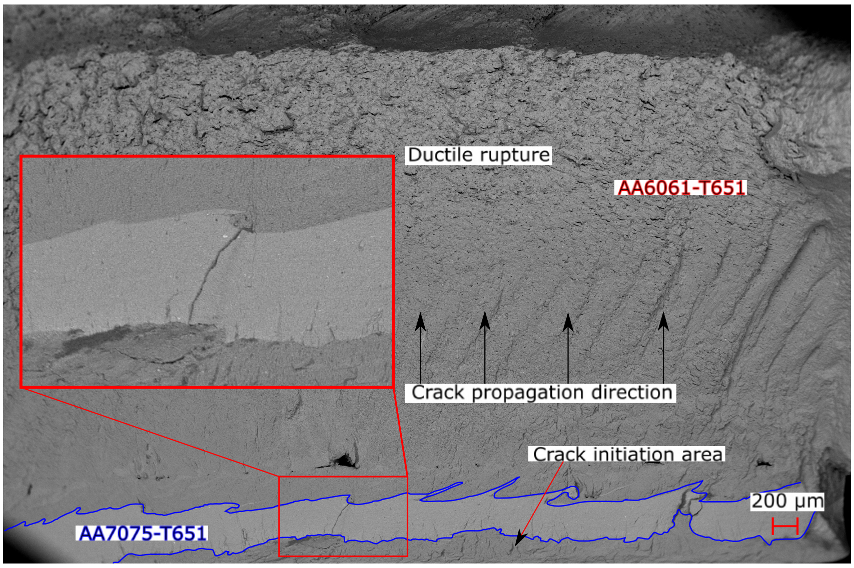

Figure V.13: BSE imaging of the fracture surface of a reference AA6061-AA7075 400 RPM, 120 mm/min, 10 kN welded joint. The stir zone is distinguishable in the crack propagation plane and both Al alloys are visible, meaning fracture happened exactly between the two plates. Also, holes are visible at the bottom of the apparent stir zone.

V.4 Conclusion

Fatigue life for FSW similar and dissimilar joints have been studied. Some general conclusions can be drawn from this study's results:

- Friction stir welded joints of dissimilar AA6061/AA7075 have been tested in fatigue. Results show that at high welding temperature and good stir zone mixing, dissimilar joints high cycle fatigue behavior are almost identical to the fatigue life of AA6061 similar joints. This result is coherent with conclusions drawn from tensile testing in Section IV.3, where dissimilar joints have macroscopic tensile properties similar to that of the weakest alloy in a dissimilar joint, i.e. AA6061 in this case.

- In the case of poor fatigue life related to low heat input during dissimilar welding, fractography has been performed on the fracture surfaces of said joints. A distinct defect in such welds have been shown to occur, leading to poor fatigue properties. This welding defect has not been seen in optical microscopy or tensile testing, rendering fatigue behavior prediction difficult.

Chapter VI

Conclusions and perspectives

VI.0..i Conclusions

Friction Stir Welding (FSW) is now a quite established process in various industrial sectors. Primarily aluminium alloys, but also copper and steel have seen industrial usage over the past two decades. However, it has so far to be implemented at a wider level inside the Thales Group, especially at the design stage. With this goal in mind, this PhD was devised and financed by Thales to achieve a global understanding of FSW of high strength aluminium alloy.

At first, a process window for aluminium to aluminium FSW had to be established. Based on a specific FSW steel tool, the welding parameters definition was explored in Chapter III. Dissimilar AA6061/AA7075 welding was used as a benchmark to determine welding parameters for all aluminium welding campaigns. Based on knowledge from the literature (see Section I.2.E) and experience from colleagues at UCLouvain, a process parameter window for these dissimilar joints have been successfully established using 3D visualization of said parameters along with basic thermal modelling based on general understanding of FSW process parameters described in the literature. Our approach to FSW of aluminium to aluminium through dissimilar welding was motivated in finding a way to transpose process parameters from one experimental plan to another. This work was successful in that regard, as process parameters from dissimilar aluminium welding were reused as is for AA7075 similar welding, and quickly adapted for AA6061 similar welding. Generally speaking, in dissimilar aluminium welding, the subsequent welding parameters derive from similar welding parameters of the strongest alloy considered in the dissimilar assembly. If confirmed for other couples of aluminium alloys, such a result could be of great interest in the future for a company like Thales, as design and research and development could be shortened.

Following the establishment of process parameters both for similar and dissimilar welding, Chapter IV details the tensile tests designed to mechanically characterize and understand the mechanical properties of aluminium FSW joints.

Regarding optical microscopy, a polishing and etching protocol yielding clear, contrasted macrographs in dissimilar aluminium welding **without** the use of any hydrofluoric acid has been found, contrary to more traditional etching methods involving Keller's or Kroll's reagents. Additionally, multiple stir zone morphologies have been observed for varying rotational speeds. Mainly, results from the literature have been confirmed [51, 85], i.e. stronger mixing occurs at higher rotational speed. But specifically in the case of dissimilar welding, questions were then raised regarding the mechanical properties of such heterogeneous welds.

Regarding hardness measurements of AA6061 similar welds, an increase in stir zone hardness at high rotational speed has been documented in this work. A probable cause has been laid out in the form of dissolution and coarsening of β phase hardening precipitates, giving naturally aged mechanical properties to high rotational speed (i.e. high welding temperature) welds. Additionally, it has been found that the stir zone of dissimilar welds exhibit a similarly interesting pattern. As the rotational speed increases, so does the hardness value and the size of the high hardness value zone inside the welded stir zone. These results were matched with observations made on macrographs of dissimilar welds (see Section IV.1.B), where stronger mixing has been observed as the rotational speed increases possibly due to AA7075 mixing. Interestingly, hardness values inside the stir zones of such dissimilar welds are higher than the AA6061-T6 base material. This fact rules out the sole explanation of reprecipitation of hardening phases of both alloys inside the stir. A possible explanation could be the diffusion of alloying elements between the AA7075 and AA6061. As the rotational speed increases, the stronger mixing and higher heat input allows such diffusion to occur.

Macroscopic tensile properties were then observed and detailed for all manufactured joints. General relationships between process parameters and measured tensile values (e.g. apparent yield strength, ultimate tensile strength, elongation at break) were established for all three types of aluminium welded joints, i.e. similar and dissimilar AA6061 and AA7075. Similarities and differences between similar and dissimilar welds were established. Industrially, such information is key to minimize research and development time as well as to optimize alloy choice and process parameters for a given part, knowing the limitation of some friction stir welded joints. However, especially in the case of dissimilar joints, strong local heterogeneities in strain distribution could be observed in DIC strain mapping. Local minimum in hardness values has been shown, in DIC, to correspond to strain localization areas during tensile testing. Particularly, the HAZ of AA6061 and AA7075 similar and dissimilar joints have shown severe strain localization during tensile testing, as the minimum in hardness for all welded joints is located in their respective HAZ. Difference in stir zone hardness has been shown to induce corresponding level of stir zone strain localization.

Thus, a micro tensile test under a scanning electron microscope has been carried out to better understand strain localization in the stir zone of heavily mixed dissimilar joints. Correlation between local alloying elements and strain localization in µm sized onion rings inside a dissimilar joint has been performed. Damage localization in such heterogeneous microstructure has been linked to coarsened inclusions in both Al alloys.

Industrially speaking, knowledge of general fatigue properties for metallic materials is crucial in design parts. Subsequently, Chapter V of this work focused on fatigue properties of friction stir welded joints, especially regarding dissimilar welding. A trend in heat input during manufacturing of said welds and their ensuing fatigue life was proposed. Interestingly, fatigue life results suggests that increasing weld heat in dissimilar joining is beneficial for fatigue life, contrary to what tensile testing suggest for static mechanical behavior. For low heat input welds, a particular defect has been observed in the stir zone, which had not been previously identified during optical microscopy and tensile testing. If the trend regarding heat input is confirmed for other aluminium alloys couples assembled via FSW, this result would have significant consequences as design teams would be required to compromise on this aspect of FSW joints.

VI.0..ii Perspectives

Throughout this work, multiple references are made to the hardening precipitates of AA6061 and AA7075, respectively β and η phase and their metastable precursors. However, conclusions reached on hardness or mechanical properties are, at best, educated guesses, as we were not able to directly observe these precipitates. One way to further characterize these welded joints would be through Transmission Electron Microscopy (TEM) analysis. By doing fine and deep analysis of the hardening precipitates in both alloys, further conclusions on overall mechanical properties could be reached. Now, as TEM sample preparation is quite time consuming, Differential Scanning Colorimetry (DSC) could also be an appropriate equipment to compare precipitates states in different zones of a larger amount of welds.

Specifically regarding the local mechanical properties described at the end of Chapter IV, EBSD could be proposed as an additional layer of analysis to refine the understanding of local mechanical properties with grain orientations and texture analysis. Additionally, other dissimilar assemblies could be tested to further study the local strain localization based on material mixing. Fatigue testing could also be done in such experimental setups to follow the damage occurrence and propagation at the local level.

Overall conclusions drawn from the analysis of process parameters on dissimilar welds need to be investigated further, with other aluminium to aluminium couples. For example, using a 5XXX strain hardened alloy in place of a precipitation hardened aluminium alloy could dramatically change some of the conclusions of this work on the optimization of Al to Al FSW. In general, fatigue life data on dissimilar alloys welding in only very limited in literature. Fatigue crack growth results would also bring further insight into the understanding of the fatigue behavior of these welds. In particular, it would allow to distinguish between the initiation and growth phase of fatigue life.

Industrially speaking, this work has been crucial for Thales. During this PhD, a qualification specification has been written as well as numerous documentations regarding Friction Stir Welding in general. The Friction Stir Welding of aluminium to aluminium has been investigated by other Thales entities before and during this work. Discussions and collaborations on those projects lead to prototypes of varying degree being manufactured, and in some cases tested. In the late stage of this work, a friction stir welded aluminium cold plate passed all quality control tests, including a pressurized leak test at 145 bars.

Appendix A

K. Colligan's data

Raw data provided by Mr Kevin Collingan from an unpublished work of his.

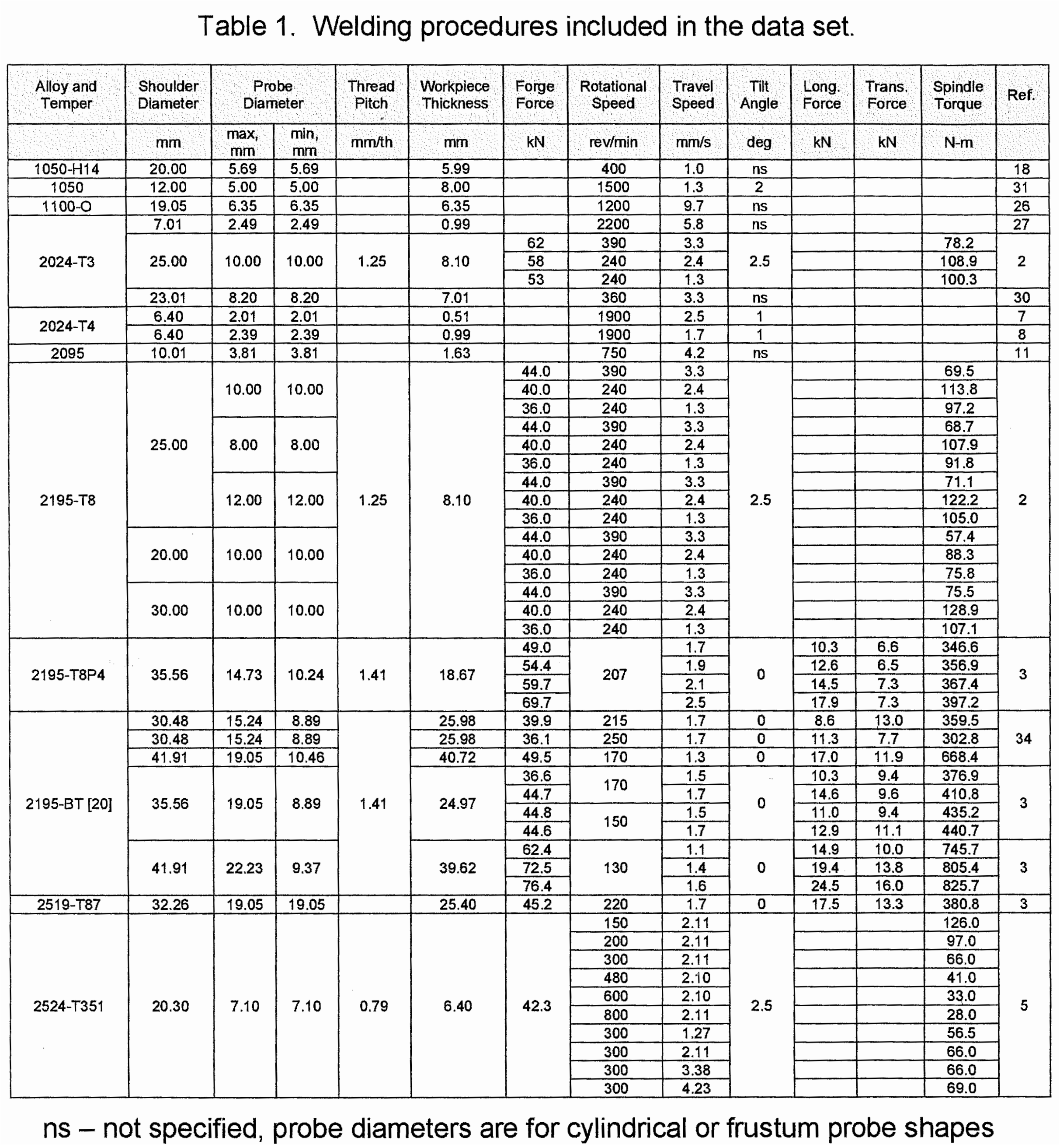

Table 1. Welding procedures included in the data set.

Alloy and Temper	Shoulder Diameter	Probe Diameter		Thread Pitch	Workpiece Thickness	Forge Force	Rotational Speed	Travel Speed	Tilt Angle	Long. Force	Trans. Force	Spindle Torque	Ref.
	mm	max, mm	min, mm	mm/th	mm	kN	rev/min	mm/s	deg	kN	kN	N-m	
1050-H14	20.00	5.69	5.69		5.99		400	1.0	ns				18
1050	12.00	5.00	5.00		8.00		1500	1.3	2				31
1100-O	19.05	6.35	6.35		6.35		1200	9.7	ns				26
2024-T3	7.01	2.49	2.49		0.99		2200	5.8	ns				27
	25.00	10.00	10.00	1.25	8.10	62	390	3.3	2.5			78.2	2
						58	240	2.4				108.9	
						53	240	1.3				100.3	
	23.01	8.20	8.20		7.01		360	3.3	ns				30
2024-T4	6.40	2.01	2.01		0.51		1900	2.5	1				7
	6.40	2.39	2.39		0.99		1900	1.7	1				8
2095	10.01	3.81	3.81		1.63		750	4.2	ns				11
2195-T8	25.00	10.00	10.00	1.25	8.10	44.0	390	3.3	2.5			69.5	2
						40.0	240	2.4				113.8	
						36.0	240	1.3				97.2	
		8.00	8.00			44.0	390	3.3				68.7	
						40.0	240	2.4				107.9	
						36.0	240	1.3				91.8	
		12.00	12.00			44.0	390	3.3				71.1	
						40.0	240	2.4				122.2	
						36.0	240	1.3				105.0	
	20.00	10.00	10.00			44.0	390	3.3				57.4	
						40.0	240	2.4				88.3	
						36.0	240	1.3				75.8	
	30.00	10.00	10.00			44.0	390	3.3				75.5	
						40.0	240	2.4				128.9	
						36.0	240	1.3				107.1	
2195-T8P4	35.56	14.73	10.24	1.41	18.67	49.0	207	1.7	0	10.3	6.6	346.6	3
						54.4		1.9		12.6	6.5	356.9	
						59.7		2.1		14.5	7.3	367.4	
						69.7		2.5		17.9	7.3	397.2	
2195-BT [20]	30.48	15.24	8.89	1.41	25.98	39.9	215	1.7	0	8.6	13.0	359.5	34
	30.48	15.24	8.89		25.98	36.1	250	1.7	0	11.3	7.7	302.8	
	41.91	19.05	10.46		40.72	49.5	170	1.3	0	17.0	11.9	668.4	
	35.56	19.05	8.89		24.97	36.6	170	1.5	0	10.3	9.4	376.9	3
						44.7		1.7		14.6	9.6	410.8	
						44.8	150	1.5		11.0	9.4	435.2	
						44.6		1.7		12.9	11.1	440.7	
	41.91	22.23	9.37		39.62	62.4	130	1.1	0	14.9	10.0	745.7	3
						72.5		1.4		19.4	13.8	805.4	
						76.4		1.6		24.5	16.0	825.7	
2519-T87	32.26	19.05	19.05		25.40	45.2	220	1.7	0	17.5	13.3	380.8	3
2524-T351	20.30	7.10	7.10	0.79	6.40	42.3	150	2.11	2.5			126.0	5
							200	2.11				97.0	
							300	2.11				66.0	
							480	2.10				41.0	
							600	2.10				33.0	
							800	2.11				28.0	
							300	1.27				56.5	
							300	2.11				66.0	
							300	3.38				66.0	
							300	4.23				69.0	

ns – not specified, probe diameters are for cylindrical or frustum probe shapes

Figure A.1

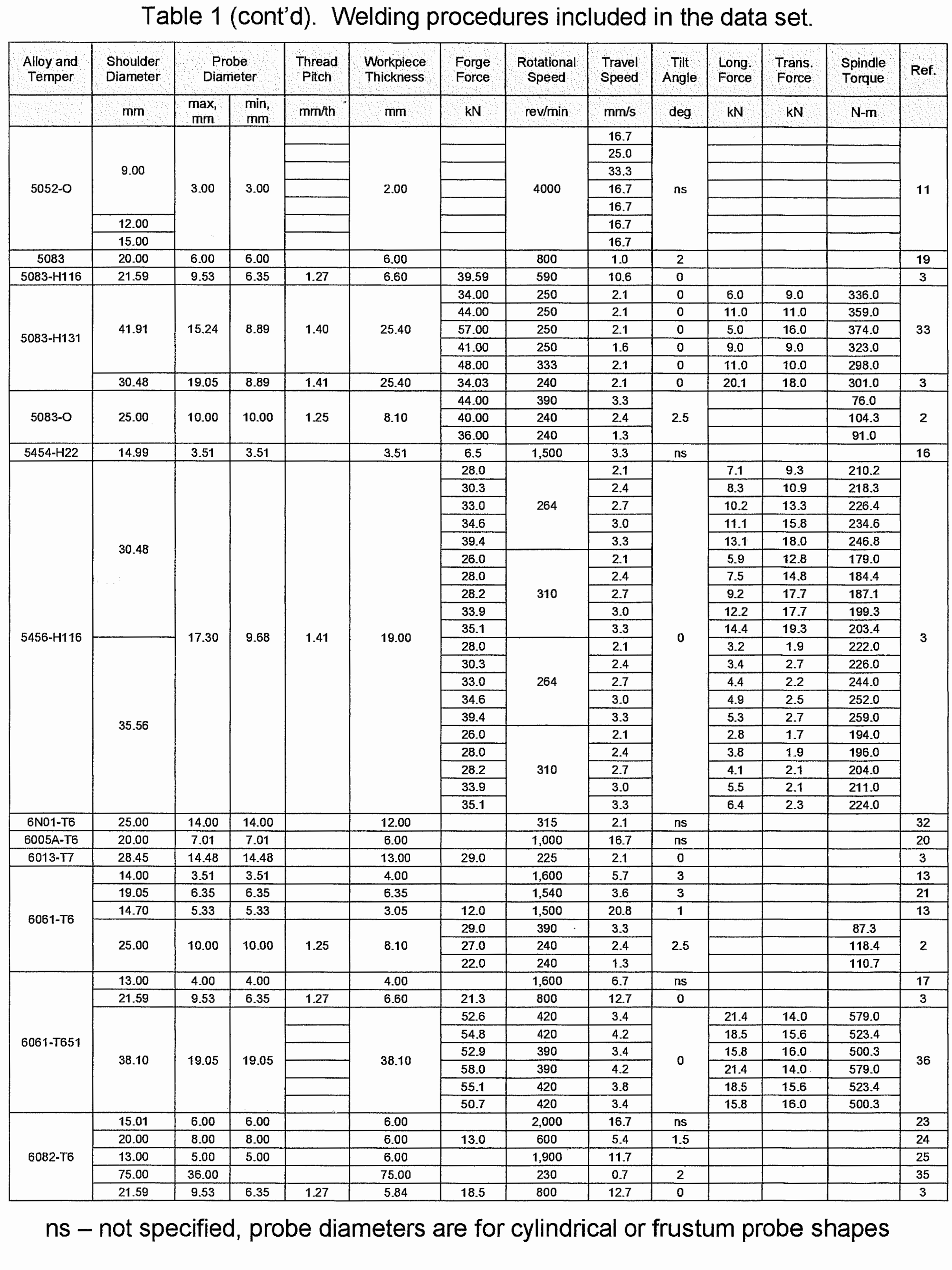

Table 1 (cont'd). Welding procedures included in the data set.

Alloy and Temper	Shoulder Diameter	Probe Diameter		Thread Pitch	Workpiece Thickness	Forge Force	Rotational Speed	Travel Speed	Tilt Angle	Long. Force	Trans. Force	Spindle Torque	Ref.
	mm	max, mm	min, mm	mm/th	mm	kN	rev/min	mm/s	deg	kN	kN	N-m	
5052-O	9.00	3.00	3.00		2.00		4000	16.7	ns				11
								25.0					
								33.3					
								16.7					
								16.7					
	12.00							16.7					
	15.00							16.7					
5083	20.00	6.00	6.00		6.00		800	1.0	2				19
5083-H116	21.59	9.53	6.35	1.27	6.60	39.59	590	10.6	0				3
5083-H131	41.91	15.24	8.89	1.40	25.40	34.00	250	2.1	0	6.0	9.0	336.0	33
						44.00	250	2.1	0	11.0	11.0	359.0	
						57.00	250	2.1	0	5.0	16.0	374.0	
						41.00	250	1.6	0	9.0	9.0	323.0	
						48.00	333	2.1	0	11.0	10.0	298.0	
	30.48	19.05	8.89	1.41	25.40	34.03	240	2.1	0	20.1	18.0	301.0	3
5083-O	25.00	10.00	10.00	1.25	8.10	44.00	390	3.3	2.5			76.0	2
						40.00	240	2.4				104.3	
						36.00	240	1.3				91.0	
5454-H22	14.99	3.51	3.51		3.51	6.5	1,500	3.3	ns				16
5456-H116	30.48	17.30	9.68	1.41	19.00	28.0	264	2.1	0	7.1	9.3	210.2	3
						30.3		2.4		8.3	10.9	218.3	
						33.0		2.7		10.2	13.3	226.4	
						34.6		3.0		11.1	15.8	234.6	
						39.4		3.3		13.1	18.0	246.8	
						26.0	310	2.1		5.9	12.8	179.0	
						28.0		2.4		7.5	14.8	184.4	
						28.2		2.7		9.2	17.7	187.1	
						33.9		3.0		12.2	17.7	199.3	
						35.1		3.3		14.4	19.3	203.4	
	35.56					28.0	264	2.1		3.2	1.9	222.0	
						30.3		2.4		3.4	2.7	226.0	
						33.0		2.7		4.4	2.2	244.0	
						34.6		3.0		4.9	2.5	252.0	
						39.4		3.3		5.3	2.7	259.0	
						26.0	310	2.1		2.8	1.7	194.0	
						28.0		2.4		3.8	1.9	196.0	
						28.2		2.7		4.1	2.1	204.0	
						33.9		3.0		5.5	2.1	211.0	
						35.1		3.3		6.4	2.3	224.0	
6N01-T6	25.00	14.00	14.00		12.00		315	2.1	ns				32
6005A-T6	20.00	7.01	7.01		6.00		1,000	16.7	ns				20
6013-T7	28.45	14.48	14.48		13.00	29.0	225	2.1	0				3
6061-T6	14.00	3.51	3.51		4.00		1,600	5.7	3				13
	19.05	6.35	6.35		6.35		1,540	3.6	3				21
	14.70	5.33	5.33		3.05	12.0	1,500	20.8	1				13
	25.00	10.00	10.00	1.25	8.10	29.0	390	3.3	2.5			87.3	2
						27.0	240	2.4				118.4	
						22.0	240	1.3				110.7	
6061-T651	13.00	4.00	4.00		4.00		1,600	6.7	ns				17
	21.59	9.53	6.35	1.27	6.60	21.3	800	12.7	0				3
	38.10	19.05	19.05		38.10	52.6	420	3.4	0	21.4	14.0	579.0	36
						54.8	420	4.2		18.5	15.6	523.4	
						52.9	390	3.4		15.8	16.0	500.3	
						58.0	390	4.2		21.4	14.0	579.0	
						55.1	420	3.8		18.5	15.6	523.4	
						50.7	420	3.4		15.8	16.0	500.3	
6082-T6	15.01	6.00	6.00		6.00		2,000	16.7	ns				23
	20.00	8.00	8.00		6.00	13.0	600	5.4	1.5				24
	13.00	5.00	5.00		6.00		1,900	11.7					25
	75.00	36.00			75.00		230	0.7	2				35
	21.59	9.53	6.35	1.27	5.84	18.5	800	12.7	0				3

ns – not specified, probe diameters are for cylindrical or frustum probe shapes

Figure A.2

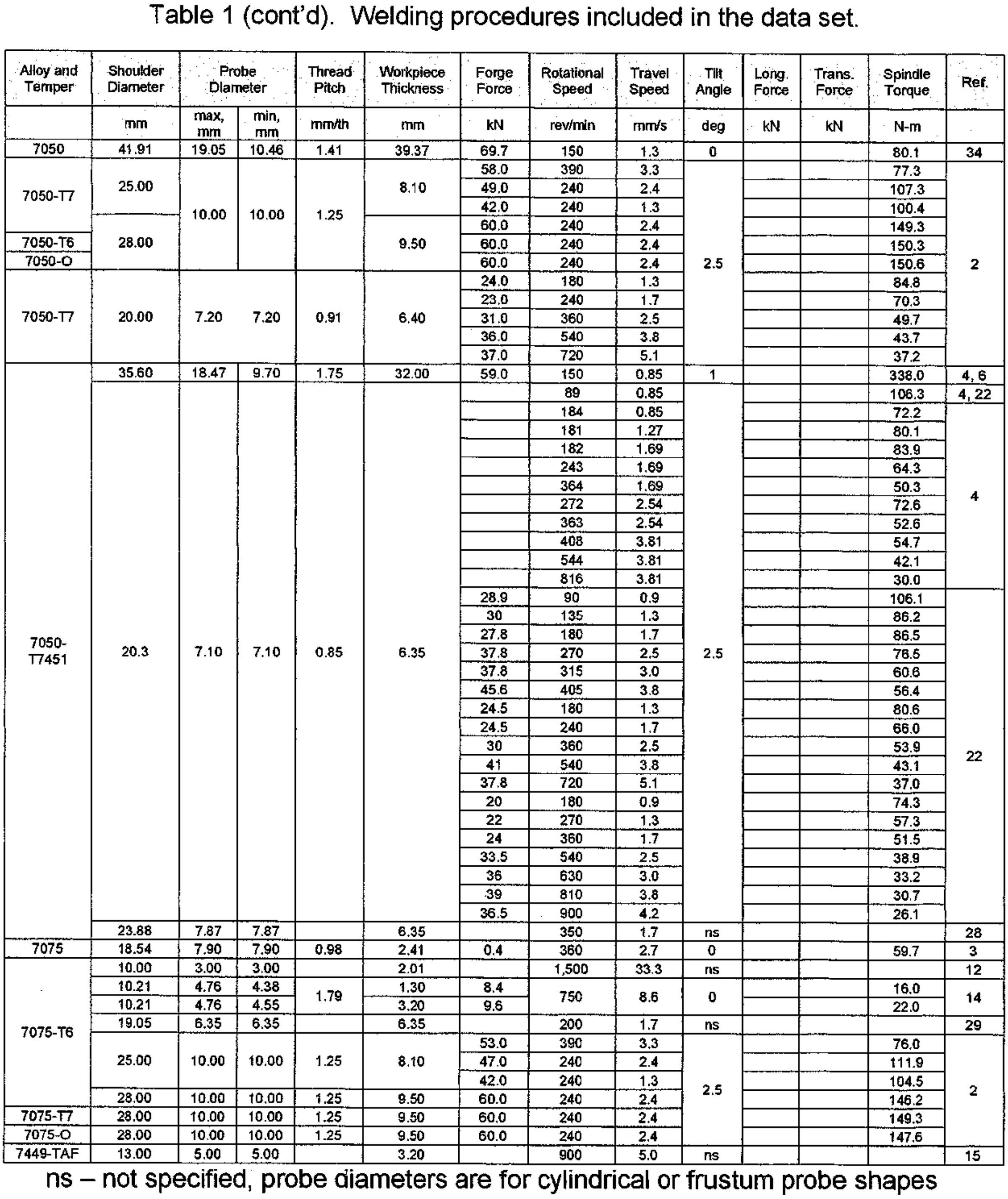

Table 1 (cont'd). Welding procedures included in the data set.

Alloy and Temper	Shoulder Diameter	Probe Diameter		Thread Pitch	Workpiece Thickness	Forge Force	Rotational Speed	Travel Speed	Tilt Angle	Long. Force	Trans. Force	Spindle Torque	Ref.
	mm	max, mm	min, mm	mm/th	mm	kN	rev/min	mm/s	deg	kN	kN	N-m	
7050	41.91	19.05	10.46	1.41	39.37	69.7	150	1.3	0			80.1	34
7050-T7	25.00	10.00	10.00	1.25	8.10	58.0	390	3.3	2.5			77.3	2
						49.0	240	2.4				107.3	
						42.0	240	1.3				100.4	
	28.00				9.50	60.0	240	2.4				149.3	
7050-T6						60.0	240	2.4				150.3	
7050-O						60.0	240	2.4				150.6	
7050-T7	20.00	7.20	7.20	0.91	6.40	24.0	180	1.3				84.8	
						23.0	240	1.7				70.3	
						31.0	360	2.5				49.7	
						36.0	540	3.8				43.7	
						37.0	720	5.1				37.2	
7050-T7451	35.60	18.47	9.70	1.75	32.00	59.0	150	0.85	1			338.0	4, 6
	20.3	7.10	7.10	0.85	6.35		89	0.85	2.5			106.3	4, 22
							184	0.85				72.2	4
							181	1.27				80.1	
							182	1.69				83.9	
							243	1.69				64.3	
							364	1.69				50.3	
							272	2.54				72.6	
							363	2.54				52.6	
							408	3.81				54.7	
							544	3.81				42.1	
							816	3.81				30.0	
						28.9	90	0.9				106.1	22
						30	135	1.3				86.2	
						27.8	180	1.7				86.5	
						37.8	270	2.5				76.5	
						37.8	315	3.0				60.6	
						45.6	405	3.8				56.4	
						24.5	180	1.3				80.6	
						24.5	240	1.7				66.0	
						30	360	2.5				53.9	
						41	540	3.8				43.1	
						37.8	720	5.1				37.0	
						20	180	0.9				74.3	
						22	270	1.3				57.3	
						24	360	1.7				51.5	
						33.5	540	2.5				38.9	
						36	630	3.0				33.2	
						39	810	3.8				30.7	
						36.5	900	4.2				26.1	
	23.88	7.87	7.87		6.35		350	1.7	ns				28
7075	18.54	7.90	7.90	0.98	2.41	0.4	360	2.7	0			59.7	3
7075-T6	10.00	3.00	3.00		2.01		1,500	33.3	ns				12
	10.21	4.76	4.38	1.79	1.30	8.4	750	8.6	0			16.0	14
	10.21	4.76	4.55		3.20	9.6						22.0	
	19.05	6.35	6.35		6.35		200	1.7	ns				29
	25.00	10.00	10.00	1.25	8.10	53.0	390	3.3	2.5			76.0	2
						47.0	240	2.4				111.9	
						42.0	240	1.3				104.5	
	28.00	10.00	10.00	1.25	9.50	60.0	240	2.4				146.2	
7075-T7	28.00	10.00	10.00	1.25	9.50	60.0	240	2.4				149.3	
7075-O	28.00	10.00	10.00	1.25	9.50	60.0	240	2.4				147.6	
7449-TAF	13.00	5.00	5.00		3.20		900	5.0	ns				15

ns – not specified, probe diameters are for cylindrical or frustum probe shapes

Figure A.3

Appendix B

FSW of Aluminium to Titanium

B.1 Titanium alloys

Ti-6Al-4V, sometimes called TA6V, has been used as the only source for titanium plate within this study. Titanium, and mainly its alloys, are today often selected for their remarkable mechanical properties, low density and good corrosion resistance. A comparison of material properties between titanium and some commonly used metals is shown in Table B.1. Because of its relatively high price, titanium remains a metal whose use is selective.

Pure titanium undergoes an allotropic transformation at 882°C from the body-centered cubic (BCC) β phase at high temperature to the pseudo-compact hexagonal α phase at lower temperature. This temperature is also referred to as the "β transus", which can be written T_β. Figure B.1 shows a representation of both these lattices.

The lattice parameters of α and β phases, at room temperature, are [177]:

- Hexagonal phase α : $c = 0.468nm$ and $a = 0.295nm$. These lattice parameters give a c/a ratio of 1.587, lower than the ideal ratio of 1.633 for a compact hexagonal lattice. Figure B.1(a) also shows the planes of maximum density: the basal plane (0002), one of the three prismatic $\{10\bar{1}0\}$ planes and one of the six pyramidal $\{10\bar{1}\}$ planes. The directions a_1, a_2 and a_3 are the directions of maximum density $< 11\bar{2}0 >$.

- β centred cubic phase: $a = 0.332nm$ with the crystallographic planes of maximum density $\{110\}$ and the four directions $< 111 >$.

Titanium is rarely used in its pure form. Several titanium alloys exist: Ti17, Ti40, Ti3Al2.5 or Ti5Al2.5Sn, depending on the intended use. The most commonly produced and used titanium alloy is Ti-6Al-4V.

The alloying elements of titanium alloys are classified into several categories: the *alphagenic* and *betagenic* elements according to their capacity to increase the stability domain of one or other of the crystallographic phases of titanium, as seen on Figure B.2. We will also find elements which will not have a significant impact on the microstructure of titanium [178]:

- The *alphagenic* elements: These elements promote the stability of the α phase. Aluminium is the most commonly used alphagenic alloying element. It is inserted as a substitution in the crystal lattice. It improves the creep strength and decreases

	Ti	Fe	Ni	Al
Melting temperature (°C)	1670	1538	1455	660
Allotropic transformation (°C)	$\beta \xrightarrow{882} \alpha$	$\gamma \xrightarrow{912} \alpha$	-	-
Crystal structure	bcc → hex	fcc → bcc	fcc	fcc
Young's modulus E, 21°C (GPa)	115	215	200	72
Bulk density (g/cm3)	4.5	7.9	8.9	2.7
Yield strength (MPa)	800-1200	230-1400	100-1200	90-500
Comparative Corrosion Resistance	Very Good	Poor	Fair	Good
Comparative oxygen reactivity	Very high	Low	Low	High

Table B.1: Comparative table of titanium and other common metals.

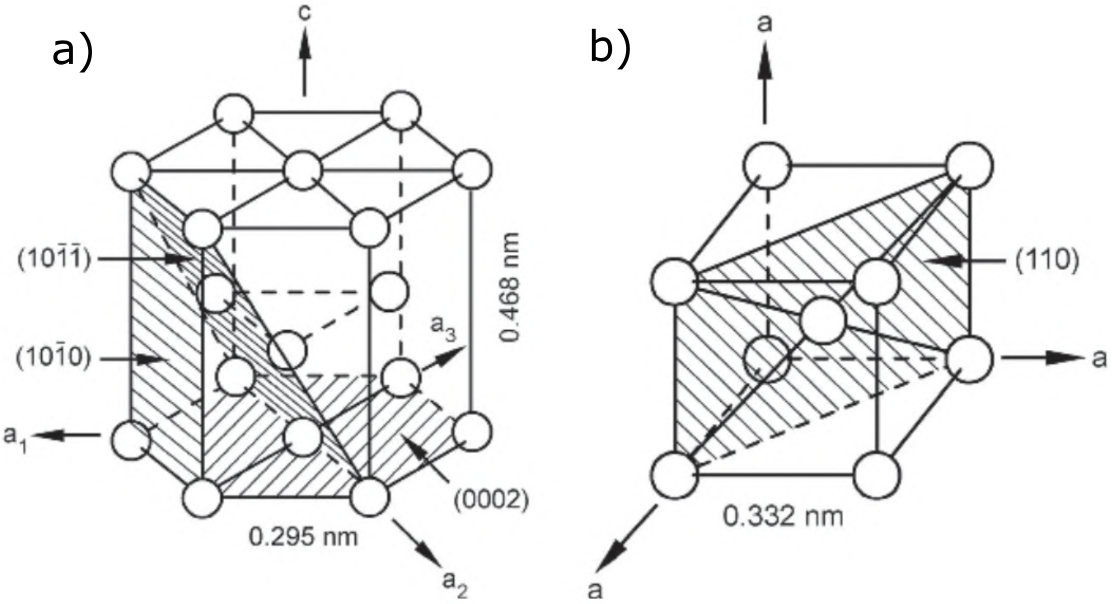

Figure B.1: (a) α and (b) β crystallographic lattice of titanium [177]

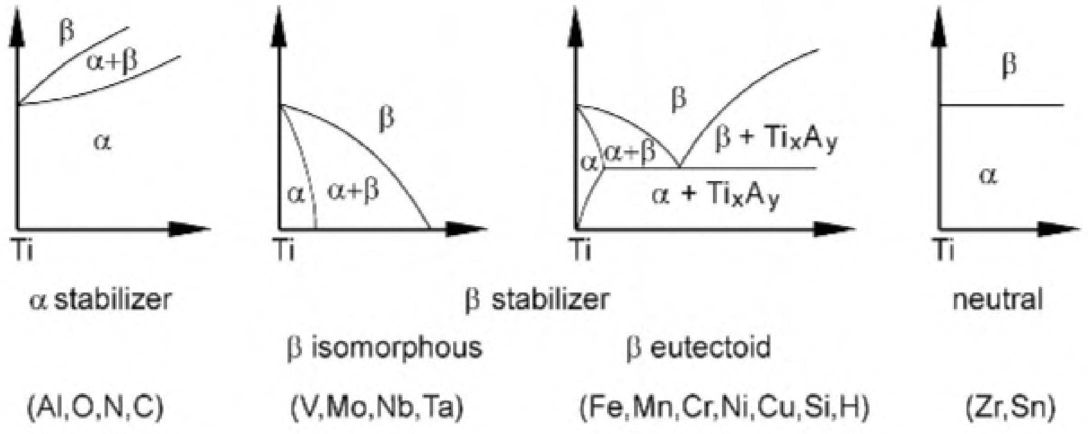

Figure B.2: Evolution of the titanium phase diagram as a function of the alloying element [177].

the ductility in tensile strength. Alphagenic interstitial elements such as boron, oxygen, nitrogen and carbon are also noted [179].

- Isomorphic elements: these elements lower the temperature of T_β and a sufficient concentration of these elements makes it possible to make the β phase stable at room temperature. These elements are miscible in all proportions in the crystal lattice. These elements include vanadium, molybdenum, nobium and tantalum.
- Eutectoid elements: these elements also lower the temperature T_β by forming precipitates with titanium. These elements include manganese, iron, chromium, silicon, nickel and copper.
- Neutral elements: these elements do not affect the phase diagram of titanium on their own. The most common neutral elements are zirconium and tin. On the other hand, these elements, in the presence of aluminium, are considered to be alphagenic elements [177].

A non exhaustive list of Ti alloy is presented in Table B.2. In this Table, the type of titanium alloy is provided. From the α and β phase fractions at room temperature, five categories of Ti alloys can be distinguished [179]:

- α alloys: made of 100% α phase
- Quasi-α alloys: have very little stable β phase and are close to α alloys
- Proper $\alpha + \beta$ alloys
- Quasi-β or β metastable alloys, having little α phase and close to β alloys
- β alloys: made of 100% β phase

Name (AFNOR)	Chemical composition (% mass)	Type	State of use	R_m (MPa)	$R_{p0.2}$ (MPa)	A (%)
Unalloyed Ti		α	Annealed	450	330	35
TA5E	Ti-5Al-2,5Sn	α	Annealed	900	800	20
TA6V	Ti-6Al-4V	$\alpha + \beta$	Annealed Quenched-tempered	1000 1150	900 1050	15 12
Ti-662	Ti-6Al-4V-2Sn	$\alpha + \beta$	Annealed Quenched-tempered	1050 1250	950 1150	12 10
TA4DE	Ti-4Al-4Mo-2Sn-0,5Si	$\alpha + \beta$	Quenched-Tempered	1120	1050	15
TV13CA	Ti-13V-11Cr-3Al	β	Hardened Quenched-tempered	950 1300	900 120	16 6
Ti-8Mn	Ti-8Mn	β	Annealed	900	800	10

Table B.2: Example of titanium alloys and their mechanical properties [178]. R_m is the ultimate tensile strength, $R_{p0.2}$ is the yield strength and A the elongation at break. The type of titanium alloy is also provided (α, $\alpha + \beta$, etc). This list of titanium alloys is non exhaustive.

B.2 State of the art: Aluminium to titanium FSW

The extensive use of Al in today's modern world has been discussed in Section I.2.D, FSW is easier to apply to Al alloys. On the other hand, the joining of dissimilar metals proves to be more challenging in many aspects. In this section, we'll explicit findings regarding Al to Ti FSW: its assembly process, microstructure and mechanical properties.

The first obstacle regarding the FSW of Al/Ti joints is the process parameters and especially the tool material selection and wear. Titanium having the stronger mechanical properties compared to aluminium in general, the tool material is primarily chosen based on the titanium metal. From tungsten based [180, 181], cobalt based [182, 183] and molybdenum based [184, 185] tools, similar Ti welds have been obtained in the past. Polycristalline Cubic Boron Nitride (PCBN) tools have also been used and excessive tool wear has been found to impact mechanical properties of the welded joints [186]. Figure B.3 shows intermetallic compounds created inside the Ti joints by the wear of the PCBN tool. Due to the extensive wear Ti FSW tools experience, it is crucial to understand the wear mechanisms and potential effect on the microstrucure.

Cases of FSW of Ti-6Al-4V alloy will now be discussed. In a review by Mironov et al. [21], the author presents several studies of FSW on this titanium alloy, and in particular hardness measurements. Figure B.4 shows the disparity that exists between different FSW studies. The complexity of titanium microstructures (see Section I.1) with its dual-phase and high sensitivity to high welding temperature with regard to the β phase lead to widely different results depending on the process parameters. It is also interesting to note the wide distribution of hardness measurements in the base material between Figure B.4(a,b,c). Mironov et al. [21] theorizes that the discrepancy probably originates from the variation of the material purity as well as the temperature of the mill-annealing

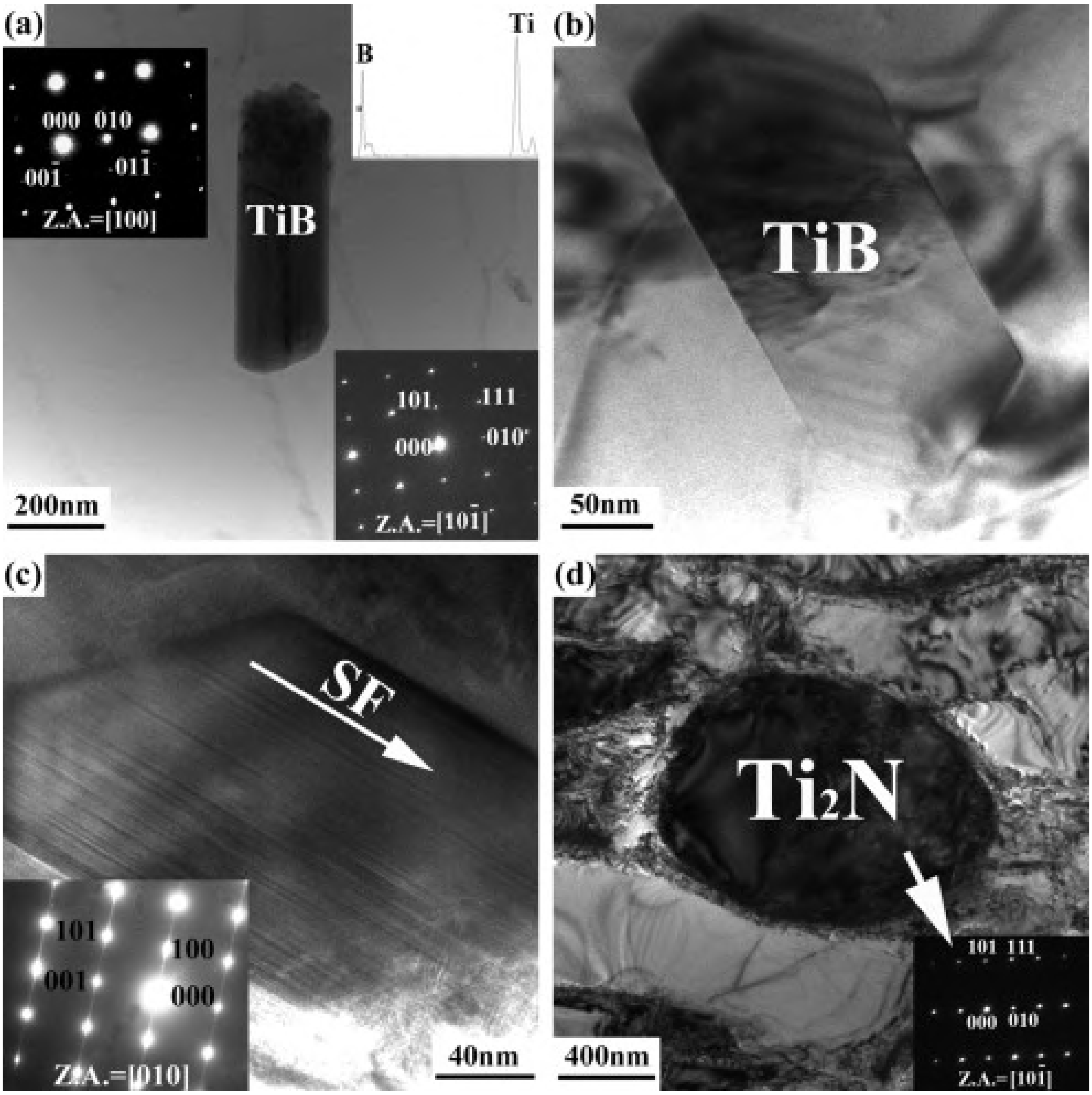

Figure B.3: TEM images of TiB phase with (a) a rod-shape with inserts showing SAD with two different zone axis patterns and an EDS image, (b) a hexagonal shape, (c) stacking faults, and (d) Ti2N phase. Tool wear inside the joint has created new intermetallic phases [186].

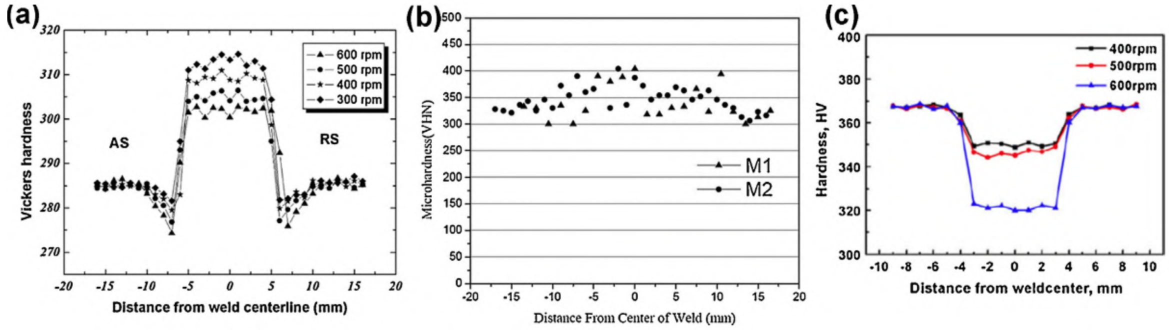

Figure B.4: Different microhardness profiles in Ti-6Al-4V after FSW from the review by Mironov et al. [21]. Scattering of hardness data is visible in the HAZ.

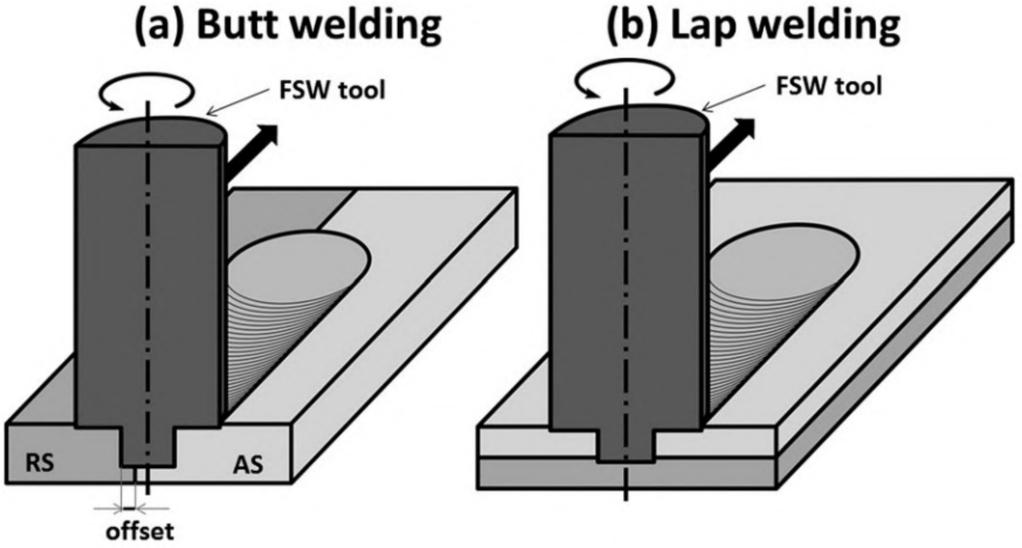

Figure B.5: Dissimilar friction stir welding for (a) butt and (b) lap joints. AS and RS are respectively the advancing and retreating sides. Tool offset in FSW butt joints is indicated [25]

treatment. It is noted that this could also contribute to the scattering of microhardness data.

With dissimilar welding in general, two approaches are encountered in the literature: overlap and butt joint welding. Figure B.5 illustrates the two welding configurations.

Specifically in the case of butt Al/Ti friction stir welds, Figure B.6 shows the effect of tool offset in the Ti-6Al-4V as well as with an increase in rotational speed on increasing Al and Ti mixing.

Overlap FSW of titanium and aluminium alloys have been studied in the literature [188–192]. On Figure B.7, multiple macrographs of the interface of Al/Ti FSW joints are presented. The interface mixing is found to be enhanced by an increase in rotational speed. At high RPM, the increase in advancing speed leads to a different scattering pattern of Ti particles in the Al matrix. High advancing speeds lead to crack formation at the interface.

On Figure B.8, an EDX analysis at the interface of an overlap FSW Ti/Al joint is

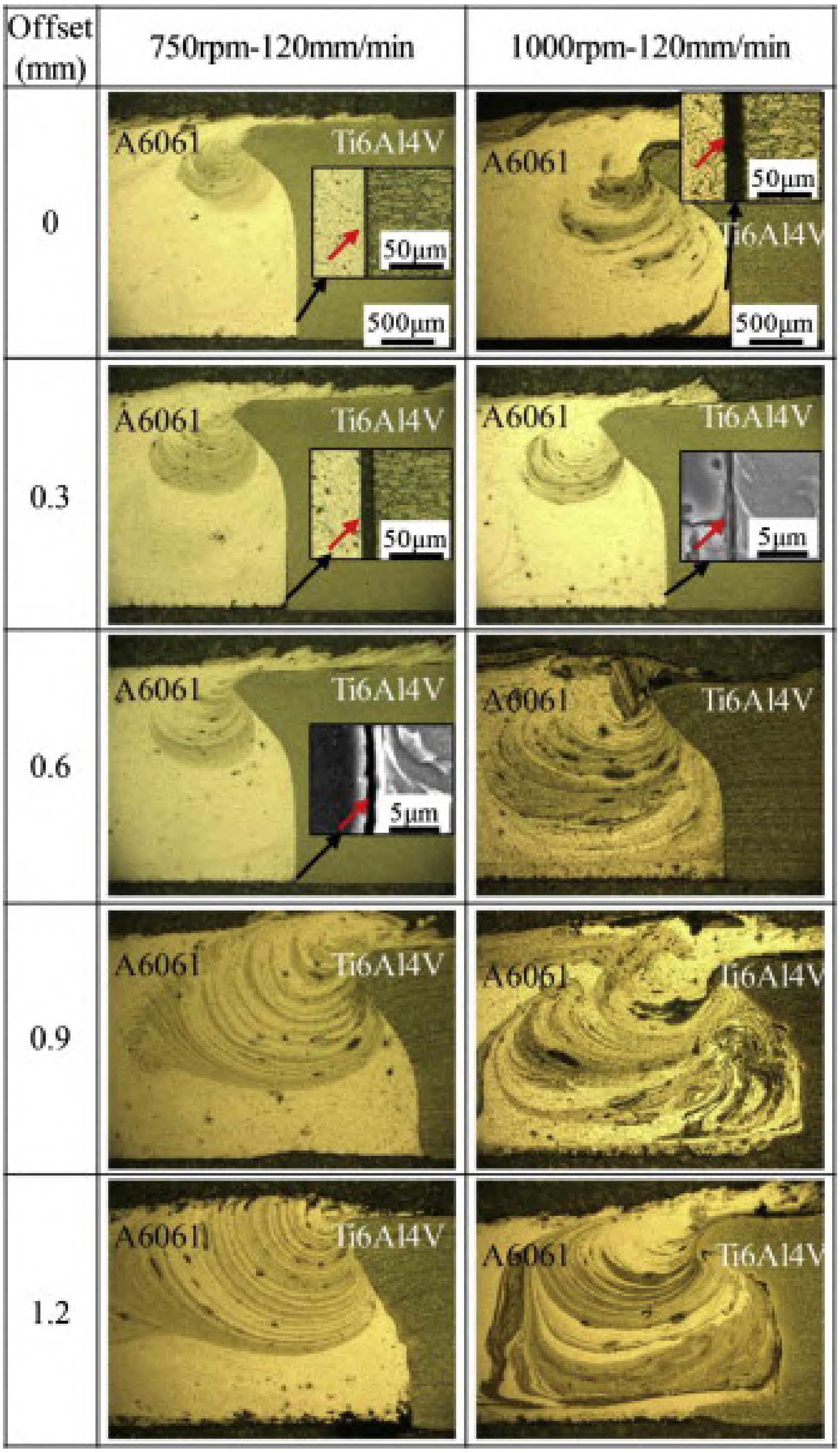

Figure B.6: Impact of the tool offset in a dissimilar AlTi butt welding configuration. Increase in tool offset and rotational speed favors mixing between the two alloys [187].

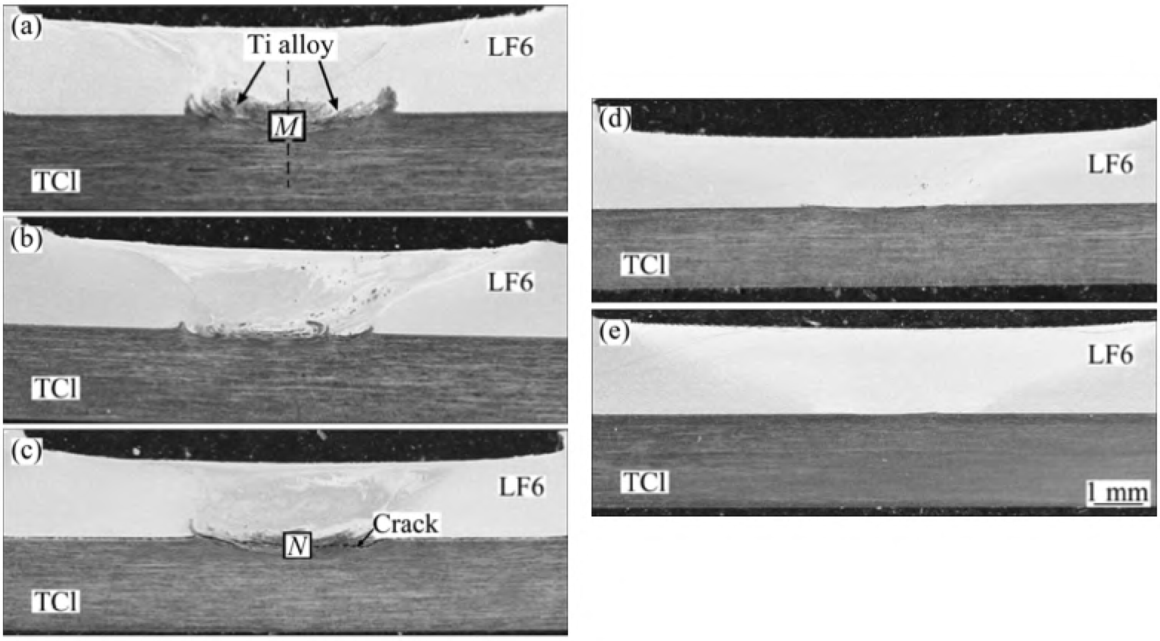

Figure B.7: Interface macrographs of lap joints Ti/Al dissimilar FSW for varying process parameters: (a) 1500 RPM and 60 mm/min (b) 1500 RPM and 118 mm/min (c) 1500 RPM and 150 mm/min (d) 950 RPM and 95 mm/min (e) 600 RPM and 95 mm/min [190].

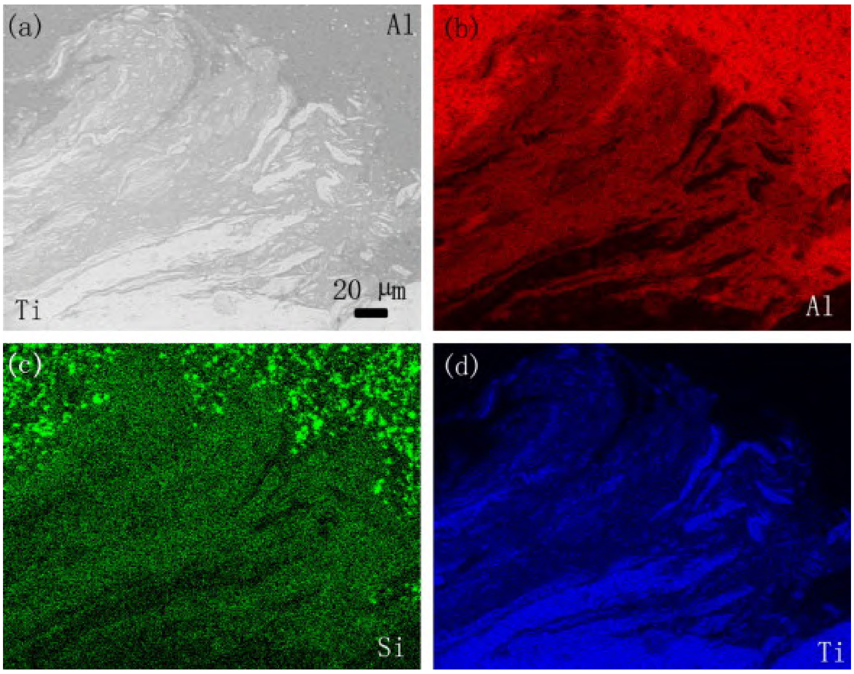

Figure B.8: EDX mapping of the interface in a FSW Al/Ti overlap joint. Ti and Al intermetallic compounds are generated [188].

presented. In Chen and Nakata [188], they observed that the materials in the welded zone have undergone the co-action of severe plastic deformation as well as high temperature. The combined effect of these phenomenon leads to the formation of Ti/Al intermetallic precipitates. The authors conclude that the transient phase $TiAl_3$ appears at the interface of the weld by diffusion reaction. The formation of this intermetallic is strongly influenced by the heat input, i.e. welding parameters, during welding.

In turn, the intermetallic formation at the interface during FSW has been linked to the mechanical properties of such welds, particularly in shear testing. Thus, on Figure B.9, two different behaviors in shear test of overlap FSW Al/Ti joints are presented [189]. On Figure B.9(a), the failure occurred at the lowest shear strength at the interface inside the titanium, compared to Figure B.9(b) where the fracture occurred perfectly at the interface, leaving the Ti/Al intermetallic to fully bear the load of the shear test. When no tool penetration occurs inside the titanium, temperatures reached during FSW inside the Al phase allow Al-to-Ti diffusion and the growth of an intermetallic interface. The thin (< 250 nm) interface layer has good shear strength and material mixing does not appear to strengthen these welded joints.

Now, in general, the lap welding of FSW of Al to Ti is still requiring further data and their mechanical properties are little detailed.

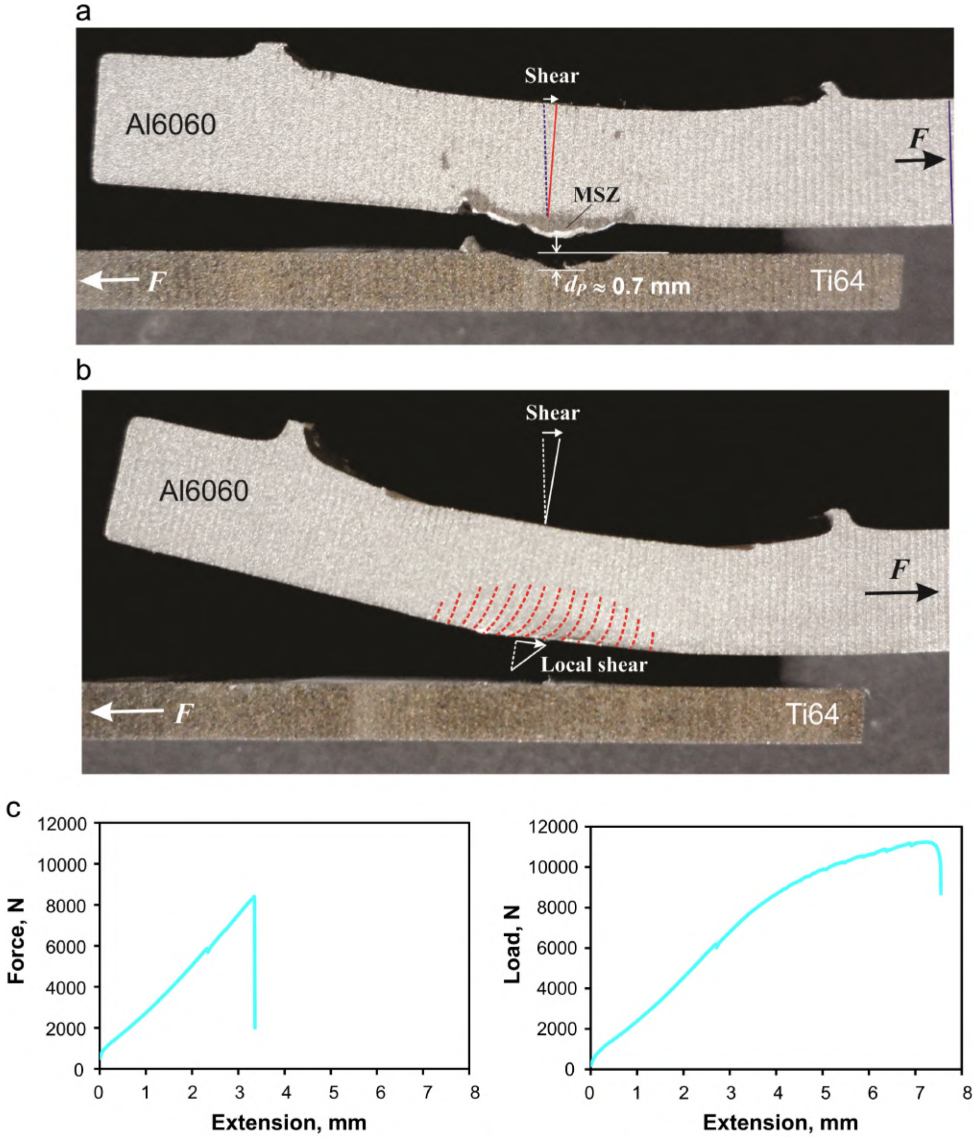

Figure B.9: Images of tensile-shear tested samples with (a) a low degree of shear strength and a fracture in the Ti alloy at the interface and (b) showing severe local shear and bending. (c) Load-extension curves of respectively sample (a) and (b) [189].

B.3 Aluminium AA6061-T6

During Al/Ti FSW joints manufacturing, 3 mm thick AA6061-T6 has been used. The alloying elements of this alloy has been measured via ICP (Induced Coupled Plasma) and is presented in Table B.3. The mechanical properties of such an alloy according to the EN 485-2 standard [115] is presented in Table B.4.

Alloying elements	Al	Cr	Cu	Fe	Mg	Mn	Ni	Si	Ti
6061-T6	Bal.	0.15	0.26	0.40	1.05	0.09	<0.10	0.47	0.01

Table B.3: Chemical composition (%wt) of the AA6061 alloy used in this study. Alloying elements composition were measure using Inductively Coupled Plasma (ICP).

Heat treatment	Thickness range (mm)	Min $R_{p0.2}$ (MPa)	Min R_m (MPa)	Min A (%)	Bend radius (°)	HBS hardness
T6/T651	3 to 6	240	290	10	$4.0 \times t$	88

Table B.4: Minimum requirements of T6 and T651 state AA6061 according to the EN 485-2 standard [115].

B.4 Titanium alloys and Ti-6Al-4V: Microstructures and mechanical properties

Ti-6Al-4V titanium alloy, sometimes referred as TA6V in french literature, is by far the most used titanium alloy in the aerospace sector. Multiple Thales products, especially at Thales Alenia Space, use TA6V. Its good ratio between strength, corrosion resistance and weight make it a prime candidate in multiple applications. The chemical composition of the Ti-6Al-4V used in this study is presented Table B.5. As mentioned in Table B.2, Ti-6Al-4V is a $\alpha + \beta$ Ti alloy, meaning that at room temperature, both titanium phases are stable in the microstructure. The proportion and morphology of these phases in the finished product vary widely depending on the manufacturing/casting process. In Ti-6Al-4V, what is called a "Widmanstätten" microstructure is often encountered. Microstructural evolution of titanium alloy during casting and forging is the $\beta \rightarrow \alpha$ transformation during cooling. On Figure B.10, the solidification path of a Widmanstätten microstructure in Ti-6Al-4V is presented.

Some of Ti-6Al-4V mechanical and physical properties are presented in Table B.6.

Alloying elements	Ti	Al	Cr	Fe	Ni	V
Ti-6Al-4V	Bal.	5.48	0.01	0.2	0.01	4.15

Table B.5: Chemical composition (%wt) of Ti-6Al-4V used in this study. Alloying elements composition were measure using Inductively Coupled Plasma (ICP).

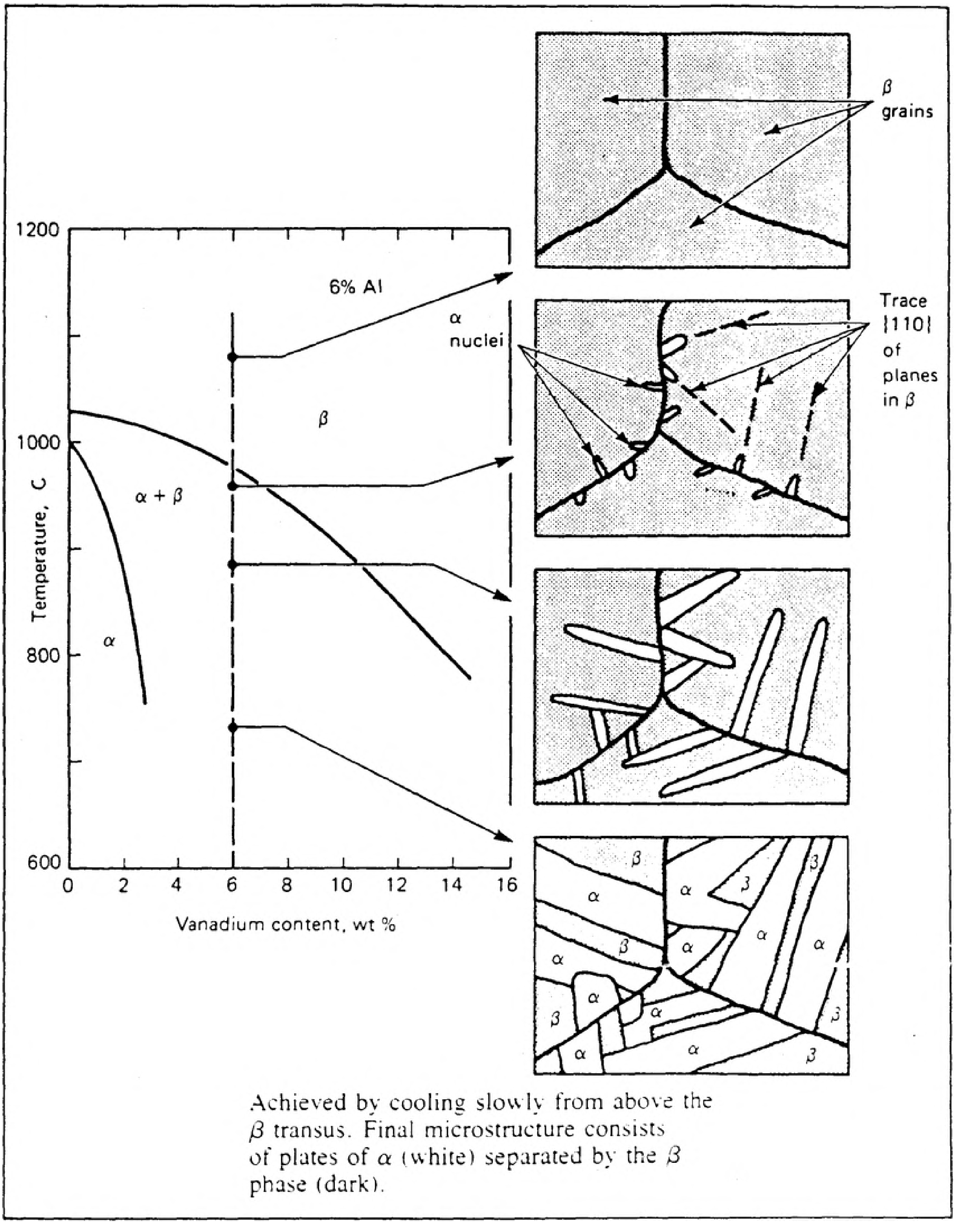

Achieved by cooling slowly from above the β transus. Final microstructure consists of plates of α (white) separated by the β phase (dark).

Figure B.10: Solidification path of the Widmanstätten microstructure inside Ti-6Al-4V [194].

Physical property	Value	Unit
Room temperature density	4420-4430	kg/m^3
Coefficient of thermal expansion at 20°C	$8-9\times10^{-6}$	K^{-1}
Coefficient of thermal expansion at 800°C	11×10^{-6}	K^{-1}
Thermal conductivity at 20°C	5.8-7.1	W/mK
Thermal conductivity at 800°C	16	W/mK
β transus, T_β	980-995	°C
Solidus temperature	1640	°C
Liquidus temperature	1660	°C
Young's modulus at 20°C	100-130	GPa
Young's modulus at 300°C	90	GPa
Young's modulus at 600°C	62	GPa
$R_{p0.2}$	950-1050	MPa
R_m	1050-1140	MPa
Elongation at break	15	%

Table B.6: General mechanical and physical properties of Ti-6Al-4V titanium alloy [193].

B.5 Al/Ti welds manufacturing

Dissimilar Al/Ti joints are manufactured in an overlap configuration. 200×80 mm plates of AA6061 and Ti-6Al-4V are overlapped in a specifically designed clamping mechanism. In this case, the 3 mm thick AA6061-T651 is on top of the 1 mm thick Ti-6Al-4V plate. Figure B.11 shows a schematic of the welding apparatus.

Before welding, both plates are roughly polished using a 320SiC grit paper and cleaned with ethanol and paper wipes. Similarly to Al/Al FSW, welds are force controlled. A picture of the welding setup is shown on Figure B.12.

On Figure B.13, two tools used in FSW Al/Ti are presented. These tools are composed of an steel body and shoulder, and a removable tip composed of 25% rhenium (Re) and

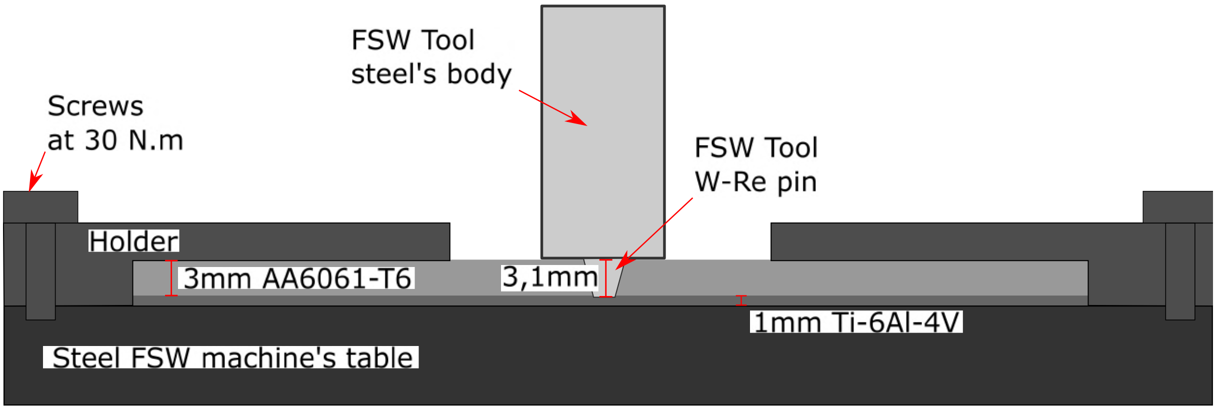

Figure B.11: Schematic of the welding setup for dissimilar AA6061-T651 and Ti-6Al-4V.

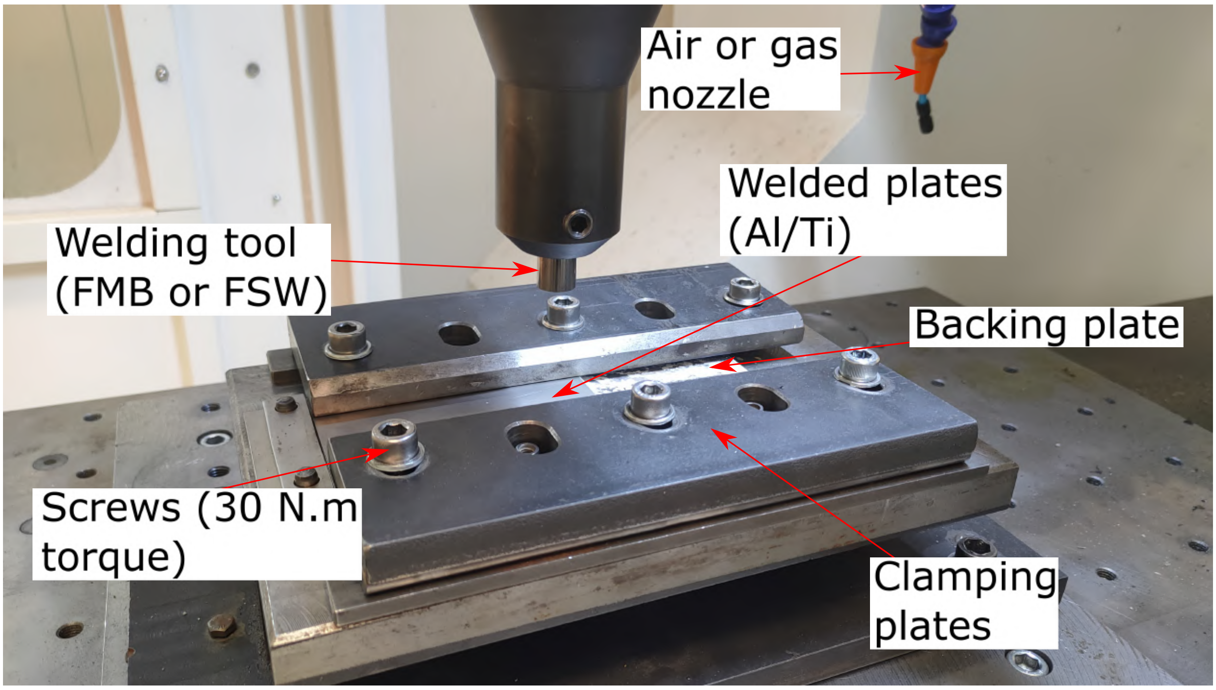

Figure B.12: Picture of the welding apparatus for dissimilar AA6061-T651 and Ti-6Al-4V. Here a different tool is installed instead of the FSW Al/Ti tool.

75% tungsten (W). The tool tip composition is similar to references found in the literature [180]. These tools were provided by StirWeld, a french tooling company. Similarly to the FSW Al/Al tool, the shoulder is grooved and the pin is threaded. The tool body and shoulder are steel based to keep manufacturing cost as low as possible as well as maximizing the heat generation of the tool, as the friction coefficient between steel and aluminium is high.

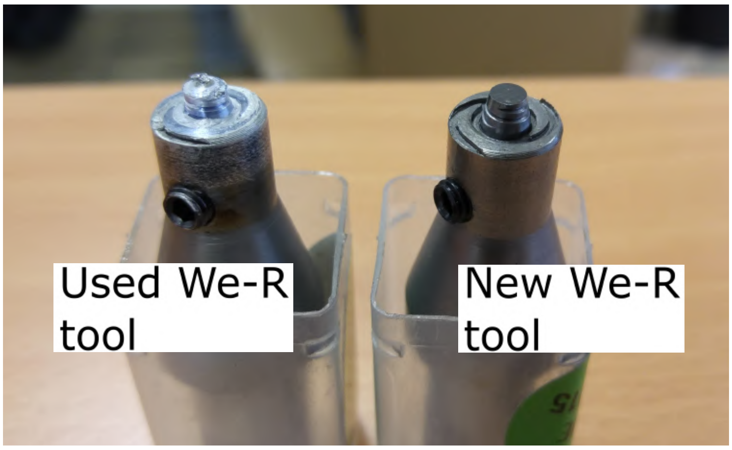

Figure B.13: We-R tools used in the manufacturing of Al/Ti FSW joints. The left tool is slightly used and aluminium is stuck on the tool tip. By comparison of the two tools, slight wear is visible on the tool tip of the used one.

B.6 Aluminium to titanium dissimilar FSW: results

In this study, dissimilar Al/Ti overlap FSW joints have been manufactured. The joining of aluminium alloy to titanium has potential applications in the aerospace industry, and especially in Thales. For example ,Yu et al. [192] mentions a potential application of overlap welding of Al skin to Ti ribs in aircraft frame manufacturing. Today's space age and its extensive use of aluminium and titanium could see potential applications of FSW overlap as well.

A similar experimental plan as described for Al/Al joints has been conducted to get a better understanding of Al/Ti overlap joints with regards to the process parameters. Optical macrographs have been performed, as well as hardness measurements in order to analyze the effect of process parameters on the morphology of the welded joints. Finally, tensile shear testing shows an apparent relationship between the obtained microstructure and the shear strength of the manufactured joints.

B.6.A Process parameters

The manufacturing of Al/Ti overlap joints has been conducted at UCLouvain. The same FSW machine as the Al/Al joints has been used. In Chapter II, Section II.2 details the machine, the welding fixing devices and tooling used. As a reminder, the Al/Ti joints are manufactured in an overlap configuration with the Al plate placed on top. The Al is a 3 mm thick AA6061-T6 alloy and the Ti alloy is 1 mm Ti-6Al-4V (see Section II.1 for chemical compositions). The welds were manufactured in a **force control** mode set at 5.5 kN. The axial load was determined from literature review as well as rapid position control spot welds to estimate the axial load's order of magnitude for sound joints. The process parameters used in this study are:

- **3 rotational speeds:** 600, 800 and 1000 RPM has been used to manufacture these joints.
- **3 advancing speeds:** for each rotational speed, three different advancing speeds have been used.

- **A single axial load** of 5.5 kN has been used.

All joints showed no significant defects, e.g. worm hole or delamination of the welded plates. Figure B.13 shows the tool used, composed of a W-25%Re tip. The pin length was set to 3.1 mm. The welds were done in a force control environment, but the 0.1 mm extra length on the tool tip compared with the Al plate thickness was chosen deliberately in order to favor some mixing of the Ti inside the Al matrix. The tool rotated in a clockwise manner.

B.6.B Optical microscopy

Figure B.6.C shows, the optical macrographs **without** etching. The retreating and advancing sides are shown on the macrographs.

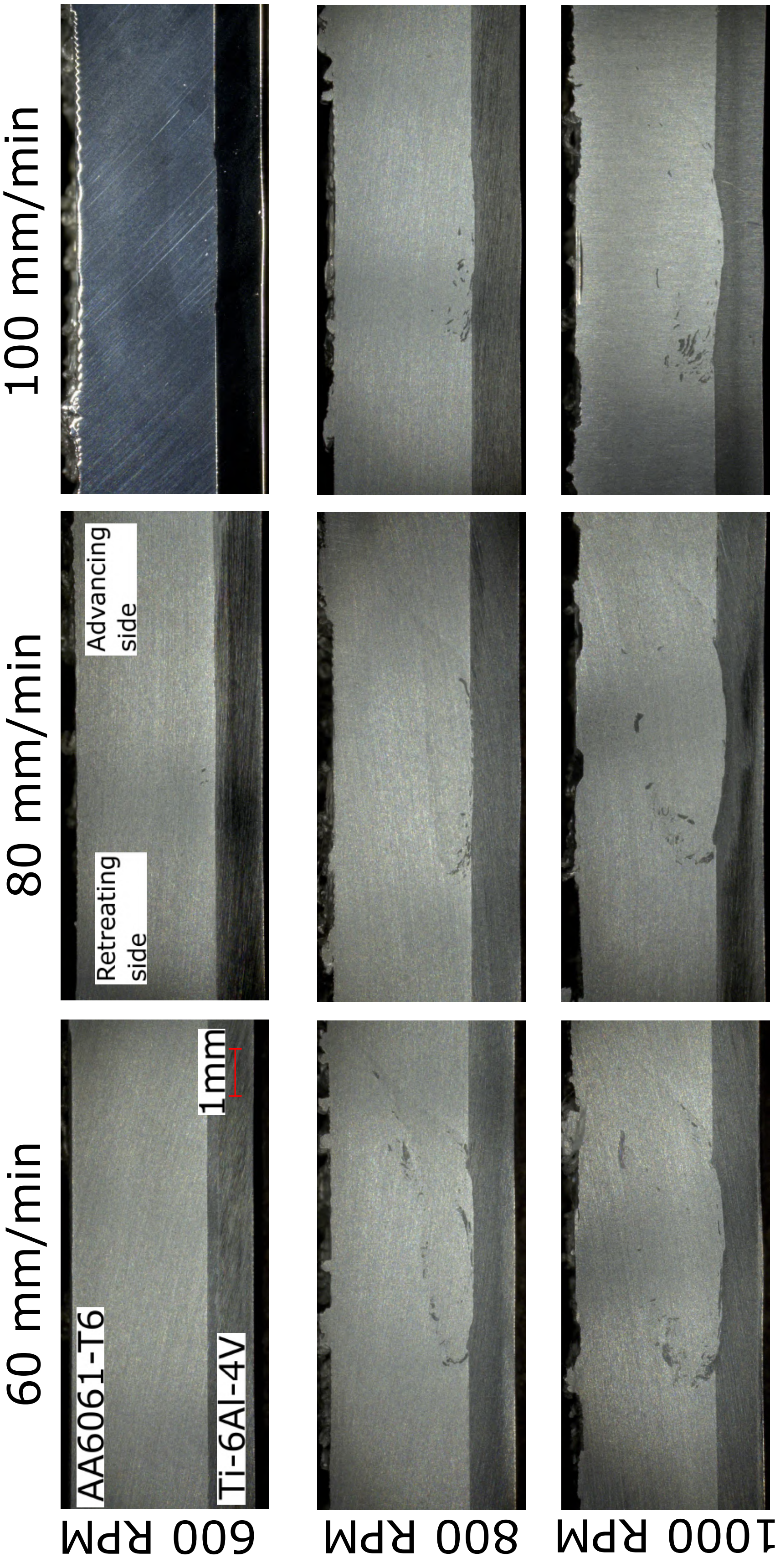

Figure B.14: Optical macrographs on Al/Ti FSW overlap joints, without eching. Three rotational and advancing speeds have been used to manufacture these joints. A single axial load set at 5.5 kN was used. The advancing side is on the right.

On these macrographs, the increase in **rotational speed** favors the mixing of Ti inside the Al matrix. Indeed, from 600 RPM to 1000 RPM, for a given advancing speed, more Ti particles of various sizes are pushed inside the Al matrix. Additionally, an indent inside the Ti plate starts to appear at 800 RPM and is more prominent at 1000 RPM. This observation is coherent with what has been reported in the literature [189, 190], and is discussed in Section B.2.

The higher rotational speed has probably a double effect. On the one hand, a higher rotational speed increases mechanical mixing. The same behavior has been noted in Section IV.1.B on Al/Al dissimilar welding. This effect is expected to contribute the most to general Ti dispersion inside the Al matrix. On the other hand, a higher rotational speed during welding means a higher welding temperature. Especially in the case of our overlap welded joints, where the tool shoulder is composed of steel and rubs against an Al plate, rendering the local heat generation similar to what has been described for Al/Al welding in Section III.4. Knowing this, and again drawing parallels with Al FSW in general, a higher welding temperature leads to material softening. In our force controlled weld, this would translate in a slightly deeper plunging of the tool tip inside the Ti plate. Ti being much harder than Al, and especially at high temperature (see Section B.4 for high temperature strength), the tool tip does not plunge deeper than a few µm. However, this small difference in force controlled plunging depth probably contributed to the indent created in the Ti plate.

Figure B.14 also shows the effect of **advancing speed**. For a given RPM, an increase in advancing speed leads to less Ti particles inside the Al matrix. At 800 RPM, this effect is clearly visible. At 1000 RPM, the mixing of Ti inside the Al matrix still occurs, but much of the Ti particles appear to be close the welding interface.

As described in Section III.4, increasing the advancing speed in a weld leads to a lower heat input and faster cooling rate. In turns, this decrease in local heat input would lead to less material softening. This effect would counteract what has been previously described with the rotational speed influence. The macrographs would tend to corroborate this hypothesis.

In conclusion, the general impact of process parameters, i.e. rotational and advancing speed, on the heat generation in a dissimilar overlap welds closely resembles those described for Al/Al welding. An increase in weld temperature, through a RPM increase or an advancing speed decrease, leads to higher material mixing and the creation of an indent inside the bottom Ti plate. Inversely, a decrease in welding temperature has the opposite effect. The creation of the indent in the Ti plate is attributed to the tool tip plunging, in force control mode, inside the Ti as the Al top plate softens due to increased welding temperature. The wider and deeper the indent is, the more Ti particles are dispersed inside the Al matrix. Understanding the effect of this material mixing on mechanical properties is crucial in understanding the subsequent mechanical properties.

On Figure B.15, a BackScatter Electron (BSE) image of a Ti particle inside the Al matrix is presented, as well as two Energy Dispersive X-ray spectroscopy (EDX) maps from this area, one for Al and the other for Ti. On Figure B.15(c), the BSE image shows that the Ti particle inside the Al matrix is broken apart. This particle is quite massive (around 150 µm in length) compared with the expected grain size of the Al microstructure, i.e. an equiaxed, fine microstructure with grains about a dozen µm in diameter (see Figure I.32). The additional BSE images for Al and Ti, respectively Figures B.15(c) and B.15(d), show probable diffusion of the Al inside the Ti and the likely formation of

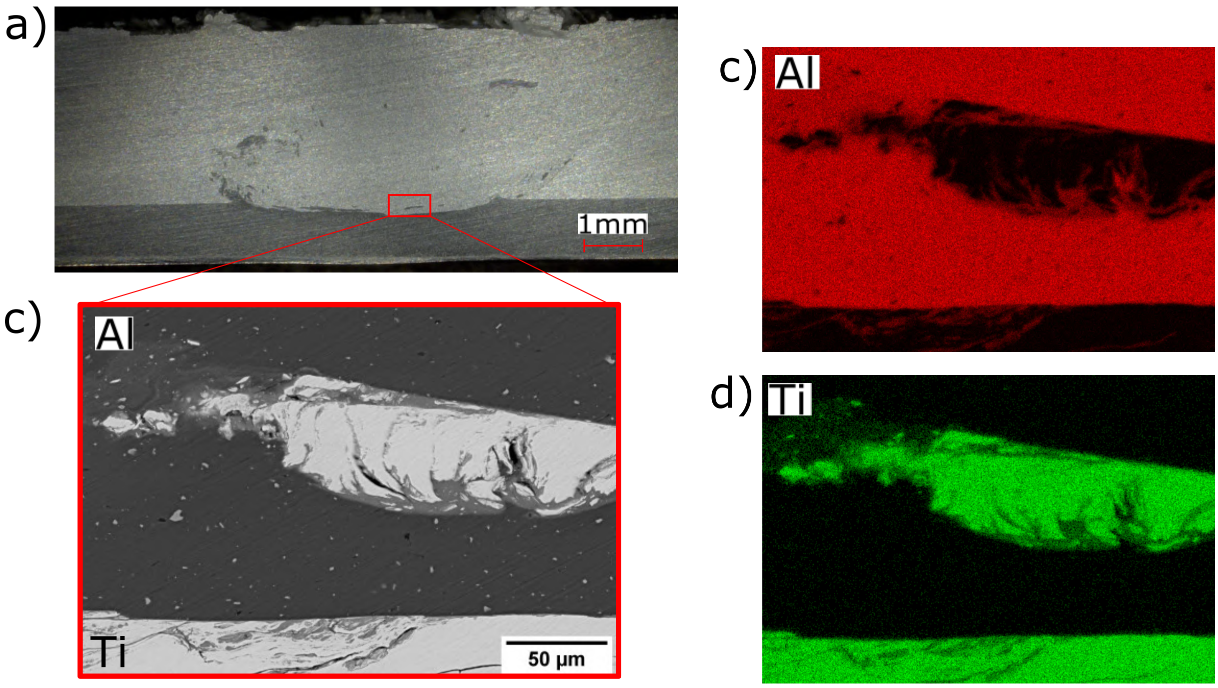

Figure B.15: (a) Macrograph of the 1000 RPM, 60 mm/min sample with (c) a backscatter electron image on of the Ti particle inside the Al matrix along with the energy dispersive x-ray maps of (c) Al and (d) Ti. The two phases are clearly distinguishable from one another in BSE. EDX seems to indicate material diffusion at the boundary between the two metals.

intermetallic (IM) compound. Indeed, the interface between the Al and Ti plate shows "stripes" of different contrast in BSE imaging that coincides with the EDX analysis. Additionally, the area surrounding the Ti particle shows both presence of Al and Ti in EDX analysis. This could be related to the size limitation of EDX analysis as it would get X-ray signals from both the Al matrix and the Ti particle in such a narrow area of analysis, but could also indicate the most likely presence of Al/Ti IM, as observed in literature [190, 192]. The impact of this IM layer (thickness, chemical composition) on mechanical properties has to be assessed.

B.6.C Hardness measurements

Hardness measurements have been performed on Al/Ti overlap joints. The hardness measurements were taken at the centerline of the Al plate, i.e. 1.5 mm below the plates top surface. Hardness measurement protocol is explained in Section II.4.A. Additional care was taken in order to avoid indenting in large, clearly visible Ti particles inside the Al matrix. The hardness data is presented such so that the advancing side is located in the x positive value, i.e. on the right of the graphs, in accordance with the way macrographs are presented in Figure B.14.

Figure B.16(a,b,c) presents the hardness measurements for 60, 80 and 100 mm/min welds. Thus, the impact of the **rotational speed** on hardness can be assessed at any given advancing speed.

Figure B.16(a), i.e. for 60 mm/min joints, shows a strong influence of the rotational speed in the stir zone. Indeed, an increase in RPM lead to a substantial increase in stir zone hardness, but only when reaching a rotational speed as high as 1000 RPM. No strong difference is noted between the 600 and 800 RPM samples in the stir zone. Additionally, increasing the rotational speed increases the width of the Heat Affected Zone (HAZ), as evidenced by the 600 and 1000 RPM samples.

Figure B.16(b), i.e. for 80 mm/min joints, shows an increase in stir zone hardness across all the rotational speeds, contrary to Figure B.16(a). In this instance, the stir zone hardness increased from 600 to 800 and then 1000 RPM. However, the width of the HAZ appears to be less affected by a RPM increase compared to 60 mm/min welds.

Figure B.16(c), i.e. for 100 mm/min joints, shows a similar influence of rotational speed on the stir zone, i.e. a RPM increase leads to a stir zone hardness increase. A similar effect to what has been described on Figure B.16(b), but the stir zone hardness for the 1000 RPM sample is significantly higher. Again, the width of the HAZ appears to be affected to a lesser degree when compared with Figure B.16(a).

In conclusion, an increase in rotational speed leads to an increase in stir zone hardness. This could result from two distinct phenomenon. On the one hand, the welding temperature increases with the rotational speed. As it has been described in Section IV.2.A, the β phase hardening precipitate of AA6061 could have been dissolved back into the Al matrix, forming new GP zones during natural aging of the welded sample and thus, increasing local hardness and mechanical properties. This effect is also corroborated by the larger HAZ when the RPM increases as discussed in in similar AA6061 welds (see Section IV.2.A) On the other hand, the macroscopic images described in the previous Section showed extensive mixing of Ti particles inside the Al matrix as the rotational speed increases. The size and distribution of these particles, as well as the potential diffusion of Ti inside the Al matrix could explain the increase in hardness value. Additionally, the absolute hardness value in the 60 and 100 mm/min curves (maximum of 110 HV at 1000 RPM and 60 mm/min in Ti/Al FSW) substantially higher than those observed in similar welding of AA6061 (maximum of 90 HV in the stir zone, see Figure IV.7), confirming that both phenomenon probably occur here.

Figure B.17(a,b,c) shows the hardness measurements for respectively 600, 800 and 1000 RPM. Thus, the impact of the **advancing speed** at a given RPM can be described.

Figure B.17(a), i.e. for 600 RPM joints, shows no significant impact of the advancing speed on the hardness can be noted. The stir zone hardness as well as the width of the HAZ are similar for all advancing speeds.

Figure B.17(b), i.e. for 800 RPM joints, shows an increase in advancing speed leads to an increase in stir zone hardness. Indeed, the hardness values for 80 and 100 mm/min are substantially higher compared with the 60 mm/min sample. On the other hand, the width of the HAZ does not appear to be significantly influenced.

Finally, Figure B.17(c), i.e. for 1000 RPM joints, shows an increase in advancing speed leads to an increase in stir zone hardness. However, contrary to 800 RPM joints, all advancing speeds have relatively high stir zone hardness to begin with, but the 100 mm/min sample has a substantially higher stir zone hardness. In this instance however, the width of the HAZ is slightly affected by the advancing speed, as it widens when the advancing speed increases.

In general, it appears that increasing the advancing speed at a given RPM leads to an increase in stir zone hardness and no notable effect is noted on the width of the HAZ. This result is interesting as it differs from the observations made in AA6061 similar hardness measurements, where no notable effect was observed on the stir zone hardness and a

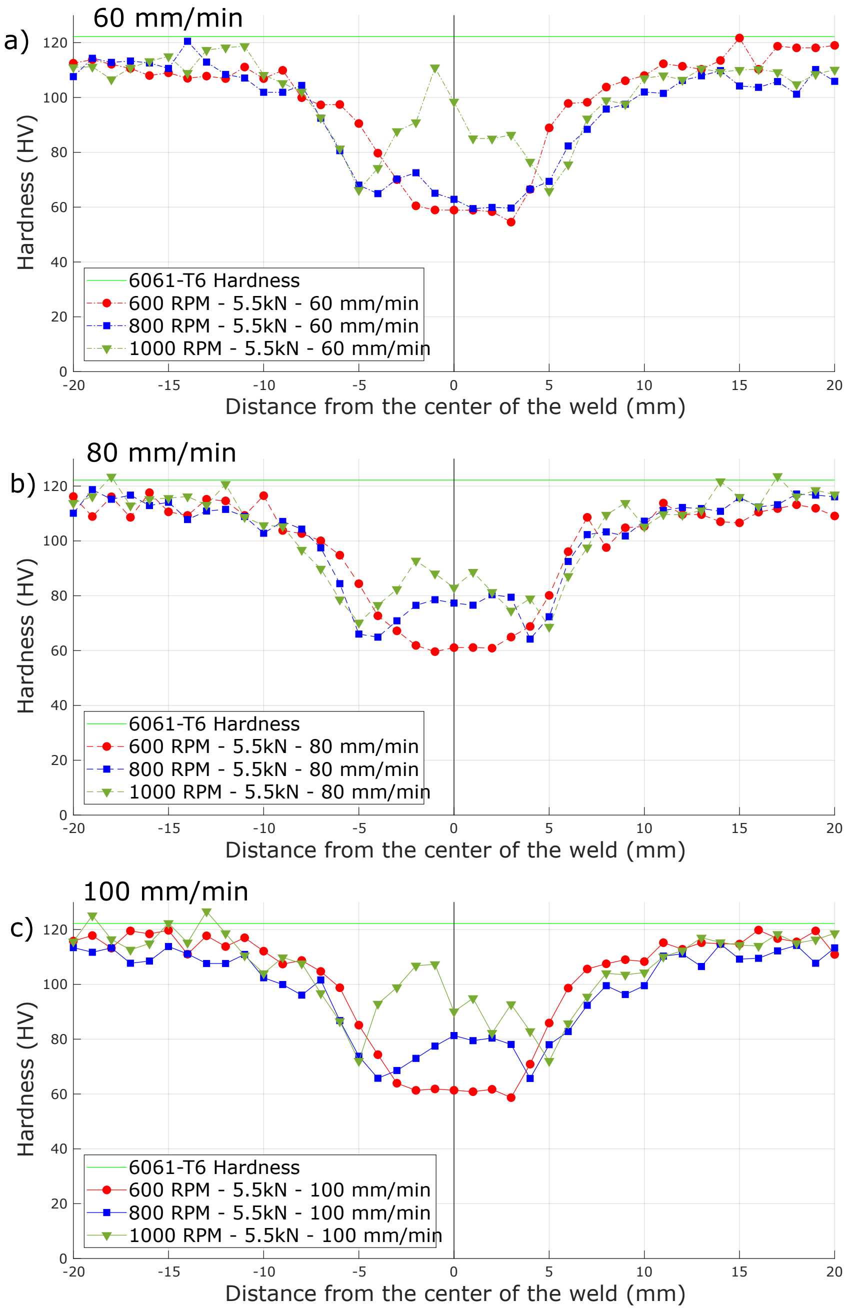

Figure B.16: Hardness measurements inside the Al plate for Al/Ti FSW overlap joints for three different rotational speeds at (a) 60, (b) 80 and (c) 100 mm/min.

distinctly larger HAZ was observed, at high rotational speed, for hotter welds, i.e. lower advancing speeds.

As a general conclusion of the hardness measurements, the effect of the welding parameters are in line with AA6061 similar welds. Hotter welds lead to larger HAZ. Now, the specificity of dissimilar Al/Ti friction stir welds is the presence of Ti debris in the stir zone that cause substantial local hardening.

B.6.D Lap shear testing

Finally, lap shear tests were conducted on Al/Ti FSW overlap joints. Samples were extracted from the welded joints and prepared by hand polishing up to 2400SiC. An MTS 250 kN tensile machine was used. Only the data for 60 mm/min welds will be exploited in this Section.

Figure B.18 shows the fracture location of the shear tested sample. At 600 RPM the sample broke at the interface between Al and Ti, whereas it broke in the Ti plate for 800 and 1000 RPM samples.

The load data for each tested samples is shown on Figure B.19(a) and is compared with the fracture strength of the base Ti alloy on Figure B.19(b). Overall, the shear load is almost identical between the different samples, with a distinct fracture behavior at low rotational speed. This difference in fracture behavior does not appear to be correlated with hardness measurements, as seen on Figure B.16(a). However, a clear distinction between these samples on macrographs, especially at the Ti/Al interface can be described. On Figure B.14, at 60 mm/min, the increase in rotational speed from 600 RPM to 800 RPM and 1000 RPM leads to a threshold effect on the mixing of alloys: at 600 RPM, no mixing of the two alloys is visible, whereas some Ti particles are mixed in the Al matrix at 800 and 1000 RPM.

Chen and Yazdanian [189] shows that when the tool tip does not plunge into the Ti plate, high temperature welding leads to diffusion of alloying elements and the creation of a particularly thin IM layer. This IM layer, contrary to the mixing of Ti particles in the Al matrix, shows significantly better mechanical properties, as seen in Section B.2 on Figure B.9. On Figure B.20, Yu et al. [192] has shown that the shear strength of such welds depends heavily on the thickness of the IM layer at the interface between the Al and Ti plate. In this study's case, a potentially similar effect could be responsible for the observed shear test results. However, additional observations are required to fully conclude on this study's findings.

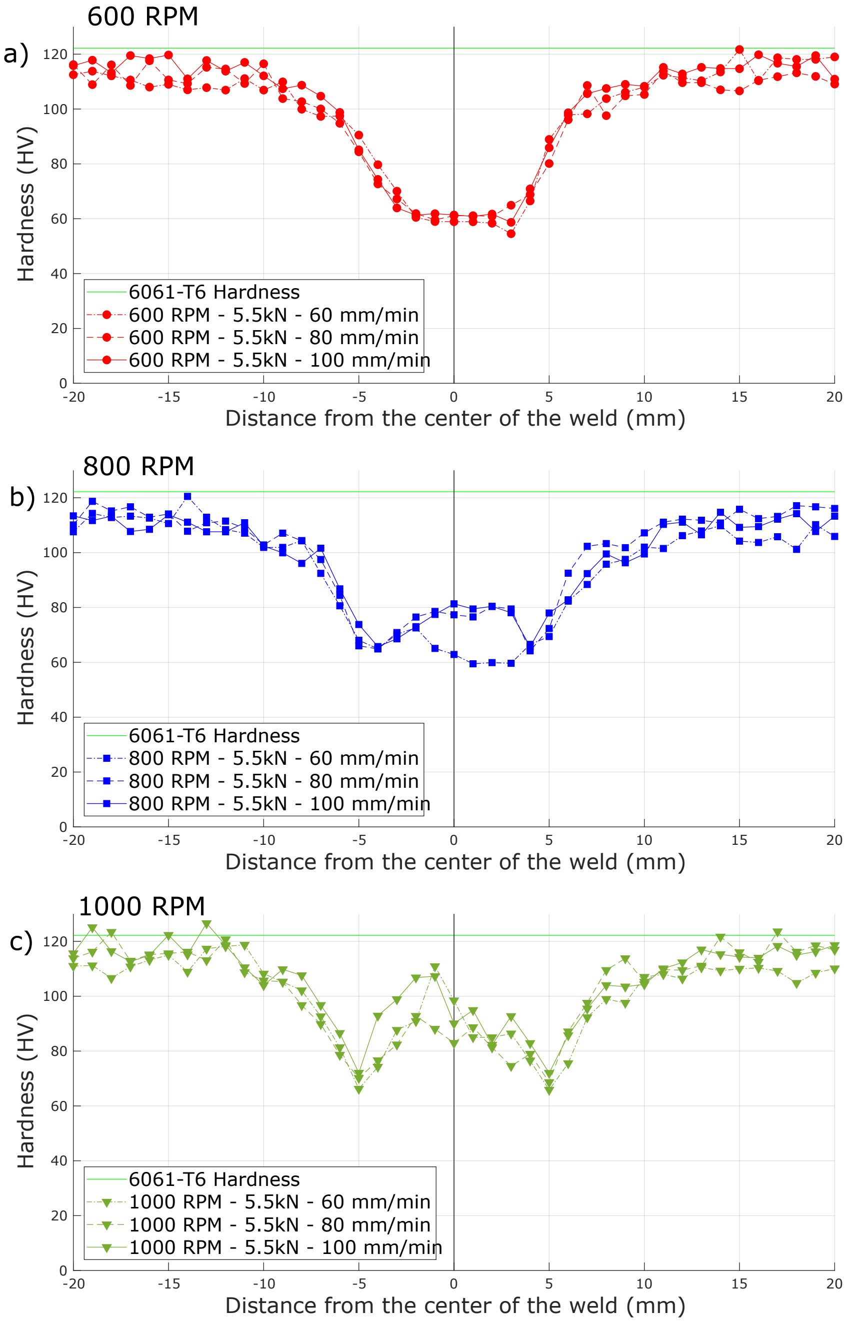

Figure B.17: Hardness measurements inside the Al plate for Al/Ti FSW overlap joints for three different advancing speeds at (a) 600, (b) 800 and (c) 1000 RPM.

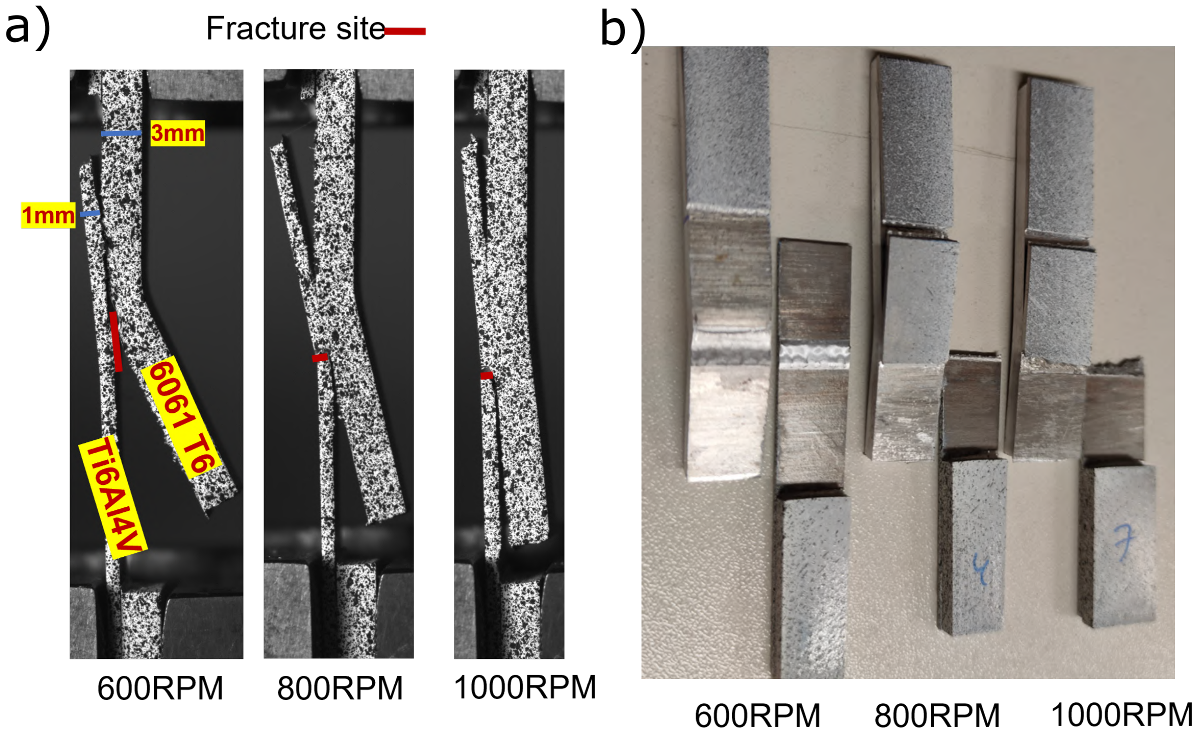

Figure B.18: (a) Pictures showing the location of failure of shear tested FSW samples at 60 mm/min. Failure occurs at the interface for the 600 RPM joint and in the titanium plate at 800 and 1000 RPM samples, as can been additionally seen on (b).

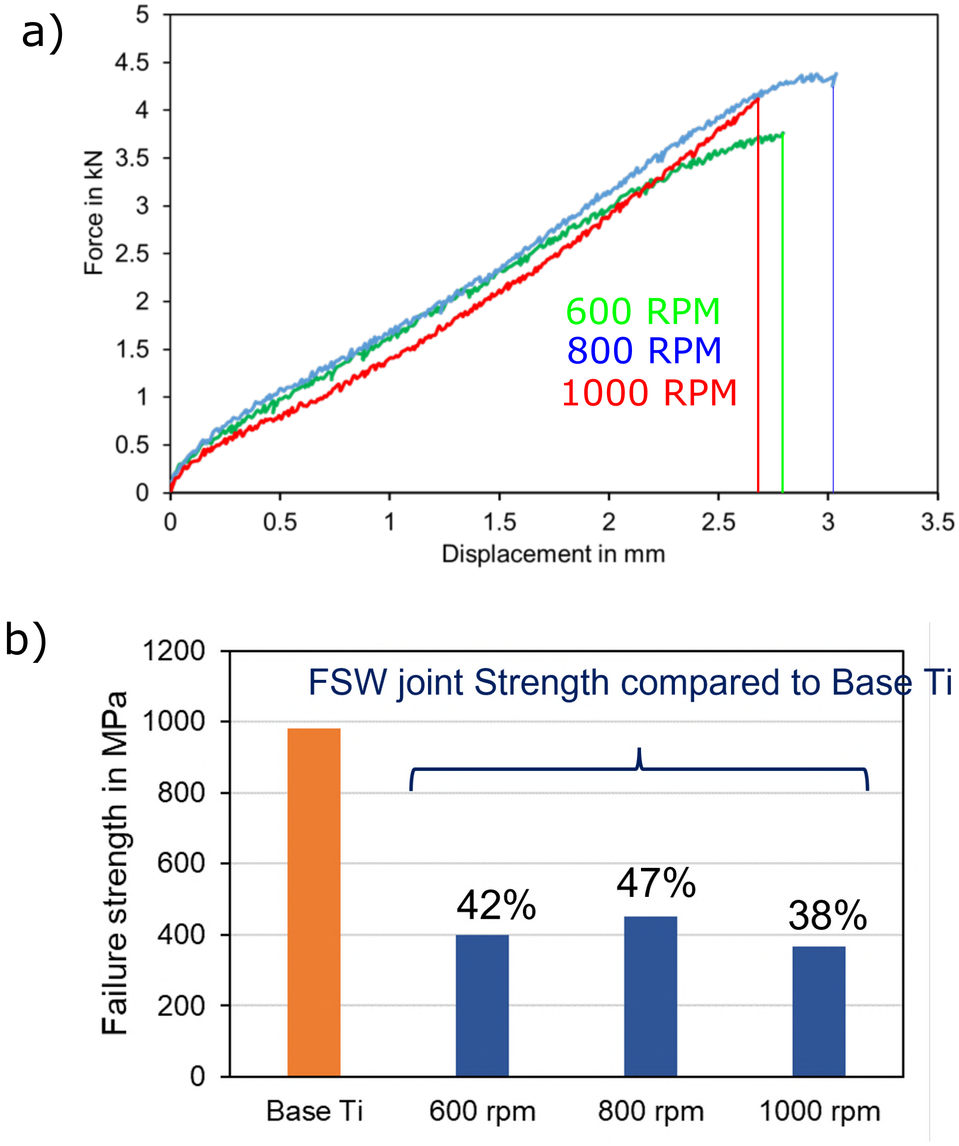

Figure B.19: (a) Force-displacement curve of the lap-shear test for Al/Ti friction stir welds performed at 60 mm/min (b) Comparison of the failure strength to the strength at failure of the base Ti alloy.

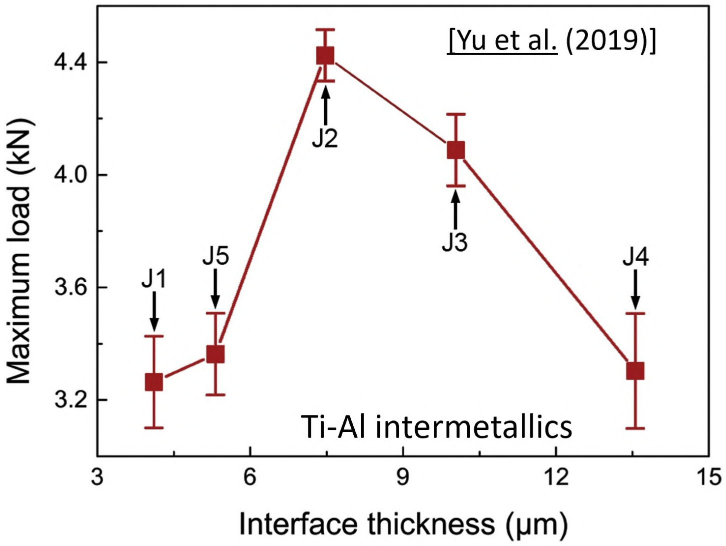

Figure B.20: Maximum load as a function of interface intermetallic layer thickness for Al/Ti friction stir welds performed by Yu et al. [192].

B.7 Conclusions

Dissimilar overlap Al/Ti FSW has been explored in this Appendix. AA6061-T6 and Ti-6Al-4V have been successfully assembled via FSW and lap shear testing along with interface characterization have shown promising results for these types of assemblies. The mixing of titanium inside the aluminium alloy has been shown to increase local hardness, but at the same time lead to different rupture mechanism in lap shear tests. Literature data suggests that the thickness of the intermetallic layer plays a key role in the mechanical properties of such joints. Data analyzed in this PhD tends to lead to similar conclusions. Assembling Al with Ti alloys with fusion based welding techniques is impossible, due to the difference in welding temperatures. Early results of Al/Ti FSW presented here offer a clear development path for Thales in the future, would the industrial need arise, for example in satellite manufacturing.

The joining of Al to Ti through means of friction needs to be further investigated. The literature on such assemblies is lacking deep level understanding on the formation of intermetallic and their subsequent impact on mechanical properties has been merely scraped. Additionally, a recent development on dissimilar assembly of metals was introduced by the IMAP laboratory at UCLouvain in the form of a new friction based welding process called Friction Melt Bonding. This process and FSW both offers great opportunities for applications in the aerospace industry.

Appendix C

Welding defects ISO

The next 4 pages display a table from ISO 25239 [61] detailing defects typical for friction stir welded joints.

Table A.1 — Imperfections, testing and examination, acceptance levels, and ISO 6520-1[3] reference number

Designation of imperfection	Remarks	Testing and examination in ISO 25239-4 [a]	Acceptance levels [a]			Reference number in ISO 6520-1[3]
			B	C	D	
Surface Imperfections Type I (not affecting weld section thickness)						
Toe flash		VT, ME	—[b]			—[c, d]
Linear misalignment	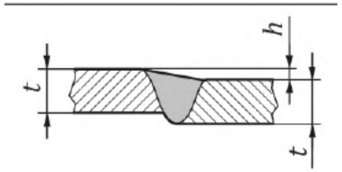	VT, ME	h ≤ 0.1t or 1 mm, whichever is less	h ≤ 0.2t or 2 mm, whichever is less	h ≤ 0.3t or 4 mm, whichever is less	507
Angular misalignment	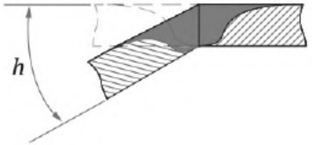	VT, ME	h ≤ 3°	h ≤ 3°	Not applicable	508
Joint area deformation	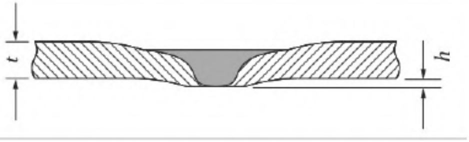	VT, ME	—[b]	h ≤ 0.4t or 2 mm whichever is less	h ≤ 0.5t or 4 mm whichever is less	—[c]
Irregular surface	Excessive surface roughness	VT	—[b]			514
Surface Imperfections Type II (affecting weld section thickness)						
Underfill	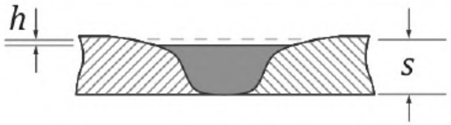	VT, ME	—[b]	h ≤ 0,1s	h ≤ 0,2s	—[c, d]
Cavity	Surface breaking cavity	VT, ME	Not permitted			—[d]
Internal imperfections						

Table A.1 *(continued)*

Designation of imperfection	Remarks	Testing and examination in ISO 25239-4 [a]	Acceptance levels [a]			Reference number in ISO 6520-1[3]
			B	C	D	
Cavity	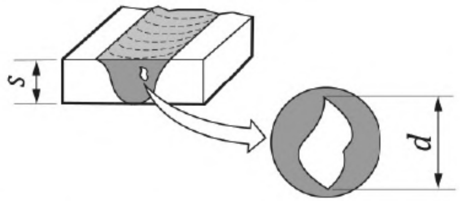 two adjacent cavities with a distance smaller than „d“ from the smaller cavity should be considered as a single cavity.	ME, RT, UT	Not permitted	d ≤ 0.2s or 4 mm whichever is less	—[b]	200
Hook	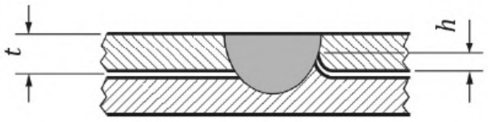	ME	—[b]	h ≤ 0.2t (to be considered only if reduces the loaded part of the joint)	h ≤ 0.5t (to be considered only if reduces the loaded part of the joint)	—[c, e]
Incomplete penetration (incorrect penetration)	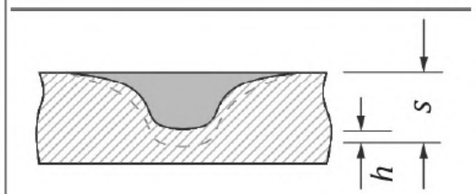 difference between the actual and the nominal penetration	ME, RT, UT	Not permitted	—[b]	h ≤ 0.2s	402
Solid inclusion	multiple incusions found in one cross section will be summed up: l = l1+l2+… inclusions smaller than 0.2mm should not be considered	ME, RT, UT	Not permitted	l ≤ 0.2s	—[b]	300
Root Flaws (See ISO 25239-1, Figure.7)						

Table A.1 *(continued)*

Designation of imperfection	Remarks	Testing and examination in ISO 25239-4 [a]	Acceptance levels [a]			Reference number in ISO 6520-1[3]
			B	C	D	
bonded joint remnant	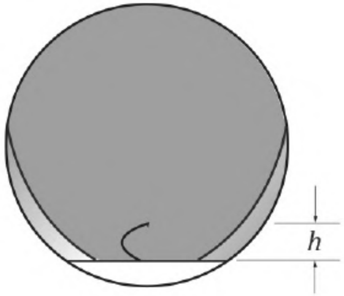 Applies only if invoked by the engineering drawing	ME, bend test	—[b]			—[c, d]
unbonded joint remnant	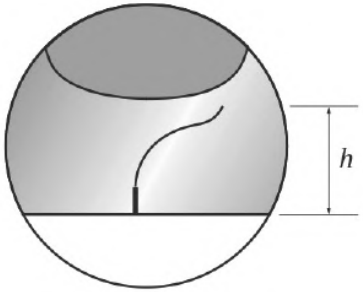	ME, bend test, PT, UT	Not permitted	—[b]	h ≤ 0.2t Short, non-systematic imperfections	—[c, d]
Multiple Imperfections						

Table A.1 *(continued)*

Designation of imperfection	Remarks	Testing and examination in ISO 25239-4 [a]	Acceptance levels [a]			Reference number in ISO 6520-1[3]
			B	C	D	
Multiple imperfections	Combination of multiple imperfections within a single cross section	-/-	The sum of all individual imperfections which reduce the weld section thickness should not exceed			—[d]
	Excluding "Surface Imperfections Type I"		—[b]	0.2s	0.5s	

Symbols and abbreviated terms

d Maximum transverse cross-sectional dimension of cavity (mm)

h height of an imperfection (mm)

s nominal weld thickness (penetration) (mm)

t nominal thickness of the parent material (mm). In case there are more than one thicknesses in the same weld, the relevant thickness shall be specified in the design specification.

ME macroscopic examination

VT visual testing

PT penetrant testing

RT radiographic testing

UT ultrasonic testing

[a] When required, non-destructive testing should be carried out in accordance with ISO 3452-1 (penetrant inspection), ISO 17636 (radiographic testing), and ISO 17640 (ultrasonic examination). Testing and examination of other imperfections and their acceptance levels shall be in accordance with the relevant requirements or the design specification.

[b] Acceptance levels shall be within the specified limit of the relevant requirements or the design specification.

[c] See ISO 25239-1.

[d] If the weld surface is not used in the as welded condition the design requirements apply.

[e] See ISO 25239-2.

Bibliography

[1] Thomas Wayne Morris, Nicholas Edward David, Needham James Christopher, Temple-Smith Peter, Klaus We Kallee Stephan Walter, and Dawes Christopher John. Friction stir welding, 1996. GB Patent, GB2306366A. 7, 15

[2] J.R. Davis. Light Metals and Alloys-Aluminum and Aluminum Alloys. *Alloying: Understanding the Basics*, pages 351–416, 2001. ISSN 0007-1072. doi: 10.1361/autb2001p351. 7, 11, 13

[3] Hale Justin. Boeing 787 from the ground up. *AERO*, 2006. 7

[4] The Aluminium Association. Aluminium Association's Website . `https://www.aluminum.org/`, 2022. 11

[5] J.G. Kaufman. *Introduction to Aluminum Alloys and Tempers.* ASM International, 2000. ISBN 9781615030668. URL `https://books.google.fr/books?id=idmZIDcwCykC`. 11

[6] Michel Stucky. Traitements thermiques des alliages d'aluminium - Matériels et recommandations. *Techniques de l'ingénieur*, 2011. 12, 13

[7] EN. Aluminium et alliages d'aluminium — Produits corroyés — Désignation des états métallurgiques. Standard, Comité européen de normalisation, 2017. 13

[8] ISO. Soudage par friction malaxage Aluminium Partie 1: Vocabulaire. Standard, International Organization for Standardization, Geneva, CH, 2012. 14

[9] R.S. Mishra and Z.Y. Ma. Friction stir welding and processing. *Materials Science and Engineering: R: Reports*, 50(1-2):1–78, aug 2005. ISSN 0927-796X. doi: 10.1016/J.MSER.2005.07.001. URL `https://www.sciencedirect.com/science/article/pii/S0927796X05000768`. 15, 45, 47, 50

[10] Dimitri Jacquin and Gildas Guillemot. A review of microstructural changes occurring during FSW in aluminium alloys and their modelling. *Journal of Materials Processing Technology*, 288:116706, February 2021. doi: 10.1016/j.jmatprotec.2020.116706. URL `https://doi.org/10.1016/j.jmatprotec.2020.116706`. 15

[11] M. Maruthapandian, R. Pugazhenhi, and C. Gnanavel. Study the impaction tool speed on the friction stir welding of magnesium alloys plates. *Materials Today: Proceedings*, August 2022. doi: 10.1016/j.matpr.2022.07.270. URL `https://doi.org/10.1016/j.matpr.2022.07.270`. 15

[12] Y.J. Kwon, I. Shigematsu, and N. Saito. Dissimilar friction stir welding between magnesium and aluminum alloys. *Materials Letters*, 62(23):3827–3829, August 2008. doi: 10.1016/j.matlet.2008.04.080. URL `https://doi.org/10.1016/j.matlet.2008.04.080`. 15

[13] A. Forsström, S. Bossuyt, Y. Yagodzinskyy, K. Tsuzaki, and H. Hänninen. Strain localization in copper canister FSW welds for spent nuclear fuel disposal. *Journal of Nuclear Materials*, 523:347–359, September 2019. doi: 10.1016/j.jnucmat.2019.06.024. URL `https://doi.org/10.1016/j.jnucmat.2019.06.024`. 15

[14] Wei Guan, Yifu Shen, Yinfei Yan, Rui Guo, and Wei Zhang. Fabrication of ultra-thin copper foil pressure welding using FSW equipment. *Journal of Materials Processing Technology*, 251:343–349, January 2018. doi: 10.1016/j.jmatprotec.2017.08.022. URL `https://doi.org/10.1016/j.jmatprotec.2017.08.022`.

[15] M.-N. Avettand-Fènoël, N. Netto, A. Simar, M. Marinova, and R. Taillard. Design of a metallic glass dispersion in pure copper by friction stir processing. *Journal of Alloys and Compounds*, 907:164522, June 2022. doi: 10.1016/j.jallcom.2022.164522. URL `https://doi.org/10.1016/j.jallcom.2022.164522`. 15

[16] S. Papaefthymiou, C. Goulas, and E. Gavalas. Micro-friction stir welding of titan zinc sheets. *Journal of Materials Processing Technology*, 216:133–139, February 2015. doi: 10.1016/j.jmatprotec.2014.08.029. URL `https://doi.org/10.1016/j.jmatprotec.2014.08.029`. 15

[17] T. Mira-Aguiar, D. Verdera, C. Leitão, and D.M. Rodrigues. Tool assisted friction welding: A FSW related technique for the linear lap welding of very thin steel plates. *Journal of Materials Processing Technology*, 238:73–80, December 2016. doi: 10.1016/j.jmatprotec.2016.07.006. URL `https://doi.org/10.1016/j.jmatprotec.2016.07.006`. 15

[18] Hidetoshi Fujii, Ling Cui, Nobuhiro Tsuji, Masakatsu Maeda, Kazuhiro Nakata, and Kiyoshi Nogi. Friction stir welding of carbon steels. *Materials Science and Engineering: A*, 429(1-2):50–57, August 2006. doi: 10.1016/j.msea.2006.04.118. URL `https://doi.org/10.1016/j.msea.2006.04.118`. 15

[19] Mageshwari Komarasamy, Christopher Smith, Jens Darsell, Woongjo Choi, Saumyadeep Jana, and Glenn Grant. Microstructure and mechanical properties of friction stir welded haynes 282. *Materials Characterization*, 182:111558, December 2021. doi: 10.1016/j.matchar.2021.111558. URL `https://doi.org/10.1016/j.matchar.2021.111558`. 15

[20] P. Edwards and M. Ramulu. Identification of process parameters for friction stir welding ti–6al–4v. *Journal of Engineering Materials and Technology*, 132(3), June 2010. doi: 10.1115/1.4001302. URL `https://doi.org/10.1115/1.4001302`. 15

[21] S. Mironov, Y.S. Sato, and H. Kokawa. Friction-stir welding and processing of ti-6al-4v titanium alloy: A review. *Journal of Materials Science and Technology*, 34(1):58–72, January 2018. doi: 10.1016/j.jmst.2017.10.018. URL `https://doi.org/10.1016/j.jmst.2017.10.018`. 183, 185

[22] Gnofam Jacques Tchein. *Étude des couplages thermomécaniques et microstructuraux d'un alliage de titane au cours du soudage FSW*. Theses, Université de Bordeaux, December 2018. URL `https://tel.archives-ouvertes.fr/tel-02056765`. 15

[23] S. RaviKumar, R. KajaBanthaNavas, and Padakandla Sai Sujeeth. Multiple Response Optimization Studies for Dissimilar Friction Stir Welding Parameters of 6061 to 7075 Aluminium Alloys. *Materials Today: Proceedings*, 16:405–412, jan 2019. ISSN 2214-7853. doi: 10.1016/J.MATPR.2019.05.108. URL `https://www.sciencedirect.com/science/article/pii/S2214785319309538`. 15, 35

[24] Aiping Wu, Zhihua Song, Kazuhiro Nakata, Jinsun Liao, and Li Zhou. Interface and properties of the friction stir welded joints of titanium alloy Ti6Al4V with aluminum alloy 6061. *Materials and Design*, 71:85–92, 2015. ISSN 18734197. doi: 10.1016/j.matdes.2014.12.015. URL `http://dx.doi.org/10.1016/j.matdes.2014.12.015`. 15

[25] Aude Simar. State of the art about dissimilar metal friction stir welding. 1718 (November), 2016. doi: 10.1080/17432936.2016.1251712. 15, 148, 185

[26] ISO. Soudage par friction malaxage Aluminium Partie 2: Conception des assemblages soudés. Standard, International Organization for Standardization, Geneva, CH, 2012. 15, 16, 17

[27] R Jeffrey Ding and Peter A Oelgoetz. Mechanical property analysis in the retracted pin-tool (rpt) region of friction stir welded (fsw) aluminum lithium 2195. In *Friction Stir Welding*, 1999. 20

[28] ASM INTERNATIONAL. Asm specialty handbook-aluminium and aluminium alloy, 1992. 20

[29] Radecki Alan. Eclispe 500 in flight, 2006. 21

[30] Brian Travis Gibson. The development of in-process monitoring and control techniques for aerospace applications of friction stir welding. *PhD Proposal*, 1:256, 2015. ISSN 1098-6596. doi: 10.1017/CBO9781107415324.004. 22

[31] CETIM. Soudage par friction-malaxage : une technologie mature
, 2015. 22

[32] Amèvi Tongne. *Étude expérimentale et numérique du procédé de soudage FSW (Friction Stir Welding). Analyse microstructurale et modélisation thermomécanique des conditions de contact outil/matière transitoires.* PhD thesis, Mines de Saint-Étienne, 2015. 22

[33] NASA. Friction Stir Welding Aids SLS, 2012. 22

[34] Jurvetson Steve. Falcon 9 booster assembled in fsw, flickr, 2008. 23

[35] SpaceFlight101. Blue Origin breaks ground at future Rocket Manufacturing Plant in Florida
, 2016. 22

[36] Groupe Roux-Jourfier. Rj industrie fournira le système industriel d'assemblage et de soudage fsw des réservoirs d'ariane 6, 2022. 22, 23

[37] The Welding Institute. Application of friction stir welding in the shipbuilding industry, 2000. 24

[38] Masaki Kumagai and Sunao Tanaka. Properties of aluminum wide panels by friction stir welding. In *The First International Symposium on Friction Stir Welding, Thousand Oaks, CA, USA*, 1999. 24

[39] The Welding Institute. Creating a stir in the rail industry, 2001. 25, 26

[40] Global Railway Review. Friction stir welding for the fabrication of aluminium rolling stock, 2008. 25

[41] Unknown. Tra-c industrie devient leader européen dans la définition, la réalisation et la mise en place de solutions intégrées de soudage fsw. *Soudage et techniques annexes*, 67, 2013. 26

[42] Institut de Soudure. Tra-C industrie mise sur le soudage FSW. *Soudage et Techniques Connexes*, 71:42–44, Septembre/Octobre 2017. ISSN 0246-0963. 26

[43] The Welding Institute. Friction Stir Welding - Process variants and developments in the automotive industry, 2006. 26, 27

[44] Yuri Hovanski, Piyush Upadhyay, John Carsley, Tom Luzanski, Blair Carlson, Mark Eisenmenger, Ayoub Soulami, Dustin Marshall, Brandon Landino, and Susan Hartfield-Wunsch. High-speed friction-stir welding to enable aluminum tailor-welded blanks. *JOM*, 67(5):1045–1053, May 2015. ISSN 1543-1851. doi: 10.1007/s11837-015-1384-x. URL `https://doi.org/10.1007/s11837-015-1384-x`. 26

[45] The Welding Institute. Copper canisters to encapsulate nuclear waste, 2013. 27

[46] The Welding Institute. Advanced techniques used for sealing nuclear waste canisters, 2013. 28

[47] Claes-Göran Andersson. Development of fabrication technology for copper canisters with cast inserts. Technical report, Svensk Kärnbränslehantering AB, 2001. 28

[48] Pabitra Maji, Ranit Karmakar, Rahul Kanti Nath, and Pritam Paul. An overview on friction stir welding/processing tools. *Materials Today: Proceedings*, 58:57–64, 2022. doi: 10.1016/j.matpr.2022.01.009. URL `https://doi.org/10.1016/j.matpr.2022.01.009`. 28

[49] P. A. Colegrove, H. R. Shercliff, and R. Zettler. Model for predicting heat generation and temperature in friction stir welding from the material properties. *Science and Technology of Welding and Joining*, 12(4):284–297, May 2007. doi: 10.1179/174329307x197539. URL `https://doi.org/10.1179/174329307x197539`. 29, 30

[50] W. Tang, X. Guo, J. C. McClure, L. E. Murr, and A. Nunes. Heat input and temperature distribution in friction stir welding. *Journal of Materials Processing and Manufacturing Science*, 7(2):163–172, October 1998. doi: 10.1106/55tf-pf2g-jbh2-1q2b. URL `https://doi.org/10.1106/55tf-pf2g-jbh2-1q2b`. 29, 30

[51] Axel Steuwer, Matthew J Peel, and Philip J Withers. Influence of welding speed on the properties of AA5083-AA6082 dissimilar Friction Stir Welds. *Materials Science*, 2006. 29, 38, 99, 107, 157, 173

[52] MJ Peel, A Steuwer, PJ Withers, T Dickerson, Q Shi, and H Shercliff. Dissimilar friction stir welds in aa5083-aa6082. part i: process parameter effects on thermal history and weld properties. *Metallurgical and Materials Transactions A*, 37(7): 2183–2193, 2006. 29

[53] W. R. Longhurst, A. M. Strauss, G. E. Cook, C. D. Cox, C. E. Hendricks, B. T. Gibson, and Y. S. Dawant. Investigation of force-controlled friction stir welding for manufacturing and automation. *Proceedings of the Institution of Mechanical Engineers, Part B: Journal of Engineering Manufacture*, 224(6):937–949, 2010. doi: 10.1243/09544054JEM1709. 30, 31

[54] L Dubourg. Friction stir welding without exit holes. In *Proceedings of the Joint International Symposium on Friction Stir Welding and Processing, Luneburg, Germany, September 28-30*, 2022. 30

[55] L Dubourg and P Dacheux. Design and properties of fsw tools: a literature review. In *Proceedings of 6th International symposium on friction stir welding, Saint-Sauveur, Quebec, Canada*, 2006. 32

[56] K. Krasnowski, C. Hamilton, and S. Dymek. Influence of the tool shape and weld configuration on microstructure and mechanical properties of the Al 6082 alloy FSW joints. *Archives of Civil and Mechanical Engineering*, 15(1):133–141, jan 2015. ISSN 1644-9665. doi: 10.1016/J.ACME.2014.02.001. URL `https://www.sciencedirect.com/science/article/pii/S1644966514000387`. 32, 33, 37, 40, 41, 44

[57] Avinish Tiwari, Piyush Singh, Pardeep Pankaj, Pankaj Biswas, and Sachin D. Kore. FSW of low carbon steel using tungsten carbide (WC-10wt.%co) based tool material. *Journal of Mechanical Science and Technology*, 33(10):4931–4938, October 2019. doi: 10.1007/s12206-019-0932-7. URL `https://doi.org/10.1007/s12206-019-0932-7`. 33

[58] F.C. Liu, Y. Hovanski, M.P. Miles, C.D. Sorensen, and T.W. Nelson. A review of friction stir welding of steels: Tool, material flow, microstructure, and properties. *Journal of Materials Science and Technology*, 34(1):39–57, January 2018. doi: 10.1016/j.jmst.2017.10.024. URL `https://doi.org/10.1016/j.jmst.2017.10.024`.

[59] S. Shashi Kumar, N. Murugan, and K.K. Ramachandran. Influence of tool material on mechanical and microstructural properties of friction stir welded 316l austenitic stainless steel butt joints. *International Journal of Refractory Metals and Hard Materials*, 58:196–205, August 2016. doi: 10.1016/j.ijrmhm.2016.04.015. URL `https://doi.org/10.1016/j.ijrmhm.2016.04.015`. 33

[60] R. Rai, A. De, H. K.D.H. Bhadeshia, and T. DebRoy. Review: Friction stir welding tools. *Science and Technology of Welding and Joining*, 16(4):325–342, 2011. ISSN 13621718. doi: 10.1179/1362171811Y.0000000023. 33

[61] ISO. Soudage par friction malaxage Aluminium Partie 5: Exigences de qualité et de contrôle. Standard, International Organization for Standardization, Geneva, CH, 2012. 34, 208

[62] ISO. Soudages et techniques connexes - Classification des défauts géométriques dans les soudures des matériaux métalliques - Partie 1 : soudage par fusion. Standard, International Organization for Standardization, Geneva, CH, 2007. 34

[63] Noor Zaman Khan, Arshad Noor Siddiquee, Zahid A. Khan, and Suha K. Shihab. Investigations on tunneling and kissing bond defects in fsw joints for dissimilar aluminum alloys. *Journal of Alloys and Compounds*, 648:360 – 367, 2015. ISSN 0925-8388. doi: https://doi.org/10.1016/j.jallcom.2015.06.246. URL `http://www.sciencedirect.com/science/article/pii/S0925838815303662`. 34

[64] Y.G. Kim, H. Fujii, T. Tsumura, T. Komazaki, and K. Nakata. Three defect types in friction stir welding of aluminum die casting alloy. *Materials Science and Engineering: A*, 415(1):250 – 254, 2006. ISSN 0921-5093. doi: https://doi.org/10.1016/j.msea.2005.09.072. URL `http://www.sciencedirect.com/science/article/pii/S0921509305011652`. 34

[65] H. Badarinarayan, Y. Shi, X. Li, and K. Okamoto. Effect of tool geometry on hook formation and static strength of friction stir spot welded aluminum 5754-o sheets. *International Journal of Machine Tools and Manufacture*, 49(11):814 – 823, 2009. ISSN 0890-6955. doi: https://doi.org/10.1016/j.ijmachtools.2009.06.001. URL `http://www.sciencedirect.com/science/article/pii/S0890695509001011`. 34

[66] A. Suri, R. S. S. Prashant, and K. H. Raj. Comparative study of friction stir welding and tungsten inert gas welding of pure aluminum. In *2013 International Conference on Energy Efficient Technologies for Sustainability*. IEEE, April 2013. doi: 10.1109/iceets.2013.6533512. URL `https://doi.org/10.1109/iceets.2013.6533512`. 35

[67] I. Radisavljevic, A. ZIVKOVIC, N. RADOVIC, and V. GRABULOV. Influence of fsw parameters on formation quality and mechanical properties of al 2024-t351 butt welded joints. *Transactions of Nonferrous Metals Society of China*, 23(12):3525 – 3539, 2013. ISSN 1003-6326. doi: https://doi.org/10.1016/S1003-6326(13)62897-6. URL `http://www.sciencedirect.com/science/article/pii/S1003632613628976`. 35, 46

[68] Miodrag Milčić, Zijah Burzić, Igor Radisavljević, Tomaž Vuherer, Dragan Milčić, and Vencislav Grabulov. Experimental investigation of fatigue properties of fsw in aa2024-t351. *Procedia Structural Integrity*, 13:1977 – 1984, 2018. ISSN 2452-3216. doi: https://doi.org/10.1016/j.prostr.2018.12.220. URL `http://www.sciencedirect.com/science/article/pii/S245232161830458X`. ECF22 - Loading and Environmental effects on Structural Integrity.

[69] H.J.K. Lemmen, R.C. Alderliesten, and R. Benedictus. Evaluating the fatigue initiation location in friction stir welded aa2024-t3 joints. *International Journal of Fatigue*, 33(3):466 – 476, 2011. ISSN 0142-1123. doi: https://doi.org/10.1016/j.ijfatigue.2010.10.002. URL `http://www.sciencedirect.com/science/article/pii/S0142112310002379`.

[70] G. Rambabu, D. Balaji Naik, C.H. Venkata Rao, K. Srinivasa Rao, and G. Madhusudan Reddy. Optimization of friction stir welding parameters for improved corrosion resistance of AA2219 aluminum alloy joints. *Defence Technology*, 11 (4):330–337, dec 2015. ISSN 2214-9147. doi: 10.1016/J.DT.2015.05.003. URL `https://www.sciencedirect.com/science/article/pii/S2214914715000355`.

[71] A. Scialpi, M. De Giorgi, L. A C De Filippis, R. Nobile, and F. W. Panella. Mechanical analysis of ultra-thin friction stir welding joined sheets with dissimilar and similar materials. *Materials and Design*, 29(5):928–936, 2008. ISSN 18734197. doi: 10.1016/j.matdes.2007.04.006. 35

[72] Anna Janeczek, Jacek Tomków, and Dariusz Fydrych. The influence of tool shape and process parameters on the mechanical properties of AW-3004 aluminium alloy friction stir welded joints. *Materials*, 14(12):3244, June 2021. doi: 10.3390/ma14123244. URL `https://doi.org/10.3390/ma14123244`. 35

[73] Raza Moshwan, Farazila Yusof, M.A. Hassan, and S.M. Rahmat. Effect of tool rotational speed on force generation, microstructure and mechanical properties of friction stir welded Al–Mg–Cr–Mn (AA 5052-O) alloy. *Materials & Design (1980-2015)*, 66:118–128, feb 2015. ISSN 0261-3069. doi: 10.1016/J.MATDES.2014.10.043. URL `https://www.sciencedirect.com/science/article/pii/S0261306914008310`. 35, 43, 44, 46

[74] H. Jamshidi Aval, S. Serajzadeh, and A.H. Kokabi. Evolution of microstructures and mechanical properties in similar and dissimilar friction stir welding of AA5086 and AA6061. *Materials Science and Engineering: A*, 528(28):8071–8083, October 2011. doi: 10.1016/j.msea.2011.07.056. URL `https://doi.org/10.1016/j.msea.2011.07.056`. 35, 56, 78

[75] S.-K. Park, S.-T. Hong, J.-H. Park, K.-Y. Park, Y.-J. Kwon, and H.-J. Son. Effect of material locations on properties of friction stir welding joints of dissimilar aluminium alloys. *Science and Technology of Welding and Joining*, 15(4):331–336, 2010. ISSN 1362-1718. doi: 10.1179/136217110X12714217309696. URL `http://www.tandfonline.com/doi/full/10.1179/136217110X12714217309696`. 35, 78, 102

[76] Igor Vysotskiy, Sergey Malopheyev, Salaheddin Rahimi, Sergey Mironov, and Rustam Kaibyshev. Unusual fatigue behavior of friction-stir welded Al–Mg–Si alloy. *Materials Science and Engineering: A*, 760:277–286, jul 2019. ISSN 0921-5093. doi: 10.1016/J.MSEA.2019.06.005. URL `https://www.sciencedirect.com/science/article/pii/S0921509319307609?via{%}3Dihub`. 35, 52, 53, 158, 159, 162, 163, 167, 170

[77] A.A.M. Da Silva, E. Arruti, G. Janeiro, E. Aldanondo, P. Alvarez, and A. Echeverria. Material flow and mechanical behaviour of dissimilar aa2024-t3 and aa7075-t6 aluminium alloys friction stir welds. *Materials and Design*, 32(4):2021 – 2027, 2011. ISSN 0261-3069. doi: https://doi.org/10.1016/j.matdes.2010.11.059. URL `http://www.sciencedirect.com/science/article/pii/S0261306910006850`. 35, 37, 39, 43, 45, 48, 99

[78] Saad Ahmed Khodir and Toshiya Shibayanagi. Friction stir welding of dissimilar AA2024 and AA7075 aluminum alloys. *Materials Science and Engineering B: Solid-State Materials for Advanced Technology*, 148(1-3):82–87, 2008. ISSN 09215107. doi: 10.1016/j.mseb.2007.09.024. 35

[79] Mohamed M. Abd Elnabi, Abou Bakr Elshalakany, M.M. Abdel-Mottaleb, T.A. Osman, and A. El Mokadem. Influence of friction stir welding parameters on metallurgical and mechanical properties of dissimilar AA5454–AA7075 aluminum alloys. *Journal of Materials Research and Technology*, 8(2):1684–1693, apr 2019. ISSN 2238-7854. doi: 10.1016/J.JMRT.2018.10.015. URL `https://www.sciencedirect.com/science/article/pii/S2238785418301856`. 35

[80] S.M. Bayazid, H. Farhangi, and A. Ghahramani. Investigation of Friction Stir Welding Parameters of 6063-7075 Aluminum Alloys by Taguchi Method. *Procedia Materials Science*, 11:6–11, jan 2015. ISSN 2211-8128. doi: 10.1016/J.MSPRO.2015.11.007. URL `https://www.sciencedirect.com/science/article/pii/S2211812815003491`. 35

[81] S. Rajakumar, C. Muralidharan, and V. Balasubramanian. Influence of friction stir welding process and tool parameters on strength properties of aa7075-t6 aluminium alloy joints. *Materials and Design*, 32(2):535 – 549, 2011. ISSN 0261-3069. doi: https://doi.org/10.1016/j.matdes.2010.08.025. URL `http://www.sciencedirect.com/science/article/pii/S0261306910005005`. 35

[82] Roland Cazes. Soudage par friction-malaxage. *Techniques de l'ingénieur*, 2003. 36

[83] H.B. Schmidt and J.H. Hattel. Thermal modelling of friction stir welding. *Scripta Materialia*, 58(5):332 – 337, 2008. ISSN 1359-6462. doi: https://doi.org/10.1016/j.scriptamat.2007.10.008. URL `http://www.sciencedirect.com/science/article/pii/S1359646207007403`. Viewpoint set no. 43 "Friction stir processing". 36, 105

[84] Ying Li, L. E. Murr, and J. C. McClure. Solid-state flow visualization in the friction-stir welding of 2024 Al to 6061 Al. *Scripta Materialia*, 40(9):1041–1046, 1999. ISSN 13596462. doi: 10.1016/S1359-6462(99)00062-7. 37

[85] Caroline Jonckheere, Bruno De Meester, Anne Denquin, and Aude Simar. Torque, temperature and hardening precipitation evolution in dissimilar friction stir welds between 6061-T6 and 2014-T6 aluminum alloys. *Journal of Materials Processing Technology*, 213(6):826–837, jun 2013. ISSN 0924-0136. doi: 10.1016/J.JMATPROTEC.2013.01.001. 38, 99, 173

[86] J.F. Guo, H.C. Chen, C.N. Sun, G. Bi, Z. Sun, and J. Wei. Friction stir welding of dissimilar materials between AA6061 and AA7075 al alloys effects of process parameters. *Materials And Design (1980-2015)*, 56:185–192, April 2014. doi: 10.1016/j.matdes.2013.10.082. URL `https://doi.org/10.1016/j.matdes.2013.10.082`. 37, 47, 48, 78, 102, 139

[87] A. Heidarzadeh, S. Mironov, R. Kaibyshev, G. Çam, A. Simar, A. Gerlich, F. Khodabakhshi, A. Mostafaei, D. P. Field, J. D. Robson, A. Deschamps, and P. J. Withers. Friction stir welding/processing of metals and alloys: A comprehensive review on microstructural evolution. *Progress in Materials Science*, 117:100752, apr 2021. ISSN 0079-6425. doi: 10.1016/J.PMATSCI.2020.100752. 40, 148

[88] Omar S. Salih, Nigel Neate, Hengan Ou, and W. Sun. Influence of process parameters on the microstructural evolution and mechanical characterisations of friction stir welded al-mg-si alloy. *Journal of Materials Processing Technology*, 275:116366, January 2020. doi: 10.1016/j.jmatprotec.2019.116366. URL `https://doi.org/10.1016/j.jmatprotec.2019.116366`. 40, 42

[89] Sergey Mironov, Kosuke Inagaki, Yutaka S. Sato, and Hiroyuki Kokawa. Effect of welding temperature on microstructure of friction-stir welded aluminum alloy 1050. *Metallurgical and Materials Transactions A*, 46(2):783–790, November 2014. doi: 10.1007/s11661-014-2651-0. URL `https://doi.org/10.1007/s11661-014-2651-0`. 40

[90] D. Yi, S. Mironov, Y. S. Sato, and H. Kokawa. Effect of cooling rate on microstructure of friction-stir welded AA1100 aluminum alloy. *Philosophical Magazine*, 96(18):1965–1977, May 2016. doi: 10.1080/14786435.2016.1185186. URL `https://doi.org/10.1080/14786435.2016.1185186`. 40

[91] Jialiang Dong, Datong Zhang, Xicai Luo, Weiwen Zhang, Wen Zhang, and Cheng Qiu. EBSD study of underwater friction stir welded AA7003-t4 and AA6060-t4 dissimilar joint. *Journal of Materials Research and Technology*, 9(3):4309–4318, May 2020. doi: 10.1016/j.jmrt.2020.02.056. URL `https://doi.org/10.1016/j.jmrt.2020.02.056`. 43

[92] E. G. Cole, A. Fehrenbacher, N. A. Duffie, M. R. Zinn, F. E. Pfefferkorn, and N. J. Ferrier. Weld temperature effects during friction stir welding of dissimilar aluminum alloys 6061-t6 and 7075-t6. *The International Journal of Advanced Manufacturing Technology*, 71(1-4):643–652, December 2013. doi: 10.1007/s00170-013-5485-9. URL `https://doi.org/10.1007/s00170-013-5485-9`. 48

[93] S. Ravikumar, V. Seshagiri Rao, and R. V. Pranesh. Effect of Process Parameters on Mechanical Properties of Friction Stir Welded Dissimilar Materials between AA6061-T651 and AA7075-T651 Alloys. *International Journal of Advanced Mechanical Engineering*, 4(1):101–114, 2014. ISSN 02613069. doi: 10.1016/j.matdes.2014.10.065. 48, 139

[94] Hasan Jafari, Hadi Mansouri, and Mohammad Honarpisheh. Investigation of residual stress distribution of dissimilar al-7075-t6 and al-6061-t6 in the friction stir

welding process strengthened with SiO2 nanoparticles. *Journal of Manufacturing Processes*, 43:145–153, July 2019. doi: 10.1016/j.jmapro.2019.05.023. URL `https://doi.org/10.1016/j.jmapro.2019.05.023`. 49

[95] Bob McGinty. Fracture mechanics, 2022. 50

[96] Fatigue Life. What is fatigue life? `https://fatigue-life.com/what-is-fatigue-life/`, 2022. 51

[97] P.A. WITHEY. FATIGUE FAILURE OF THE DE HAVILLAND COMET i. In *Failure Analysis Case Studies II*, pages 185–192. Elsevier, 2001. doi: 10.1016/b978-0-08-043959-4.50018-3. URL `https://doi.org/10.1016/b978-0-08-043959-4.50018-3`. 50

[98] S. Tanaka M. Kumagai. Properties of aluminum wide panels by friction stir welding. In *Proceedings of the First International Symposium on Friction Stir Welding, Thousand Oaks, CA, USA, June 14–16*, 1999. 50

[99] G Bussu and P.E Irving. The role of residual stress and heat affected zone properties on fatigue crack propagation in friction stir welded 2024-T351 aluminium joints. *International Journal of Fatigue*, 25(1):77–88, jan 2003. ISSN 0142-1123. doi: 10.1016/S0142-1123(02)00038-5. URL `https://www.sciencedirect.com/science/article/pii/S0142112302000385`. 50

[100] M Ericsson. Influence of welding speed on the fatigue of friction stir welds, and comparison with MIG and TIG. *International Journal of Fatigue*, 25(12):1379–1387, December 2003. doi: 10.1016/s0142-1123(03)00059-8. URL `https://doi.org/10.1016/s0142-1123(03)00059-8`. 50

[101] Caizhi Zhou, Xinqi Yang, and Guohong Luan. Fatigue properties of friction stir welds in Al 5083 alloy. *Scripta Materialia*, 53(10):1187–1191, nov 2005. ISSN 1359-6462. doi: 10.1016/J.SCRIPTAMAT.2005.07.016. URL `https://www.sciencedirect.com/science/article/pii/S1359646205004409`. 170

[102] P.M.G.P. Moreira, M.A.V. de Figueiredo, and P.M.S.T. de Castro. Fatigue behaviour of FSW and MIG weldments for two aluminium alloys. *Theoretical and Applied Fracture Mechanics*, 48(2):169–177, October 2007. doi: 10.1016/j.tafmec.2007.06.001. URL `https://doi.org/10.1016/j.tafmec.2007.06.001`.

[103] S. Malarvizhi and V. Balasubramanian. Fatigue crack growth resistance of gas tungsten arc, electron beam and friction stir welded joints of AA2219 aluminium alloy. *Materials & Design*, 32(3):1205–1214, mar 2011. ISSN 0261-3069. doi: 10.1016/J.MATDES.2010.10.019. URL `https://www.sciencedirect.com/science/article/pii/S0261306910006151`.

[104] D. Texier, F. Atmani, P. Bocher, F. Nadeau, J. Chen, Y. Zedan, N. Vanderesse, and V. Demers. Fatigue performances of FSW and GMAW aluminum alloys welded joints: Competition between microstructural and structural-contact-fretting crack initiation. *International Journal of Fatigue*, 116:220–233, nov 2018. ISSN 0142-1123. doi: 10.1016/J.IJFATIGUE.2018.06.020. 50, 52, 53

[105] S. Lomolino, R. Tovo, and J. Dos Santos. On the fatigue behaviour and design curves of friction stir butt-welded Al alloys. *International Journal of Fatigue*, 27(3): 305–316, mar 2005. ISSN 01421123. doi: 10.1016/j.ijfatigue.2004.06.013. 52, 162

[106] Shusheng Di, Xinqi Yang, Guohong Luan, and Bo Jian. Comparative study on fatigue properties between AA2024-T4 friction stir welds and base materials. *Materials Science and Engineering: A*, 435-436:389–395, nov 2006. ISSN 0921-5093. doi: 10.1016/J.MSEA.2006.07.009. 52, 162, 170

[107] P.M.G.P. Moreira, A.M.P. de Jesus, A.S. Ribeiro, and P.M.S.T. de Castro. Fatigue crack growth in friction stir welds of 6082-T6 and 6061-T6 aluminium alloys: A comparison. *Theoretical and Applied Fracture Mechanics*, 50(2):81–91, oct 2008. ISSN 0167-8442. doi: 10.1016/J.TAFMEC.2008.07.007. URL `https://www.sciencedirect.com/science/article/pii/S0167844208000487`. 52

[108] Sangshik Kim, Chang Gil Lee, and Sung-Joon Kim. Fatigue crack propagation behavior of friction stir welded 5083-H32 and 6061-T651 aluminum alloys. *Materials Science and Engineering: A*, 478(1-2):56–64, apr 2008. ISSN 0921-5093. doi: 10.1016/J.MSEA.2007.06.008. URL `https://www.sciencedirect.com/science/article/pii/S0921509307012993`. 52

[109] M.N James, D.G Hattingh, and G.R Bradley. Weld tool travel speed effects on fatigue life of friction stir welds in 5083 aluminium. *International Journal of Fatigue*, 25(12):1389–1398, dec 2003. ISSN 0142-1123. doi: 10.1016/S0142-1123(03)00061-6. URL `https://www.sciencedirect.com/science/article/pii/S0142112303000616`. 52

[110] T. L. Dickerson and J. Przydatek. Fatigue of friction stir welds in aluminium alloys that contain root flaws. *International Journal of Fatigue*, 25(12):1399–1409, dec 2003. ISSN 0142-1123. doi: 10.1016/S0142-1123(03)00060-4. 52

[111] E. Maggiolini, D. Benasciutti, L. Susmel, D. G. Hattingh, M. N. James, and R. Tovo. Friction stir welds in aluminium: Design S-N curves from statistical analysis of literature data. *Fatigue and Fracture of Engineering Materials and Structures*, 41 (11):2212–2230, 2018. ISSN 14602695. doi: 10.1111/ffe.12805. 52

[112] Y. Uematsu, Y. Tozaki, K. Tokaji, and M. Nakamura. Fatigue behavior of dissimilar friction stir welds between cast and wrought aluminum alloys. *Strength of Materials*, 40(1):138–141, January 2008. doi: 10.1007/s11223-008-0036-6. URL `https://doi.org/10.1007/s11223-008-0036-6`. 54

[113] R.I. Rodriguez, J.B. Jordon, P.G. Allison, T. Rushing, and L. Garcia. Low-cycle fatigue of dissimilar friction stir welded aluminum alloys. *Materials Science and Engineering: A*, 654:236–248, January 2016. doi: 10.1016/j.msea.2015.11.075. URL `https://doi.org/10.1016/j.msea.2015.11.075`.

[114] Pengliang Niu, Wenya Li, Chenggang Yang, Yuhua Chen, and Daolun Chen. Low cycle fatigue properties of friction stir welded dissimilar 2024-to-7075 aluminum alloy joints. *Materials Science and Engineering: A*, 832:142423, January 2022. doi: 10.1016/j.msea.2021.142423. URL `https://doi.org/10.1016/j.msea.2021.142423`. 54, 170

[115] NF EN. Aluminium et alliages d'aluminium - Tôles, bandes et tôles épaisses - Partie 2 : caractéristiques mécaniques. Standard, European Standard, 2016. 55, 56, 57, 117, 130, 190, 191

[116] Robert E. Sanders. Technology innovation in aluminum products. *JOM*, 53(2): 21–25, February 2001. doi: 10.1007/s11837-001-0115-7. URL https://doi.org/10.1007/s11837-001-0115-7. 55

[117] I. Dutta and S. M. Allen. A calorimetric study of precipitation in commercial aluminium alloy 6061. *Journal of Materials Science Letters*, 10(6):323–326, 1991. doi: 10.1007/bf00719697. URL https://doi.org/10.1007/bf00719697. 56

[118] G.A. Edwards, K. Stiller, G.L. Dunlop, and M.J. Couper. The precipitation sequence in al–mg–si alloys. *Acta Materialia*, 46(11):3893–3904, July 1998. doi: 10.1016/s1359-6454(98)00059-7. URL https://doi.org/10.1016/s1359-6454(98)00059-7. 56

[119] Li X.-M. and MJ Starink. Effect of compositional variations on characteristics of coarse intermetallic particles in overaged 7000 aluminium alloys. *Materials science and technology*, 17(11):1324–1328, 2001. 57

[120] Matthieu Lezaack. *Fracture of 7xxx aluminium alloys with tailored friction stir processed microstructures.* PhD thesis, Université Catholique de Louvain, 2022. 57, 108, 136

[121] M. Fourmeau, C.D. Marioara, T. Børvik, A. Benallal, and O.S. Hopperstad. A study of the influence of precipitate-free zones on the strain localization and failure of the aluminium alloy AA7075-t651. *Philosophical Magazine*, 95(28-30):3278–3304, May 2015. doi: 10.1080/14786435.2015.1040099. URL https://doi.org/10.1080/14786435.2015.1040099. 57

[122] Yichang Wang, Xiaodong Wu, Lingfei Cao, Xin Tong, Yan Zou, Qianqian Zhu, Songbai Tang, Hui Song, and Mingxing Guo. Effect of ag on aging precipitation behavior and mechanical properties of aluminum alloy 7075. *Materials Science and Engineering: A*, 804:140515, February 2021. doi: 10.1016/j.msea.2020.140515. URL https://doi.org/10.1016/j.msea.2020.140515. 58

[123] Li Gao, Yohei Harada, and Shinji Kumai. Microstructural characterization of aluminum alloys using weck's reagent, part i: Applications. *Materials Characterization*, 107:426–433, September 2015. doi: 10.1016/j.matchar.2015.01.005. URL https://doi.org/10.1016/j.matchar.2015.01.005. 65

[124] Olaf Engler and Valerie Randle. *Introduction to Texture Analysis.* CRC Press, nov 2009. ISBN 9780429191909. doi: 10.1201/9781420063660. URL https://www.taylorfrancis.com/books/9781420063660. 68

[125] ISO. Metallic materials Vickers hardness test . Standard, International Organization for Standardization, Geneva, CH, 2018. 70

[126] ISO. Friction stir welding — Aluminium — Part 4: Specification and qualification of welding procedures. Standard, International Organization for Standardization, Geneva, CH, 2019. 70

[127] ASTM. Standard Test Methods for Tension Testing of Metallic Materials. Standard, ASTM International, 2016. 72, 156

[128] L. Allais, M. Bornert, T. Bretheau, and D. Caldemaison. Experimental characterization of the local strain field in a heterogeneous elastoplastic material. *Acta Metallurgica et Materialia*, 42(11):3865–3880, November 1994. doi: 10.1016/0956-7151(94)90452-9. URL `https://doi.org/10.1016/0956-7151(94)90452-9`. 75, 150

[129] Minyoung Lee. High temperature hardness of tungsten carbide. *Metallurgical Transactions A*, 14(8):1625–1629, August 1983. doi: 10.1007/bf02654390. URL `https://doi.org/10.1007/bf02654390`. 88

[130] P. J. Hartley W. J. Arbegast. In *Proceedings of the Fifth International Conference on Trends in Welding Research, Pine Mountain, GA, USA*, 1998. 88

[131] Vijay Shivaji Gadakh and Kumar Adepu. Heat generation model for taper cylindrical pin profile in FSW. *Journal of Materials Research and Technology*, 2(4):370–375, October 2013. doi: 10.1016/j.jmrt.2013.10.003. URL `https://doi.org/10.1016/j.jmrt.2013.10.003`. 88, 89

[132] Michele Trancossi and Antonio Dumas. Direct drive friction welding: A comprehensive mathematical model. In *SAE Technical Paper Series*. SAE International, September 2010. doi: 10.4271/2010-01-1869. URL `https://doi.org/10.4271/2010-01-1869`. 89

[133] Kevin Colligan. Analysis of torque data from friction stir welds in aluminium. In *Joint International Symposium on Friction Stir Welding and Processing*, 2022. 90

[134] Abbas Tamadon, Dirk Pons, Kamil Sued, and Don Clucas. Development of metallographic etchants for the microstructure evolution of a6082-t6 BFSW welds. *Metals*, 7(10):423, October 2017. doi: 10.3390/met7100423. URL `https://doi.org/10.3390/met7100423`. 95

[135] S. T. Amancio-Filho, S. Sheikhi, J. F. dos Santos, and C. Bolfarini. Preliminary study on the microstructure and mechanical properties of dissimilar friction stir welds in aircraft aluminium alloys 2024-T351 and 6056-T4. *Journal of Materials Processing Technology*, 206(1-3):132–142, sep 2008. ISSN 0924-0136. doi: 10.1016/J.JMATPROTEC.2007.12.008. 102

[136] Rajiv Sharan Mishra, Partha Sarathi De, and Nilesh Kumar. *Friction Stir Welding and Processing*. Springer International Publishing, 2014. doi: 10.1007/978-3-319-07043-8. URL `https://doi.org/10.1007/978-3-319-07043-8`. 102

[137] T. Long, W. Tang, and A. P. Reynolds. Process response parameter relationships in aluminium alloy friction stir welds. *Science and Technology of Welding and Joining*, 12(4):311–317, May 2007. doi: 10.1179/174329307x197566. URL `https://doi.org/10.1179/174329307x197566`. 103

[138] A. Simar, Y. Bréchet, B. de Meester, A. Denquin, and T. Pardoen. Sequential modeling of local precipitation, strength and strain hardening in friction stir

welds of an aluminum alloy 6005a-t6. *Acta Materialia*, 55(18):6133–6143, October 2007. doi: 10.1016/j.actamat.2007.07.012. URL `https://doi.org/10.1016/j.actamat.2007.07.012`. 103

[139] YS Sato, Y Kurihara, and H Kokawa. Microstructural characteristics of dissimilar butt friction stir welds of aa7075 and aa2024. In *Proc. 6th Int. FSW Symp., Saint-Sauveur, Que., Canada*, 2006. 103

[140] A. Simar, Y. Bréchet, B. de Meester, A. Denquin, and T. Pardoen. Microstructure, local and global mechanical properties of friction stir welds in aluminium alloy 6005a-t6. *Materials Science and Engineering: A*, 486(1-2):85–95, July 2008. doi: 10.1016/j.msea.2007.08.041. URL `https://doi.org/10.1016/j.msea.2007.08.041`. 105

[141] D LASSANCE, D FABREGUE, F DELANNAY, and T PARDOEN. Micromechanics of room and high temperature fracture in 6xxx al alloys. *Progress in Materials Science*, 52(1):62–129, January 2007. doi: 10.1016/j.pmatsci.2006.06.001. URL `https://doi.org/10.1016/j.pmatsci.2006.06.001`. 120

[142] Zhiyong Wang, Hao Wu, Kai Kang, Shibin Wang, Yuehua Li, Weijie Hou, Hussain Riaz, Lin'an Li, and Chuanwei Li. DIC/moiré hybrid method based on regular patterns for deformation measurement. *Optics Express*, 27(13):18435, June 2019. doi: 10.1364/oe.27.018435. URL `https://doi.org/10.1364/oe.27.018435`. 131

[143] A A M Da Silva, E. Arruti, G. Janeiro, E. Aldanondo, P. Alvarez, A. Echeverria, A. A.M. da Silva, E. Arruti, G. Janeiro, E. Aldanondo, P. Alvarez, and A. Echeverria. Material flow and mechanical behaviour of dissimilar AA2024-T3 and AA7075-T6 aluminium alloys friction stir welds. *Materials and Design*, 32(4): 2021–2027, 2011. ISSN 02641275. doi: 10.1016/j.matdes.2010.11.059. URL `http://dx.doi.org/10.1016/j.matdes.2010.11.059http://www.sciencedirect.com/science/article/pii/S0261306910006850`. 148

[144] L. E. Murr. A review of FSW research on dissimilar metal and alloy systems. *Journal of Materials Engineering and Performance*, 19(8):1071–1089, 2010. ISSN 10599495. doi: 10.1007/s11665-010-9598-0. 148

[145] A. Simar, C. Jonckheere, K. Deplus, T. Pardoen, and B. de Meester. Comparing similar and dissimilar friction stir welds of 2017–6005A aluminium alloys. *Science and Technology of Welding and Joining*, 15(3):254–259, 2010. ISSN 1362-1718. doi: 10.1179/136217110x12665048207737. 148

[146] M.-N. Avettand-Fènoël, R. Taillard, and G. Ji. *Quality of interfaces in Cu/Al dissimilar friction-stirred welds*, volume 706-709. 2012. ISBN 9783037853030. doi: 10.4028/www.scientific.net/MSF.706-709.959.

[147] H. Jamshidi Aval, S. Serajzadeh, N.A. Sakharova, A.H. Kokabi, and A. Loureiro. A study on microstructures and residual stress distributions in dissimilar friction-stir welding of AA5086-AA6061. *Journal of Materials Science*, 47(14):5428–5437, 2012. doi: 10.1007/s10853-012-6430-2.

[148] E.E. Feistauer, L.A. Bergmann, L.S. Barreto, and J.F. dos Santos. Mechanical behaviour of dissimilar friction stir welded tailor welded blanks in al-mg alloys for marine applications. *Materials and Design*, 59:323–332, 2014. doi: 10.1016/j.matdes.2014.02.042.

[149] M. I. Costa, D. Verdera, C. Leitão, and D. M. Rodrigues. Dissimilar friction stir lap welding of AA 5754-H22/AA 6082-T6 aluminium alloys: Influence of material properties and tool geometry on weld strength. *Materials and Design*, 87:721–731, 2015. ISSN 18734197. doi: 10.1016/j.matdes.2015.08.066. URL `http://dx.doi.org/10.1016/j.matdes.2015.08.066`.

[150] E.E. Feistauer, L. Bergmann, and J.F. Dos Santos. *Performance of friction stir welded Tailor welded blanks in AA5059 and AA6082 alloys for marine applications*, volume 710. 2016. ISBN 9783038356219. doi: 10.4028/www.scientific.net/KEM.710.91.

[151] W. Noh, J. H. Song, I. J. Jang, S. H. Gwak, C. Kim, and C. Y. Jung. Numerical and experimental investigation for formability of friction stir welded dissimilar aluminum alloys. *IOP Conference Series: Materials Science and Engineering*, 418(1), 2018. ISSN 1757899X. doi: 10.1088/1757-899X/418/1/012056.

[152] Tianhao Wang, Mageshwari Komarasamy, Kaimiao Liu, and Rajiv S. Mishra. Friction stir butt welding of strain-hardened aluminum alloy with high strength steel. *Materials Science and Engineering A*, 737(May):85–89, 2018. ISSN 09215093. doi: 10.1016/j.msea.2018.09.035. URL `https://doi.org/10.1016/j.msea.2018.09.035`.

[153] G. Peng, Y. Ma, J. Hu, W. Jiang, Y. Huan, Z. Chen, and T. Zhang. Nanoindentation Hardness Distribution and Strain Field and Fracture Evolution in Dissimilar Friction Stir-Welded AA 6061-AA 5A06 Aluminum Alloy Joints. *Advances in Materials Science and Engineering*, 2018, 2018. doi: 10.1155/2018/4873571.

[154] E.E. Feistauer, L.A. Bergmann, and J.F. dos Santos. Effect of reverse material flow on the microstructure and performance of friction stir welded T-joints of an Al-Mg alloy. *Materials Science and Engineering A*, 731:454–464, 2018. doi: 10.1016/j.msea.2018.06.056.

[155] G. Peng, Y. Ma, J. Hu, W. Jiang, Y. Huan, Z. Chen, and T. Zhang. Nanoindentation Hardness Distribution and Strain Field and Fracture Evolution in Dissimilar Friction Stir-Welded AA 6061-AA 5A06 Aluminum Alloy Joints. *Advances in Materials Science and Engineering*, 2018, 2018. doi: 10.1155/2018/4873571.

[156] Alessandro Barbini, Jan Carstensen, and Jorge F. dos Santos. Influence of a non-rotating shoulder on heat generation, microstructure and mechanical properties of dissimilar AA2024/AA7050 FSW joints. *Journal of Materials Science and Technology*, 34(1):119–127, 2018. ISSN 10050302. doi: 10.1016/j.jmst.2017.10.017. URL `http://dx.doi.org/10.1016/j.jmst.2017.10.017`.

[157] Tianhao Wang, Harpreet Sidhar, Rajiv S. Mishra, Yuri Hovanski, Piyush Upadhyay, and Blair Carlson. Effect of hook characteristics on the fracture behaviour of dissimilar friction stir welded aluminium alloy and mild steel sheets. *Science*

and Technology of Welding and Joining, 24(2):178–184, 2019. ISSN 17432936. doi: 10.1080/13621718.2018.1503801. URL `https://doi.org/13621718.2018.1503801`.

[158] Najib A. Muhammad and Chuan Song Wu. Evaluation of capabilities of ultrasonic vibration on the surface, electrical and mechanical behaviours of aluminium to copper dissimilar friction stir welds. *International Journal of Mechanical Sciences*, 183 (January):105784, 2020. ISSN 00207403. doi: 10.1016/j.ijmecsci.2020.105784. URL `https://doi.org/10.1016/j.ijmecsci.2020.105784`.

[159] I. Scheider, A. Barbini, and J.F. dos Santos. Numerical residual strength prediction of stationary shoulder friction stir welding structures. *Engineering Fracture Mechanics*, 230, 2020. doi: 10.1016/j.engfracmech.2020.107010.

[160] Harish Suthar, Anirban Bhattacharya, and Surajit Kumar Paul. Local deformation response and failure behavior of AA6061-AA6061 and AA6061-AA7075 friction stir welds. *CIRP Journal of Manufacturing Science and Technology*, 30:12–24, 2020. ISSN 17555817. doi: 10.1016/j.cirpj.2020.03.006. URL `https://doi.org/10.1016/j.cirpj.2020.03.006`. 148, 149

[161] M. Geyer, V. Vidal, T. Pottier, C. Boher, and F. Rézaï-Aria. Investigations on the material flow and the role of the resulting hooks on the mechanical behaviour of dissimilar friction stir welded Al2024-T3 to Ti-6Al-4V overlap joints. *Journal of Materials Processing Technology*, 292, 2021. doi: 10.1016/j.jmatprotec.2021.117057.

[162] Harish Suthar, Anirban Bhattacharya, and Surajit Kumar Paul. Determination of local constitutive properties in similar and dissimilar friction stir welded joints from DIC based surface strain measurement in two mutually perpendicular surfaces. *Mechanics of Materials*, 160(May):103930, 2021. ISSN 01676636. doi: 10.1016/j.mechmat.2021.103930. URL `https://doi.org/10.1016/j.mechmat.2021.103930`.

[163] I. Hadji, R. Badji, M. Gaceb, and B. Cheniti. Dissimilar FSW of AA2024 and AA7075: effect of materials positioning and tool deviation value on microstructure, global and local mechanical behavior. *International Journal of Advanced Manufacturing Technology*, 118(7-8):2391–2403, 2022. doi: 10.1007/s00170-021-08120-0.

[164] Y. Uematsu, T. Kakiuchi, K. Niimi, and P.D.T. Caiza. Local strain analysis under quasi-static tensile loading in Al/steel dissimilar friction stir weld by a digital image correlation method. *International Journal of Advanced Manufacturing Technology*, 120(1-2):349–360, 2022. doi: 10.1007/s00170-021-08481-6.

[165] Harish Suthar, Anirban Bhattacharya, and Surajit Kumar Paul. DIC-based approach to predict post necking behavior for AA6061, AA7075 and their friction stir welded joints. *Mechanics of Materials*, 172:104364, sep 2022. ISSN 0167-6636. doi: 10.1016/J.MECHMAT.2022.104364.

[166] J. Hiscocks, B.J. Diak, A.P. Gerlich, and M.R. Daymond. Strain localisation and failure of dissimilar magnesium-based alloy friction stir welds. *Science and Technology of Welding and Joining*, 23(7):628–634, 2018. doi: 10.1080/13621718.2018.1450704. 148, 149

[167] D. Texier, Y. Zedan, T. Amoros, E. Feulvarch, J.C. Stinville, and P. Bocher. Near-surface mechanical heterogeneities in a dissimilar aluminum alloys friction stir welded joint. *Materials and Design*, 108:217–229, 2016. doi: 10.1016/j.matdes.2016.06.091. 149

[168] M. Masoumi Khalilabad, Y. Zedan, D. Texier, M. Jahazi, and P. Bocher. Effect of heat treatments on microstructural and mechanical characteristics of dissimilar friction stir welded 2198/2024 aluminum alloys. *Journal of Adhesion Science and Technology*, 36(3):221–239, 2022. doi: 10.1080/01694243.2021.1917868. 149

[169] Fanny Mas, Guilhem Martin, Pierre Lhuissier, Yves Bréchet, Catherine Tassin, François Roch, Patrick Todeschini, and Aude Simar. Heterogeneities in local plastic flow behavior in a dissimilar weld between low-alloy steel and stainless steel. *Materials Science and Engineering: A*, 667:156–170, jun 2016. ISSN 0921-5093. doi: 10.1016/J.MSEA.2016.04.082. 149

[170] Yanis Balit, Eric Charkaluk, and Andrei Constantinescu. Digital image correlation for microstructural analysis of deformation pattern in additively manufactured 316L thin walls. *Additive Manufacturing*, 31:100862, jan 2020. ISSN 2214-8604. doi: 10.1016/J.ADDMA.2019.100862.

[171] C. C. Tasan, J. P.M. Hoefnagels, M. Diehl, D. Yan, F. Roters, and D. Raabe. Strain localization and damage in dual phase steels investigated by coupled in-situ deformation experiments and crystal plasticity simulations. *International Journal of Plasticity*, 63:198–210, dec 2014. ISSN 0749-6419. doi: 10.1016/J.IJPLAS.2014.06.004. 149

[172] Noor Zaman Khan, Arshad Noor Siddiquee, Zahid A. Khan, and Suha K. Shihab. Investigations on tunneling and kissing bond defects in FSW joints for dissimilar aluminum alloys. *Journal of Alloys and Compounds*, 648:360–367, nov 2015. ISSN 0925-8388. doi: 10.1016/J.JALLCOM.2015.06.246. 150

[173] M. Bourcier, M. Bornert, A. Dimanov, E. Héripré, and J. L. Raphanel. Multiscale experimental investigation of crystal plasticity and grain boundary sliding in synthetic halite using digital image correlation. *Journal of Geophysical Research: Solid Earth*, 118(2):511–526, 2013. ISSN 21699356. doi: 10.1002/jgrb.50065. 150

[174] W. Boas and M. Hargreaves. On the inhomogeneity of plastic deformation in the crystals of an aggregate. *Proceedings of the Royal Society of London. Series A. Mathematical and Physical Sciences*, 193(1032):89–97, April 1948. doi: 10.1098/rspa.1948.0035. URL `https://doi.org/10.1098/rspa.1948.0035`. 153

[175] Jaap Schijve. *Fatigue of structures and materials.* Springer, 2009. 162

[176] Lan Zhang, Huilong Zhong, Shengci Li, Hongjin Zhao, Jiqiang Chen, and Liang Qi. Microstructure, mechanical properties and fatigue crack growth behavior of friction stir welded joint of 6061-T6 aluminum alloy. *International Journal of Fatigue*, page 105556, feb 2020. ISSN 0142-1123. doi: 10.1016/J.IJFATIGUE.2020.105556. URL `https://www.sciencedirect.com/science/article/pii/S0142112320300876`. 170

[177] Gerd Lütjering and James C Williams. *Titanium.* Springer Science & Business Media, 2007. 180, 181, 182

[178] Bernard DE GELAS, Marcel ARMAND, Léon SERAPHIN, and Roland TRICOT. Titane et alliages de titane. *Techniques de l'ingénieur*, 1976. 180, 183

[179] Yves Combres. Propriétés du titane et de ses alliages. *Techniques de l'ingénieur*, 2010. 182

[180] A.L. Pilchak, D.M. Norfleet, M.C. Juhas, and J.C. Williams. Friction stir processing of investment-cast ti-6al-4v: Microstructure and properties. *Metallurgical and Materials Transactions A*, 39(7):1519–1524, July 2007. doi: 10.1007/s11661-007-9236-0. URL `https://doi.org/10.1007/s11661-007-9236-0`. 183, 194

[181] Paul D. Edwards and M. Ramulu. Comparative study of fatigue and fracture in friction stir and electron beam welds of 24 mm thick titanium alloy ti-6al-4 v. *Fatigue and Fracture of Engineering Materials and Structures*, 39(10):1226–1240, March 2016. doi: 10.1111/ffe.12434. URL `https://doi.org/10.1111/ffe.12434`. 183

[182] Sungook Yoon, Rintaro Ueji, and Hidetoshi Fujii. Effect of initial microstructure on ti–6al–4v joint by friction stir welding. *Materials and Design*, 88:1269–1276, December 2015. doi: 10.1016/j.matdes.2015.09.128. URL `https://doi.org/10.1016/j.matdes.2015.09.128`. 183

[183] Sungook Yoon, Rintaro Ueji, and Hidetoshi Fujii. Microstructure and texture distribution of ti–6al–4v alloy joints friction stir welded below beta-transus temperature. *Journal of Materials Processing Technology*, 229:390–397, March 2016. doi: 10.1016/j.jmatprotec.2015.09.041. URL `https://doi.org/10.1016/j.jmatprotec.2015.09.041`. 183

[184] S. Mironov, Y. Zhang, Y.S. Sato, and H. Kokawa. Crystallography of transformed beta microstructure in friction stir welded ti–6al–4v alloy. *Scripta Materialia*, 59 (5):511–514, September 2008. doi: 10.1016/j.scriptamat.2008.04.038. URL `https://doi.org/10.1016/j.scriptamat.2008.04.038`. 183

[185] Yu Zhang, Yutaka S. Sato, Hiroyuki Kokawa, Seung Hwan C. Park, and Satoshi Hirano. Microstructural characteristics and mechanical properties of ti–6al–4v friction stir welds. *Materials Science and Engineering: A*, 485(1-2):448–455, June 2008. doi: 10.1016/j.msea.2007.08.051. URL `https://doi.org/10.1016/j.msea.2007.08.051`. 183

[186] L.H. Wu, D. Wang, B.L. Xiao, and Z.Y. Ma. Tool wear and its effect on microstructure and properties of friction stir processed ti–6al–4v. *Materials Chemistry and Physics*, 146(3):512–522, August 2014. doi: 10.1016/j.matchemphys.2014.04.002. URL `https://doi.org/10.1016/j.matchemphys.2014.04.002`. 183, 184

[187] Zhihua Song, Kazuhiro Nakata, Aiping Wu, Jinsun Liao, and Li Zhou. Influence of probe offset distance on interfacial microstructure and mechanical properties of friction stir butt welded joint of ti6al4v and a6061 dissimilar alloys. *Materials and Design*, 57:269–278, May 2014. doi: 10.1016/j.matdes.2013.12.040. URL `https://doi.org/10.1016/j.matdes.2013.12.040`. 186

[188] Y.C. Chen and K. Nakata. Microstructural characterization and mechanical properties in friction stir welding of aluminum and titanium dissimilar alloys. *Materials and Design*, 30(3):469–474, March 2009. doi: 10.1016/j.matdes.2008.06.008. URL `https://doi.org/10.1016/j.matdes.2008.06.008`. 185, 188

[189] Z.W. Chen and S. Yazdanian. Microstructures in interface region and mechanical behaviours of friction stir lap al6060 to ti–6al–4v welds. *Materials Science and Engineering: A*, 634:37–45, May 2015. doi: 10.1016/j.msea.2015.03.017. URL `https://doi.org/10.1016/j.msea.2015.03.017`. 188, 189, 198, 202

[190] Yu hua CHEN, Quan NI, and Li ming KE. Interface characteristic of friction stir welding lap joints of ti/al dissimilar alloys. *Transactions of Nonferrous Metals Society of China*, 22(2):299–304, February 2012. doi: 10.1016/s1003-6326(11)61174-6. URL `https://doi.org/10.1016/s1003-6326(11)61174-6`. 187, 198, 199

[191] Morgane Geyer, Vanessa Vidal, Thomas Pottier, Christine Boher, and Farhad Rézaï-Aria. Investigations on the material flow and the role of the resulting hooks on the mechanical behaviour of dissimilar friction stir welded al2024-t3 to ti-6al-4v overlap joints. *Journal of Materials Processing Technology*, 292:117057, 2021. ISSN 0924-0136. doi: https://doi.org/10.1016/j.jmatprotec.2021.117057. URL `https://www.sciencedirect.com/science/article/pii/S0924013621000170`.

[192] Mingrun Yu, Hongyun Zhao, Zhihua Jiang, Fan Guo, Li Zhou, and Xiaoguo Song. Microstructure and mechanical properties of friction stir lap AA6061-ti6al4v welds. *Journal of Materials Processing Technology*, 270:274–284, August 2019. doi: 10.1016/j.jmatprotec.2019.03.007. URL `https://doi.org/10.1016/j.jmatprotec.2019.03.007`. 185, 195, 199, 202, 206

[193] Julie Maisonneuve. *Fabrication directe de pièces aéronautique en TA6V et IN718*. Theses, Ecole Nationale Supérieure des Mines de Paris, November 2008. URL `https://pastel.archives-ouvertes.fr/tel-03173887`. thèse confidentielle jusqu'en 2011. 193

[194] C.R. Brooks. *Heat Treatment, Structure, and Properties of Nonferrous Alloys*. American Society for Metals, 1982. ISBN 9780871701381. URL `https://books.google.be/books?id=E32IAQAACAAJ`. 192

ECOLE
DOCTORALE

Titre : Soudures par friction malaxage dissimilaire Al6061/Al7075: procédé, propriétés statiques et en fatigue

Mots clés : Aluminium, Friction Malaxage, Traction, Fatigue, Soudage, Titane

Résumé : Le soudage par friction-malaxage, appelé aussi Friction Stir Welding (FSW), est une technique de soudage sans fusion ni ajout de matière. Breveté pour la première fois en 1991 par le Welding Institute (Cambridge, Royaume-Uni), il consiste à mélanger le matériau des deux pièces à assembler par déformation plastique. Le soudage par friction-malaxage permet des connexions homogènes ou bi-matériaux avec une légère diminution des caractéristiques mécaniques du joint (par rapport aux assemblages conventionnels) ainsi qu'une excellente répétabilité. Cette technologie présente l'avantage de ne pas utiliser de consommable et d'être adaptable à une machine-outil conventionnelle, par exemple un centre d'usinage. Initialement conçu sur les aluminiums, ce procédé est également applicable sur des alliages à bas point de fusion tels que le cuivre ou encore le magnésium. Des nombreux exemples d'applications industrielles impliquant l'utilisation de ces matériaux avec le FSW existent. Néanmoins, de nombreuses questions restent en suspens quand à certaines propriétés mécaniques des assemblages d'aluminium, particulièrement dans le domaine de la fatigue, et plus particulièrement lorsque des assemblages dit ≪ dissimilaires ≫ (contenant plusieurs alliages d'aluminiums) sont concernés. Après une introduction sur le procédé en lui même, ainsi que la présentation d'un panel d'applications, les principaux résultats de la littérature concernant les propriétés mécaniques et microstructurales de joints d'aluminium réalisés par FSW sont présentés. Un attention particulière est portée sur l'impact des paramètres procédés sur les différentes propriétés précédentes. Un chapitre détaille alors la mise au point de paramètres procédés dans le cadre du soudage bout à bout d'AA6061 et AA7075 : méthodologie, contrôle des joints et aspects thermiques. S'en suit alors la caractérisation des joints obtenus (dissimilaires et similaires) par divers moyens : microscopie optique, filiation de dureté Vickers et essais de traction avec l'utilisation de corrélation d'image (DIC). Des liens sont alors établis entre les différentes observations et les paramètres utilisés lors de la fabrication des joints. Un essai de traction sous microscopie électronique est alors présenté pour étudié en détail la déformation plastique au sein de la zone de soudage. Enfin, des essais de fatigue sont réalisés pour caractériser plusieurs joints et un lien est établi entre la température lors du soudage et la morphologie de la zone soudée et la vie en fatigue. Des essais exploratoires de soudures aluminium titane sont également présentés et caractérisés en annexe.

Title : Dissimilar Al6061 to Al7075 friction stir welds: processing, static and fatigue properties

Keywords : Aluminium, Friction Stir, Tensile, Fatigue, Welding, Titanium

Abstract : Friction Stir Welding (FSW) is a solid state (without fusion) welding technique involving no filler material. Patented for the first time in 1991 by The Welding Institute (Cambridge, UK), it consists in the mixing of the material of two parts to be assembled by plastic deformation. Friction Stir Welding allows homogeneous or bi-material joints with a small decrease in the mechanical properties (compared to conventional assembly processes) as well as an excellent repeatability. This technology does not use consumables and is adaptable to conventional CNC machines. Initially conceived for aluminium alloys, this process is applicable to other alloys with low melting temperatures, such as copper or magnesium. Numerous industrial examples using FSW on these alloys exist. Nevertheless, questions still remain regarding some mechanical properties of aluminium assemblies, particularly in the case of fatigue of so called dissimilar joints (welds containing multiple aluminium alloys). After a brief introduction on the process in and of itself and a wide range of industrial applications, majors results from the literature regarding mechanical and microstructural properties of aluminium FSW joints are presented. A particular attention is devoted to the impact of process parameters on previously described properties. A chapter first describes the methodology used to establish a process window for AA6061/AA7075: welds quality control and thermal aspects are described as well. It is then followed by the characterization of said joints (similar and dissimilar) by various means: optical microscopy, Vicker hardness measurements and tensile testing using Digital Image Correlation (DIC). Links between these properties and process parameters used in the manufacturing of the joints are established. A tensile test carried out inside a scanning electron microscope is presented in order to analyze local plastic deformation distribution inside the stir zone of a dissimilar joint. Finally, fatigue testing is carried out on some samples and relationships are established between thermal input during welding as well as stir zone morphology and fatigue life properties. Exploratory aluminium and titanium friction stir welds are presented and characterized in the appendix.

Institut Polytechnique de Paris
91120 Palaiseau, France